2012

Bolt profile configuration and load transfer capacity optimisation

Chen Cao
University of Wollongong

Bolt Profile Configuration and Load Transfer Capacity Optimisation

A thesis submitted in fulfillment of the

requirements for the award of the degree

DOCTOR OF PHILOSOPHY

from

UNIVERSITY OF WOLLONGONG

By

CHEN CAO

B.Sc, Mathematics B.Eng. Mining

School of Civil, Mining and Environmental Engineering

2012

AFFIRMATION

I, Chen Cao, declare that this thesis, submitted in fulfillment of the requirements for the award of Doctor of Philosophy, in the School of Civil, Mining and Environmental Engineering, Faculty of Engineering, University of Wollongong, is wholly my own work unless otherwise referenced or acknowledged. The thesis was completed under the supervision of Dr. J. Nemcik and Prof. N. I. Aziz and has not been submitted for qualification at any other academic institution.

Chen Cao

2012

PUBLICATIONS

The following publications are the result of this thesis:

1. Aziz, N, Nemcik, J, **Cao, C** and Jalalifar, H, 2009. Bolt Profile configuration and load transfer capacity optimisation, *in proceedings* 28th *International Conference on Ground Control in Mining*, August, 2-4, Morgantown, WV, USA, pp 48-52. http://icgcm.conferenceacademy.com/papers/detail.aspx?subdomain=icgcm&iid=225

2. **Cao, C**, Nemcik, J and Aziz, N, (2010), Advanced numerical modelling methods of rock bolt performance in underground mines, in Aziz, N (ed), 10th Underground Coal Operators' Conference, University of Wollongong & the Australasian Institute of Mining and Metallurgy, 2010, 326-329.

3. **Cao C**, J Nemcik, N Aziz, 2011. Improvement of the rock bolt profile using analytical and numerical methods, *in proceedings 11th Underground Coal operators Conference*, Wollongong, February 10/11, ISBN 978-1-921522-16 -1, pp 307-314, (Eds. N Aziz, B Kinninmonth, Jan Nemcik, Ting Ren), pp 141-147. http://ro.uow.edu.au/coal/350/

4. **Cao C.**, Nemcik, J, Aziz, N,(2011), Analytical derivations of bolt profile shear strength, *in Proceedings 12h ISRM International Congress ob Rock Mechanics*, Beijing, China, 18-21, October. Pp 1473-1476. Published in Harmonising Rock Engineering and the Environment –Qian and Zhou (eds), 2012 Taylor and Francis Group, London, ISBN, 978-0-415-80444-8, pp1473-1476.

5. **Cao, C.,** J Nemcik, Aziz N. 2011. Analytical and numerical study of steel bolt profile to optimise shear strength of rock bolt. *Proceedings of the 2nd International Symposium on Computational Geomechanics (COMGEO II*), Cavtat-Dubrovnik, 27-29 April, 2011, pp 893-903.

6. **Cao, C**, Nemcik, J, Aziz, N, and Ren, T, (2012). Failure modes of rock bolting, *in proceedings, in proceedings 11th Underground Coal operators Conference*, Wollongong, February 10/11, ISBN 978-1-921522-57 -4 (Eds. N Aziz, B Kinninmonth, Jan Nemcik, Ting Ren) , pp138-154. http://ro.uow.edu.au/coal/401/

7. **Cao**, **C.** J. Nemcik, N. Aziz and T. Ren, (2012), A study of rock bolting failure modes, International Journal of Mining Science and Technology (in press).

8. **Cao**, **C.** J. Nemcik, N. Aziz and T. Ren, (2012), Analytical study of steel bolt profile and its influence on bolt load transfer, International Journal of Rock Mechanic and Mining Science (in press).

9. **Cao**, **C.** J. Nemcik and N. Aziz, (2013), An Investigation of Dilational Slip Angle of Rebar Bolt under Axial Loading, 13th Coal Operators' Conference, University of Wollongong & the Australasian Institute of Mining and Metallurgy (in press)

ACKNOWLEDGEMENTS

I wish to express my sincere gratitude to my thesis supervisor Dr Jan Nemcik, faculty of engineering University of Wollongong, for his supervision, generous support, encouragement, and guidance provided during the research.

I would also like to express my sincere thanks to Prof. Naj. I. Aziz, my thesis co-supervisor for his helpful advice in this thesis, and also providing the necessary facilities and financial support to conduct my research work during three years.

I also would like to thank the technical staffs in the School of Civil, Mining and Environmental Engineering, especially Colin Devenish, for laboratory assistance.

A special thank is given to Bob Kinninmonth for his final correction of grammatical and spelling errors.

Forever, I am indebted to my family members my mother and my brother, especially my beloved wife and son. Without their love and support, I would never reach this point.

ABSTRACT

Rapid advances in rock bolting technology over the past four decades have firmly established the usage of rock bolts as the primary rock reinforcement system in underground mine support design.

Experimental studies have confirmed that bolt surface profile plays an important role on load transfer of fully grouted rockbolting systems. However, there are no related theories nor mechanical models to explain these experimental observations and to identify the role of bolt profile in the load transfer mechanisms. In traditional rockbolting mechanism studies, the shear resistance caused by the bolt profile reacting with surrounding materials is termed “mechanical interlock” of the system. The effect of the mechanical interlock is integrated into proposed load transfer models by various manners, such as zigzag dilation, supposed shear stress-displacement behaviour, or supposed shear stress-strain behaviour. The interaction between the bolt rib profile and surrounding mediums, which is the origin of mechanical interlock, is ignored in all analytical approaches.

This research work provides a fundamental understanding of the role of the bolt profile and its influence on rock bolting failure. In addition, the research outcomes provide theoretical support for achieving optimum bolt design in engineering applications.

A series of experimental studies were undertaken to identify the interactions between the bolt profile and the resin under axial or lateral loading. Accordingly, the failure modes of the resin around a bolt profile have been classified into two categories: “parallel shear failure” and “dilational slip failure”. Parallel shear failure of the resin is characterised by a cylinder failure surface, which just passes through the tips of the bolt profiles. It occurs if the bolt has closely spaced profiles, or is confined by high radial stiffness materials. Dilational slip failure is characterised by lodged resin in front of the bolt profile forming a conical shaped failure surface. It occurs in lower confinement stiffness (soft rock) or when rib spacing is large.

An achievement of this research work was to formulate dilational slip failure of rock bolting. The governing equation for this kind of failure mode has been derived as:

$$F = \pi(R^2 - r^2)\left[\frac{\cos\phi}{\sin(i)\ \cdot \cos(i+\phi)} \cdot c + \frac{\tan(i+\phi)}{\sin(i)} \cdot p\right]$$

Where F is bolt axial load when failure occurs, R and r are bolt rib geometrical parameters, c and ϕ are the mechanical properties of the grouting material, i is dilational slip face angle and p is radial pressure. Once the dilational slip face angle, i, is acknowledged, the influence of bolt profile geometry on rock bolting failure can be analytically evaluated.

The domain of *dilational slip face angle*, which is different to *bolt rib face angle*, can be estimated by derived equation:

$$\sin(\phi + 2i) \geq \frac{R^2 - r^2}{RL}\cos\phi + \sin\phi$$

Where L is the rib geometric parameter. In addition, the most vulnerable surface of dilational slip failure has also been predicted. Consequently, the influence of the bolt profile in load transfer mechanism of rockbolting system can be predicted using the governing equation of dilational slip failure mode.

Furthermore, the direct parallel shear failure of rock bolting has been investigated using a stress analysis method. The stress field within the resin annulus introduced by the axial load of the bolt has been formulated based on the half space theory. That is, parallel shear failure will occur if:

$$T_0 = \frac{F}{\pi}(G_2 - G_1 tan\phi)$$

Where:

T_0 = the initial shear resistance of the failure surface;

$$G_1 = (sin\theta - sin2\theta)[m(\pi - \theta - \gamma) + ksin\theta + \gamma cos\theta] + (\cos2\theta + sin^2 2\theta)\gamma sin\theta$$
$$+ksin^2\theta(2sin\theta sin2\theta - 1) + 2sin^2\theta(kcos\theta - km + m\,lnm - \gamma sin\theta)$$
$$G_2 = \gamma sin\theta(\sin\theta - \sin2\theta cos2\theta) + cos2\theta[m(\pi - \theta - \gamma) + ksin\theta + \gamma cos\theta]$$
$$+ ksin\theta\cos^2 2\theta - sin2\theta cos\theta(kcos\theta - km + m\,lnm - \gamma sin\theta)$$

θ is bolt rib face angle

k, m and γ are geometric parameters of the bolt profile.

Parametric studies of the bolt profile have also been undertaken. Results show that smaller rib face angle or smaller profile height to length ratio bolts are favourable to transfer load radially. Hence, they should be used in hard rock environments. Large rib face angle with higher rib height to length ratio bolts will transfer the major part of axial load into the resin annulus at a direction parallel to the bolt axis. They should be used in soft rock conditions.

TABLE OF CONTENTS

CHAPTER THREE

REVIEW OF ROCK BOLTS SUBJECTED TO AXIAL LOADING

CHAPTER FOUR

LABORATORY STUDIES AND MATERIAL PROPERTIES

CHAPTER FIVE

FAILURE MODES ANALYSIS AND LOAD PREDICTION IN BOLT PULL OUT TESTS

CHAPTER SIX

BOLT PROFILE ANALYSIS USING HALF SPACE METHOD

CHAPTER SEVEN

CONCLUSIONS AND RECOMENDATIONS

TABLE OF FIGURES

LIST OF TABLES

LIST OF SYMBOLS AND ABBREVIATIONS

SYMBOLS

σ_b	Bolt axial stress
σ_c	UCS of rock
σ_y	Yield stress of bolt
σ_n	Normal stress on joint and
σ_{ec}	Failure stress of the bolt
b	Spacing between adjacent rows of bolts,
L	Roof span,
N	Bolt number per row,
l	Bolt length,
t_{avg}	Average thickness of the bolted roof, and
W_{avg}	Average unit weight of the bolted rocks.
φ_j	Friction angle of the joint
T	Shear force carried by bolt;
d_b	Bolt diameter;
β	Angle between bolt and normal to the joint.
p	Axial load corresponding to the yield strength due to shear displacement
A_j	Joint area
T_b	Reinforcement effect
T_d	Dowel effect
T_f	Friction of joint
p_u	Bearing capacity of the grout or rock

t	Axial bolt load in the position of the plastic moment,
t_y	Axial load corresponding to the yield strength
i	Dilation angle
T_u	Ultimate strength of the bolt
t_r	Load induced in the bolt
Q	Force due to dowel effect
α	Angle between the joint and the dowel axis and
F	Global reinforced joint resistance.
Q_{oe}	Shear force acting at point O at the yield stress of the bolt
N_{oe}	Axial force acting at shear plane at the yield stress of the bolt
Q_{of}	Shear force acting at shear plane at failure of the bolt
N_{of}	Axial force acting at shear plane at failure of the bolt
k_s	Support stiffness
u_r	Axial displacement of the bolt;
s	Measurement of the strength loss immediately after peak strength.
a	Tunnel radius;
S_T	Tangential (circumferential) bolt spacing
S_L	Longitudinal bolt spacing.
σ_r	Original radial stress of the rock mass
σ_t	Original tangential stress of the rock mass
σ_{mr}	Radial and stress caused by the rock bolt
σ_{mt}	Tangential stress caused by the rock bolt
v	Poisson's ratio of the rock mass
r_g	Radius of the grout borehole
G_g	Shear modulus of the grout mortar

G_r Rock rigidity modulus

E_b Bolt elastic modulus

E_r Rock elastic modulus

E_g Grout elastic modulus

τ_x Shear or bond stress

$\sigma_r(x)$ Radial stress at the bolt − grout interface

i_0 Dilation angle at the bolt/grout interface

β Reduction coefficient of dilation angle

r_e Radius of the cracked zone

u_0 Maximum dilation ≈ teeth height

A Interface contact area;

ϕ_{g-s} Sliding friction between grout and steel

ϕ_g Internal angle of friction for grout

c_g Grout cohesion.

u_a Axial displacement

C Torsional rigidity of cable;

l Pitch length of cable bolt

L_f Free length of the cable between test and anchor sections

L_e Embedment length of cable bolt

L_s Sheared length of the grout flutes

v_{r0} Dilation generated by splitting without confinement

K_{r0} Radial stiffness immediately following splitting without confinement

P Ultimate pullout load,

d_g Diameter of the grout annulus

s_r	Residual shear strength
s_p	Peak shear strength
γ	Shear strain
r	Distance from axis
r_0	Radius of anchorage
τ_0	Shear stress of anchorage surface
s	Soil displacement.
$\bar{P}$	Normalised axial load
$\bar{\Delta}$	Normalised axial displacement
T_0	Initial shear resistance
p	Distributed normal load
q	Distributed shear load
θ	Bolt rib face angle
i	Dilational slip face angle
F1	Axial load to cause direct parallel shear failure
F2	Axail load to cause dilational slip
F3	Axial load to caused parallel shear failure after dilation

ABREVIATIONS

JRC	Joint roughness coefficient
JCS	Joint compressive strength

CMC	Continuous Mechanically Coupled
CFC	Continuous Frictionally Coupled
DMFC	Discreetly Mechanical or Frictionally Coupled
BSM	Bond Strength Model
ISS	Interfacial Shear Stress
RF	Reinforcement Factor
FLAC	Fast Lagrangian Analysis of Continua
RMR	Rock Mass Rate
UCS	Uniaxial Compression Strength
UTS	Uniaxial Tension Strength
FE	Finite Element
SETP	Short Encapsulation Pull Testing

CHAPTER ONE

INTRODUCTION

INTRODUCTION

1.1 GENERAL

The stability and improvement of underground excavations and surface slopes is of major concern to geotechnical engineers and mine operators. The conditions associated with rock instability of an excavation must be clearly understood so that stabilisation of the structure can be undertaken. Rock reinforcement belongs to the general category of improvement methods to increase the strength or decrease the deformability of a rock mass. In contemporary civil and mining engineering projects rock bolting forms effective system ground reinforcement. Various kinds of rock bolts are available to provide such effective and the principal support members.

Application of rock bolting as a ground support system has grown rapidly during the past four decades due to a better understanding of load transfer mechanisms and advances made in the bolt system technology. Bolts are used as permanent and temporary support systems in tunnelling and mining operations. In surface mining they are used to stabilise slopes and in underground workings they are used for roadway development, shaft sinking, and various stoping operations.

A rock reinforcement system increases the safety factor against crack initiation. Rock bolts are installed around openings in mines and tunnels to tie weaker layers to stronger ground stratification layers above, to prevent sagging and separation and to provide a reinforcement zone that makes greater use of a rocks mass strength to enable it to be self supporting.

The concept of a reinforcement system is extremely important. A reinforcement scheme is an arrangement of primary, secondary and tertiary reinforcement systems in various configurations. They may be un-tensioned, pre-tensioned or post-tensioned. A review of reinforcement systems (Windsor, 1997) has indicated that three classes of device have developed: rockbolt (generally less than 3 m), cable bolt (generally in the range from 3 to 15 m) and ground anchor (generally longer than 10 m). All of them comprise

four principal components as shown in Figure 1.1:

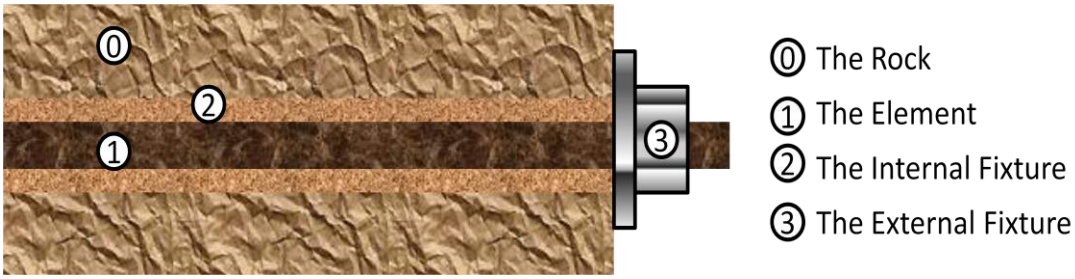

Figure 1.1 Four principal components of a reinforcement system, modified from Windsor (1997).

For reinforcement with a bolt, the reinforcing element refers to the bolt and the external fixture refers to the face plate and nut. The rock is not generally thought of as being a component of the reinforcement system, but has a great influence on behaviour of the system. The internal fixture is a medium, such as cementitious grout or resin for bolt encapsulation, or a mechanical action like friction at the bolt interface for frictionally coupled bolts. The internal fixture provides a coupling condition at the interface. With reference to the component of internal fixture, the reinforcement system has been catalogued into three fundamental types (Windsor and Thompson, 1993):

- Continuous Mechanically Coupled (CMC) systems,
- Continuous Frictionally Coupled (CFC) systems and
- Discreetly Mechanical or Frictionally Coupled (DMFC) system.

According to this classification system, cement and resin grouted bolts belong to the CMC system while split set and Swellex bolts belong to the CFC system. The third group can be anchored by a slit and wedge mechanism or an expansion shell.

Fully grouted rock anchors have been implemented extensively in a wide range of geotechnical and mining applications as temporary or permanent ground supports. To minimise roof failures, fully grouted rather than mechanically anchored bolts are increasingly being used in mines because grouted bolts have a greater area of anchorage. About 66% of nearly 100 million roof bolts installed in United States mines in 2011 were fully grouted resin bolts. Fully grouted rock bolts reinforce rock walls around underground excavations are very effective in closely jointed or soft rocks. A fully grouted reinforcement system transfers unstable fractured rock layers to self supported stable rock mass.

A grouted anchor is defined as a structural support comprised of a tendon which is inserted into a drilled hole and then grouted. Grouted steel anchors can be made from solid bar or stranded wire cables. Solid bars can be either smooth or deformed with the latter being further classified as either "threadbar" or "rebar". If not pretensioned, a fully grouted bolt is a passive roof support system, which is activated by the movement of the surrounding rock. To examine the effectiveness of the bolting anchorage system, the experimental studies such as pullout tests are often employed in laboratory and in field.

The load transfer concept is central to the understanding of reinforcement system behaviour and their effects on excavation stability. This concept is composed of basic mechanisms of load transfer from unstable region to a stable region via reinforcing element.

In a fully grouted rock bolt, the grout supplies a mechanism for transferring the load between the rock and reinforcing element. This redistribution of forces along the bolt is the result of movement in the rock mass, which transfers the load to the bolt via shear resistance in the grout. Therefore, the load transfer mechanism of a fully grouted rock bolt depends on the developed shear stress on the bolt-resin and resin-rock interfaces. In addition, peak shear stress capability and shear stress modulus of the interfaces determine the reaction of the bolt to the surrounding materials.

It is commonly accepted that the fully grouted bolt provides greater shear surface to transmit the load from rock to bolt and vice versa. In general, only resinous grouts can meet the high strength required for short anchorages. A grouted bolt is stiffer and can transfer greater loads than expanded shell or wedge type anchorages.

1.2 THEORIES OF ROCKBOLTING MECHANISMS

Lutz (1970), Hollingshead (1971), Littlejohn and Bruce (1975), Farmer (1975), Nitzsche and Haas (1976), Sun (1983), Yap and Rodger (1984), Aydan *et al* (1985), Serbousek and Signer, (1987), Aydan (1989), Signer (1990), Holmberge (1991), Bawden *et al* (1992), Hyett *et al* (1992, 1995, 1996), Kaiser *et al* (1992), Yazici and Kaiser (1992), Littlejohn (1993), Benmokrane *et al* (1995), Li and Stillborg (1999),

Mark *et al* (2002), Kilic *et al* (2002 a and 2002 b), Aziz and Webb (2003), Ivanovic (2003, 2009), Compton and Oyler (2004), Cai *et al* (2004 a and 2004 b), Aziz *et al* (2004, 2005, 2006, 2008), Moosavi *et al* (2005), Jalalifar (2006), Xiao and Chen (2008), Ren *et al* (2010) and Martin *et al* (2011) carried out theoretical and experimental studies to define bolt behaviour under axial loading.

Rockbolting failure is a major concern of the reinforcement system. From pullout tests, it is observed that the ultimate failure of rockbolts may occur:

- in the bolt,
- in the grout,
- in the rock,
- at the bolt–grout interface,
- at the grout–rock interface and
- a combination of these failures.

Using data from pullout tests, bond forces radiate out into the surrounding media from the bonding surface of an anchored steel bar. Studies of bonding forces for plain reinforcing bars and rebar show that bond for plain bars is made up of three components:

- Chemical adhesion,
- Friction and
- Mechanical interlock.

The adhesive strength between the bolt-resin interface is negligible. Signer (1990) demonstrated that there was no adhesion between the grout to bolt and grout to rock interface. Aziz and Webb (2003) reported that there is very small adhesion between the bolt surface and resin as demonstrated in Figure 1.2. In addition, the adhesive strength of the bond cannot be mobilised with frictional strength during the pullout tests (Yazici and Kaiser, 1992).

The frictional components of the bond strength can be categorised into dilation slip, shear failure of surrounding medium and torsional unscrewing of bolt (Hyett *et al*, 1995). Each of the components depends on the pressure generated at the bolt-grout

interface, which in turn depends on the internal reaction forces of the whole system.

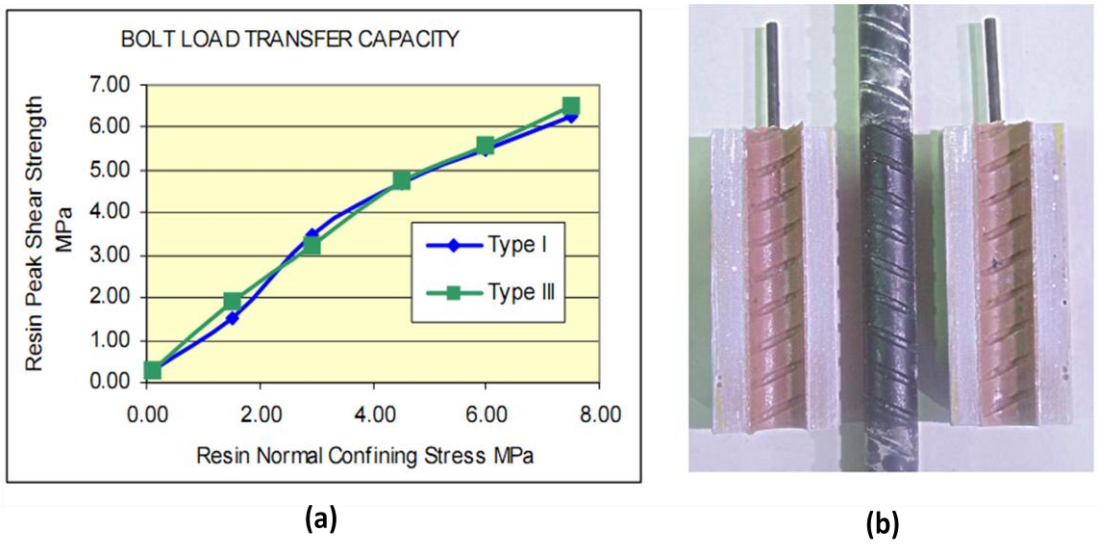

Figure 1.2 (a) Shear strength of resin/bolt interface under various confinement. (b) Resin bolt separation after post encapsulation (Aziz and Webb, 2003).

The mechanical interlock component of the bond strength plays an important role in the load transfer capacity of the rockbolting system. It is commonly accepted that the mechanical interlock is created by the bolt profile configuration. However, there are only a few experimental studies to examine the influence of bolt profile in the rock bolting system, and there is no related theoretical model to evaluate the role of the bolt profile in the load transfer mechanisms.

Farmer (1975) did fundamental work on theoretical studies of fully grouted rock bolting subjected to axial loading. The model shows an exponential decay of the axial stress along the bolt in the case of perfect bonding and elastic deformation. This solution is widely accepted by subsequent research works of rock bolting mechanisms.

Yazici and Kaiser (1995) proposed a Bond Strength Model (BSM) to predict the ultimate load transfer capacity of fully grouted cable bolts. In this model, the mechanical interlock is simulated as a zig-zag surface of the cable, which generates dilation or radial movement when debonding occurs. For the same problem, Hyett *et al* (1995) emphasised the 'unscrewing' effect during the deformation of the cable bolt and introduced an untwisting component to quantify the interaction of the bolt and the grouting material.

In the so-called 'Interfacial Shear Stress' (ISS) model, the deformation of surrounding materials is lumped into a zero thickness interface, which is assigned with specific shear stress displacement or shear stress strain behaviour. Li and Stillborg (1999) developed an ISS model for predicting the behaviour of rock bolts in pullout tests, in uniformly deformed rock mass and when subjected to opened joints. The deformation of the interface coupling was considered in four stages: elastic, linear softening, residual and debonding. Ivanovic and Neilson (2009) developed a lumped parameter model with varying shear load failure properties along the fixed anchor length to analyse the bolt behaviour under static or dynamic load. More recently, closed-form solutions were obtained for the prediction of the full range behaviour of fully grouted rockbolts under axial load (Ren *et al* 2010 and Martin *et al* 2011). A tri-linear bond-slip model with residual strength at the grout-bolt interface was used and five consecutive deformation stages of the interface were identified.

These models are outstanding theoretical achievements of rock bolting mechanism up-to-date. However, they described the effect of the interaction between bolt, grout and rock under axial loading but the profile configuration of a bolt and its influence on the bolting performance are ignored.

1.3 INFLUENCE OF REBAR PROFILE

In most of the cases, rockbolting failure is not due to the excessive tension in the bar; rather it is related to slip. Therefore bond is recognised as a critical parameter in reinforced rock design. To improve bolt loading capacity through the steel bolt profile design, it is necessary to have a good understanding of the interaction between the rock bolt and the surrounding mediums.

The bolt profile configuration is defined by the rib profile shape, profile height, angle of wrap and spacing between the ribs, as shown in Figure 1.3.

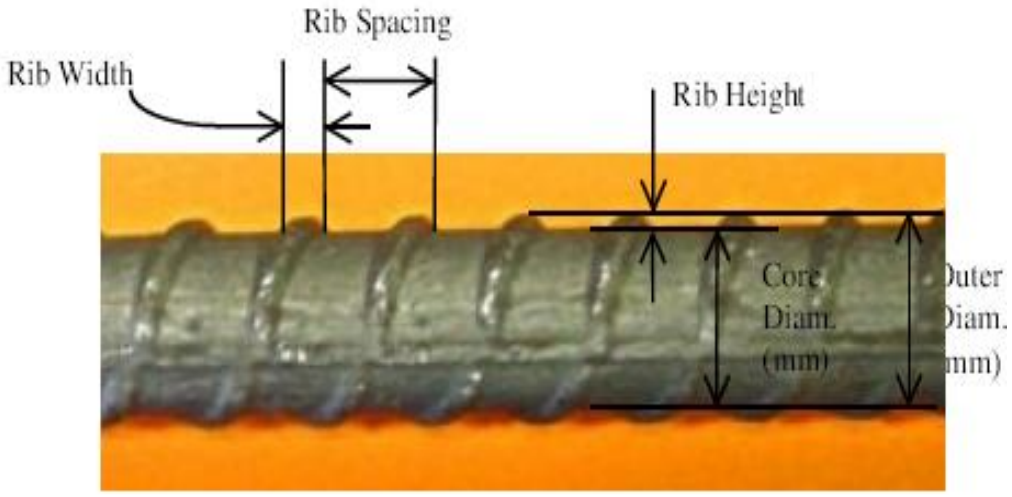

Figure 1.3 Steel bolt rib profile configuration (Jalalifar, 2006).

For smooth bar, the bond strength mainly depends on adhesion and after slip, on friction. There is also a little interlocking due to the roughness of the bar surface (Aziz and Web, 2003). Research work has shown that smooth bar has a very low load transfer capacity compared with ribbed bar, for example Aydan (1989), Aziz and Web (2003) and Kilic *et al* (2002). In another extreme, if a bolt has too many ribs, such as a closely spaced thread bar, its load bearing capacity is also small (Kilic *et al* 2002 and Ito *et al* 2001). In fact, a threaded bar with closely spaced ribs can be thought of as a smooth bar with a larger diameter.

For ribbed bars, the bolt-resin interface is irregular. Consequently, bond slip is no longer a separation of two materials at the contact surfaces but rather it is the shear failure of the grout material around the bolt. Laboratory studies suggest that there are two major failure sub-modes around the bolt-resin contact when bond slip occurs, namely:

- *Parallel shear failure*: cylinder failure surface caused by the bolt ribs crush the grout material parallel to the bolt axis.
- *Dilational slip failure:* conical failure surface caused by the bolt ribs split the surrounding material by wedging action.

The bond failure of smooth bolts and closely spaced rebars can be categorised into parallel shear failure. The transverse and longitudinal cracking in the surrounding medium are often observed in pullout tests, but they are the effect of the dilational slip

around the bolt ribs.

The influence of bolt profile has been investigated in some research work. Lutz (1970) found that during the pullout tests from the reinforced concrete beams, the ribbed bar could crush the concrete in certain pattern consisting of primary cracks, radial cracks and cone cracks. Tepfers (1975) reported that for deformed bars with a rib face angle varying between 40° and 105°, it is likely to produce approximately identical behaviour of the concrete during the pullout tests. If the face angle is less than 30°, then the bonding action is different. After the concrete is crushed to a compacted powder, it becomes lodged in front of the ribs.

Fabjanczyk and Tarrant (1992) conducted a series of push tests and suggested that a substantial increase in load transfer capacity could be obtained from specific rib shapes on rock bolts. Later research work undertaken by Gray *et al* (1998) indicated that rib shape could be used not only to maximise load transfer capacity, but also to optimise resin mixing and minimise cavities forming in the resin.

Ito *et al* (2001) used an X-ray CT scanner to visualize the patterns of failure in pullout tests on four types of bolts grouted into an artificial rock with cement paste. The results showed strong influence of bolt types on the load-displacement deformational behaviour. Kilic *et al* (2002 a) studied cone shaped lugs of cement grouted steel bolt by pullout tests. Results showed that there was a strong influence of the bolt shape on the load bearing capacity and deformational behaviour.

Studies undertaken by Aziz *et al* (2008) indicated that, increased bolt profile spacing contributed to improvement in bolt anchorage stiffness. The extent of the anchorage performance was found to reach the optimum with the bolt profile spacing of 37.5 mm.

Since these attempts, there has been no further analytical or numerical work being undertaken to advance the load transfer capacity of the bolts with respect to profile configuration. Accordingly, this aspect of the topic is currently being further evaluated analytically, which is the subject of this thesis.

1.4 KEY OBJECTIVES

- Design a testing method to observe the failure procedure when bond slip occurs,
- Identifying and classifying the failure modes/sub-modes when a ribbed bolt is subjected to axial loading,
- Developing theoretical analysis to describe the role of the bolt profile in the rock bolting mechanisms,
- Constructing mechanical models to evaluating the influence of the bolt profile configuration on load transfer mechanics.

1.5 METHODOLOGY

Developing new analytical model of rockbolting connecting with bolt rib profile constitutes the main components of this study. To simplify the problem, one bolt segment between two profiles was studied. Failure modes were observed in pull out tests, double shear tests and Constant Normal Stiffness (CNS) tests in laboratory. Failure modes analysis was developed using Mohr-Coulomb's failure criterion. Pull out test procedure was formulated for certain failure modes. The half space theory was introduced to identify the stress field around rock bolt when subjected to axial load. The closed form solution was obtained and parametric studies of bolt profile were undertaken. Numerical models, using Fast Lagrangian Analysis of Continua (FLAC), were developed to verify and validate the newly constructed models and their assumptions.

1.6 SCOPE

Chapter 1 presents the general purpose, methodology, and key objectives of this thesis.

Chapter 2 reviews bolting theories, failure modes, mechanism of reinforcement system and analytical descriptions of the load transfer mechanism when rock bolting is subjected to shear loading.

Chapter 3 reviews experimental, numerical and analytical studies of rockbolting

subjected to axial loading with emphasis on failure modes identification and theoretical descriptions. The traditional Interfacial Shear Stress (ISS) model and its closed form solutions are presented.

Chapter 4 presents the experimental procedure and results including pullout tests, double shear tests and CNS tests. The mechanical properties of the experimental materials used in this study including the bolts, resin, and concrete are also evaluated.

Chapter 5 identifies various failure modes in pullout tests. After introducing the concepts “dilational slip failure” and “parallel shear failure”, the failure modes are differentiated and corresponding mathematical descriptions are developed. Consequently, for certain failure modes, the pull out procedure is identified. Thick walled cylinder theory and review of research work concerning with rib profile are also included in this chapter.

Chapter 6 develops a stress analysis method based on half space theory to model the parallel shear failure of rockbolting subjected to axial load. Parameters of the bolt profile geometry are included in the model, and closed form solution is achieved under Mohr-Coulomb’s failure criteria. Parametric studies of the bolt rib profile are undertaken and application is addressed.

Chapter 7 summarises the results and principal conclusions of the work presented in this thesis, further discussions are conducted and recommendations for further research are offered.

CHAPTER TWO

REVIEW OF ROCK BOLTING MECHANISMS

REVIEW OF ROCKBOLTING MECHANISMS

2.1 INTRODUCTION

Rock bolting as a reinforcement system in tunnelling and mining operations has advanced rapidly due to the development of load transfer mechanisms of the system. Rock bolts are installed around openings in mines and tunnels to tie weaker layers to stronger layers above to reduce subsidence and separation. They basically provide a reinforcement zone across the fractured rock that makes greater use of the rock mass strength to enable it to be self supporting.

The application of bolts as a means of ground control was first reported in 1872 from a slate quarry located in North Wales. However the development of rock bolting as a practical and economical technology began with the Norwegians in the late 1940s. To reduce the number of fatal accidents caused by roof falls, the U.S Bureau of Mines (USBM) began to use roof bolting technology in 1947. Their use spread throughout the U.S., such that by 1952, annual consumption of bolts reached 25 million (Jalalifar, 2006).

Rock bolting in Australia began with the Snowy Mountains Hydroelectric Scheme (SMHS, 1949-1969), during which time the use of grouted rock bolts for permanent reinforcement was pioneered. In Australian coal mines, the application of roof bolting in conjunction with normal timber supports was reported from Elrington Colliery, New South Wales in 1949 (Jalalifar, 2006). Since 1983, bolts have become the main method of support in most underground openings in Australian mines. Nearly seven million various bolts are currently installed by the Australia mining industry annually.

Nowadays, the application of rock bolts for ground reinforcement and stabilisation is used worldwide and the level of bolt usage has contributed to variations in design and purpose. In US coal mines around 15,000 km of entries are excavated every year and around 100 million rock bolts are installed in those entries, and a survey revealed that worldwide usage was in excess of 500 million annually (Windsor, 1997).

Rock reinforcement includes all methods to increase the strength and reduce the deformability of the rock mass. The words ‘support’ is often used interchangeably to ‘reinforcement’. However, support is the application of a reactive force at the face of the excavation. Reinforcement is considered to be an improvement of the overall rock mass properties and hence include all techniques and devices that act within the rock mass, e.g. rock bolts, cable bolts and ground anchors.

Rock bolts are the main elements of support to resist shear deformation. They work as an additional resistance against shear failure along weakness planes. The internal steel bar within the system is the main element resisting shear loads caused by beam bending and slip on joints. Bolt behaviour under load and how the load is transferred along its length are important.

The overall behaviour of the reinforcement system is determined by the cumulative result of the component interactions of the system. The types of a reinforcement system can be a combination of primary, secondary and tertiary reinforcement systems in various configurations. The spatial configurations are uniform geometric arrangements (pattern reinforcement), discretionary arrangements (spot reinforcement) or combinations of the two (combination reinforcement). There are two fundamental reinforcement patterns: the rectangular arrangement and the slant arrangement (Windsor, 1997).

The concept of a reinforcement system is extremely important. A reinforcement scheme is an arrangement of primary, secondary and tertiary reinforcement systems in various configurations. Analytical axisymmetric models are now widely used in tunnelling design. Rock mass reinforcement, such as by means of fully grouted rebar bolts or cable bolts, has been included in the scheme but problems have been encountered due to the presence the bolt-rock interaction. Brown *et al* (1983) analysed systematic bolting as a pressure applied at the tunnel perimeter, while later researchers modelled the bolt action as elastic perfectly plastic behaviours. Stille *et al* (1989) presented a closed form elastoplastic solution of grouted bolts by considering four different approaches of bolt performance. Indraranta and Kaiser (1990 a and 1990 b) introduced the global behaviour of a bolted rock mass into the base equation of the axisymmetric problem. In this approach, the bolt influence was simulated by a reinforced rock mass zone with geomechanical properties (both cohesion and friction angle) increased with

respect to the natural rock mass.

Laboratory and field studies, numerical simulation and theoretical derivation are the common methods used to study the bonding strength, bearing capacity of rock bolts, the load transfer characteristics of bolts, the failure mechanism and hence the effectiveness and reliability of reinforcement systems.

2.2 CONCEPTS OF ROCKBOLTING

2.2.1 Rockbolt theories

In general, rock bolting is effective in a variety of geological conditions. The main function of roof bolting is to fasten together stratified or broken rocks such as those with bedding planes, joints and fractures, or artificial cracks caused by mining activities. The theories used to explain bolting mechanisms vary from place to place and sometimes are not conclusive. However, it is broadly believed that bolt binding effects are accomplished by one or a combination of the following three basic mechanisms: suspension, beam building, and keying (Luo *et al*, 1998).

Whenever an underground opening is made, the strata directly overhead tend to displace. If not supported in time, the immediate roof could separate from the main roof and fall out. In such situations, roof bolts anchor the immediate roof to the main roof by the applied tension. It appears that the immediate roof is suspended from the main roof by the bolts, or weak strata are suspended from more stable strata.

Although in most cases, the strong main roof is beyond the distance that ordinary roof bolts can reach, roof bolts can be applied in such situation with great success. In fact, bending and separation of roof strata cause both vertical and horizontal movements along the bedding interfaces. Bolts through these layers can greatly reduce horizontal movement by shear resistance, and the tension induced by rock displacement clamps the layers together, making all the layers to move with the same magnitude of vertical displacement. Such bolting pattern is very similar to clamping a number of thin weak layers into a thicker strong composite beam.

The stability of the bolted strata increases with the thickness of the bolted strata. The important parameters include bolt length, bolting pattern and tension applied to the bolt. The relationship between the decrease in maximum bending strain, ΔE_f, due to the beam effect and the maximum bending strain of the unbolted strata, E_{nfs}, is expressed by the following equation (Khair, 1998):

$$\frac{\Delta E_f}{E_{nfs}} = -0.375 tan\varphi_j \sqrt{bL} \left[\frac{N\sigma_b (\frac{l}{t_{ave}} - 1)}{W_{avg}} \right]^{1/3} \quad (2.1)$$

Where:

φ_j =friction angle of the joint

b =spacing between adjacent rows of bolts,

L =roof span,

N = bolt number per row,

σ_b =bolt axial stress

l =bolt length,

t_{avg} = average thickness of the bolted roof, and

W_{avg} = average unit weight of the bolted rocks.

The Reinforcement Factor (*RF)* due to bolting effect is defined as:

$$RF = \frac{1}{1 + \frac{\Delta E_f}{E_{nfs}}} \quad (2.2)$$

In most situations, where the immediate roof consists of laminated strata, both suspension and beam building effects coexist.

The principle of the keying effect is based on the development of resistance force in the joint interface. When the roof strata are highly fractured, or the immediate roof contains one or several sets of joints with different orientations, bolting provides significant frictional forces along weak planes. Sliding and/or separation along the interface is thus prevented or reduced. Peng (1984) reported the reinforcing effect of

keying in underground excavation and developed the relationships shown in Table 2.1 for different orientation of the bolts installed in relation to the fracture plane.

Table 2.1 Axial stress of the bolt in different orientations (Peng, 1984).

Bolts perpendicular to the fracture	Bolt perpendicular to the roof line
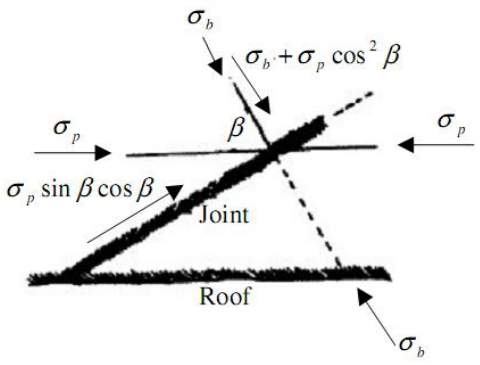	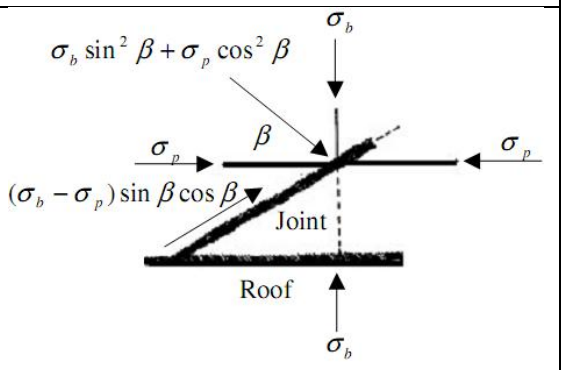
$\sigma_b = \frac{\sigma_p(sin\beta - cos\beta tan\varphi_j)}{(cos\beta + sin\beta tan\varphi_j)tan\varphi_j}$ σ_b=bolt axial stress σ_p=horizontal stress φ_j=fracture friction angle	$\sigma_b = \frac{\sigma_p(sin\beta cos\beta - cos^2\beta tan\varphi_j)}{tan\varphi_j}$

Equations demonstrate that the minimum axial stress is proportional to the horizontal stress in both cases. The smaller the horizontal stresses, the more effective the keying effect. Also σ_b becomes zero if β is equal to φ_j, indicating that stability can be maintained without using any bolt.

The keying effect mainly depends on active bolt tension or, under favorable circumstances, passive tension induced by rock mass movement. It has been shown that bolt tension produces stresses in the stratified roof, which are compressive both in the direction of the bolt and orthogonal to the bolt (Luo, 1999). Superposition of the compressive areas around each bolt forms a continuous compressive zone in which tensile stresses are offset and the shear strength is improved.

Table 2.2 lists the various theories reported by Jalalifar (2006) proposed for ground support using rock bolts. As can be seen, the selection of any theory depends on the methodology of bolt application and geological conditions.

Table 2.2 Bolting theories (reported by Jalalifar, 2006)

Theory	Description	Shape	Comments
Suspension	Dead weight load of the strata transferred between the bolt head and the anchor.	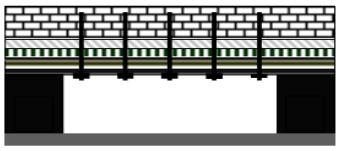	Upper layer should be strong enough to anchor the bolts
Beam building	Bolts bind the strata layers together, which prevents or greatly reduce the movements. The frictional effect generated by bolt pretensioning increases the shear strength between the layers,	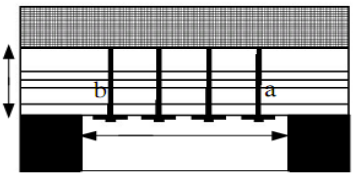	Tensile failure is prevented because of the increase in binding strength and stiffness effect However, failure may still occur by shearing at the two ends. Hence **bolts a and b** are most effective in this method.
Keying effect	When the roof strata are highly fractured and blocky, or planes of weakness intersect the immediate roof strata, keying effect roof support may be used. Roof bolting provides significant frictional forces along fractures, cracks, and weak planes	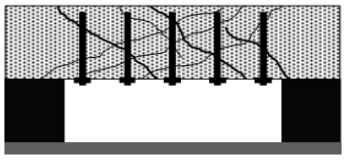	Confinement is provided by way of tensioned roof bolts, and then the strata material will be locked or keyed together.
Arching Action	The main aim of the arching theory is to increase the value of compressive stresses in the roof so that the tensile stress is ignored and the shear resistance increased. Arching provides very strong roof profile, which is one of the strongest roof profiles	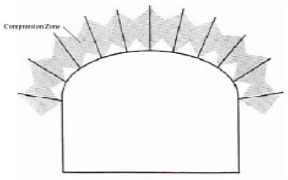	To support the weakened zones between bolts, the use of wire mesh and shotcrete is recommended

2.2.2 Load transfer mechanisms

The load transfer concept is central to the understanding of reinforcement system behaviour, and the mechanical action of the different devices and their effects on excavation stability. This concept can be visualised as being composed of three basic mechanisms (Stille *et al*, 1992):

- Rock movement and load transfer from an unstable zone to the reinforcing element;
- Transfer of load from the unstable region to a stable interior region via element;
- Transfer of the reinforcing element load to the stable rock mass.

Fully grouted bolting consists of bolt, grout, and surrounding rock. The relationships between them belong to the continuous mechanically coupled bolt system. A fully grouted bolt is a passive roof support system, which is activated by movement of the surrounding rock. The efficiency of load transfer is affected by the type and properties of the grout, surface profile of the rock bolt, thickness of the grout annulus, anchorage length, rock properties, confining pressure and installation procedure.

Rock bolts are the main elements resisting shear failure along joints and weakness planes. They generally work by development of the axial force and bending moment along the steel bars during movement of the supported rock blocks. The axial force in the bolt consists of a component perpendicular to the joint surfaces, which contributes confining pressure, and a component parallel to the joint plane, which contributes to the shear resistance.

In a fully grouted rock bolt the load transfer mechanism depends on the developed shear stress on the bolt-resin and resin-rock interfaces. Peak shear stress capability and shear stress modulus of the interfaces determine the reaction of the bolt to the strata. Hence, the load transfer is determined by measuring the peak shear stress capacity and system stiffness. In addition, stress concentration is induced by the surface profile of the bolt. This localised stress concentration could go over the strength of the grouting material and resulting in localised crushing that allows additional deformation in the steel.

2.2.3 Fully grouted rockbolts

A fully grouted bolt provides greater shear surface for transmitting the load from rock to bolt and vice versa. The grout supplies a mechanism for transferring the load between the rock and reinforcing element. This redistribution of forces along the bolt is the result of movement in the rock mass, which transfers the load to the bolt via shear resistance in the grout. This resistance can be the result of adhesion and /or mechanical interlocking. Adhesion is the actual bonding between grout, steel, and rock, and the mechanical interlocking is a keying effect created when grout fills irregularities between bolt and the rock.

Stillborg (1994) carried out a series of tests on different kinds of rock bolts installed across two high strength concrete blocks. The tests revealed that the rate of load transfer in resin grouted rock bolt is higher than for other kinds of bolts (Figure 2.1).

Many researchers have worked theoretically and experimentally on the mechanism of load transfer of fully grouted rock bolts. Up-to-date, it is commonly accepted that fully grouted bolts are much more successful in supporting roof strata than other bolting systems. The reasons are as follows (reported by Jalalifar, 2006):

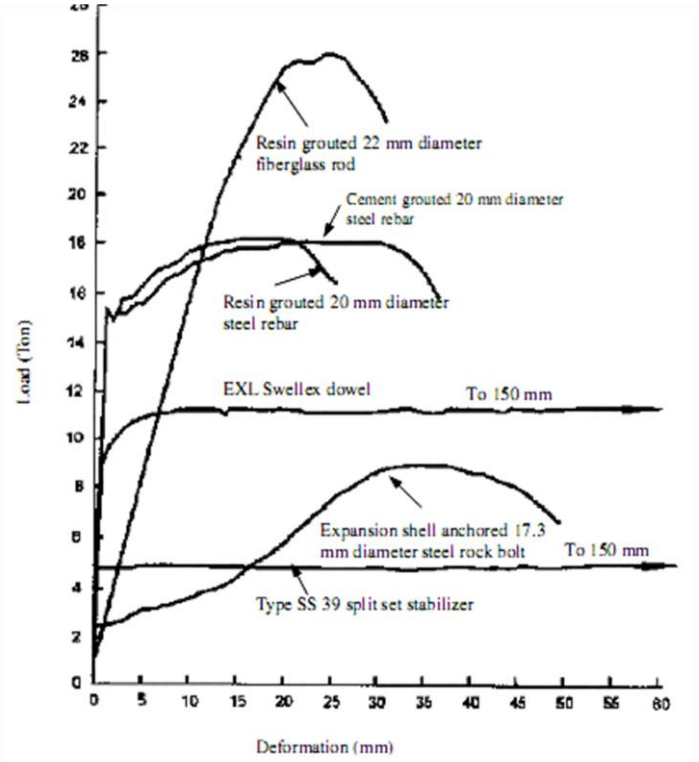

Figure 2.1 Results of load deformation in different bolts (Stillborg, 1994)

- Fully grouted bolts come in full contact with the surrounding rock, and join the roof layers together to reduce sagging by their inherent stiffness.
- Fully grouted bolts are loaded as long as the surrounding rock deformation continues. They have the capability of sustaining high peak load.
- Fully grouted bolts can provide greater support to the rock mass than point anchored bolts even with the same strength of steel.
- They can produce a higher degree of load transfer in comparison to other types of bolts.
- Fully grouted rock bolts can be about five times more effective in reducing beam deflection than mechanical bolts when the roof is suspended from competent rock.
- The axial stiffness of fully grouted bolts is 10-20 times greater than mechanical bolts.

2.2.4 Un-stressed, pre-stress and post-stress

Rockbolts may be installed as un-tensioned, pre-tensioned or post-tensioned. Pre-tensioning is the application of an initial tension to the reinforcing system during

installation. Post-tensioning is the tensioning or re-tensioning of the reinforcement system subsequent to initial installation.

The introduction of the pre-tension is to try to generate a compressive force into the rock strata immediately adjacent to the bolt. The pre-tensioned load can be very high, 20 tons pre-tensioned cable bolts have been used in Australian coal mine industry. Nitzsche and Haas (1976) found that the stresses are quite localized when the bolts are tensioned by application of bearing plates and nuts to the ends of the bolts. In addition, nearly all of the bolt load is transmitted through the grout annulus into the rock over a short distance. Under these conditions, then, one may conclude, in the case of the fully grouted post-tensioned roof bolt, that the post-tensioning effect created when a nut is tightened against a bearing plate may help hold up loose material near the hole collar, for example, a loose slab close to the skin surface. However, one cannot expect the post-tensioning to have any significant effect in pulling strata together if the separation plane is some distance above the roof.

Saleh *et al* (2004) studied high pre-tensioned loads on the stability of coal mine roadway roofs using FLAC software. For a single pre-tensioned cable bolt, the model showed that the compressive zone covers a small area around the cable, it means that tensioned bolt can provide little compression to the triangle zones in the bolting theory. For coal main roof, pre-tensioning is more effective when the Rock Mass Rate (RMR) is lower or the *in-situ* stress field is lower. These suggest that pretension should be introduced for bad roof, and/or installed after initial stress release.

Ivanovic *et al* (2002) developed a lumped parameter model to investigate how the anchorage system may respond to potential failure modes under dynamic loading and the influence of prestress on anchorage. Results showed that prestressing the rockbolts decreased the effect of the blast vibrations; and that an increase in prestress load resulted in a decrease in the magnitude of the dynamic component of the stress distribution along the fixed anchorage length.

In this study, experimental results suggested that pretension influenced the shear modulus of the bolted joint, indicated by the rate of the shear resistance increment that dropped significantly once the axial loading exceeded the pretension load.

Up to now, the utilization of pre-tensioned bolts mainly depends on empirical experience because of lack of knowledge about the mechanism of pre-stress state in rockbolting system. It is generally accepted that pre-tension is more effective in controlling block falls in hard rock. But there are arguments on the effect of minimising strata separation via pre-tensioning.

2.2.5 Rockbolt installation

Resin loss during rockbolt installation is a problem for rockbolting. It is recommended that 25 to 30% more resin should be used than the theoretical annulus volume (Aziz *et al*, 1992). Via physical examinations of bolts, Compton and Oyler (2004) reported that significant quantities of resin (averaging 44%, but up to 50%) were lost in weak rock through extrusion of resin into existing fractures or fractures created by the installation. They conducted tests which employed bolts installed in strain gauged steel tubes to explore the installation induced pressure which was one possible explanation for the resin loss. The results indicated that significant pressures (greater than 27MPa) could be generated during bolt installation (Figure 2.2), unless extrusion of resin into the roof rock took place. In weak roof rock resin loss of this magnitude could have a detrimental effect upon bolt performance and possibly upon mine roof conditions, especially where the lower portions of the bolts were left ungrouted by the resin loss. However, the tests also suggested that resin extrusion may be common and minor extrusion of resin, as long as sufficient resin was present to ensure that bolts remain fully grouted, may not have a detrimental effect.

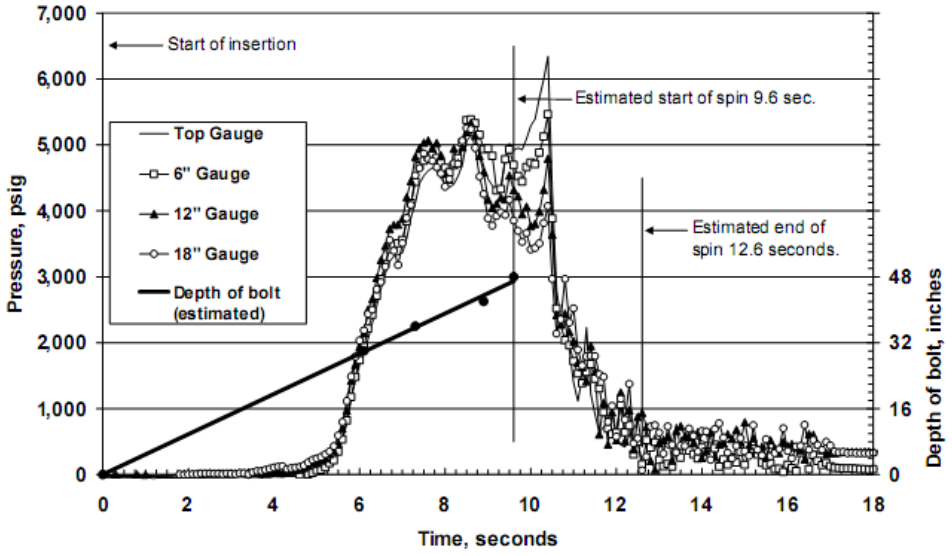

Figure 2.2 Pressure at 4 locations when bolt is installed (Compton and Oyler, 2004).

2.3 ROCKBOLT SUBJECTED TO SHEAR LOAD

Dulascka (1972), Bjurstrom (1974), Haas (1976,1981), Hibin and Motojim (1981), Dight (1983), Yoshinaka *et al* (1987), Holmberg (1991), Ferrero (1995), Pellet and Egger (1996), Aziz *et al* (2003, 2005), Jalalifar *et al* (2004, 2006), Jalalifar (2006) and Craig and Aziz (2010), worked on the mechanical behaviour of rock bolts when they were subjected to shear loading.

Dulascka (1972) carried out a series of single shear tests to investigate the effectiveness of rock bolts in resisting shear displacement along pre-existing fracture surfaces (Figure 2.3). Results showed that the crushing strength of the concrete was more than five times the compressive strength. An analytical solution based on an idealised stress distribution at the point of contact and the development of a plastic hinge at the point of maximum moment was established. However, equilibrium condition was not considered in the derived equation. The shear force carried by a bolt was calculated by:

$$T = 0.2 d_b^2 \sigma_y \left[\sqrt{1 + \frac{\sigma_c}{0.03 \sigma_y \, sin^2 \, \beta}} - 1 \right] \qquad (2.3)$$

Where:

T = Shear force carried by bolt;

σ_c= Uniaxial Compression Strength (UCS) of rock;

d_b = Bolt diameter;

σ_y= Yield stress of bolt;

β = Angle between bolt and normal to the joint.

Bjurstrom's (1974) carried out a series of direct shear tests on cement grouted bolts in granite blocks. The influence of various factors affecting the shear strength of rock joints was evaluated. Results showed that for bolts inclinations less than 40º with respect to the joint surface the bolts failed in tension and for greater than 40º the bolts failed in a combination of shear and tension. Based on equilibrium of forces acting on the system, an analytical solution was provided and the total shear strength of a bolt

reinforced joint has three components:

- reinforcement effect $T_b = p(sin\beta + cos\beta tan\varphi)$ (2.4.1)
- dowel effect $T_d = 0.67 d_b^2 \sqrt{\sigma_c \sigma_y}$ (2.4.2)
- friction of joint $T_f = A_j \sigma_n tan\varphi$ (2.4.3)

where:

p = Axial load corresponding to the yield strength due to shear displacement

β = Initial angle between bolt and normal to the joint

φ_j = The friction angle of the joint

d_b = Bolt diameter

σ_y = Bolt yield strength

σ_c = Uniaxial compression strength of the rock

A_j = Joint area

σ_n = Normal stress on joint and

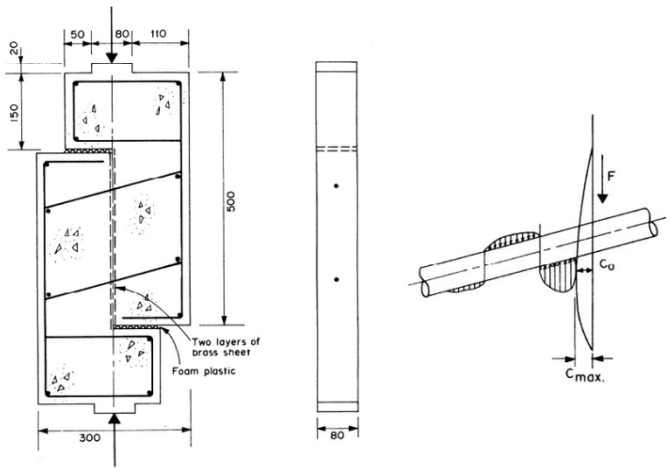

Figure 2.3 (a) Shear test arrangement; (b) probable load generation (Dulascka, 1972)

Accordingly, the total contribution of the bolt to the shear strength of the joint was the sum of three effects (Figure 2.4).

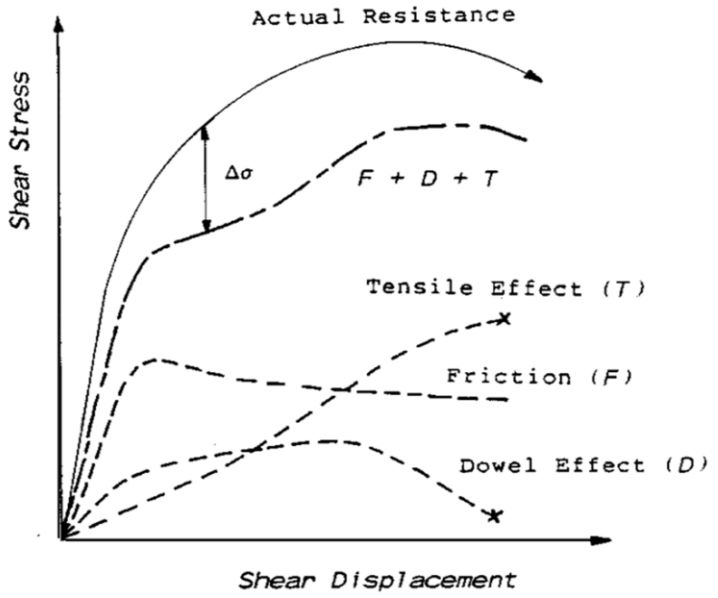

Figure 2.4 Components of shear resistance offered by a bolt (Bjurstrom, 1974)

Haas (1976 and 1981) carried out series of single shear tests on chalk and limestone. The effectiveness of rock bolts in resisting shear displacement along fracture surfaces was investigated using variables of type of bolt, normal pressure on the interface and different orientation of bolt relative to shear surface (0°, +45° and -45°) as shown in Figure 2.5. Results showed that bolts increased the shear resistance along a fracture when the average normal stress was in the order of 170kPa and when the bolt was inclined at an acute angle to the shear surface such that it tended to lengthen as the shear progressed. In addition, for bolts with a bearing plate, the shear resistance increased. However, the stresses on both sides of the shear joint were suggested to be different in the tests. It reveals a non-equilibrium state along the joint plane and suggests that the single shear test has difficulties in equal load distribution (Figure 2.6).

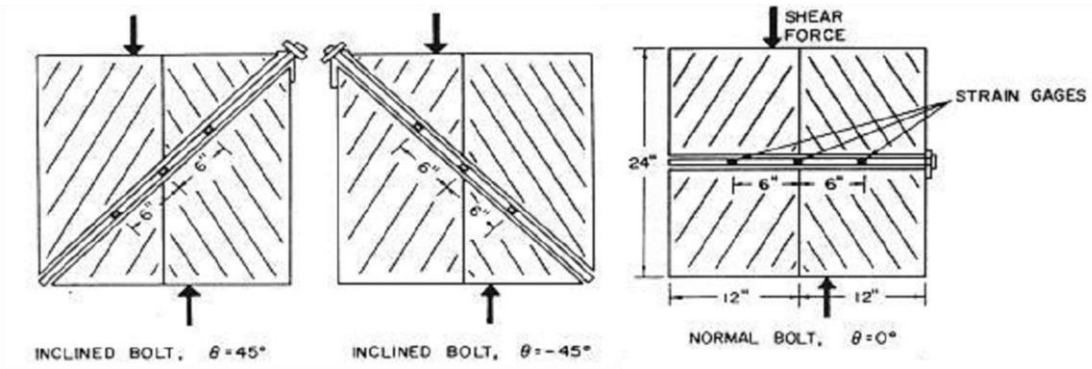

Figure 2.5 Arrangement for bolt shear testing (Haas, 1981)

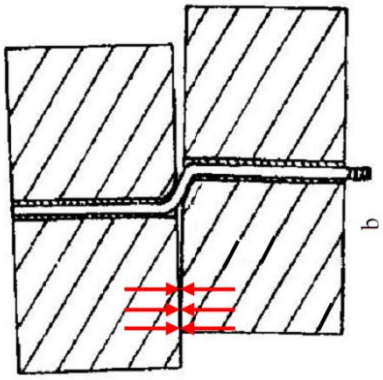

Figure 2.6 Non-equilibrium in vicinity of shear joint (Haas, 1976).

Under the assumption that the total bolt contribution was a resultant of tensile force in the bolt and the dowel effect (Figure 2.7), Dight (1982) provided a theoretical analysis of the grouted bolt contribution to the strength of a sheared joint. In the model, elastic deformation of the bolt was ignored, that is, bolt provides yield strength once axial force developed. Results suggested that joints with inclined bolts had stiffer behaviour than those perpendicular ones. In addition, the deformed length of the bolt was related to the deformability of the rock.

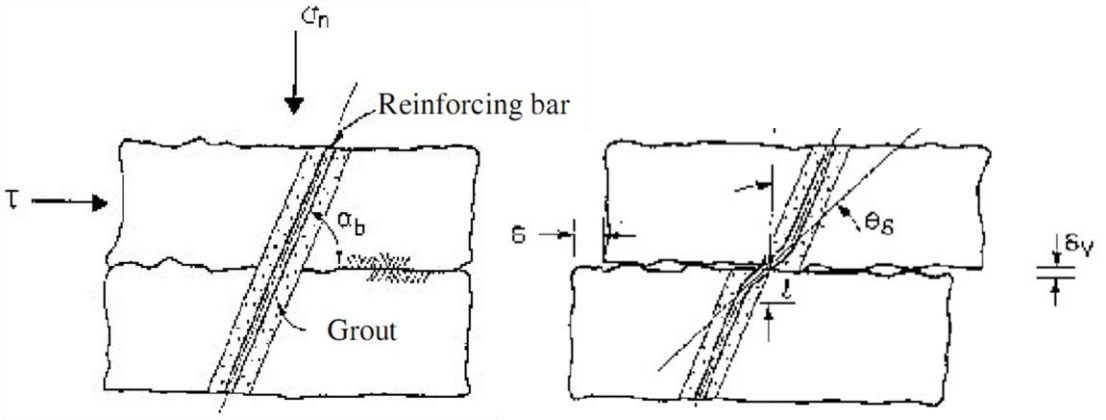

Figure 2.7 General deformation patterns for a dowel in shear

The tensile force which was considered as a component of axial load and the dowel force were determined by:

$$t_c = t_y\left[sin\beta + cos\beta tan\left(\varphi_j + i\right)\right] \qquad (2.5.1)$$

$$t_p = \frac{{d_b}^2}{4}\sqrt{1.7\sigma_y p_u \pi\left(1 - \left(\frac{t}{t_y}\right)^2\right)} \qquad (2.5.2)$$

Where:

t_c = Tensile force of the bolt

t_y = Axial load corresponding to the yield strength

β = Angle between bolt and normal to the joint.

φ_j = Joint friction angle.

i = Dilation angle

t_p = Dowel force

d_b = Bolt diameter

σ_y = Yield stress of the steel

p_u = The bearing capacity of the grout or rock

t = Axial bolt load in the position of the plastic moment,

And the bolt contribution would be a summation of equations (2.5.1) and (2.5.2).

A study by Yoshinaka *et al*. (1987) on the direct shearing of 16mm diameter bolts suggested that inclined bolts were the most favourable to resist joint shearing, as shown in Figure 2.8.

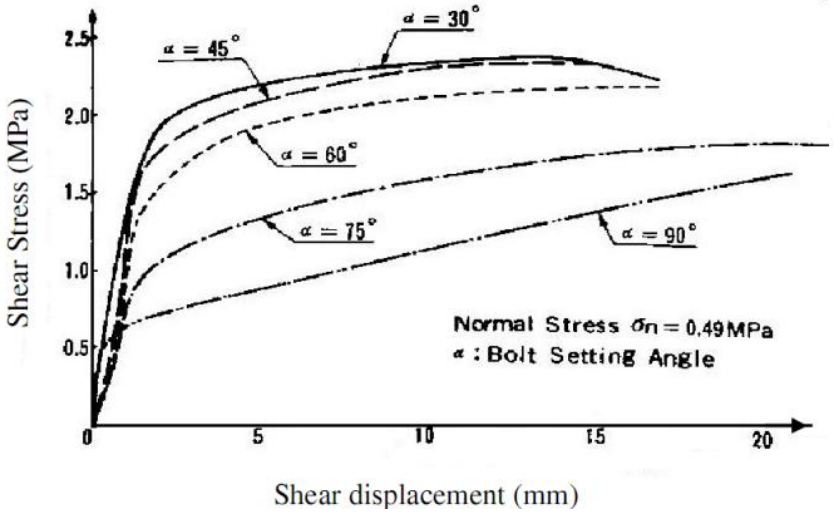

Figure 2.8 Shear behaviour under different inclined angles (Yoshinaka *et al*, 1987)

Holmberg (1991) developed mechanical models for grouted rock bolt subjected to shear loading in elastic and yielding conditions. The analytical models were based on the equilibrium and the deformation of the system was expressed in four stages as (Figure 2.9):

- Bolt and surrounding medium in an elastic state,

- Bolt in elastic and surrounding medium in a yielding state,
- Bolt and surrounding medium yielded,
- Ultimate condition.

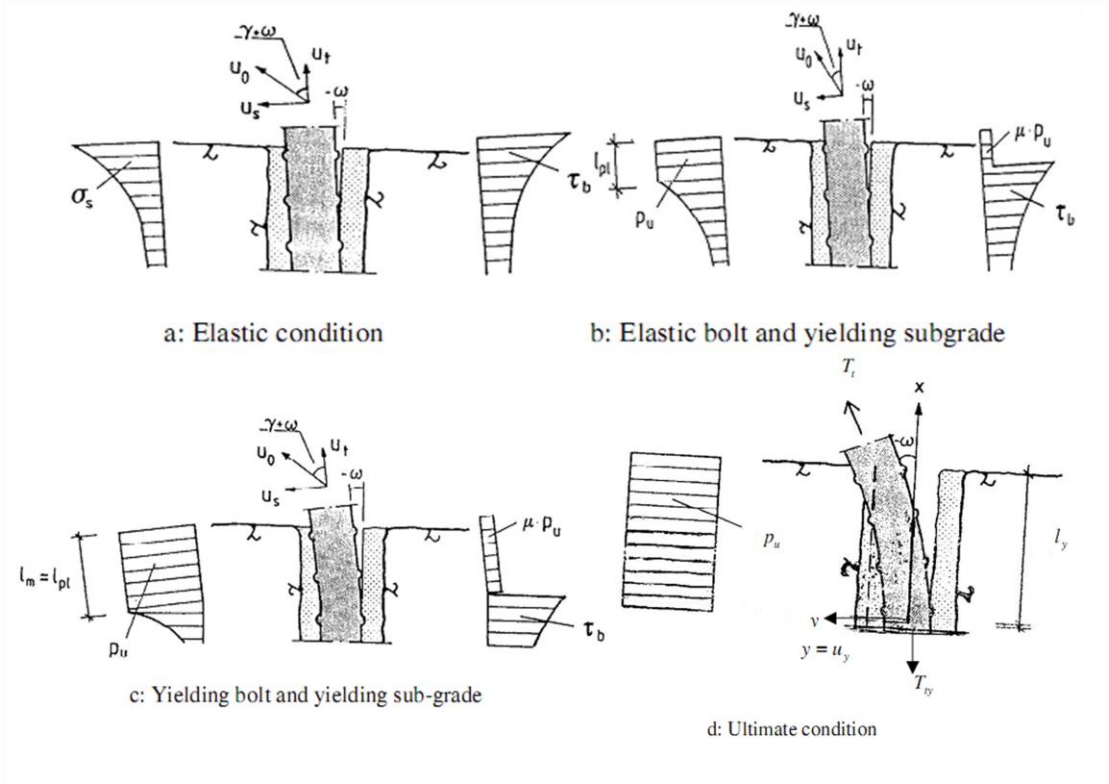

Figure 2.9 Bolt grout behaviour (Holmberg, 1991)

Holmberg's theory suggested that the bolt's contribution to the shear resistance from dowelling and axial load which could be determined as a function of deformation for different load conditions. Factors influencing this included, bolt and hole diameter, steel quality, bolt elongation, rock and grout strength. The angle between the bolt and the joint is important for the behaviour of the bolted joint surface, especially in determining the failure mode. If the angle is < 35° it seems to be a tension failure, and if the angle is approximately 90°, it is failure in shear.

Based on the numerical and laboratory studies of reinforced rock joints, Ferrero (1995) proposed a shear strength model which was applicable to bolts installed perpendicular to the joint surfaces. The global reinforced shear resistance was expressed as:

$$F = t_r cos\alpha - Qsin\alpha - (t_r sin\alpha - Qcos\alpha)tan\varphi_j \qquad (2.7)$$

Where:

t_r =Load induced in the bolt

α = Angle between the joint and the dowel axis and

Q = Force due to dowel effect

φ_j = Joint friction angle

Failure analysis was conducted based on failure modes study. According to experimental and modelling evidence, possible ways of failure include: (1) the combination of the axial and shear force acting at the bolt-joint intersection; and (2) the axial force following the formation of hinge points. The first yielding mechanism was likely to occur with stronger rock as shown in Figure 2.10.1. The bolt was loaded by the axial and frictional forces that developed between the bolt and the surrounding grout. The relationship between the bar tension at the point of maximum moment and bolt-joint intersection were developed. The second failure mechanism occurred when the maximum bending moment at point A in Figure 2.10.2 exceeded the maximum yielding moment of the bolt. It normally occurred in weak and less stiff rocks. In addition, Ferrero stated that pre-tension did not influence maximum resistance of the system.

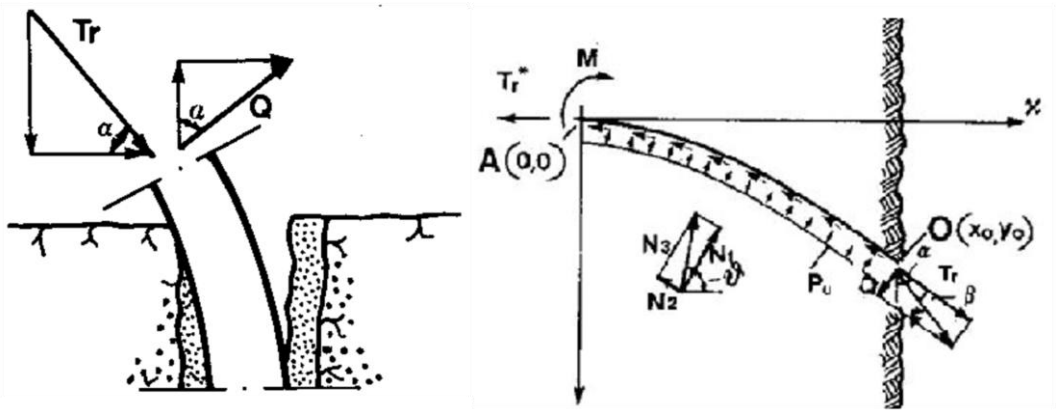

Figure 2.10 (1) Resistance of a reinforced rock joint; and (2) forces while failure (Ferrero, 1995).

Pellet and Egger (1996) proposed a shear strength model for reinforced rock joints. The interaction between the axial and the shear forces in the bolt was investigated and large plastic displacements of the bolt during loading were taken into account. In the model, the bolt behaviour was divided into elastic stage and plastic stage. The stressed bolt and the failure envelope for both elastic and plastic deformations are shown in

Figures 2.11 and 2.12 respectively.

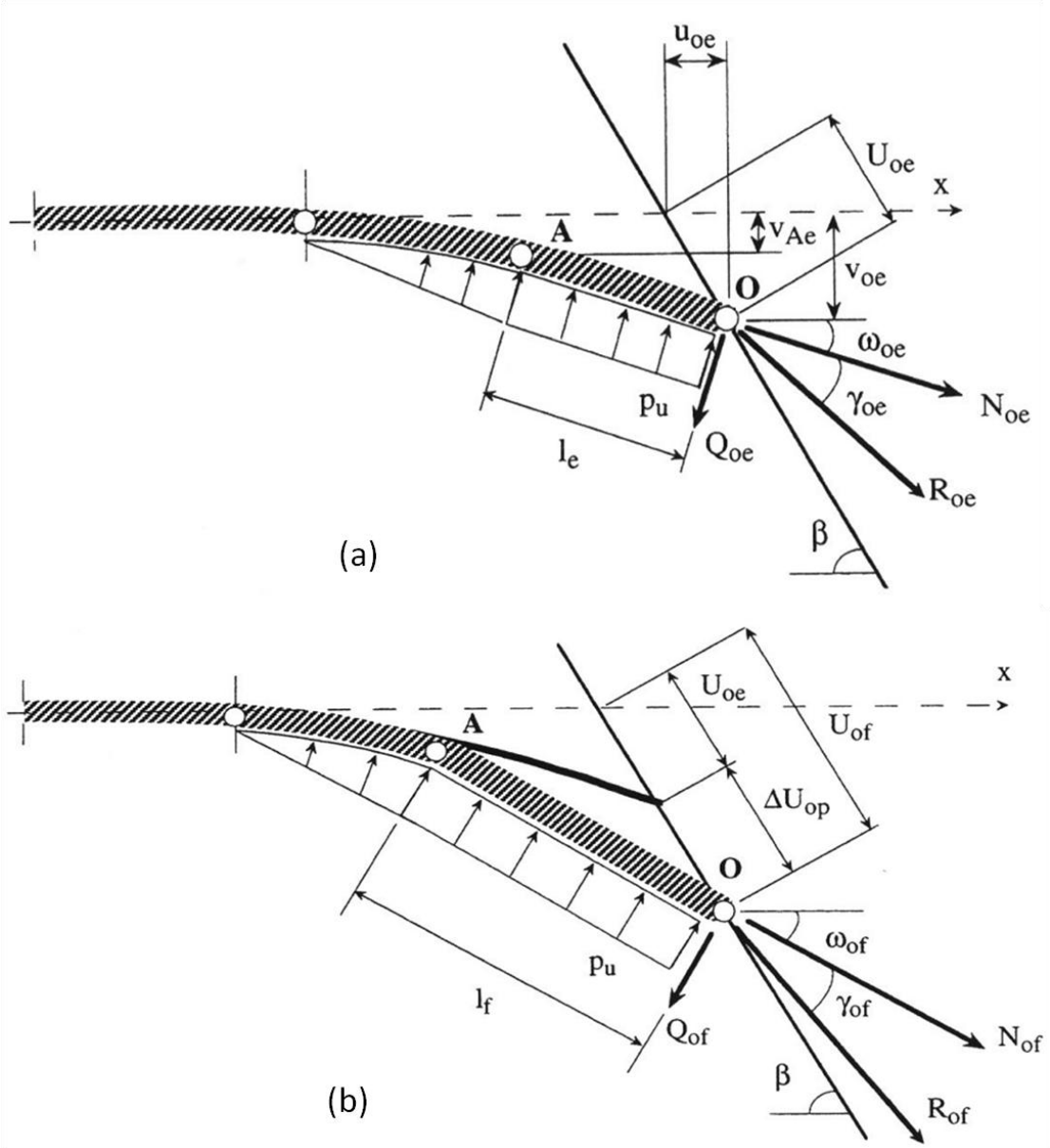

Figure 2.11 Force components and deformation of a bolt (a) in elastic zone, and (b) in plastic zone (Pellet and Egger, 1996)

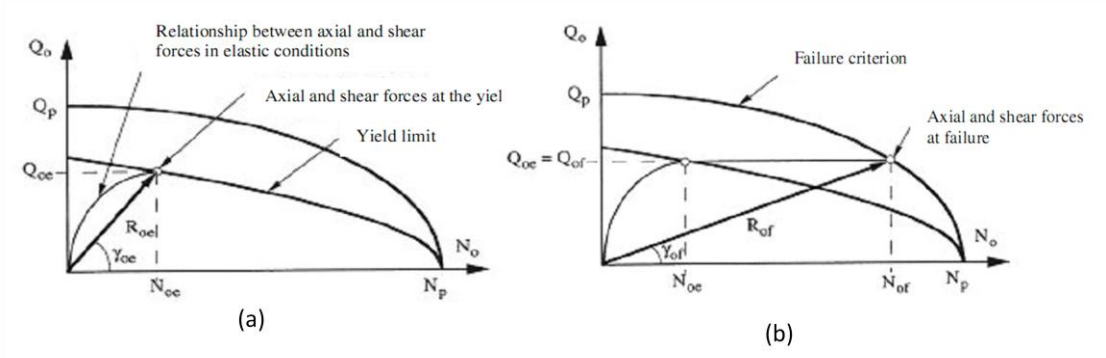

Figure 2.12 Evolution of shear and axial forces in a bolt (a) in elastic zone, and (b) in plastic zone (Pellet and Egger, 1996)

The shear forces and corresponding displacements of the bolt at the end of the elastic stage and plastic region were expressed as:

$$Q_{oe} = 0.5\sqrt{p_u D_b \left(\frac{\pi D_b \sigma_y}{4} - N_{oe}\right)} \quad (2.8.1)$$

$$Q_{of} = \frac{\pi D_b^2}{8}\sigma_{ec}\sqrt{1 - 16\left(\frac{N_{of}}{\pi D_b^2 \sigma_{ec}}\right)^2} \quad (2.8.2)$$

$$u_{oe} = \frac{8192 Q_{oe}^4 b}{E\pi^4 D_b^4 p_u^3 sin\beta} \quad (2.8.3)$$

$$u_{of} = \frac{Q_{oe} sin\Delta\omega_{op}}{p_u sin\,(\beta - \Delta\omega_{op})} \quad (2.8.4)$$

Where:

Q_{oe} =Shear force acting at point O at the yield stress of the bolt

p_u = The bearing capacity of the grout or rock

D_b= Diameter of the bolt

σ_y= Yield stress of the bolt

N_{oe}= Axial force acting at shear plane at the yield stress of the bolt

Q_{of} =Shear force acting at shear plane at failure of the bolt

σ_{ec}= Failure stress of the bolt

N_{of}= Axial force acting at shear plane at failure of the bolt

u_{oe} = Axial displacement at point O

E = bolt elasticity

$\beta = \tan^{-1}\frac{v_{oe}}{u_{oe}}$

v_{oe} = Shear displacement at point O

$$\Delta\omega_{op} = cos^{-1}\left[\frac{l_e}{l_f}sin^2\beta \pm \sqrt{cos^2\beta(1-\left(\frac{l_e}{l_f}\right)^2 sin^2\beta)}\right]$$

l_e= Distance between point O and point A

l_f= The length of the part O-A at failure

Pellet and Egger's evaluations showed that bolt inclination had a significant influence on maximum joint displacement. The greatest displacement was reached when the bolt was normal to the joint. As the angle between bolt and joint decreases, displacement drops rapidly (Figure 2.13).

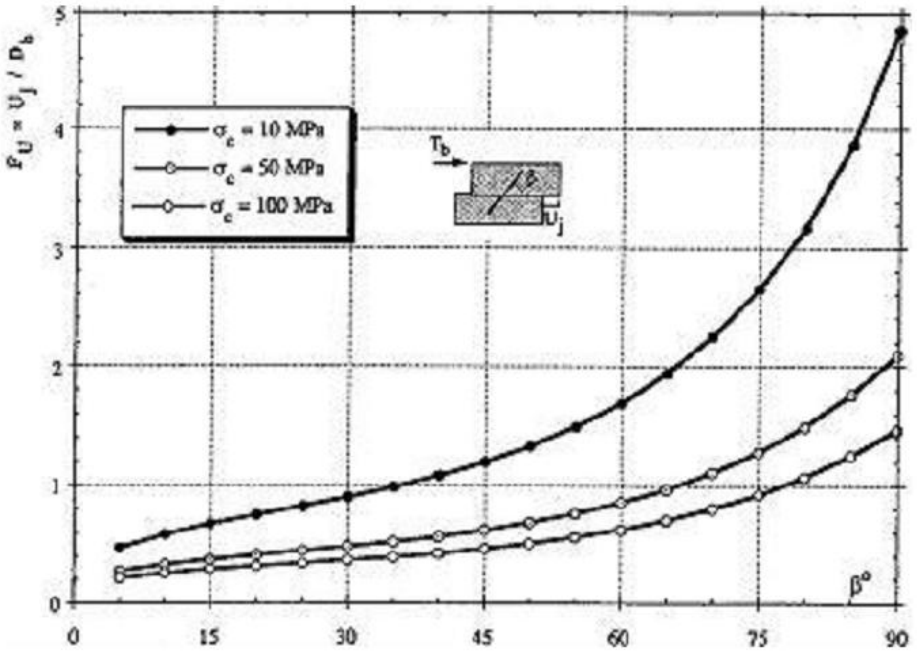

Figure 2.13 Joint displacement as a function of angle β for different UCS (Pellet and Egger, 1996).

2.4 MECHANISM OF ROCKBOLTING SYSTEM

2.4.1 Point loads simulation

In the 1960s, despite rockbolting of tunnel walls as a means of structural support gaining in popularity, much of its systematic design relied largely on empirical experience due to the lack of theoretical solution. McNiven and Ewoldsen (1968 a and 1968 b) did pioneer work to develop a design procedures in a circular tunnel by

simplifying a single rockbolt with a pair of point loads.

The idea is that, once the geometry of the tunnel, mechanical properties of the rock and the *in situ* stress are known, the stress field around the tunnel after excavation running through a half-space can be found using the theory of elasticity. The rock is assumed to be an isotropically elastic, homogeneous material. For ground supports, rockbolting will set up another stress field surrounding the tunnel. Therefore, the object of the design is to construct this second stress field so that when this field is added to the first, the total field will contain stresses that are within the stress capacity of the rock.

A single rockbolt is simulated as a pair of point forces, one loading at the surface and another loading at an interior point of the half space, as shown in Figure 2.14. For the point load at the surface, Boussinesq's equations can be applied. A point load at an interior point of the half-space is one of Mindlin's problems. The mining introduced stress field can be evaluated using elasticity theory. The total stress field surrounding a rockbolted tunnel can be obtained via superposition of the stress field caused by excavation with the stress fields induced by rockbolting. In addition, several kinds of different *in situ* stress fields, shown in Figure 2.15, were also discussed.

This early model is a good analytic approximation to the real rock bolt stress field. However, it is only a suitable estimation for point anchor bolts. In addition, this model does not consider the borehole induced stresses. As a result, the solutions are valid as long as the radial distance is large compared to the hole radius. The stress analysis based on half space theory presented in this research work has been adopted to investigate the effect of bolt rib profile in this study.

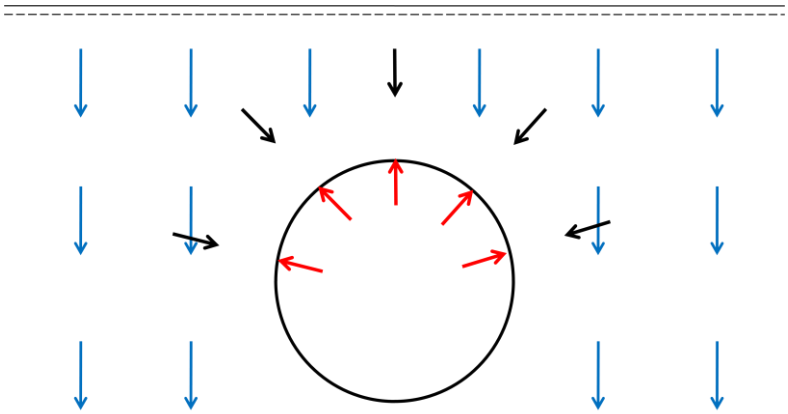

Figure 2.14 The stress field surrounding a rockbolted tunnel (modified from McNiven and Ewoldsen, 1968 a).

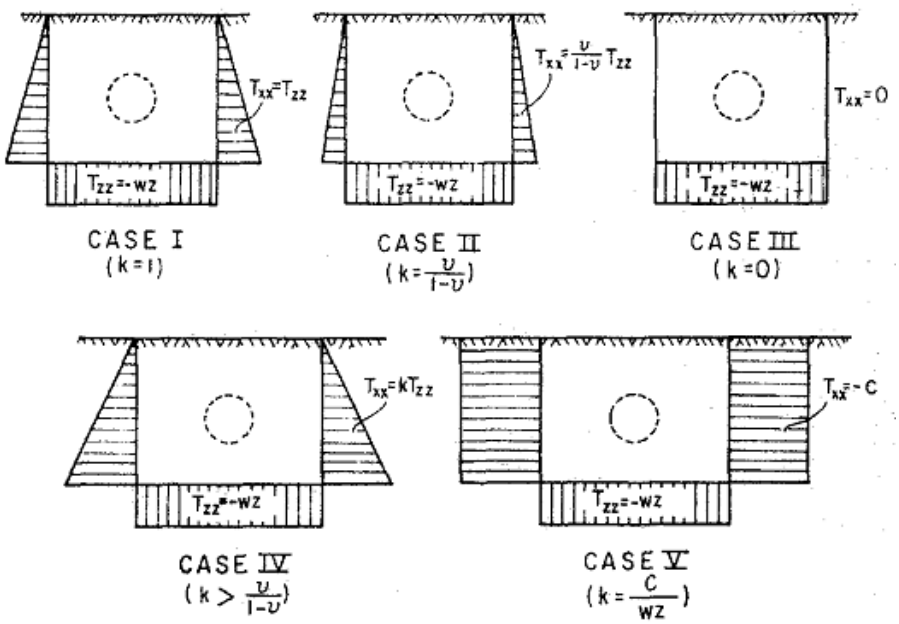

Figure 2.15 The different *in situ* stress fields (McNiven and Ewoldsen, 1968 b).

Wijk (1978) pointed out that in McNiven and Ewoldsen's model, i.e. using a pair of point loads to simulate a single bolt, the two point loads introduced a stress component normal to the borehole wall that should be zero but it did not in the model. A comparative sketch is illustrated in Figure 2.16. As a result, the solution of the model yielded large tensile stresses in the tunnel surface, and in some regions there were also small tensile stresses in tangential and longitudinal directions around the borehole. To avoid these errors, the disturbing of stress field by the borehole installation must be considered. But it may lead to extremely cumbersome mathematical expressions for the stress field.

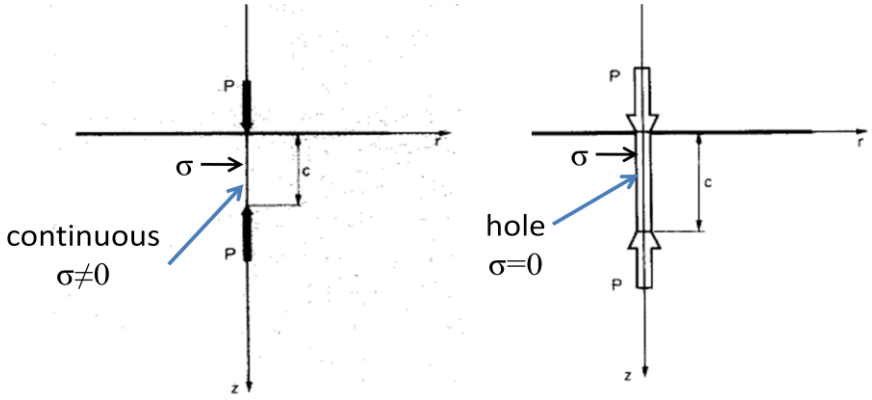

Figure 2.16 left: McNiven and Ewoldsen's model; right: real rockbolt problem. (Modified from Wijk, 1978)

Since tensile rock failure in the tunnel walls is exactly what the rock bolts are intended to prevent, it is clear that a more accurate theory is needed in order to understand how to use rock bolts for stress re-distribution.

2.4.2 Convergence-confinement approach

In spite of some understanding of the load transfer mechanism of rockbolting, such as the exponential decay of axial load of fully grouted bolt, it was not being applied to underground excavation until the 1990s. In one classical paper, Brown *et al* (1983) used 'ground response curves' to deal with rock support interaction and to aid in the dimensioning of tunnel support elements. The deformations around an excavation in rock were thought as a result of the interaction between rock mass, initial stress condition and the rock support. The interdependence of these various factors was represented by ground characteristic lines and support reaction lines on a ground-support interaction diagram, shown in Figure 2.17.1. The radial support pressure, p_i, required at a particular point on the excavation boundary to limit the local radial convergence to δ_i, was given by the ground characteristic line. In this case, support is installed at P after a radial wall displacement of δ_{i0} had occurred. Stress built up in the support with displacement along PC until equilibrium was reached at C.

Many approaches to the calculation of ground response curves for a particular tunnel have been reported in the literature. The problem is often defined as a circular tunnel in a homogeneous, isotropic, initially elastic rock mass subjected to a hydrostatic stress field (Figure 2.17.2). The rock mass can be assigned for different elasto-plastic behaviours. More complex engineering problems involving complex excavation geometries and stress fields have also been studied using numerical methods. The support system is just assumed to provide a uniform radial support pressure p_i. After calculating the ground response curve, a critical value of internal support pressure can be found.

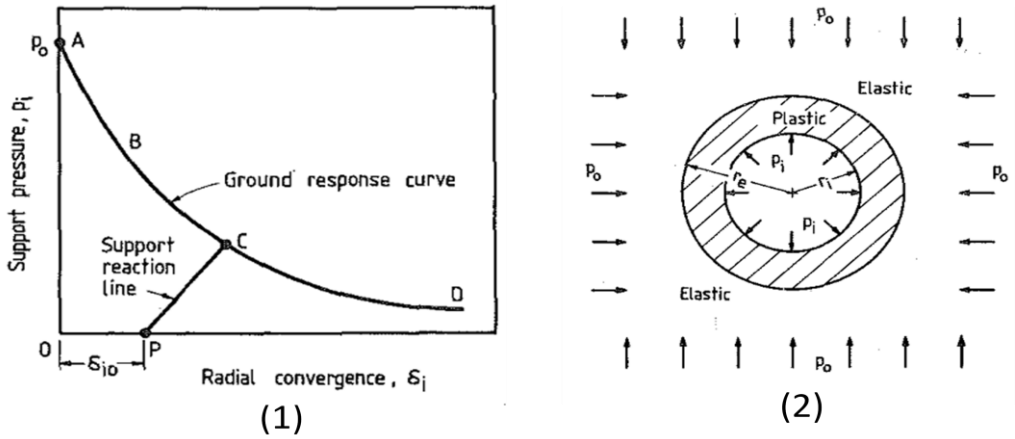

Figure 2.17 (1) Ground-support interaction diagram, and (2) The axisymmetric tunnel problem (Brown *et al*, 1983).

In this so-called convergence-confinement approach for tunnel construction, the rock bolt is expected to add an equivalent internal pressure to the tunnel wall. This equivalent internal pressure is considered to originate from the axial force of the rockbolt, which is influenced by the behaviour of rock mass. However, the behaviour of the rockbolt is not considered in this approach. As a result, it is difficult to determine a bolting pattern via the value of equivalent internal pressure.

Stille *et al* (1989) presented a closed form elasto-plastic analytical solution using the ground reaction curve concept. The behaviour of the rock support using anchor bolts was simulated as a support line expressed by (Figure 2.18.1):

$$p_i = k_s \Delta u_i + p_{pre} \qquad (2.9)$$

Where:

p_i = support pressure

Δu_i = relative displacement

k_s = support stiffness;

p_{pre} = pre − stress load, as shown in Figure 2.18.1.

The supports were no longer considered to establish radial pressure on the rock surface but to increase the strength of the rock mass compared to the unsupported rock. Four different situations for a rock mass with grouted bolts were considered (Figure 2.18.2) as:

- Elastic bolt in a plastic rock mass: the rock mass and the bolt are assumed to have the same strain. The tensile load in the bolt will imply a corresponding additional compressive stress in the rock mass. Radial stress in the rock mass will then be calculated as the sum of mining introduced stress and the bolting support.
- Plastic bolt in a plastic rock mass: the interaction between rock mass and bolt is idealised as a perfect plastic behaviour.
- Plastic deformation of the grouting material: the bolt is in elastic condition and load only depends on the residual capacity of the grout to transfer load between rock mass and bolt.
- Elastic bolt with nut and end plate and plastic deformation of the grout materials:

the shear strength of the grouting material is exceeded in the outer part of the bolt and the load depends on the local deformations of the rock mass under the end plate and the residual capacity of the grout to transfer load between rock mass and bolt. The end plate acts theoretically as a circular spread load.

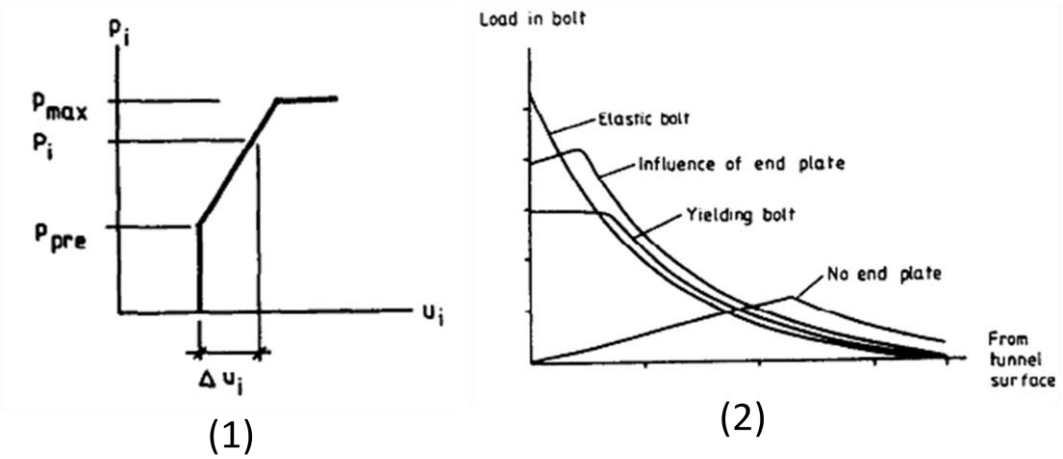

Figure 2.18 (1) Support reaction line for anchor bolts. (2) Load distribution along the bolt in different situations (Stille *et al*, 1989).

In the aforementioned studies, the conditions at the bolt head and the tunnel perimeter were assumed to be either perfect bonding or zero force. In real tunnels however, an intermediate condition exists. Oreste and Peila (1996) developed a procedure for the computation of the convergence-confinement curves of a bolted tunnel with emphasis on the different bolt end plate response curves. In Figure 2.19, curve (a) is the tie characteristic line linking the force applied at the end-plate and the displacement of the centre plate; curve (b) is the bolt head reaction to the applied force.

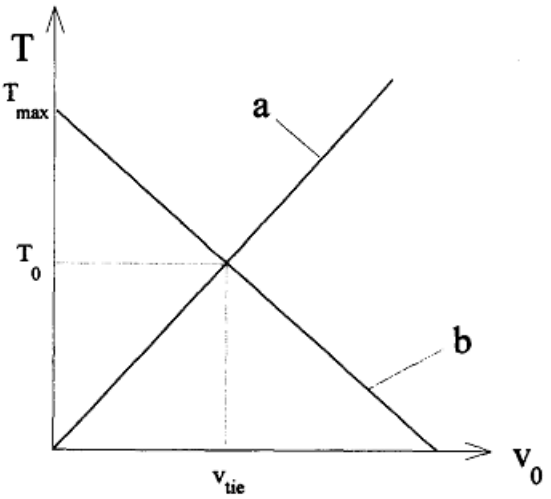

Figure 2.19 Definition of the force, T_0, applied by the bolt on the tunnel surface (Oreste and Peila, 1996).

2.4.3 Neutral point and equivalent strength

Based on field studies of yielding rocks, Sun (1983) expressed a theoretical model to predict stress distribution along the bolt. The concept of a "neutral point", where there was zero relative displacement between bolt and rock, was introduced (Figure 2.20). The shear stress distribution was characterised by dividing the bolt into a "pick up length" and an "anchor length" on either side of the neutral point. A positive frictional force was generated between the rock and bolt interface towards the far field; and a negative frictional force formed from the rock to the bolt but towards the tunnel face. It should be noted that bolts *in situ* have a pick up length and an anchor length while those in pull out test only have an anchor length and the axial load distribution in the two cases produce different results.

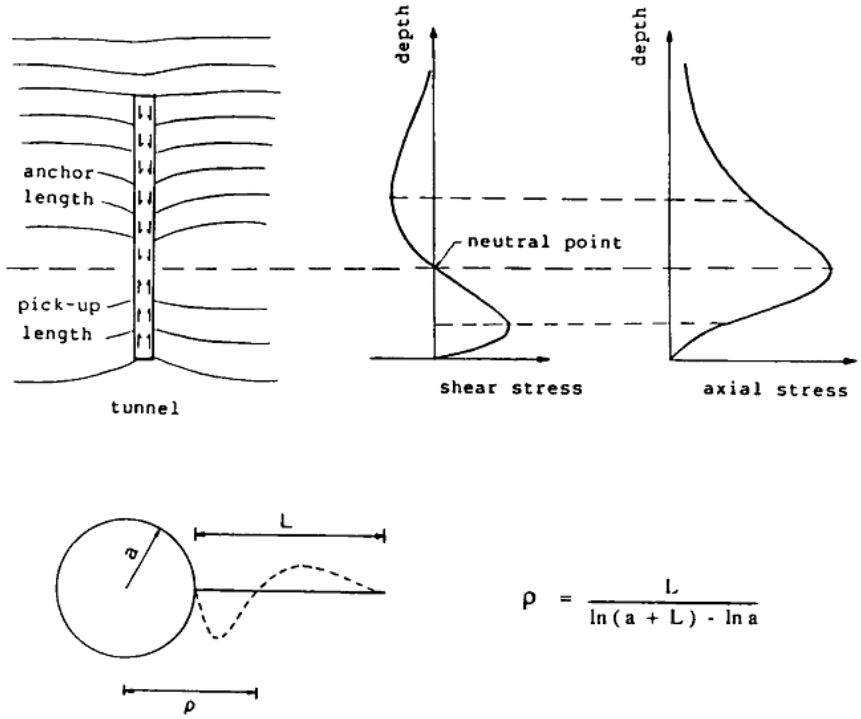

Figure 2.20 Stress distribution model for grouted bolts, ρ is the length from tunnel center to the neutral point (Sun, 1983).

Considering a bolt with linear shear behaviour at the bolt-grout interface grouted into a circular tunnel for which the rock displacement is described by equation (2.10), according to the definition of neutral point, the location of the neutral point can be found using equation (2.11).

$$u_r = u_{r0} a \frac{1}{x} \tag{2.10}$$

$$\rho = \frac{L}{ln\,(1 + \frac{L}{a})} \qquad (2.11)$$

Where:

x = the radius at any point around the tunnel;

u_r = axial displacement of the bolt;

a = the radius of the tunnel, and

u_{ro} = the displacement at the tunnel wall.

L = the bolt length (Figure 2.20).

However, the shear stress plot in Figure 2.20 is incorrect (Hyett *et al,* 1996). Since the bolt is assumed to be rigid, the shear stress and axial force are shown in Figure 2.21.

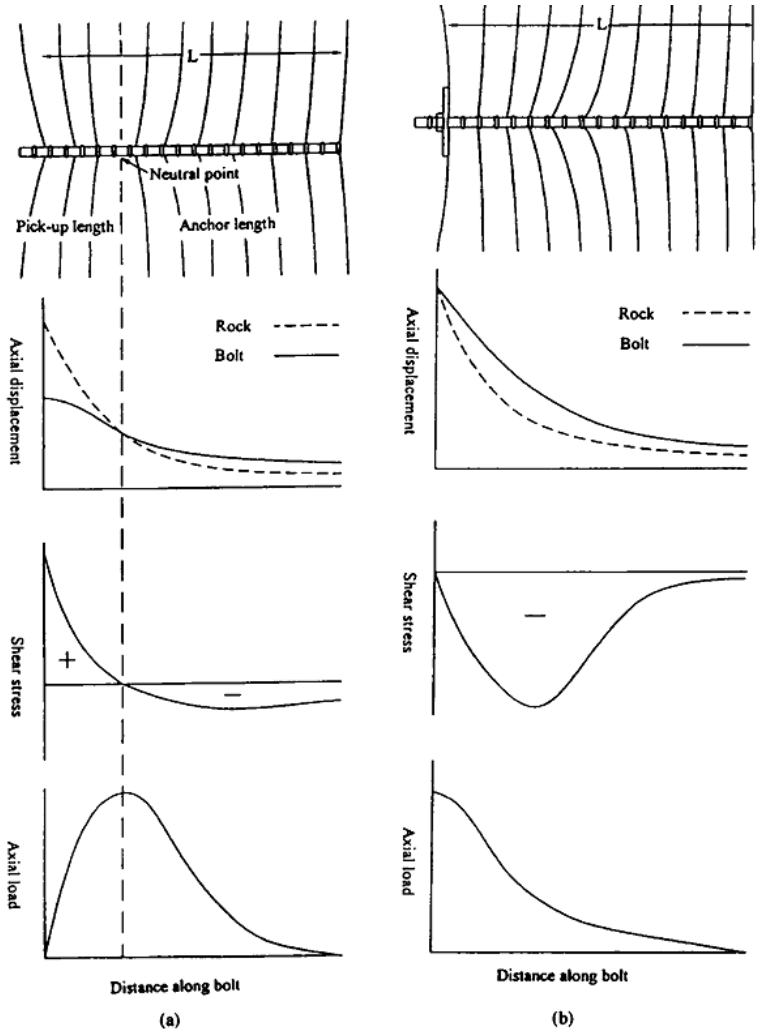

Figure 2.21 Shear stress and axial force for grouted bolts, (a) two free ends, and (b) face plate attached at the excavation surface (Hyett *et al,* 1996).

In later research work on the concept of the neutral point, the position of the neutral point was still doubtful, at least when slippage took place at the interface or if a pre-stress state exists. In addition, there may be several neutral points along the rock bolt. In fact, the axial force in the rock bolt is caused by the deformation or displacement of the rock mass, and the neutral point is influenced by the interaction behaviour of the rock bolt and the rock mass.

Based on the considering the position of neutral point, an approach to model a fully grouted bolts reinforced circular tunnel in a homogeneous, isotropic medium was described by Indraranta and Kaiser (1990 a and 1990 b). The analytical solution was still based on elasto-plasticity of an axisymmetric problem, but they introduced the concept of equivalent strength of the rock to simulate the rockbolting effect. In this literature, the yield initiation of the unsupported rock was assumed to occur following a linear Mohr-Coulomb failure criterion:

$$\sigma_\theta = m\sigma_r + s\sigma_c \qquad (2.12.1)$$

where:

$m = tan^2\left(\frac{\pi}{4} + \frac{\varphi}{2}\right)$;

$s \in (0, 1)$ is a measure of the strength loss occurring immediately after the peak strength is reached.

The equilibrium of an element near an unsupported opening was represented by:

$$\frac{d\sigma_r}{dr} + \frac{\sigma_r - \sigma_\theta}{r} = 0 \qquad (2.12.2)$$

Combination of equation (2.12.1) and (2.12.2) leads to:

$$\frac{d\sigma_r}{dr} + \frac{(1-m)\sigma_r}{r} = \frac{s\sigma_c}{r} \qquad (2.12.3)$$

In a bolted element, however, the equilibrium condition can be represented by:

$$\frac{d\sigma_r}{dr} + \frac{[1 - m(1+\beta)]\sigma_r}{r} = \frac{s\sigma_c(1+\beta)}{r} \qquad (2.12.4)$$

where:

$\beta = \frac{\pi D_d \lambda a}{S_L S_T}$ is the bolt density parameter;

$\lambda = \frac{1}{\pi D_d \sigma_\theta} \frac{d\tau}{dr}$ is analogous to the coefficient of friction

D_d=bolt diameter;

a =tunnel radius;

S_T=tangential (circumferential) bolt spacing

S_L=longitudinal bolt spacing.

Equations (2.12.3) and (2.12.4) contained the same algebraic structure, which was the concept of "equivalent strength parameters".

Indraranta and Kaiser (1990 a and 1990 b) also pointed out that failure of a bolt-ground composite took place along the weakest interface unless the bolt itself yields. It may occur by the bolt pulling out, as was sometimes observed in the case of smooth bars. Such failure could be prevented by shaping the bolt surface, which increased the magnitude of λ. However, failure may also initiate within the grout annulus or at the grout/rock interface owing to impaired grout strength development. After introducing the flow rule $\varepsilon_r^p + \alpha \varepsilon_\theta^p = 0$ to the linear Mohr-Coulomb failure criterion, where the parameter α is the dilation coefficient that characterises the volume change in the plastic zone, the concept of "equivalent plastic zone" was introduced to describe the extent of yielding around the circular tunnel. Three categories of yield propagation were analysed with respect to the relative location of the plastic boundary from the neutral point, and the stress and displacement fields were determined correspondingly.

By combining and advancing Farmer's and Sun's models, Hyett *et al* (1996) assumed that the shear force for a unit length of bolt was a linear function of the relative slip between the bolt and the rock. The distribution of displacement along the bolt was described by the second-order inhomogeneous linear differential equation, whose general form solution is:

$$u_x = c_1 e^{\alpha x} + c_2 e^{-\alpha x} + \frac{e^{\alpha x}}{2\alpha} \int e^{-\alpha x} u_r(x) dx - \frac{e^{-\alpha x}}{2\alpha} \int e^{\alpha x} u_r(x) dx \qquad (2.13)$$

where $\alpha^2 = \frac{k}{AE_b}$ and c_1 and c_2 can be determined from the end conditions.

If u_r can be represented by an analytical function of x $(0<x<L)$, closed form solutions can be found. Several $u_r(x)$ examples are shown in Figure 2.22. The examples show that the maximum axial load developed in the bolt for discontinuous case is significantly higher than for the continuous case.

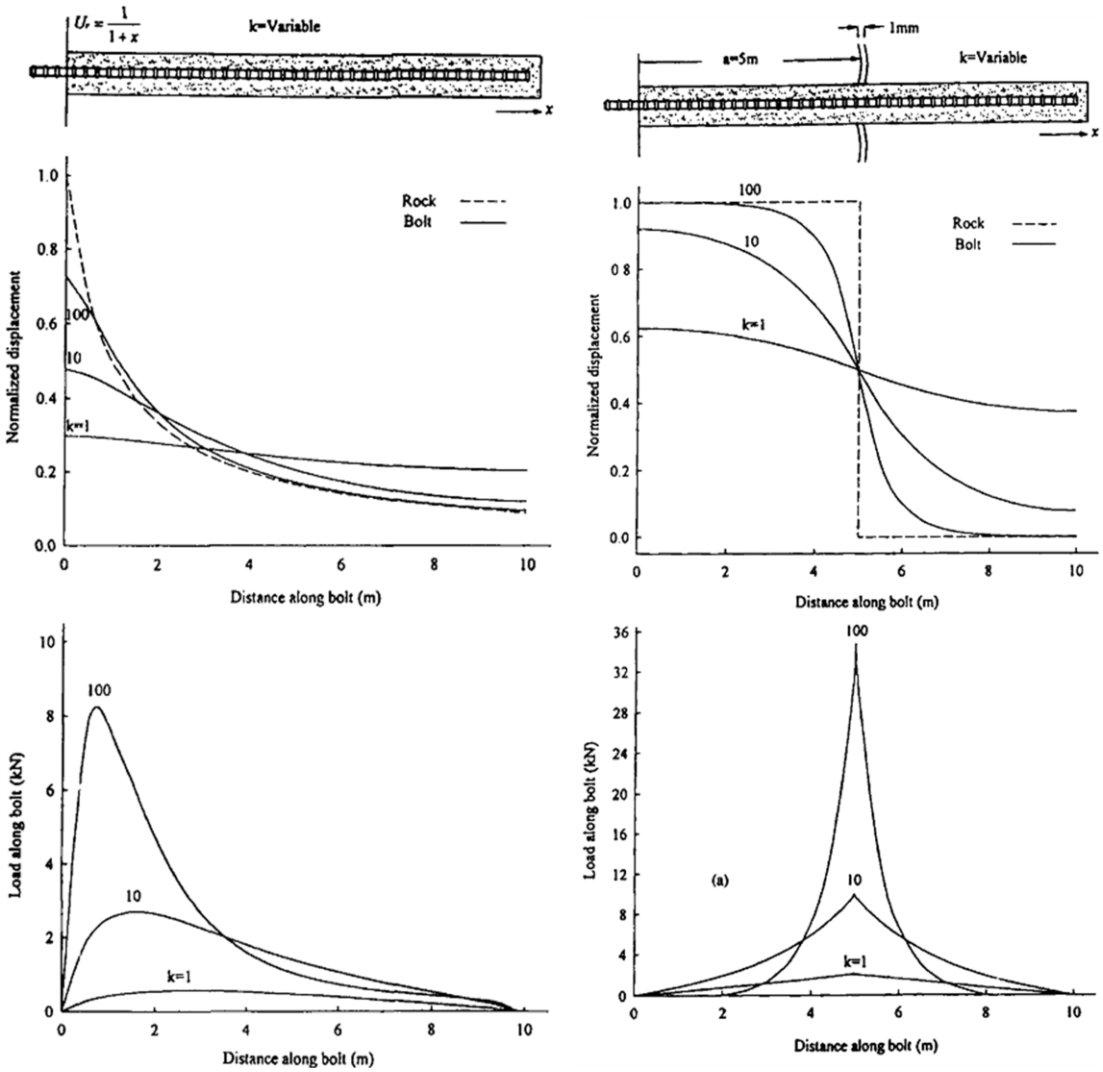

Figure 2.22 Analytical solutions (U_{r0}=1mm) of axial load and displacement for a bolt with two free ends (Hyett *et al*, 1996).

2.4.4 Shear-lag model

Cai *et al* (2004 a and 2004 b) proposed an analytical model to predict the axial force of grouted rockbolts in tunnelling design. Coupling and decoupling behaviours of the rock bolt around a circular tunnel have been analysed.

In the model, the reinforced tunnel is separated into two parts, one is the original rock mass without the rock bolt, and the other is the reinforcing element loaded with the induced axial force of the rock bolt. Actual total stress is the sum of the two parts.

The original stress of the rock mass without the rock bolt can be obtained according to the different constitutive laws. Figure 2.23 shows the equilibrium state of the infinitesimal element of the reinforcement. The initial displacement of the rock mass without bolting is u_{ini}, it is restrained to be u_m by the rock bolt, and correspondingly, the displacement of the rock bolt becomes u_b. The basic constitutive law of the induced stress can be expressed as:

$$\frac{dP(x)}{dx} = -2\pi r_b \tau(r_b, x) \tag{2.14.1}$$

$$\frac{\partial \sigma_m(r,x)}{\partial x} + \frac{\partial \tau(r,x)}{\partial r} + \frac{\tau(r,x)}{r} = 0 \tag{2.14.2}$$

$$\frac{dP(x)}{dx} + 2\pi \int_{r_b}^{R} r \frac{d}{dx} \sigma_m(r,x) dr = 0 \tag{2.14.3}$$

Where:

$P(x)$ = axial load along the bolt

x = distance along the axial of reinforcement

r_b = the radius of the reinforcement

$\tau(r_b, x)$ = the shear stress on the reinforcement

$\sigma_m(r,x)$ = the additional radial stress caused by the rock bolt

$\tau(r,x)$ = the resultant shear stress at the position (r, x)

r = perpendicular to its axis in a cylinder coordinate

R = the influence radius of a single reinforcement

The interaction mechanism between the rock mass and the grouted bolts is complicated. A coupling model is often proposed to describe the behaviour based on the shear-lag model (SLM). The shear-lag assumptions in Cai's model are:

$$\frac{dP(x)}{dx} = H(u_b - u_m) \qquad (2.14.4)$$

$$\tau(r,x) = \tau(r_b,x)f(r) \qquad (2.14.5)$$

H is the material parameter which describes the interaction physical properties of the rock bolt and the surrounding rock mass and *f(r)* describe the distribution of resultant shear stress in the rock mass.

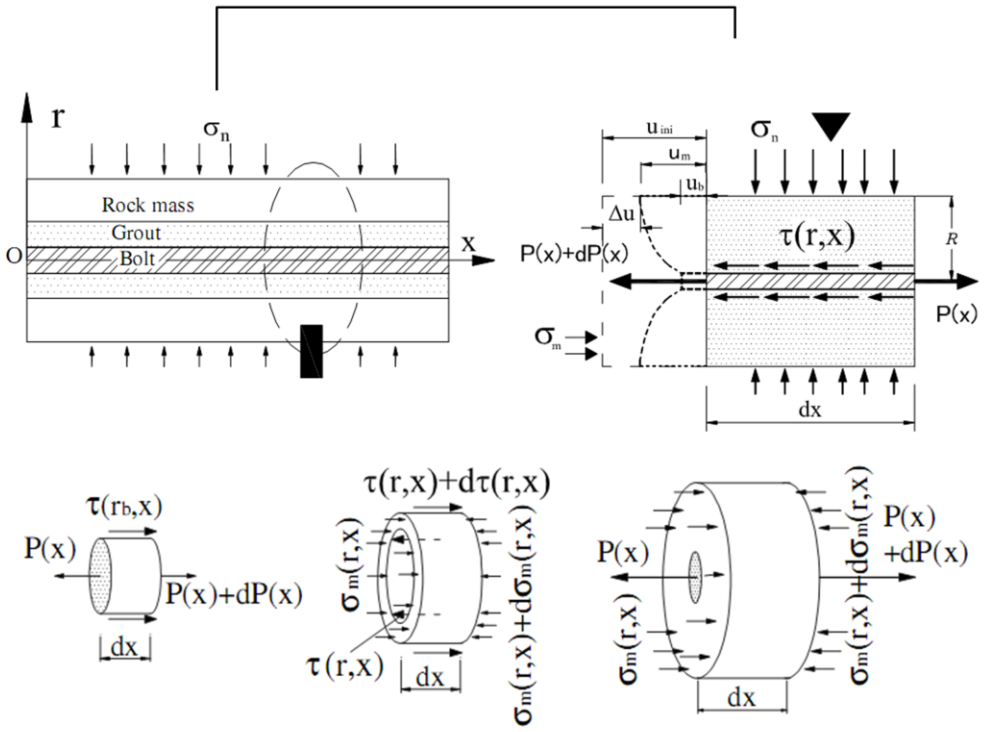

Figure 2.23 Equilibrium element of the rock bolt, rock mass and composite in cylinder coordinate. (Cai *et al*, 2004 a)

If uniform distribution of anti-pressure from the rock bolt is assumed, the shear stress distribution function can be solved as:

$$f(r) = r_b(R^2 + r_b^2 - r^2)/(R^2 r)$$

$$H = \frac{2\pi G_g G_r}{\left(ln\frac{R}{r_b} - \frac{1}{2}\right)G_g + G_r ln\frac{r_g}{r_b}}$$

Where:

r_g = the radius of the grout borehole

G_g = the shear modulus of the grout mortar

G_r = the shear modulus of the rock

According to the shear lag model, the resultant axial force of the rock bolt depends on the released deformation of the rock mass. The behaviour of the soft rock around a tunnel shows significant strain softening characteristics under a low confining pressure. Three kinds of zones such as a plastic flow zone, a plastic softened zone and an elastic zone may co-exist around the tunnel, as shown in Figure 2.24. If the rock bolt was installed in different zones, continuous boundary conditions had to be considered because the deformation behaviour of the rock mass was not the same in different regions. The constitutive equation of the single rock bolt is expressed as

$$\frac{d^2P(x)}{dx^2} = H\left(\frac{P(x)}{E_bA_b} + \frac{P(x)}{E_mS} - \frac{\partial u(x)}{\partial x}\right) \qquad (2.14.6)$$

And the *u(x)* is the displacement of the plastic zone, the soften zone and the elastic zone respectively.

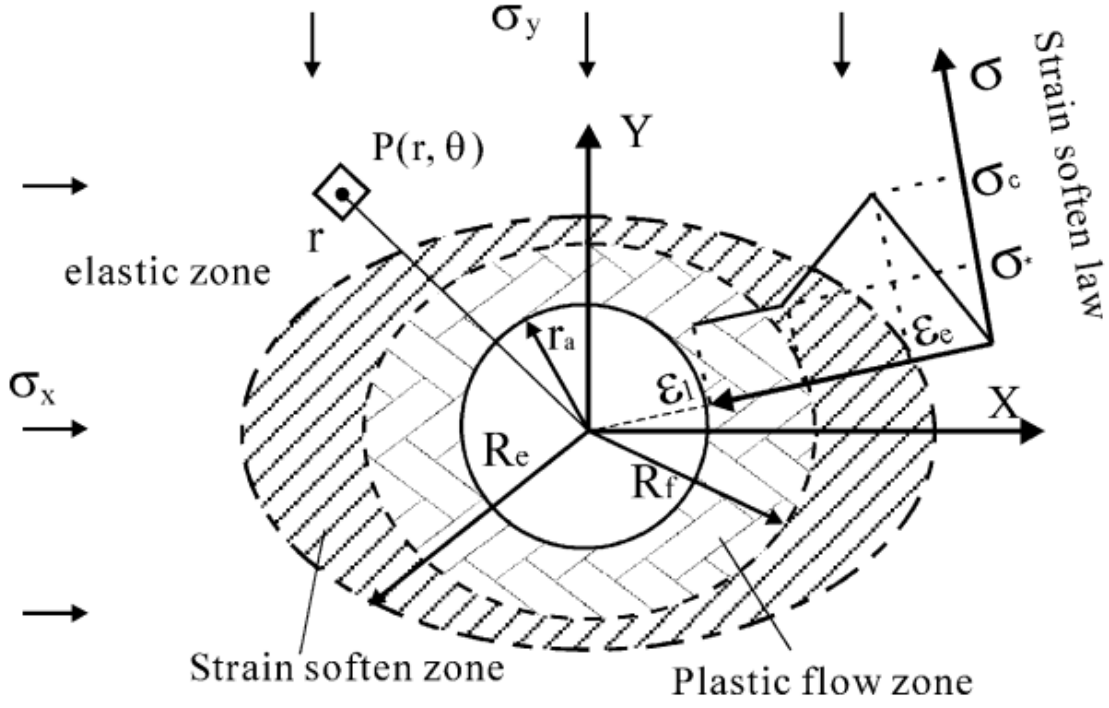

Figure 2.24 Rock deformations in tunnel cross-section (Cai *et al*, 2004 b)

2.5 CONCLUSIONS

Rock bolting is the main element of support in reinforcement systems. It is used to tie together stratified or broken rocks or cracks caused by mining activities. The binding effects are accomplished by one or a combination of several basic mechanisms: suspension, beam building, arching and keying.

In general, a fully grouted rock bolt can transfer greater loads than expanded shell or wedge type anchorages. Hence, fully grouted bolts are increasingly being used in mines. In addition, only resinous grouts can meet the high strength required for short anchorages. This may be essential in weaker rock strata where high loads have to be transferred over a short length borehole.

For bolt reinforcement across joint planes, the bolt orientation, installation type, joint surface friction and medium strength are important factors for the reinforcement effectiveness. Bolts installed at inclination to the sheared joint plane contribute to a greater resistance to shearing than perpendicular bolts.

The majority of the reported shear tests have been conducted under single shear test condition, where there is asymmetric and a non-uniform distribution of load across the joint plane. The effect of pre-tension load on shear behaviour and load transfer mechanism has not been subjected to qualitative analysis. There is no reported citing of any study making reference to bolt surface profile configuration on the load transfer mechanism across the bolt.

In tunnelling design, the rock bolting effects are simulated as internal pressure on ground sewing, or structure making, or ground arch making, or properties improving. Generally, the reinforced zone is assumed as a whole and the interaction between rock bolt and rock mass is ignored. It is more rational to regard the interaction characteristic in rock bolting design or in a convergence-confinement approach.

CHAPTER THREE

REVIEW OF ROCK BOLTS SUBJECTED TO AXIAL LOADING

REVIEW OF ROCK BOLTS SUBJECTED TO AXIAL LOADING

3.1 INTRODUCTION

Bolt reinforcement around underground excavations is very effective. It increases the safety factor against crack initiation and influences the orientation of existing cracks by transferring the load from unstable rock layers to stable rock.

When studying the bond strength, laboratory and/or field pullout tests are commonly employed. It seems to over-simplify the problem, but in fact it closely represents the realistic situations, as demonstrated by Hyett *et al* (1992) in Figure 3.1.

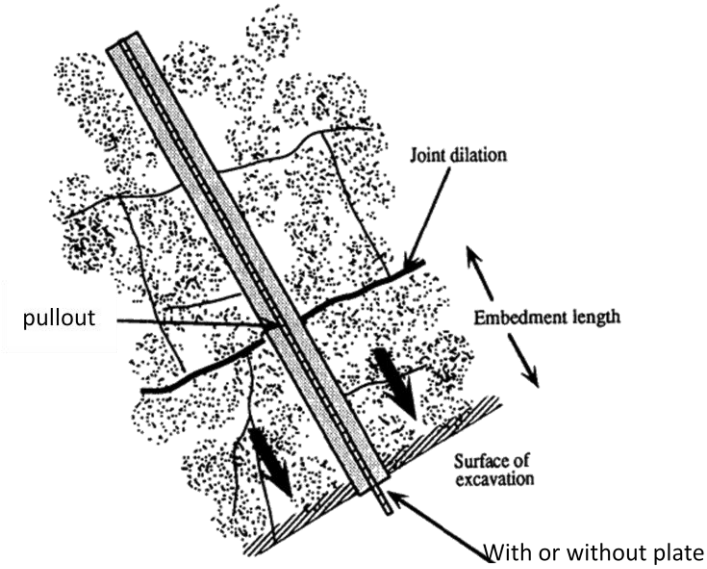

Figure 3.1 Rockbolt is being "pulled out" by joint separation (Hyett *et al*, 1992).

The load transfer between rock bolt and borehole depends on borehole diameter, grout properties and bolt profile. In a fully grouted rock bolt, the load transfer mechanism depends on the shear stress developed on the bolt resin interface. Many researchers have considered theoretical and experimental approaches to define bolt behaviour under axial loading. They tried to describe the interaction between bolt, grout, and rock, under axial loading but there has been almost no research on the role of bolt profile in the mechanism of load transfer.

A great number of pullout tests have been conducted, such as those by Lutz (1970),

Tepfers (1973), Farmer (1975), Littlejohn and Bruce (1975), Serbousek and Signer (1987), Aydan (1989), Signer (1990), Bawden *et al* (1992), Hyett *et al* (1992), Kaiser *et al* (1992), Benmokrane *et al* (1995), Mark *et al* (2002), Kilic *et al* (2002 a and 2002 b), Compton and Oyler (2004), Jalalifar (2006), Aziz *et al* (2003, 2004, 2006, 2009). Figure 3.2 illustrates a typical load displacement profile in pullout tests Jalalifer (2006). Pullout resistance refers to the axial force (MN/m) required to pull a bolt out of a grouted hole and the bond strength of a bolt (MPa) refers to the shear resistance per unit contact surface, which is obtained by dividing the pullout resistance force by the surface area of the bolt.

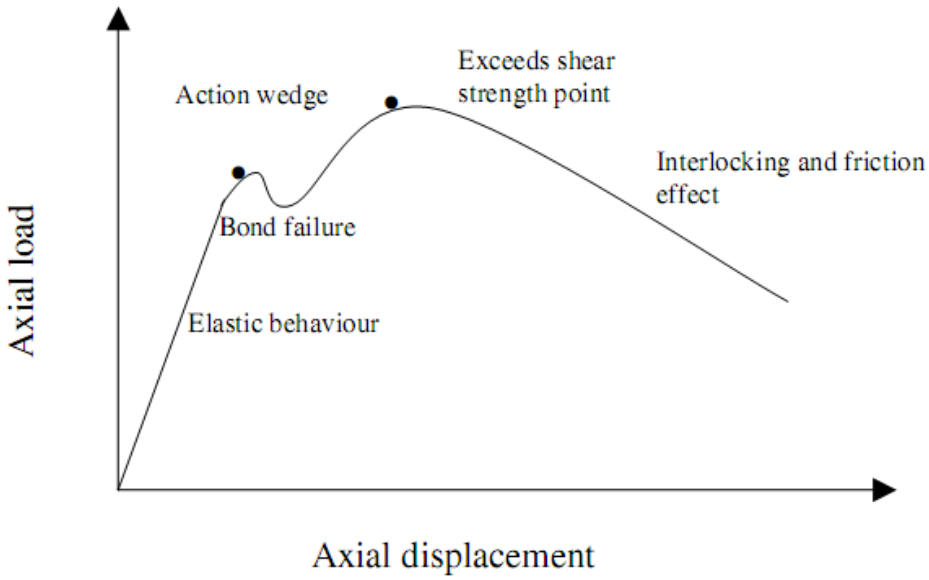

Figure 3.2 General trend of pullout test, Jalalifar (2006).

Using data from pull out tests of plain reinforcing bars and rebar, engineers have been aware that the bond strength of anchorage has three components: cohesion, friction and mechanical interlock. In traditional rockbolting load transfer mechanism analysis, the affect of mechanical interlocking is often integrated into the analytical model using various ways without considering the rib geometry.

Rockbolting failure is a major concern of reinforcement. Littlejohn and Bruce (1975) conducted the first systematic study on the failure of a rock bolt system and suggested three modes of failure: failure of rock mass, failure of rock bolt and failure at the grout - rock interface. Later research work, for example Aydan (1989), Hyett *et al* (1992), Ren *et al* (2009), focus on general classification of failure modes but there is seldom structural differentiation analysis on the failure modes.

3.2 PULLOUT TESTS

Serbousek and Signer (1987) conducted a series of pullout tests in grouted rock bolts and compared the results with analytical and numerical modelling. The tests were conducted on 1.2m and 0.3m bolts in 25.4mm and 44.4mm diameter holes. The applied load was limited to elastic response so that failures did not occur. Examination of resin bond showed no chemical adhesion by the grout. In addition, the hole size and grout type did not have a large influence on the elastic load transfer rates. It can be concluded that irregularities on the surface of the bolt and the hole cause a mechanical interlock, which will transfer shear resistance from one medium to another until maximum shear strength is reached.

Aydan (1989) carried out a series of push and pullout tests to investigate the anchorage mechanism of grouted rock bolts and the affect of various parameters such as the ratio of the bolt to borehole diameter and the behaviour of the bolt to grout interface under triaxial stress. Two steel bars 13mm and 19mm in diameter were tested. The results showed that the load bearing capacity of bolts was 25% higher in push out tests than pullout tests. Aydan stated that this increase in push test values was attributed to the Poisson's ratio effect (The radial stress is of a compressive character in the push out case while it tends to become tensile in the pull out tests). Later research work showed lower difference around 13-19% in push and pull tests (Aziz 2004 and Jalalifar 2006). It is suggested that all results are correct to some extent, as the difference of load capacity in push and pull tests relies on the Poisson's ratio effect as well as the rib profile. In addition, the Poisson's ratio effect is a function of the embedded length.

Aydan observed that although shearing failure along one of the interfaces was the main cause, some samples split without confining pressure. This was attributed to geometrical dilation of the bolt-grout interface during shearing which causes an internal pressure on the borehole. This phenomenon was also observed in the pullout tests conducted with 300mm concrete blocks.

Signer (1990) conducted a series of laboratory and field pull tests to investigate the load transfer from bolt head to the rock using resin and gypsum grout with a 19mm diameter bolt in 25.4mm hole. The results indicated that 0.56m of length was required to transfer 90% of the load from the bolt to the rock. Figure 3.3 shows a comparison of

load distribution in different test conditions along the bolt length.

The results showed that the applied load was rapidly dissipated into the rock from the bolt head. It suggested that the grouted bolt could still be an effective support past the yield point of the steel if there was sufficient length of bolt past the yield zone. However, the anchorage at the end of the bolt was not measured in the tests.

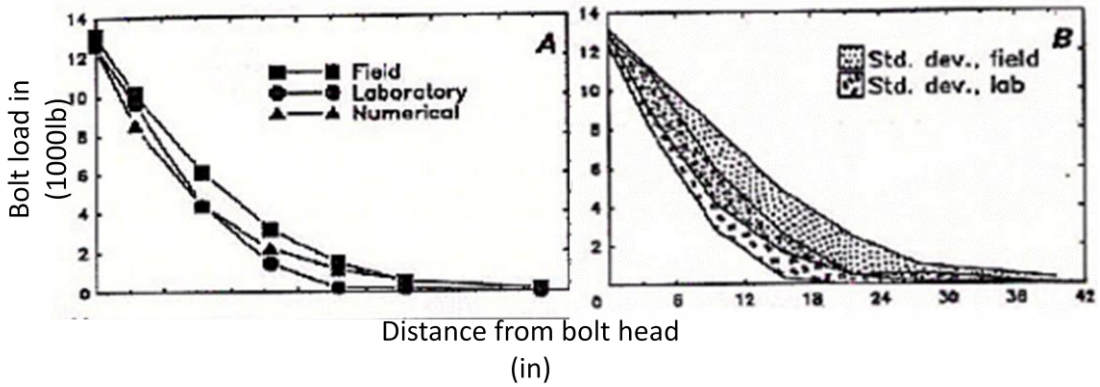

Figure 3.3 Comparison of load distribution along the bolt length (Signer, 1990).

In cable bolt *in situ* pullout tests, Bawden *et al* (1992) found that standard 7-strand cable had lower torsional rigidity compared to a rock bolt, and therefore, the short embedment length test section was able to fail by a simple "unscrewing" mechanism which had little relevance to the mining application. The pullout response when rotation of the pulling set up allows unscrewing and when it was prevented were compared in Figure 3.4.

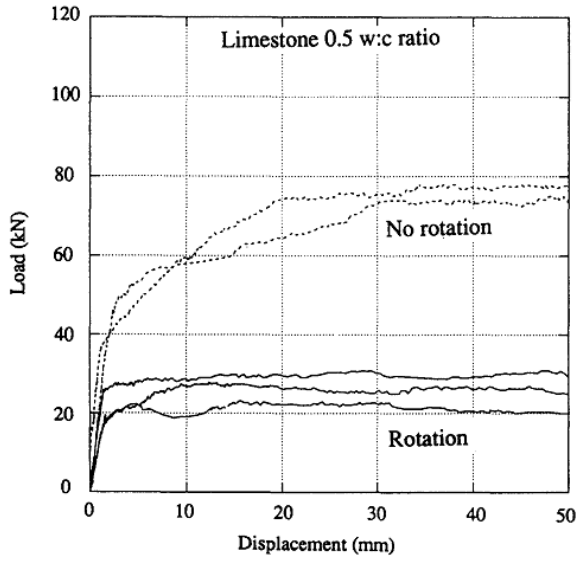

Figure 3.4 Pullout response for cases in which rotation of the pulling system is allowed and prevented (Bawden *et al*, 1992).

In case of tension free, the pullout response was almost perfectly plastic as would be expected for slip between the steel cable and cement in the absence of dilatation. However, if rotation is prevented, strain hardening was observed up to relatively high displacements, due to an additional frictional component related to the mobilisation of geometric mismatch between the cable and cement as displacement proceeds. This study addressed an important issue in cable bolt pullout tests, and indicated different failure modes depending on whether the cable bolt was torsion free or not.

Hyett *et al* (1992) carried out a series of laboratory and field pullout tests to investigate the major factors influencing the bond capacity of grouted cable bolts. All tests were conducted on 15.9 mm diameter 7-strand cable grouted using type 10 Portland cement pastes. The boundary conditions of the cable bolt system are shown in Figure 3.5.

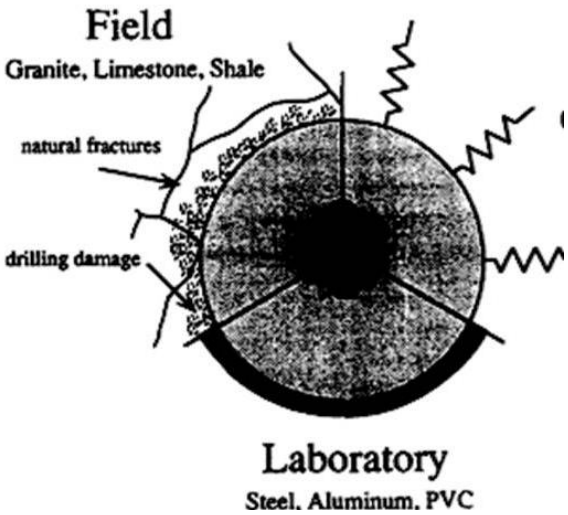

Figure 3.5 The boundary conditions of the cable bolt system: conceptual, in the laboratory and in the field (Hyett *et al*, 1992).

The results indicated that cable bolt capacity most critically depended on the cement properties, embedment length and radial confinement. It was found that cable bolt capacity increased with embedment length although not in direct proportion. More significantly, in laboratory "split-pipe" tests using PVC, aluminium and steel pipes to provide radial confinement, and in field test sites chosen in granite, limestone and shale rock masses, it was concluded that higher capacities were obtained under conditions of higher radial confinement.

Mark *et al* (2002) conducted a series of pull tests on fully grouted rock bolts. The issue of poor anchorage was addressed, particularly where the roof was very weak. When an

anchorage was poor the bolt could be pulled out of the upper portion of the hole at loads less than its yield strength. It was supposed that the two most likely causes of poor anchorage were weak rock and poor quality installation.

Compton and Oyler (2004) investigated the behaviour of fully grouted roof bolts in the weak roof rock of the Safety Research Coal Mine (SRCM). A series of 24 pull tests of 15.9mm (5/8 inch) fully grouted bolts were carried out. The results showed that there was no significant difference in pullout load between the offset-head bolts and the standard bolts. Another series of pullout tests, comparing the SEPT bolts and the partially overcored fully grouted bolts, indicated that SEPT significantly underestimated the bolt anchorage grip factor, suggesting that the SEPT was a conservative measure of actual bolt performance.

Kilic *et al* (2002 a) conducted about 80 laboratory rockbolt pullout tests in basalt blocks to investigate fully cement grouted rockbolts. A number of empirical formulae have been developed for calculating the pull out load capacity of the bolts on the basis of the shear strength, the UCS of the grouting material, the bolt length, the bolt diameter and the bonding area.

The experimental results showed that the maximum pull out load (P_b in Figure 3.6) increased linearly with the bolt diameter and embedment length. It should be noted that the maximum embedded bolt length was 320 mm in the tests.

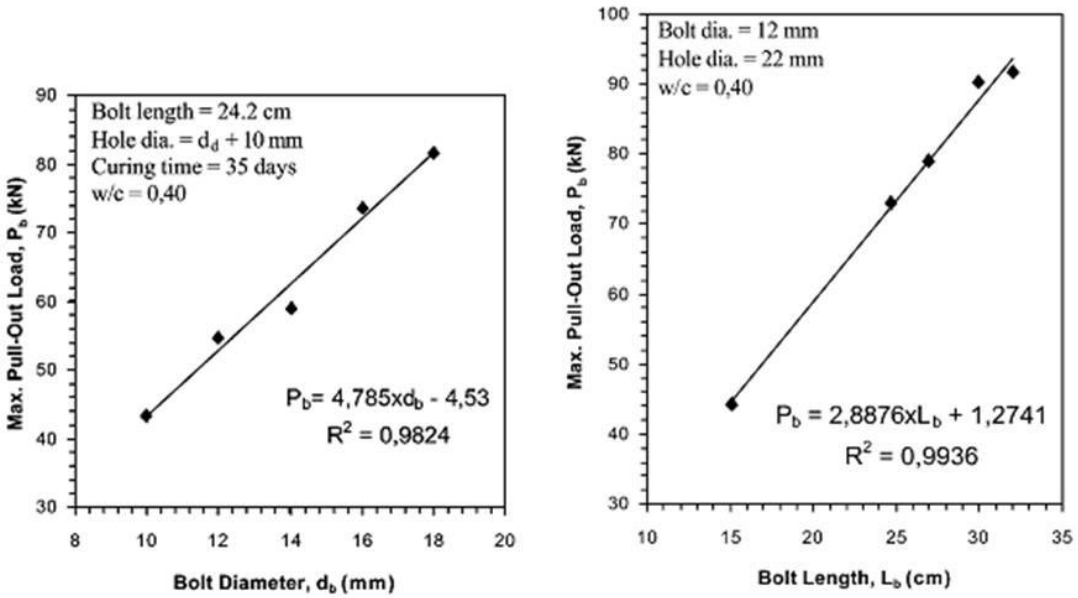

Figure 3.6 Influence of the bolt diameter and embedment length (Kilic *et al*, 2002 a).

The influence of the mechanical properties of the grouting materials on the bolt load capacity was nonlinear (Table 3.1). Improving the mechanical properties of the grouting material increased the bolt bearing capacity logarithmically.

Table 3.1 Influence of the mechanical properties of the grouting materials on the bolt load capacity (Kilic *et al*, 2002 a)

Grout type	UCS_g (MPa)	E_g (GPa)	τ_g (MPa)	P_b (kN)	A_b (cm^2)	τ_b (MPa)
$w/c=0.40$[a]	5.30	1.15	2.04	16.53	84	1.94
$w/c=0.40$[b]	12.84	2.74	4.99	43.75	84	5.20
$w/c=0.40$[c]	17.74	2.96	6.22	55.28	84	6.63
$w/c=0.40$[d]	20.80	3.39	7.95	57.59	84	6.83
$w/c=0.40$[e]	22.94	3.79	9.17	59.84	84	7.14
10% sand[f]	31.60	6.22	6.73	55.45	83	6.73
10% fly ash[f]	30.58	4.89	7.34	58.15	83	6.32
5% fly ash[f]	33.33	5.25	8.05	56.01	83	6.73
White cement[f]	37.72	6.63	8.15	58.15	83	7.03
$w/c=0.40$[f]	32.01	7.40	10.30	75.26	102	7.34
$w/c=0.38$[f]	33.33	8.05	10.70	77.39	102	7.54
$w/c=0.36$[f]	38.94	9.12	11.30	78.99	102	7.75
$w/c=0.34$[f]	42.00	9.30	11.93	80.87	102	7.95

Curing time: [a]1 day; [b]3 days; [c]5 days; [d]7 days; [e]14 days; [f]21 days.

3.3 FAILURE MODES

Aydan (1989) showed that an increase in bearing capacity was attributable to the normal compressive stress resulting from the geometric dilation of the surface. This suggested that shearing might occur along one of the surfaces of weakness in the rock bolt system (grout-rock interface and bolt-grout interface), and classified the failure modes in the push and pull tests as follows:

- Failure along the bolt-grout interface. This occurred in every test on bars with a smooth surface and deformed bars installed in a large borehole.
- Failure along the grout-rock interface. This occurred in deformed bars installed only in smaller diameter boreholes.
- Failure by splitting of grout and rock annulus

Littlejohn (1993) classified various types of axial failure when using grouted bolts in one or more of the manners: the bolt, the grout, the rock, the bolt-grout interface or grout-rock interface. The type of axial failure depended on the properties of individual elements. The steel bar governed the axial behaviour of the bolt, which was much stiffer and stronger than the grout and rock. If the bolt had sufficient length to transfer

the entire load to the rock it would fail. The shear stress at the bolt-grout interface was greater than at the grout-rock interface because of the smaller effective area. If the grout and rock were of similar strengths, failure could occur at the bolt-grout interface. If the surrounding rock was softer then failure could occur at the grout-rock interface.

From pullout tests of cable bolts in the laboratory and in the fields, Hyett *et al* (1992) have identified two failure modes in cementitious grouted cable bolt. One mode involved radial splitting of the concrete cover surrounding the cable, and the other shearing of the cable against the concrete. The radial splitting mechanism was induced by the wedging action between the lugs of the bar and the concrete. This exerted an outward pressure on the inside of the concrete annulus that was balanced by the induced tensile circumferential stress within the annulus. However, if the tensile strength of the cement was exceeded, radial splitting occurred, the circumferential stress in the concrete annulus reduced to zero as well the associated reaction force at the steel-concrete interface, so resulting in failure. The shearing mechanism involved crushing of the concrete ahead of the ribs on the bar, eventually making pullout along a cylindrical frictional surface possible. It could be concluded that as the degree of radial confinement increased the failure mechanism changed from radial fracturing and lateral displacement of the grout annulus under low confinement, to shear of the cement flutes and pullout along a cylindrical frictional surface under high confinement.

Hyett *et al* (1992) summarised schematically the successive stages in the failure during a pull test shown in Figure 3.7. In the essentially linear response (stage 1), as the experimental initial stiffness was significantly less than that predicted from elastic solutions (either analytic or numerical), Hyett *et al* argued that the adhesion bond between the cable and the cement was negligible because (1) the cement paste was porous, and (2) the bond was not continuous but comprised a series of point contacts. Consequently, the mechanical interlock and frictional resistance was related to the initial linear response during a pull test, although partial adhesion strength probably involves additional components. From stage 2, the failure mechanism was dependent on the radial confining pressure. The stress drop may correspond to radial fracturing of the grout annulus and/or shear failure through the grout flutes. From then on, as cable displacement increased, the radial confining pressure was controlled by the potential for greater geometric mismatch between the cable and cement flutes. How far the

individual wedges that now comprised the grout annulus could be pushed aside was determined by the radial stiffness of the confining medium. If the radial stiffness was low the favourable failure mechanism was lateral displacement of the wedges; when it was higher, dilation was suppressed and failure was more likely to occur by shear of the grout flutes and pull out along a cylindrical frictional surface.

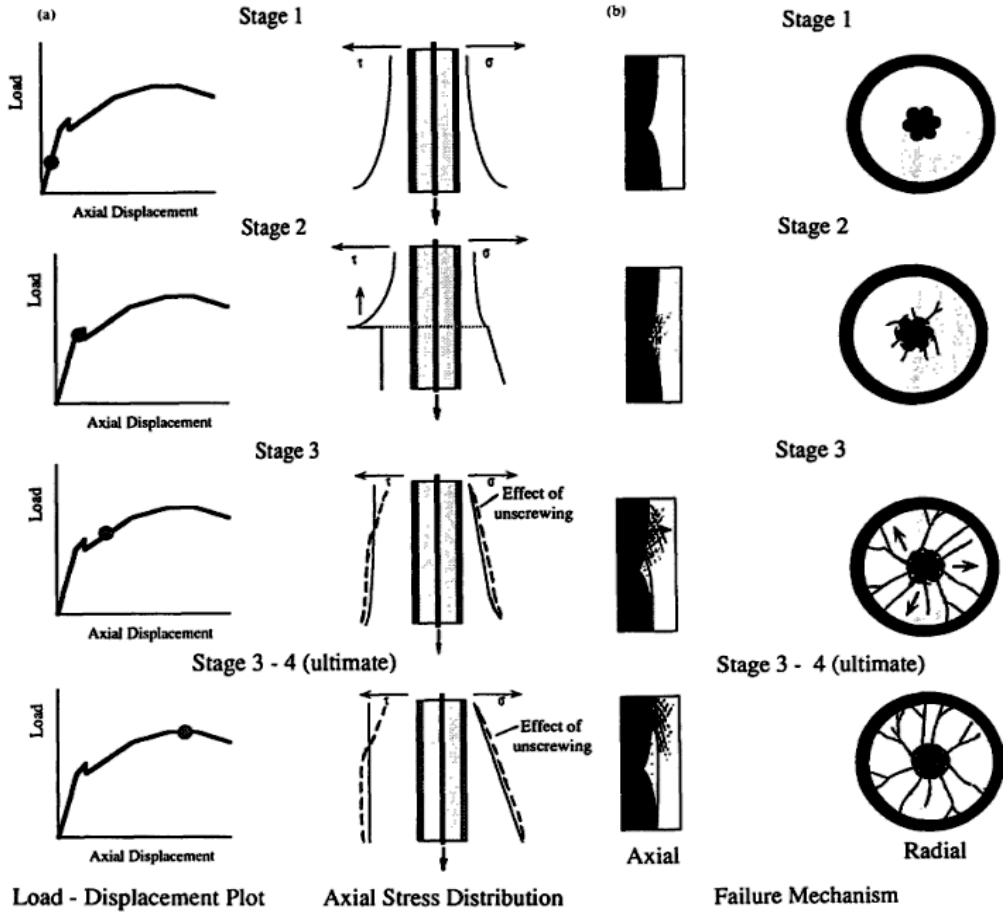

Figure 3. 7 Successive stages in the failure during a pull test (Hyett *et al*, 1992)

3.4 MECHANISMS OF TWO-MATERIAL-SYSTEM

Via pulling out a steel bar embedded in a concrete column (note: there is no grout material), engineers have been aware that the bond forces radiate out into the surrounding media from the bonding surface of an anchored steel bar. In 1913, Abrams presented the principal stress distribution in a pullout specimen as shown in Figure 3.8 (cited by Tepfers, 1973). Since then the knowledge concerning bond has considerably increased owing to measurements of the bond distribution, investigation

of the stresses and displacement fields in the surrounding media and tests on the failure modes.

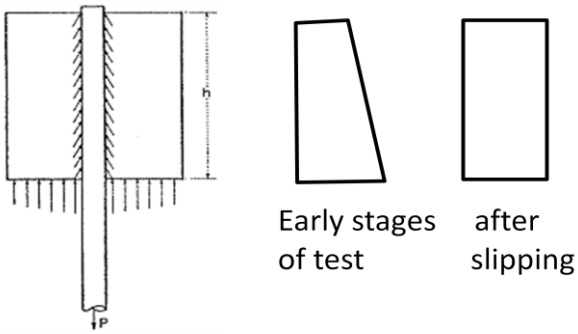

Figure 3.8 Principal stresses in a pull-out specimen, cited by Tepfers (1973)

Studies of bonding forces for plain reinforcing bars and rebar by Lutz (1970) showed that bond strength of smooth bars mainly depended on the chemical adhesion and after slip, on friction. The effect of chemical adhesion was small and friction did not occur until there was slip between bar and concrete.

For rebar, slip can occur in two ways: (1) The ribs could split the concrete by wedging action, and (2) The ribs could crush the concrete. When concrete was crushed to a "compacted powder" it became lodged in front of the ribs. In addition, even when slip and separation occurred, additional transverse cracks and splitting cracks were very probable. Thus, large axial displacement could not occur without transverse and radial cracking in the surrounding concrete.

Lutz outlined several forms of cracks of a concrete cylinder with an axially embedded steel bar to identify the failure modes of reinforcement. The break of concrete beam into small columns was called ‘primary crack’ which was the major failure mode. In addition, bond slip and dense minor radial cracks were also presented, as shown in Figure 3.9.

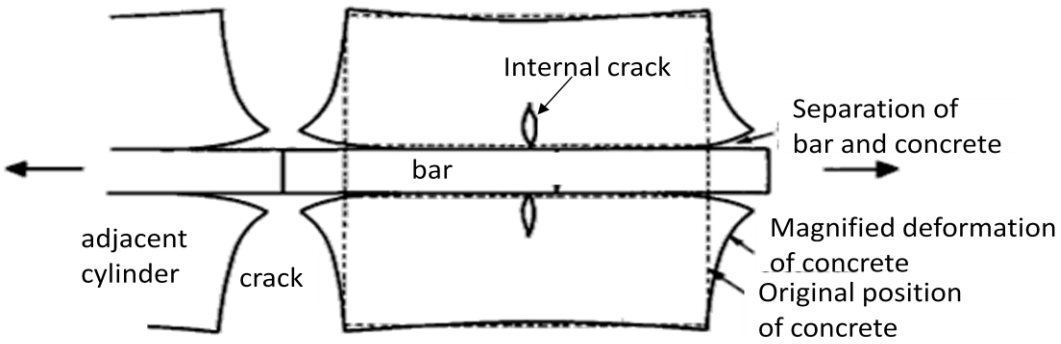

Figure 3.9 Deformations of a concrete cylinder with pulled plain bar (Lutz, 1970).

Working with the strength of overlapped splices in civil engineering, Tepfers (1973, 1979) established an analytical model for the tensile stress distribution caused by development of the radial splitting cracks. The object studied was still a plain steel bar axially embedded in a concrete cylinder. When pulling out, the interface resulted in significant stress concentrations. Due to these accumulated stresses, the debonding process started and extended inside the specimen along the reinforcing bar. Experiments have clarified two types of cracks: cone-shaped cracks and radial splitting cracks, both of which start at the interface (Figure 3.10). The crack patterns depend on the interface geometry and the properties of the interface and the surrounding concrete; furthermore, these different crack patterns do not form independently but interact through complicated non-linear mechanisms.

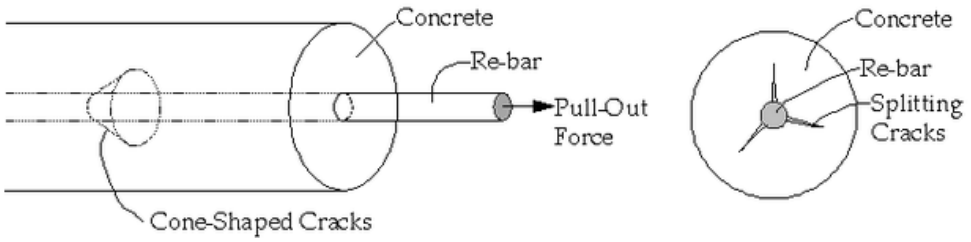

Figure 3.10 Internal cone shaped cracks and longitudinal splitting cracks, according to Tepfers (1973).

It is thought that the tensile stress was the cause of development of the splitting cracks. Tepfers assumed that the radial components of the bond forces could be regarded as a hydraulic pressure, acting on a thick-walled concrete ring surrounding the reinforcing bar. The shear stress at the interface is distributed into the surrounding material by compression under a certain angle and was balanced by tensile stress rings in the concrete (Figure 3.11). Thus, the radial stress due to bond action on the concrete, which is also regarded as the hydraulic pressure against a thick-walled concrete cylinder, could be calculated out via shear stress of the interface.

For determination of the resistance against radial cracking, Tepfers applied three different stress distributions referred to as:

- Uncracked elastic,
- Partly cracked, and
- Uncracked plastic stage.

In the elastic stage (Figure 3.12.1), the tangential stress could be found using thick walled cylinder theory. When the bond acted in the plastic stage, the cylinder did not break until the stresses in the tangential direction at every part of the cylinder have reached the ultimate tensile strength (Figure 3.12.3). In the intermediate stage of the above two cases (Figure 3.12.2), the ring had internal partial cracks where the circumferential stresses have reached the ultimate tensile concrete stress. The bond force was transferred through the concrete teeth between the internal cracks to the un-cracked part of the ring.

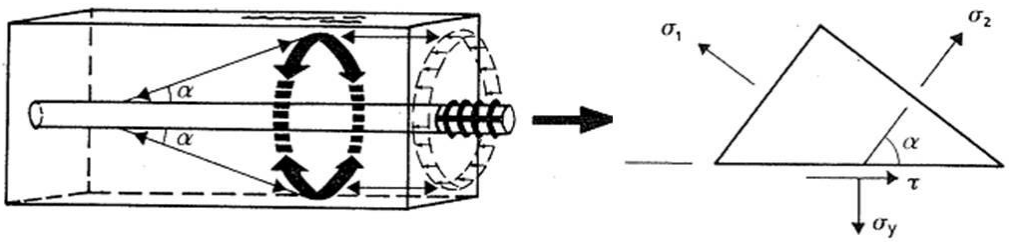

Figure 3.11 The radial components of the bond forces are balanced against tensile stress rings (Tepfers, 1973).

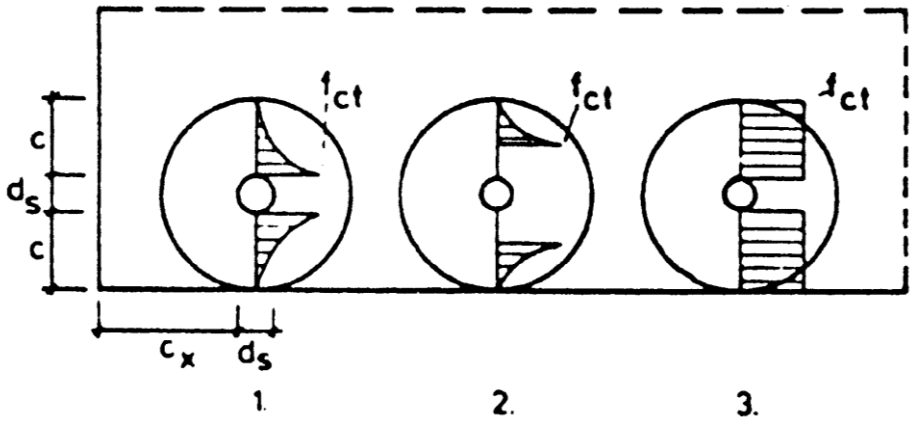

Figure 3.12 Tensile stress in the concrete cover (1) Elastic (2) Partial crack (3) Completely plastic (Tepfers, 1973).

Tepfers's model is based on the specific bond failure modes, i.e. cone cracks and radial cracks. In the rockbolting system, however, it is not the case because of the existence of grouting material which dominates the bond failure of rockbolting. The thick-wall cylinder theory and associated methodology of elastic and plastic analysis used in the study are admirable and employed in later research work on the fully grouted rockbolt composed of three phase materials with two interfaces. The thick-walled cylinder theory is adopted in this study to describe the behaviour of confining material such as steel sleeve and high strength concrete blocks.

There were also Finite Element (FE) models to analyse the stress distribution along a steel bolt grouted into rock in spite of the limitation of the computer in those days. Hollingshead (1971) modelled upon field pullout tests: 45mm diameter smooth bolts which were embedded for 0.7m and failed at an average load of 10 tonnes. The FE mesh (Figure 3.13) was coarse but designed to behave as an elastio-plastic medium yielding in accordance with the Tresca yield criterion.

The results of the model indicated that the grout was the weak link in the system. In addition, the load-displacement curve suggested that the bottom end of the anchor held firm at a pull load of 55MPa. In fact, the bar could not be pulled out until the last element yielded. This is a strong support to exponential decay theory developed later by Farmer (1975). However, Hollingshead did not provide further discussion on it.

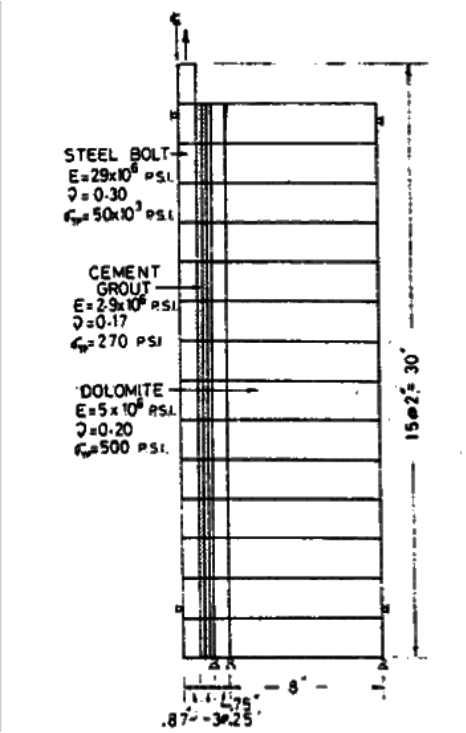

Figure 3.13 Hollingshead's FE model and material properties

3.5 EXPONENTIAL DECAY MODEL

Farmer (1975) proposed a fundamental theoretical solution of fully grouted anchor stress distribution, and compares his results with experimental data from tests on instrumented resin anchors in concrete, limestone and chalk.

The anchor is regarded as elastic with Young's modulus (E) surrounded by an elastically shearable grout with rigidity shear modulus (G) which is confined by a rigid borehole symmetrically. If a tensile force is applied to the steel bolt, this will be transferred to the grout through the interface, causing differential bolt extension and grout shear along the anchor, shown in Figure 3.14.

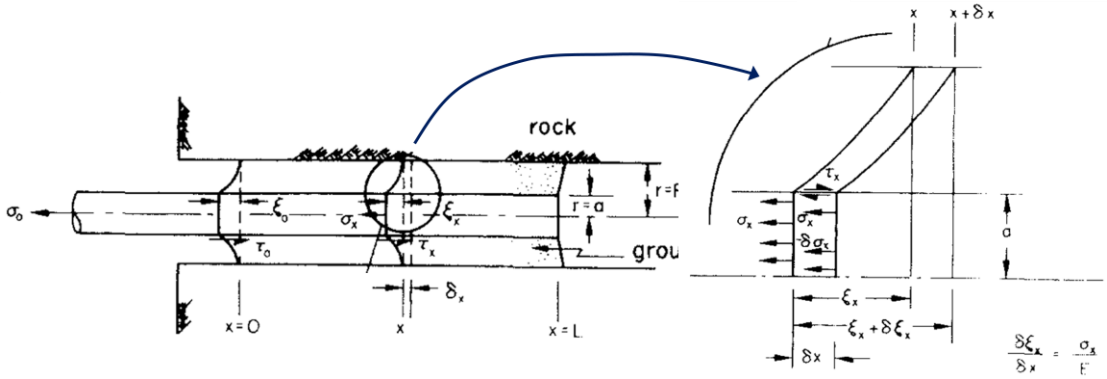

Figure 3.14 Stress and deformation in a grouted anchor (Farmer, 1975).

For the steel bolt:

$$\frac{d\sigma_x}{dx} = \frac{2}{a}\tau_x \qquad (3.1.1)$$

For the interface, the deformation is assumed to be elastic, therefore:

$$\sigma_x = E\frac{d\xi_x}{dx} \qquad (3.1.2)$$

The shear stress-strain relationship of grout annulus material is:

$$\tau_x = G\frac{\xi_x}{R-a} \qquad (3.1.3)$$

Substituting (3.1.1), (3.1.3) into (3.1.2), and taking standard form differential equation:

$$\frac{d^2\xi_x}{dx^2} - \alpha^2\xi_x = 0 \qquad (3.1.4)$$

where: $\alpha^2 = \dfrac{2G}{Ea(R-a)}$

Its standard solution is:

$$\xi_x = Ae^{\alpha x} + Be^{-\alpha x} \qquad (3.1.5)$$

In boundary conditions of: $\sigma_x = \sigma_0$ when $x = 0$ and $\sigma_x = 0$ when $x = L$, parameters *A* and *B* in the solution can be resolved. Substituting into equation (3.1.2) yields:

$$\xi_x = \frac{\sigma_0}{E\alpha}\frac{cosh\alpha(L-x)}{sinh\alpha L} \qquad (3.1.6)$$

Using $L>>1/\alpha$ to further simplify, the solution becomes a simple exponential decay:

$$\xi_x = \frac{\sigma_0}{E\alpha}e^{-\alpha x} \qquad (3.1.7)$$

For typical resin/steel anchor combinations $2G=0.01E$ and $(R-a)/a=0.25$, an indication of shear stress distribution along a resin anchor is illustrated in Figure 3.15.

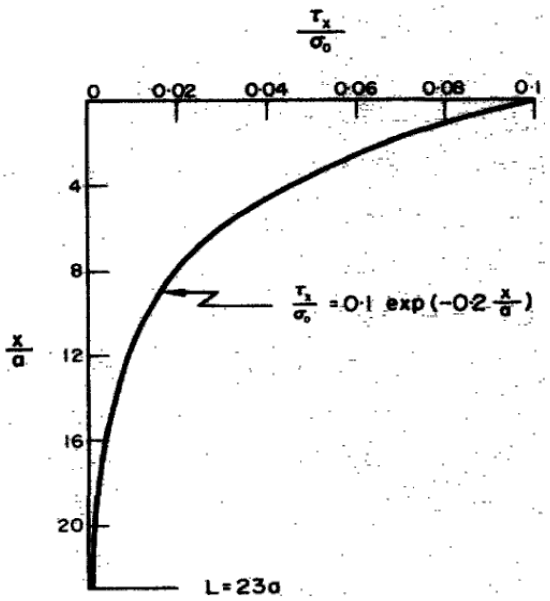

Figure 3.15 Theoretical stress distribution along a resin anchor in a rigid socket and having a thin resin annulus (Farmer, 1975).

To compare theoretical results, Farmer carried out a series of pullout tests on instrumented 20mm diameter steel bolts grouted into 28mm holes in concrete, limestone, and chalk. The results showed good correlation for low axial loads in concrete (Figure 3.16) but were different in weaker limestone and chalk. The experimental shear stress distribution of concrete at a pullout force of 20kN is very close to the theoretical stress distribution, however, there is a substantial difference at 40kN pullout force and this difference increases with increasing load. These

discrepancies are explained as, at higher stresses, the whole of the fixed anchor length has debonded and that pull out resistance is largely attributable to a high level of skin friction. For weaker confining materials such as limestone or chalk, debonding occurs at all stages of the loading process.

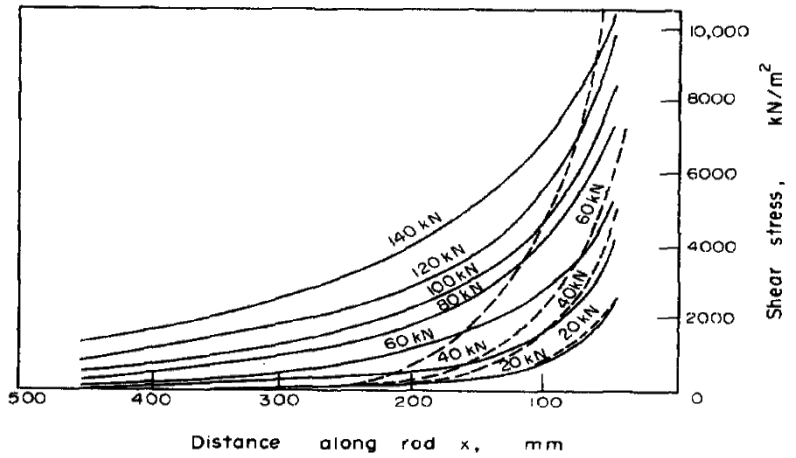

Figure 3.16 Shear stress distribution curves of 500mm resin anchors in concrete. (Broken lines =theoretical and solid lines = measured, by Farmer 1975).

This is a piece of fundamental work on the rockbolting mechanism. The discrepancies with experimental results can be explained by unrealistic assumptions of the mechanical model, e.g. perfect bonding, elastic deformation of the grout and a rigid borehole. The boundary conditions used to solve the differential equation have been verified by the following research work. Figure 3.17 shows a typical diagram of the displacement at two ends of the bolt in pullout test (Benmokrane *et al* 1995). The exponential decay of the axial stress and shear bond stress are also verified and widely accepted by subsequent studies.

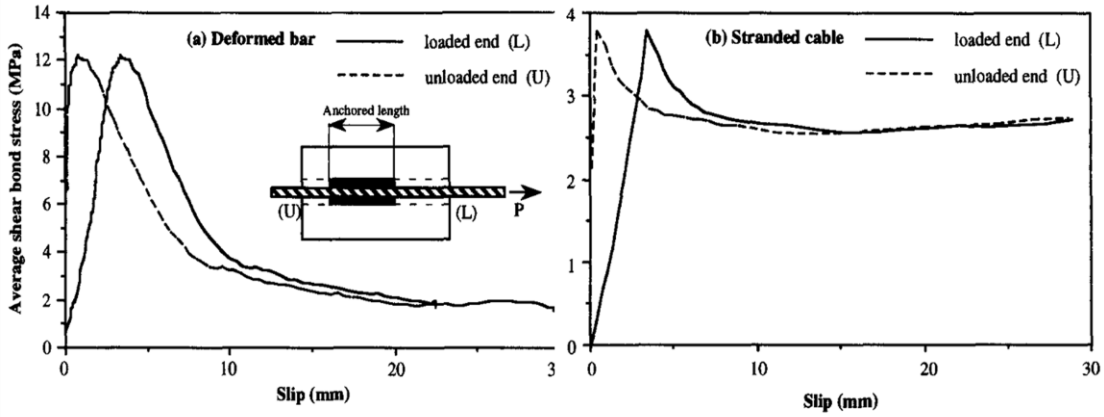

Figure 3.17 Movements of loaded end and un-loaded end for steel bolt and cable, the anchor length is four times the bolt diameter (Benmokrane *et al*, 1995).

Studying the installation induced stresses for grouted roof bolts, Nitzsche and Haas (1976) found the exponential decay pattern in term of bolt load along a fully grouted post-tensioned rockbolt via FE model. To avoid the complication of adding stresses, they employed a set of displacement boundary conditions to supply the interaction between the stress field and the bolts. The lateral surface at a radial distance of one-half the bolt spacing was constrained from radial movement and the top was completely fixed, as shown in Figure 3.18-a. When load was applied to the bolt to simulate the post tension, the deformation of each component was axisymmetric. Again, in this FE model all materials were assumed to be elastic, homogeneous, and isotropic; whose mechanical material properties were as illustrated in Figure 3.18-b.

Their analysis showed that the grout annulus transferred nearly all of the bolt load into the rock within a distance equal to 12 hole diameters from the point of load application, as shown in Figure 3.19. Furthermore, the principal stress fields for the grout and rock also rapidly decreased radially from the collar of the hole.

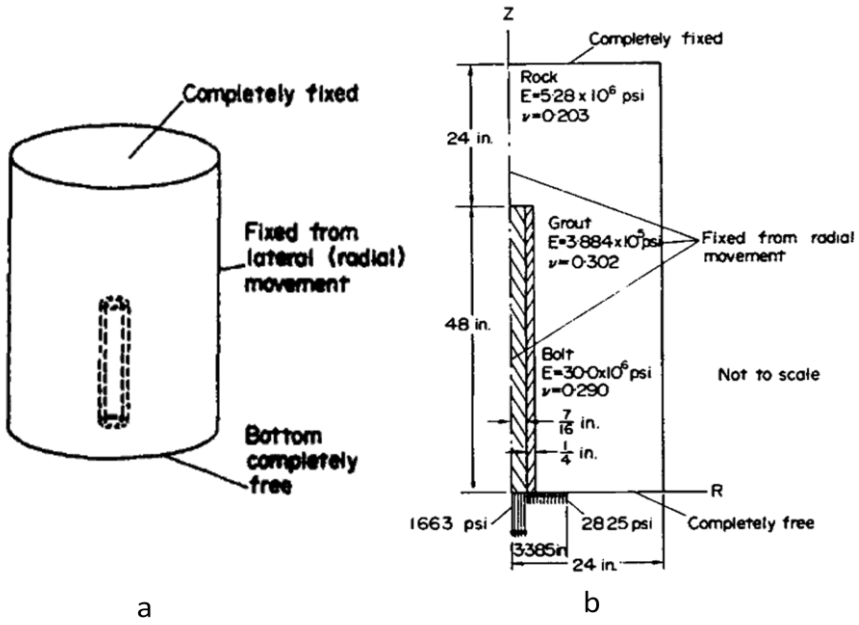

Figure 3.18 Boundary conditions and material properties of FE model of a fully grouted post-tensioned roof bolt (Nitzsche and Haas, 1975).

Nitzsche and Haas's FE model is simple but comprehensive, and still frequently used in computer based simulation nowadays. Moreover, the effect of the plate at the surface is considered. The disadvantages of this work are mainly the assumption of perfect bond for both interfaces; and their results are only presented in terms of principal stress vectors rather than stress tensor.

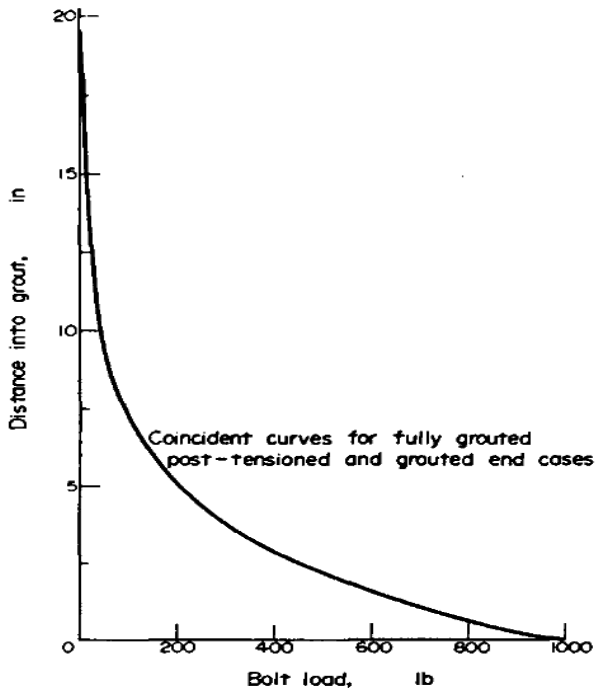

Figure 3.19 Variation in bolt load with distance into the grout (Nitzsche and Haas, 1975).

Yap and Rodger (1984) set up an axisymmetric FE model using three phase materials with two interfaces, shown in Figure 3.20. The two interfaces were still assumed to be perfectly bonded, but the materials were assumed following elasto-plastic stress-strain behaviour under the octahedral yield criterion. Therefore, the outcomes of the model relied on the material properties.

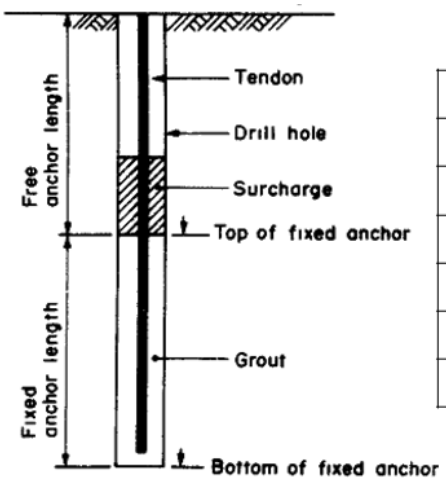

	Rock	Grout	Steel
E (Gpa)	10	21	196
v	0.15	0.15	0.30
UCS (MPa)	10	58	--
σ_{Yield} (MPa)	--	--	1653
β	1.16	1.16	--
α	0.05	0.10	--

Figure 3.20 Anchor definition and material properties (Yap and Rodger 1984).

The vertical displacement of the rock at various horizontal levels of a 0.75m fully grouted anchor is shown in Figure 3.21-a. The largest displacement occurred adjacent to the borehole at the surface. This dissipated rapidly to a negligible value at a

horizontal distance of about seven diameters from the centre of the borehole. In the case of radial strain, it was found that dilation of the grout and rock took place near the top of the anchor, as shown in Figure 3.21-b.

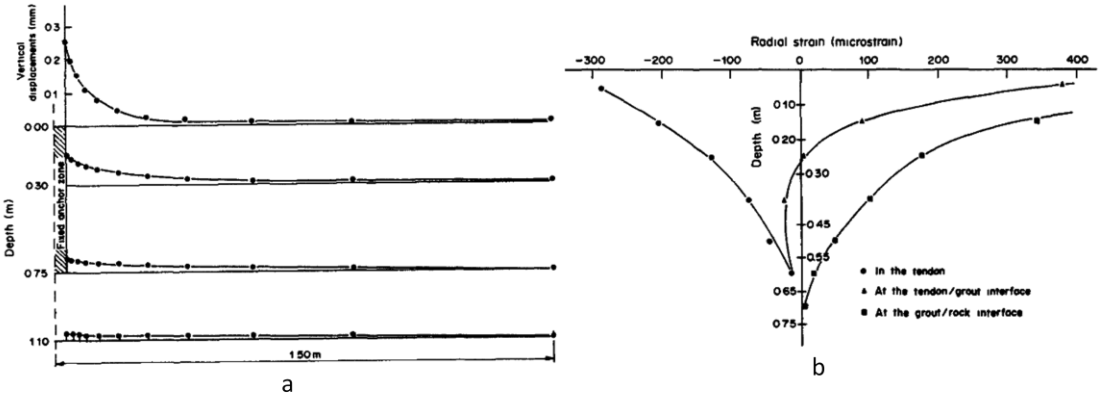

Figure 3.21 a: Vertical displacements at different horizontal levels of a 1.51 m anchor; b: radial strain with depth of a 0.75m fully grouted anchor in rock at 400kN load (Yap and Rodger, 1984).

The FE method permits the anchor load-transfer mechanism to be assessed providing a complete picture of the stresses and strains around the fixed anchor. It should be recognised however that the solution is dependent on the properties of the host rock. In addition, the perfect bonding of the interfaces is unrealistic which decreases the accuracy of the results and hence restricts its applications.

3.6 MECHANISMS OF CABLE BOLTING

Yazici and Kaiser (1992) developed a conceptual model for fully grouted cable bolts as shown in Figure 3.22, called ‘Bond Strength Model’ (BSM).

According to their theory the bond strength is mainly frictional and hence depends on the pressure build-up at the interface which in turn depends on the dilational movement against the confining grout or rock. The surface of the cable bolt was simplified to be zigzag (that means, twisting of the cable is ignored), thus a bilinear dilation-dependent joint strength concept introduced by Patton can be applied as that:

$$\tau = \sigma \, tan(i_0 + \phi) \qquad (3.2.1)$$

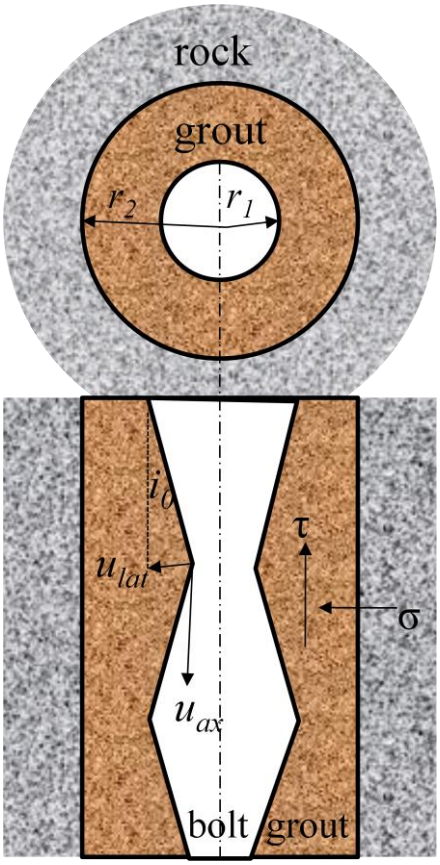

Figure 3.22 Schematic diagram reflecting the geometry of a rough cable bolt, modified from Yazici and Kaiser (1992).

For situations where asperities are partially sheared off at elevated radial stresses, the above equation (3.2.1) is modified by establishing an apparent dilation angle *i*:

$$tani = (tani_0)\left[1 - \left(\frac{\sigma}{\sigma_c}\right)^{\beta}\right] \qquad (3.2.2)$$

For small angles, the bond strength can be expressed in terms of friction and dilation angle:

$$\tau = \sigma\, tan\left(i_0\left[1 - \left(\frac{\sigma}{\sigma_c}\right)^{\beta}\right] + \phi\right) \qquad (3.2.3)$$

Where:

$\tau =$ shear or bond stress

$\sigma =$ radial stress at the bolt $-$ grout interface;

$i_0 =$ dilation angle at the bolt/grout interface (Figure 3.22)

$\beta =$ reduction coefficient of dilation angle

$\sigma_c =$ compressive strength of grout

$\phi =$ friction angle between the steel and grout.

The BSM involves four main components: axial displacements, lateral displacements, confining pressure and bond strength. In Figure 3.23, schematic diagram illustrates these interrelated components in four quadrants:

(1) The first quadrant shows the variation of bond strength with axial displacement. It represents the pullout test graph.

(2) The second quadrant relates to the confining pressure at the bolt-grout interface to the bond strength using equation (3.2.1).

(3) The third quadrant shows the relation between axial and lateral displacements. Since apparent dilation angle is not constant, the relation is non-linear and asymptotically approaches an ultimate lateral displacement.

(4) The dilation acts outward on the grout column and creates the interface pressure as illustrated by the fourth quadrant. The straight lines showed that the grout may split under the dilational pressure.

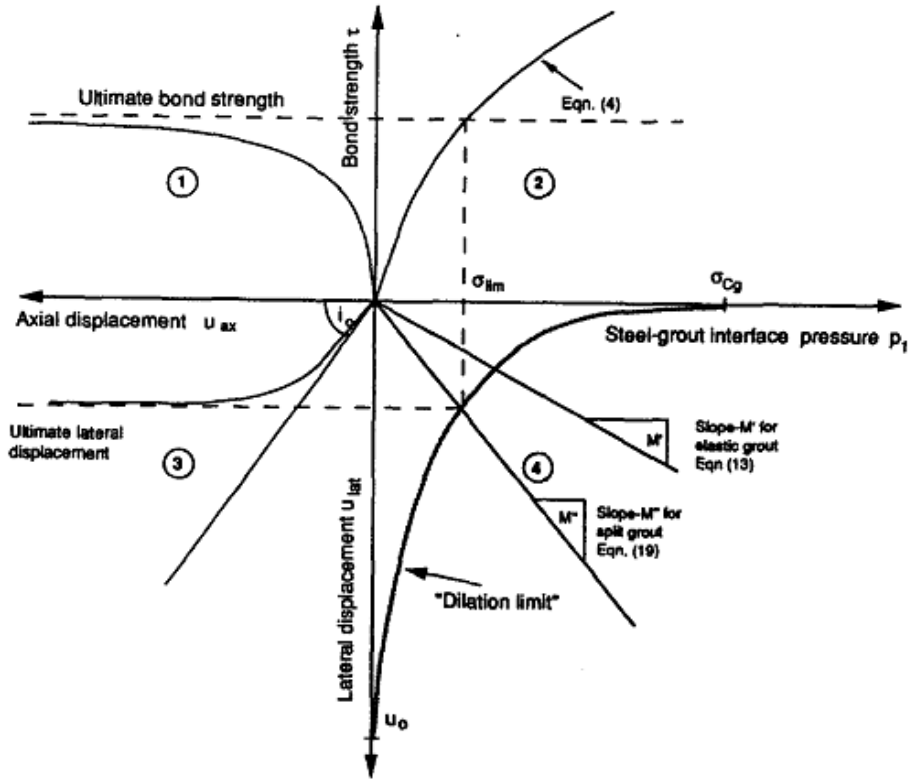

Figure 3.23 Schematic diagram relating components of bond strength model (Yazici and Kaiser 1992).

In the fourth quadrant of the BSM, the dilational behaviour of grout is: (i) elastic; (ii) fully split; or (iii) a transition zone of partially split with an elastic portion. In the elastic grout expansion (Figure 3.24.1), the radial displacement at the bolt-grout interface can be derived from the plane strain thick-walled cylinder equations:

$$u_{1g} = \frac{(1+v_g)(1-2v_g)}{E_g}\frac{p_1 r_1^2 - p_2 r_2^2}{r_2^2 - r_1^2} r_1 + \frac{(1+v_g)}{E_g}\frac{(p_1 - p_2) r_1^2 r_2^2}{r_2^2 - r_1^2}\frac{1}{r_1} \qquad (3.3.1)$$

$$u_{2g} = \frac{(1+v_g)(1-2v_g)}{E_g}\frac{p_1 r_1^2 - p_2 r_2^2}{r_2^2 - r_1^2} r_2 + \frac{(1+v_g)}{E_g}\frac{(p_1 - p_2) r_1^2 r_2^2}{r_2^2 - r_1^2}\frac{1}{r_2} \qquad (3.3.2)$$

The radial displacement of the rock, induced by an internal pressure in a circular hole of radius in an infinite medium, is given by:

$$u_{2g} = \frac{p_2 r_2}{E_r}(1+\nu_r) \qquad (3.3.3)$$

Combining equations (3.3.1), (3.3.2) and (3.3.3), the displacement at the bolt-grout interface can be expressed in terms of the internal pressure in the form:

$$u_{1g} = M' p_1 \qquad (3.4.1)$$

where:

$$M' = \frac{(1+v_g)(1-2v_g)}{E_g}\frac{r_1^2 - \frac{r_2^2}{X}}{r_2^2 - r_1^2} r_1 + \frac{(1+v_g)}{E_g}\frac{\left(1-\frac{1}{X}\right) r_1^2 r_2^2}{r_2^2 - r_1^2}\frac{1}{r_1}$$

$$X = \frac{\frac{1+\nu_r}{E_r} + \frac{1+\nu_g}{E_g(r_2^2 - r_1^2)}\left[(1-2\nu_g) r_2^2 + r_1^2\right]}{\frac{1+\nu_g}{E_g(r_2^2 - r_1^2)}\left[(1-2\nu_g) r_1^2 + r_1^2\right]} \qquad (3.4.2)$$

If the tangential stress exceeds the tensile strength of the grout, the grout will fully split and the tangential stress in the grout column becomes zero. This changes the thick-walled grout cylinder to a wedge-shaped geometry (Figure 3.24.2). The new state of stress can be found by:

$$p_1 r_2 = p_1 r_2 \qquad (3.4.3)$$

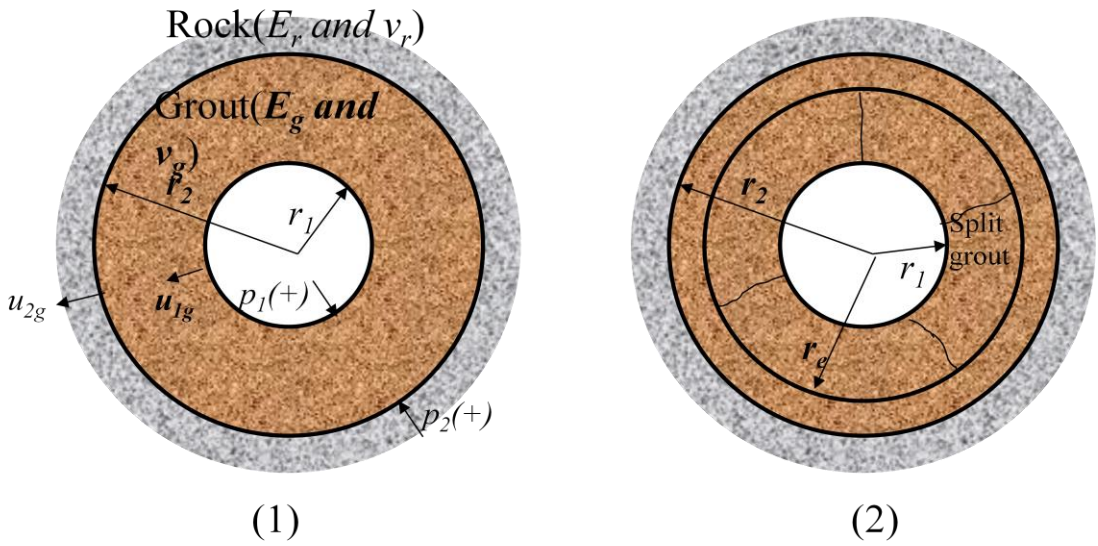

Figure 3.24 (1) Cross-section of a grouted bolt. (2) Conceptual cross-section of a fully-split grout column, modified from Yazici and Kaiser (1992).

Consequently, the difference of the displacements between the boundaries of the split grout column can be calculated:

$$u_{1g} - u_{2g} = \frac{1 - v_g^2}{E_g} p_1 r_1 ln \frac{r_2}{r_1} \qquad (3.4.5)$$

Substituting u_{2g} with equation (3.3.3), the displacement at the bolt-grout interface for the totally split grout cylinder is:

$$u_{1g} = M'' p_1 \qquad (3.4.6)$$

where: $M'' = r_1 \left(\frac{1 + v_r}{E_r} + \frac{1 - v_g^2}{E_g} ln \frac{r_2}{r_1} \right)$

In the transition zone of the above two cases, the interface pressure at the crack propagation is obtained by:

$$p_1 = \frac{\sigma_T (r_2^2 - r_e^2)}{\frac{r_1}{r_e}\left[r_e^2 + r_2^2 \left(1 - \frac{2}{X} \right) \right]} \qquad (3.4.7)$$

where:

$r_e =$ radius of the cracked zone and

X is obtained from equation (3.4.2) using $r_1 = r_e$

The dilation for partially split grout is found by algebraically adding the displacements for split and intact grout:

$$u_{1g} = M''' p_1 \qquad (3.4.8)$$

$$M''' = \frac{r_1}{r_e}\left[\frac{(1+\nu_g)(1-2\nu_g)}{E_g}\frac{\left(r_e^2 - \frac{r_2^2}{X}\right)}{r_2^2 - r_e^2} r_e + \frac{(1+\nu_g)}{E_g}\frac{\left(1-\frac{1}{X}\right) r_e^2 r_2^2}{r_2^2 - r_e^2}\frac{1}{r_e}\right] + r_1\left(\frac{1+\nu_r}{E_r} + \frac{1-\nu_g^2}{E_g}\ln\frac{r_e}{r_1}\right)$$

This equation is only applicable for $r1 < r_e < r2$. Interface pressure u_{1g} is not a linear function of p_1 because the length of crack r_e is also a function of p_1. A closed-form solution could not be found and, hence, u_{1g} is determined iteratively starting from $r_e = r_1$.

To complete BSM, "dilation limit" must be determined. While failure occurs, the area of the grout teeth in contact with the bolt decreases but the stress acting on an individual tooth increases leading eventually to complex modes of failure. Yazici and Kaiser choose an empirical model to describe it as:

$$u_{1g} = u_0\left(1 - \frac{p_1}{\sigma_c}\right)^{B/\sigma_c} \qquad (3.4.9)$$

Where:

u_0=maximum dilation ≈ teeth height;

σ_c = compressive strength of grout and

B = a constant which can be determined from pullout data.

As the BSM of fully grouted cable bolts is primarily frictional and depends on the pressure at the cable-grout interface, Kaiser *et al* (1992) further studied the effect of stress change on the bond strength (Figure 3.25). Combining "load induced" and "excavation-induced" bond strength components in the BSM, they evaluate a range of cable bond strength parameters listed in Table 3.2. These ranges cover most common conditions encountered in hard rock mining operations.

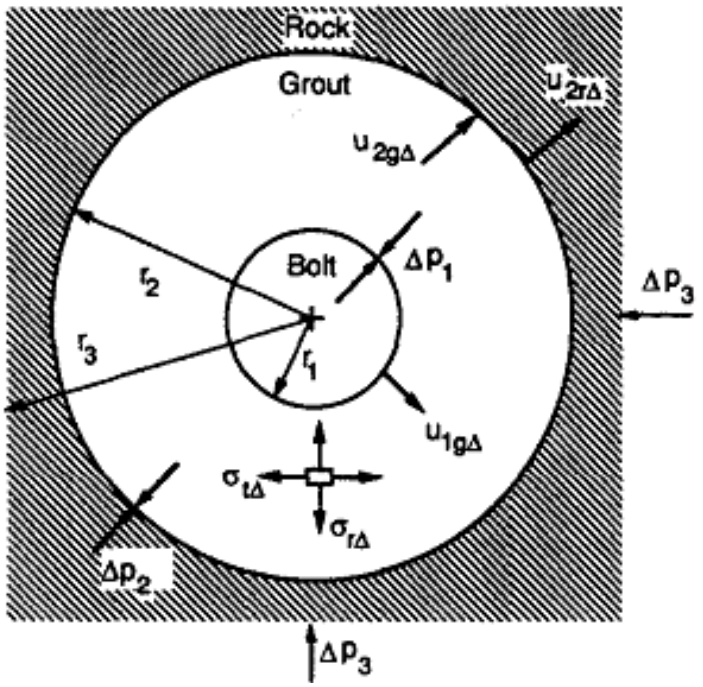

Figure 3.25 Mining induced stress Δp_3 is included in the BSM (Kaiser *et al*, 1992).

Table 3.2 Practical range of cable bolt parameters and resulting bond strengths of a 7-strand cable.

	Practical range of parameters			Bond strength (MPa)		
Parameters	Minimum	Normal	Maximum	Minimum	Normal	Maximum
Young's modulus of rock (GPa)	5	30	60	5.5	7.3	7.5
Friction angle between cable steel and grout	15	28	35	3.7	7.3	9.6
Diameter of borehole (mm)	15	50	70	8.5	7.3	6.9
Mining-induced stress change (MPa)	−30	0	30	3.8	7.3	14.9
Mining-induced stress change (MPa)	−15	0	15	4.9	7.3	10.2
Young's modulus of rock (GPa)	5	30	60	5.5	7.3	7.5
Water/cement ratio of grout	0.5	0.4	0.3			
Compressive strength of grout (MPa)	50	61	73	5.2	7.3	9.5
Young's modulus of grout (GPa)	8.1	10.5	12.9			

This is a piece of fundamental work on cable bolting mechanism. However, it is limited to the assumption of linear dilation in the pull out procedure. In addition, twisting behaviour of the cable is ignored which is a characteristic feature of cable bolting. As a result, the parameter *B* in equation (3.4.9) relies on empirical solutions.

To construct a mechanical model for bond failure of fully grouted cable bolts, Hyett *et al* (1995) conducted another series of pull tests, in which the confining pressure of the cement annulus was maintained constant using a modified Hoek cell (Figure 3.26). The data were used to develop a frictional-dilational model for cable bolt failure in mathematical form which is amenable to implementation in numerical programs.

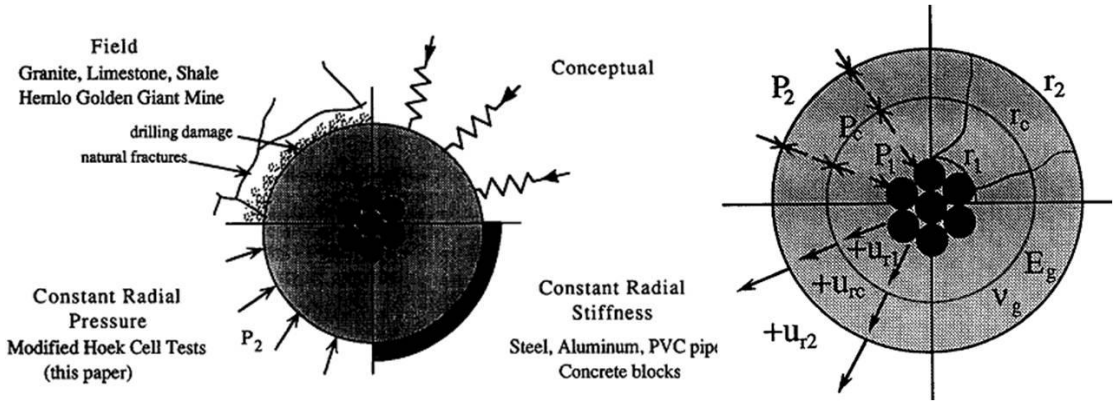

Figure 3.26 Left: Boundary conditions of the cable-bolt system, Right: Terminology and sign convention (Hyett *et al*, 1995).

In the Hyett's model, the bond strength is frictional, so it depends on the pressure generated at the cable-grout interface, which in turn depends on the reaction force generated at the borehole wall caused by dilation during bond failure. The frictional resistance can be catalogued into:

- for dilational slip, $f = A \cdot p_1 \cdot tan(\phi_{g-s} + i)$ (3.5.1)
- for non − dilational unscrewing; $f = \frac{A \cdot p_1 \cdot tan\phi_{g-s}}{sin\alpha} + Q$ (3.5.2)
- for shear failure of the cement flutes: $f = A(c + p_1 tan\phi_g)$ (3.5.3)

Where:

i = dilation angle;

A = interface contact area;

ϕ_{g-s} =sliding friction between grout and steel;

ϕ_g =internal angle of friction for grout and

c = grout cohesion.

Micrographs revealed that shearing of the grout flutes only occurred within 75mm of the exit point. It could be explained that, along the majority of the test section, failure involved unscrewing of the cable from the cement annulus. To formulate this unscrewing effect, a pullout force component required to untwist the free length of cable, Q, was introduced. Based on work considerations, Q is given by:

$$Q = \frac{4\pi^2 C u_a}{l^2(u_a + L_f)} \qquad (3.5.4)$$

Where:

u_a = axial displacement

C = torsional rigidity of cable;

l = pitch length and

L_f = free length of the cable between test and anchor sections.

After 50mm of axial displacement, the radial dilations measured at the midpoint of the test section were from approximately 0.15mm for 1MPa radial confining pressure, to 0.02mm for 15MPa. Since the dilation angles were small (i < 0.2°), the pull force component related to dilational slip was ignored. Thus, the axial pull out force ,F_a, may be approximately written as:

$$F_a = \frac{L_s}{L} \cdot A\left(c + p_1 tan\phi_g\right) + \left(1 - \frac{L_s}{L}\right) \times \frac{A \cdot p_1 \cdot tan\phi_{g-s}}{sin\alpha} + Q \qquad (3.5.5)$$

Where:

L = embedment length and

L_s = sheared length of the grout flutes.

However, as the shear failure length was undeterminable, an average coefficient of friction (φ') over the whole test section was introduced, then:

$$F_a = A \cdot p_1 \cdot tan(\varphi') + Q \qquad (3.5.6)$$

The average coefficient of friction angle can be evaluated as the slope of the linear portion of plot $(F_a - Q)/A$ against confine pressure, which in turn is independent of confining pressure.

In the cable grout interface, the pressure dependent closure was assumed to be hyperbolic, and then the total dilation due to splitting may be written as:

Radial splitting dilation: $v_r = v_{r0} - \frac{p_1 \cdot v_{r0}}{K_{r0} \cdot v_{r0} + p_1} \qquad (3.5.7)$

Where:

v_{r0} = dilation generated by splitting when $p_1=0$,

K_{r0} = radial stiffness (MPa/mm) immediately following splitting, when p_1=0.

If the cable is not rigid, radial contraction of the cable due to the application of p_1 is considered and evaluated as p_1/K_{rc} (Hyett used K_{rc} =2500MPa/mm). The Poisson's effect is ignored as the Poisson's ratio is low (about 0.02). Therefore:

Radial splitting dialtion: $$v_r = v_{r0} - \frac{p_1 \cdot v_{r0}}{K_{r0} \cdot v_{r0} + p_1} - \frac{p_1}{K_{rc}} \qquad (3.5.8)$$

Based on this, Hyett then assumed a simple mechanical model to characterise the radial deformability of the cable-grout interface after the cable has been pulled by an amount u_{r1}:

$$u_{r1} = \frac{k_1}{p_1}(u_a - 1) + v_{r0} - \frac{p_1 \cdot v_{r0}}{K_{r0} \cdot v_{r0} + p_1} - \frac{p_1}{K_{rc}} \qquad (3.5.9)$$

Where:

u_a = axial displacement

k_1 = empirical constant determined by best fit (Hyett used k_1=0.012MPa).

Combining equations (3.5.6) and (3.5.9), a differential formulation for the deformability of the cable joint interface during bond failure, i.e. tangent stiffness matrix, can be obtained;

$$\begin{bmatrix} dF_a \\ dp_1 \end{bmatrix} = \begin{bmatrix} K_1^i & K_2^i \\ K_3^i & K_4^i \end{bmatrix} \begin{bmatrix} du_{r1} \\ du_a \end{bmatrix} \qquad (3.5.10)$$

The behaviour of grout annulus was discussed in three cases based on the assumption that it had fully split after 1mm of axial pull. Thereafter, the cement annulus was unable to support a tensile tangential stress. That is, the fracture is free to open or close depending on confining pressure p_2 and dilation u_{r1}.

While the tangential stresses are compressive, the grout annulus will behave identically to an intact hollow cylinder, and the plane strain elastic solution for a thick walled

hollow cylinder can be applied. For the case when the radial fractures are fully open, a series of individual grout wedges are formed. The solution to the stresses and dilations are similar to Yazici and Kaiser (1992). If the radial fractures are partially open, i.e. the outer annulus is in compression but the inner annulus is in tension, the tangential stress at the common boundary must be zero. According to this, the radius size at which fractures are open can be solved. Consequently, the radial displacement equation and stiffness matrix can be formulated.

Compared with BSM, this model has considered the twisting effect in cable pullout. However, the equation (3.5.4) is doubtful because once $L_f = 0$, u_a will be cancelled. Moreover, simplifying equation (3.5.5) to equation (3.5.6) the solution becomes an empirical approach.

3.7 INTERFACIAL SHEAR STRESS (ISS) MODEL

ISS model is only concerned with the debonding failure at the interfaces. Under the debonding failure, zero thickness interface represents the materials adjacent to the surface where debonding occurs. The deformation of the surrounding rock or grout is ignored, i.e. all deformations in the surrounding materials outside the failure surface are lumped into an idealised interface. As a result, the bolt can be assumed to be under uni-axial tension and the bolt–grout interface layer under interfacial shear deformation only. If debonding occurs at the grout–rock interface, the model is applicable, by treating the bolt and grout together as a ‘‘hybrid bolt” under uni-axial tension.

Li and Stillborg (1999) developed an analytical model for predicting the behaviour of rock bolts under three different conditions,

- for bolts in pullout tests,
- for bolts installed in a uniformly deformed rock mass and,
- for bolts subjected to the opening of rock joints.

The development of these models was based on the description of the mechanical coupling at the interface between the bolt and grout medium.

Based on the exponential decay theory and thinking of decoupling of the bond, they constructed a model for the shear stress along a fully grouted bolt. Figure 3.27.1 show the shear stress distribution along a fully grouted rockbolt subjected to an axial load before decoupling occurs. After decoupling occurs, the shear stress profile (Figure 3.27.2) includes a completely decoupled section with a zero shear stress from the collar to the point x_0, a segment of partially decoupled with a residual shear strength s_r till x_1, followed by the residual shear strength linearly increasing to the peak strength s_p from x_1 to x_2, and then exponentially towards the far end of the bolt.

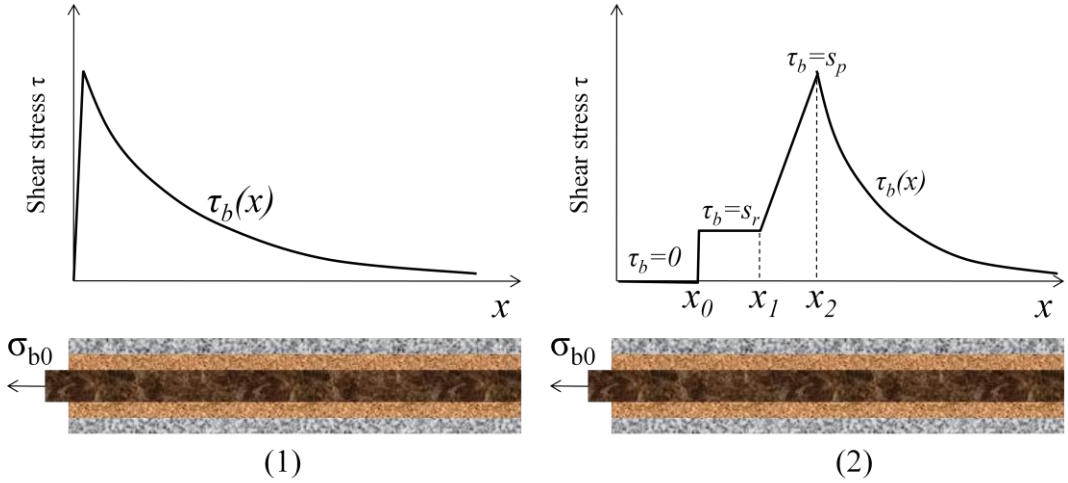

Figure 3.27 Shear stress along a fully grouted rockbolt subjected to an axial load. (1) before decoupling (2) after decoupling (modified from Li and Stillborg, 1999)

Before decoupling occurs at the interface for fully grouted rockbolts, the attenuation of the shear stress is expressed as:

$$\tau_b = \frac{\alpha}{2}\sigma_{b0}e^{-2\alpha\frac{x}{d_b}} \tag{3.6.1}$$

where: $\alpha^2 = \dfrac{2G_rG_g}{E_b\left[G_r\, ln\dfrac{d_g}{d_b} + G_g\, ln\dfrac{d_0}{d_g}\right]}$

After decoupling occurs, for equilibrium of the bolt, the applied load P_0 should equal the total shear force at the bolt interface, *i.e.:*

$$P_0 = \pi d_b\left[s_r(x_1 - x_0) + \frac{1}{2}s_p\Delta(1+\omega) + \frac{d_b}{2\alpha}s_p\left(1 - e^{-\frac{2\alpha}{d_b}(L-x_2)}\right)\right] \tag{3.6.2}$$

And the maximum applied load can be expressed as:

$$P_{0max} = \pi d_b s_p \left[\omega\left(L + \frac{d_b}{2\alpha} ln\omega - \Delta - x_0\right) + \frac{1}{2}\Delta(1+\omega) + \frac{d_b}{2\alpha}(1-\omega)\right] \quad (3.6.3)$$

Where:

L=length of the bolt;

$\Delta = x_2 - x_1$; $\omega = s_r/s_p$; and

$$x_2 = x_0 + \frac{1}{2\omega}\left[\frac{2P_0}{\pi d_b s_p} - \frac{d_b}{\alpha} - \Delta(1+\omega)\right] \quad (3.6.4)$$

Rock bolts *in situ* tend to restrain the deformation of rock with an increase in their axial loads. For uniformly deformed rock mass, the expression of the shear stress without debonding can be expressed as:

$$\tau_b(x) = \xi G_r \left[\frac{A}{\pi d_b}\frac{d^2u}{dx^2} - \frac{\alpha}{2}\int_{r_i}^{x} \frac{d^2u}{dt^2} e^{-2\alpha\frac{x-t}{d_b}}\, dt\right] \quad (3.6.5)$$

Where:

$$\xi = \frac{2(1+v_r)SE_b}{AE_b + SE_r}$$

$u =$ original radial displacement of the rock at x without bolt

S = the influencing area of the bolt

Benmokrane *et al* (1995) reported a laboratory study on six different types of cement-based grouts and two types of steel rock anchors. Pullout tests of grouted, 7-strand steel cable and solid steel threadbar were conducted for different grouts and embedment lengths (Figure 3.28). An empirical equation was derived for the estimation of anchor pullout resistance for a given embedment length and a tri-linear constitutive model for shear bond stress-slip model at the anchor-grout interface is proposed.

Model A was used to study the anchor pullout strength as a function of the Anchored Length (*AL*), which varied between 7 and 20*Φ*, where *Φ* is the nominal diameter of the anchor (*Φ*= 15.8mm). It is found that the maximum load carrying capacity increases

with anchored length (but is not linear). The following empirical equation was proposed:

$$P = a + b\frac{AL}{\Phi} \qquad (3.7)$$

Where:

P=ultimate pullout load,

a and *b* are coefficients determined from tests.

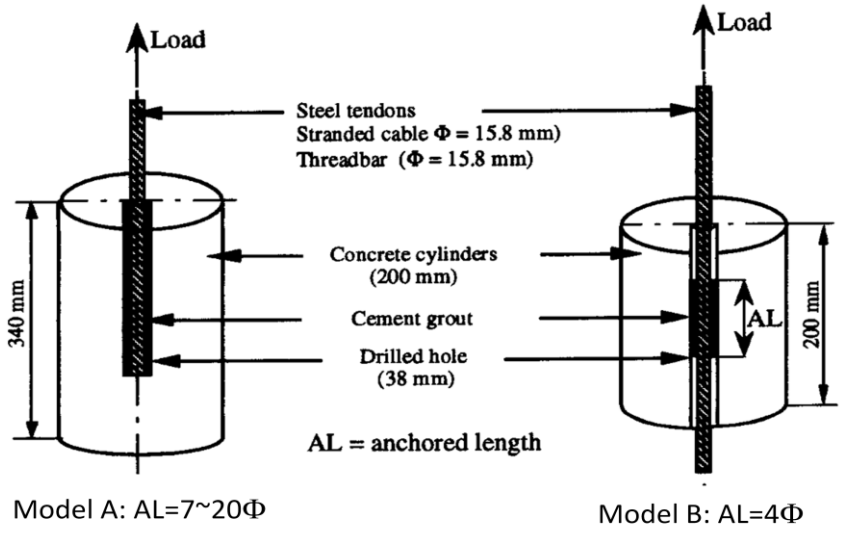

Figure 3.28 Experimental assemblage (Benmokrane *et al*, 1995)

All pullout shear failure mechanisms occurred at the anchor-grout interface. The average shear bond strength at the grout-anchor interface at failure is derived by dividing the maximum pullout load by the product of the anchor perimeter and the actual anchored length. The averages of ultimate bond stress at the anchor-grout interface of stranded cables are lower (approximately one-third) than those of threadbars.

Model B was used to determine the constitutive relation between the bond stress and the anchor slip. A short anchored length of $<4\Phi$ was used to obtain an approximately uniform distribution of the bond stress along the grout-tendon interface near failure. Based on the pullout data, an analytical model was proposed by trilinear shear bond model as shown in Figure 3.29. The values of τ_1, τ_2, s_1 and s_2 can be derived from pullout tests. As can be seen, this model consists of three linear stages (I, II, III). The first stage corresponds to the elastic behaviour, and is characterised by a linear relation

between bond stress (τ) and slip (s). The second stage corresponds to the process of debonding characterised by decreasing bond strength. The third stage represents the residual resistance developed by friction.

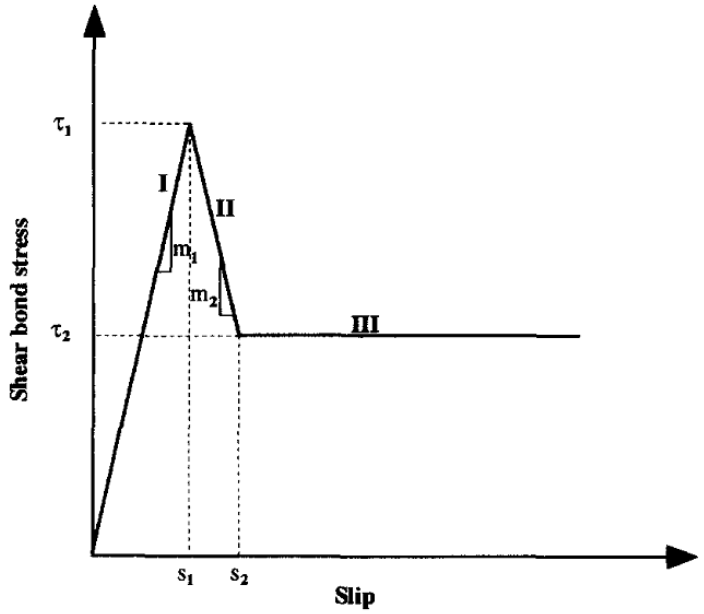

Figure 3.29 Tri-linear bond slip model

Ground anchoring is also a common reinforcing method in civil engineering. It can make effective use of the soil potential and enhance its self-stability. According to the modes of load transfer, anchorage can be divided into three types: tension, pressure and shearing. Tension anchoring is more commonly used and its reinforcement mechanism transmits the supporting force from anchor to stable stratum through bonding resistance. There are three failure modes of the tension anchor, that is:

- anchor breaking,
- anchor and grout body bonding failure, and
- the anchorage body and soil shear failure.

The former two failure modes hardly occur in practice so the main task of soil anchorage design is to determine the side resistance distribution between anchorage body and surrounding soil to avoid the anchorage body and soil shear failure mode.

Xiao and Chen (2008) present a model to characterise the load transfer mechanism of tensile anchor using the shear displacement method (Figure 3.30.1). In the model, softening features of the soil was considered. Shear stress-strain relationship of soil

surrounding the anchorage body was simplified into a tri-lines model consisting of elastic phase, elasto-plastic phase and residual phase (Figure 3.30.2).

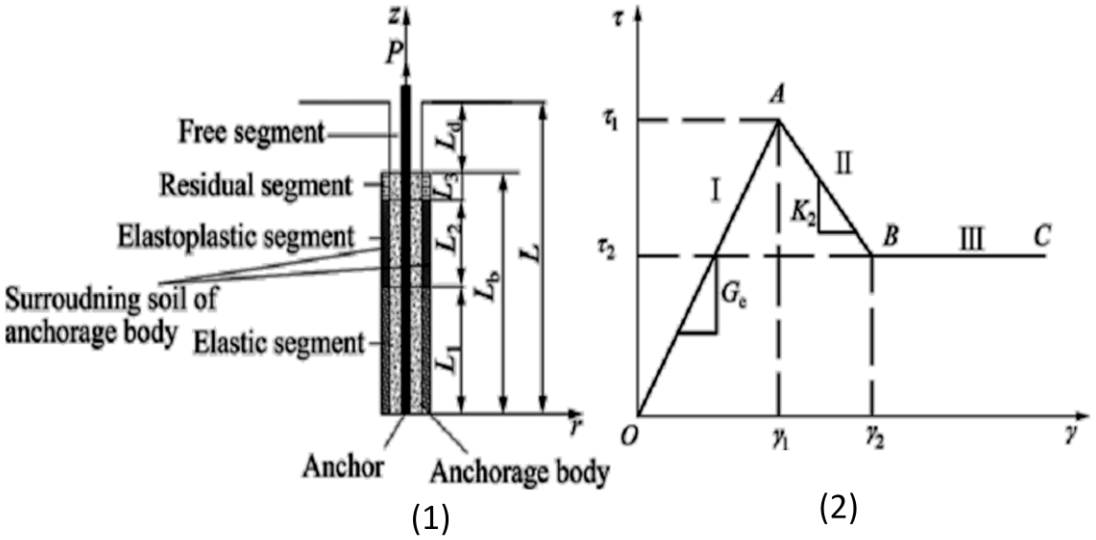

Figure 3.30 Tension anchor and shear stress strain relationship (Xiao and Chen, 2008).

The shear stress strain relationship can be expressed as:

$$\gamma = \frac{\tau}{G} \qquad \text{elastic phase} \qquad (3.8.1)$$

$$\gamma = \frac{\tau_1}{G} + \frac{\tau - \tau_1}{K_2} \qquad \text{elasto} - \text{plastic phase} \qquad (3.8.2)$$

$$\gamma = \frac{\tau_1}{G} + \frac{\tau_2 - \tau_1}{K_2} \qquad \text{residual phase} \qquad (3.8.3)$$

According to elastic theory, the shear stress and strain of soil surrounding a pile are:

$$\tau = \frac{\tau_0 r_0}{r} \qquad (3.9.1)$$

$$\gamma = \frac{ds}{dr} \qquad (3.9.2)$$

Where:

r = distance from soil to pile center;

r_0 = radius of anchorage;

τ_0 = shear stress of anchorage surface;

s = soil displacement.

At a depth z, the soil displacement at the anchor interface can be obtained as

$$s = \frac{\tau_0 r_0}{G} ln \frac{r_m}{r_0} \quad \text{elastic phase} \quad (3.10.1)$$

$$s = \frac{\tau_1 r_0}{G} ln \frac{r_m}{r_0} + \frac{\tau_1 r_0}{K} ln \frac{\tau_0}{\tau_1} \quad \text{elastoplastical phase} \quad (3.10.2)$$

$$\text{uncertainty} \quad \text{residual phase} \quad (3.10.3)$$

where r_m is the soil radius surrounding anchorage body where shear displacement can be ignored.

The shear displacement, s, is also a function of depth z. According to the definition, the shear displacement in the phase I and II (Figure 3.30) are:

$$s = \frac{\tau_0(z) r_0}{G} ln \frac{r_m}{r_0} \quad 0 \le z \le L_b \quad (3.11.1)$$

$$s = \frac{\tau(z) r_0}{G} ln \frac{r_m}{r_0} \quad 0 \le z \le L_1 \quad (3.11.2)$$

$$s = \frac{\tau_1(z) r_0}{G} ln \frac{r_m}{r_0} + \frac{\tau(z) r_0}{K} ln \frac{\tau(z)}{\tau_1} \quad L_1 \le z \le L_b \quad (3.11.3)$$

The governing equation is still:

$$\frac{d^2 s}{dz^2} - \frac{2}{r_0 E} \tau = 0 \quad (3.12)$$

When only elastic deformation exists, this equation can be solved in closed form. When the surrounding soil enters into elastoplastic phase, the equation is a transcendental equation but Xiao and Chen solved the equation in closed form that does not appear to be correct. Their solution in this part is doubtful. Nevertheless, they provide a potential method to predict the full range behaviour of anchorage.

Ren *et al* (2010) developed a solution for the prediction of the full-range mechanical behaviour of fully grouted rockbolts subjected to axial loading. In this approach, a

tri-linear bond slip model was used to describe the stress strain behaviour of the interface between the grout and the bolt, as shown in Figure 3.31. The shear stress strain relationship includes an increased branch up to the peak stress at (δ_1, τ_f) followed by a softening branch down to (δ_f, τ_r), and then a horizontal branch representing the non-zero residual frictional strength τ_r after complete debonding. Consequently, the full-range behaviour was defined by five consecutive stages. For each stage, closed form solutions for the load-displacement relationship, interfacial shear stress distribution and bolt axial stress distribution along the bond length were derived.

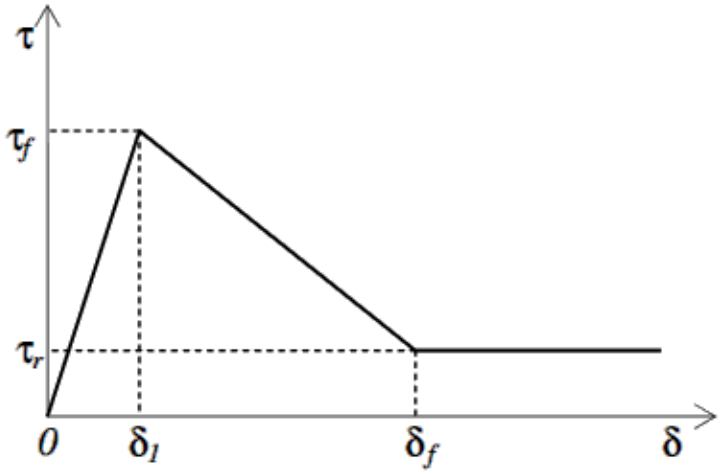

Figure 3.31 Tri-linear bond-slip model (Ren *et al*, 2010).

Defining k as $\tau_r = k\tau_f$, the shear stress can be expressed as:

$$\tau(\delta) = \frac{\tau_f}{\delta_1}\delta \qquad \text{for } 0 \le \delta \le \delta_1 \qquad (3.13.1)$$

$$\tau(\delta) = \frac{k\tau_f(\delta - \delta_1) + \tau_f(\delta_f - \delta)}{\delta_f - \delta_1} \qquad \text{for } \delta_1 \le \delta \le \delta_f \qquad (3.13.2)$$

$$\tau(\delta) = k\tau_f \qquad \text{for } \delta_f \le \delta \qquad (3.13.3)$$

When k = 0, the model reduces to the bilinear model used to rockbolts without friction after complete debonding. When k = 1, it can be used to analyse frictional rockbolts whose bearing capacity is solely due to interface friction.

The governing equation of the grouted rockbolt and the axial stress in the bolt are:

$$\frac{d^2\delta}{dx^2} - \frac{\delta_f}{\tau_f}\lambda^2\tau(\delta) = 0 \qquad (3.14)$$

where: $\lambda^2 = \dfrac{2\tau_f}{\delta_f E_b r_b}$

It can be solved once $\tau(\delta)$ is defined.

Figure 3.32.1 illustrates the evolution of ISS distribution of each stage: (a,b) Elastic stage; (c,d) elastic softening stage; (e,f) elastic softening debonding stage; (g) softening debonding stage; (h,i) debonding stage; and I, II and III represent elastic, softening and debonding stress states respectively. The corresponding points in the load–displacement curve are shown in Figure 3.32.2.

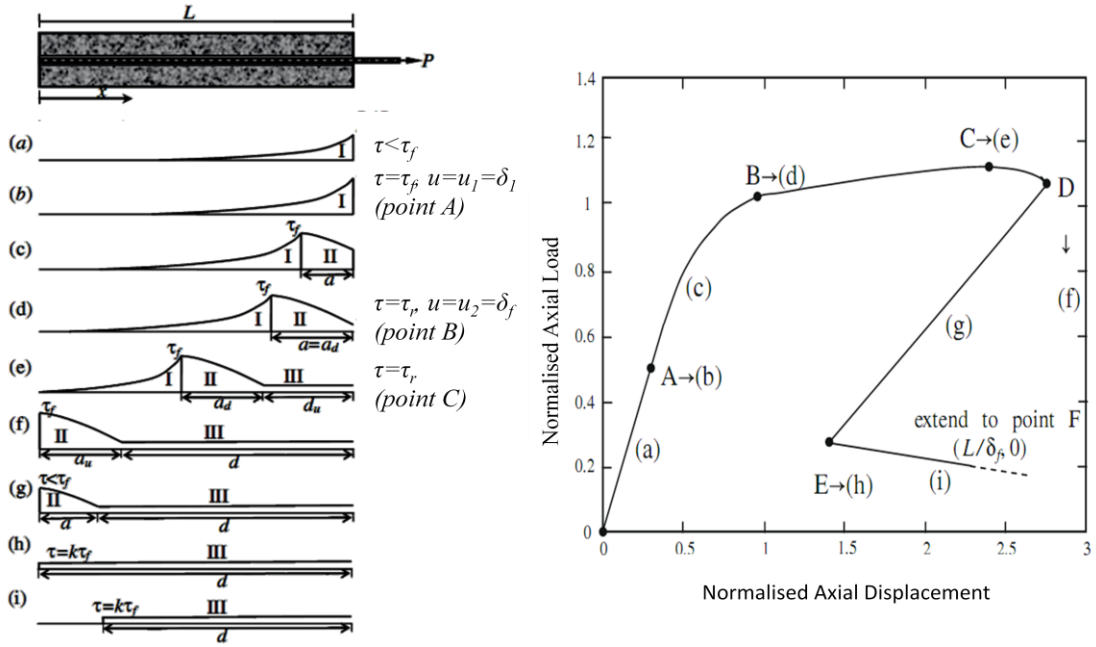

(1) (2)

Figure 3.32 (1) ISS distribution and propagation of debonding. (2) Non-dimensional load displacement curve (Ren *et al*, 2010).

In the elastic stage, the solutions of the governing equations are:

$$\delta = \frac{\delta_1 P\lambda_1 cosh\,(\lambda_1 x)}{2\pi r_b \tau_f sinh\,(\lambda_1 L)} \qquad (3.15.1)$$

where: $\lambda_1^2 = \dfrac{\delta_f}{\delta_1}\lambda^2 = \dfrac{2\tau_f}{\delta_1 E_b r_b}$

The slip at the loaded end with $x = L$ is defined as the displacement of the rockbolt and is denoted as Δ. The following load–displacement expression can then be obtained:

$$P = \frac{2\pi r_b \tau_f \tanh(\lambda_1 L)}{\delta_1 \lambda_1} \Delta \tag{3.15.2}$$

Normalisation of load and displacement by:

$$\bar{P} = \frac{\lambda P}{2\pi r_b \tau_f} \tag{3.15.3}$$

$$\bar{\Delta} = \frac{\Delta}{\delta_f} \tag{3.15.4}$$

The expression of the normalised load and displacement is:

$$\bar{P} = \frac{\lambda \delta_f \tanh(\lambda_1 L)}{\delta_1 \lambda_1} \bar{\Delta} \quad for \ 0 \le \bar{\Delta} \le \frac{\delta_1}{\delta_f} \tag{3.15.5}$$

The elastic stage ends when the shear stress reaches the bond shear strength τ_f at a slip of δ_1 at $x = L$. Setting $\Delta = \delta_1$, the load at the initiation of interface softening is found to be:

$$P_{sof} = \frac{2\pi r_b \tau_f \tanh(\lambda_1 L)}{\lambda_1} \tag{3.16.1}$$

For an infinite bond length, it reduces to:

$$P_{sof} = \frac{2\pi r_b \tau_f}{\lambda_1} \tag{3.16.2}$$

As the pullout force increases, softening commences at the loaded end ($x = L$) and the peak shear stress is transferred towards the embedded end, as shown in Figure 3.32.1 (state II). With the development of the softening length a, the load P continues to increase because more interface is mobilsed to resist the pullout force. At the end of this stage (point B in Figure 3.32), P reaches the debonding load P_{deb}. The following differential equations for the elastic–softening stage can be obtained:

$$\frac{d^2\delta}{dx^2} - \lambda_1^2\delta = 0 \quad \text{when } 0 \le \delta \le \delta_1 \tag{3.17.1}$$

$$\frac{d^2\delta}{dx^2} + (1-k)\lambda_2^2\delta = \lambda_2^2(\delta_f - k\delta_1) \quad \text{when } \delta_1 \le \delta \le \delta_f \tag{3.17.2}$$

where: $\lambda_2^2 = \dfrac{\delta_f}{\delta_f - \delta_1}\lambda^2 = \dfrac{2\tau_f}{(\delta_f - \delta_1)E_b r_b}$

The boundary conditions are:

$\sigma_b = 0 \;\; at \;\; x = 0$

$\delta = \delta_1 \; or \; \tau = \tau_f \;\; at \;\; x = L - a$

$\sigma_b = \dfrac{P}{\pi r_b^2} \;\; at \;\; x = L$

The solution for the elastic region of the interface with $0 \le x \le L-a$ is:

$$\delta = \frac{\delta_1 cosh\,(\lambda_1 x)}{cosh[\lambda_1(L-a)]} \tag{3.18.1}$$

The solution for the softening region with $L-a \le x \le L$ is:

$$\delta = (\delta_f - \delta_1)\left[\frac{\lambda_2 sin\left[\lambda_2(x-L+a)\sqrt{1-k}\right]tanh[\lambda_1(L-a)]}{\lambda_1\sqrt{1-k}} - \frac{cos\left[\lambda_2(x-L+a)\sqrt{1-k}\right]}{1-k} + \frac{\delta_f - k\delta_1}{(1-k)(\delta_f - \delta_1)}\right] \tag{3.18.2}$$

Consequently,

$$P = \frac{2\pi r_b \tau_f}{\lambda_2\sqrt{1-k}}\left[\frac{\lambda_2\sqrt{1-k}}{\lambda_1} cos\left[a\lambda_2\sqrt{1-k}\right]tanh[\lambda_1(L-a)] + sin\left[a\lambda_2\sqrt{1-k}\right]\right] \tag{3.18.3}$$

$$\Delta = (\delta_f - \delta_1)\left[\frac{\lambda_2 sin[a\lambda_2\sqrt{1-k}]tanh[\lambda_1(L-a)]}{\lambda_1\sqrt{1-k}} - \frac{cos[a\lambda_2\sqrt{1-k}]}{1-k} + \frac{\delta_f - k\delta_1}{(1-k)(\delta_f - \delta_1)}\right] \quad (3.18.4)$$

Debonding is initiated at the loaded end when τ reduces to τ_r at $x = L$. Substituting $\tau=\tau_r$ and $x = L$ into shear equation leads to:

$$\frac{\lambda_2\sqrt{1-k}}{\lambda_1} sin[\lambda_2 a\sqrt{1-k}]tanh[\lambda_1(L-a)] - cos[\lambda_2 a\sqrt{1-k}] = -k$$

Thus the softening length a at the initiation of debonding at the loaded end, denoted as a_d, can be solved as:

$$a_d = \frac{1}{\lambda_2\sqrt{1-k}} sin^{-1}\left[\frac{\sqrt{\delta_f - \delta_1}\left[\sqrt{\delta_f - k\delta_1 - k^2(\delta_f - \delta_1)} - k\sqrt{\delta_1(1-k)}\right]}{\delta_f - k\delta_1}\right] \quad (3.19.1)$$

Debonding load P_{deb} can be found as:

$$P_{deb} = \frac{2\pi r_b \tau_f}{\lambda_2\sqrt{1-k}}\left[\frac{\lambda_2\sqrt{1-k}}{\lambda_1} cos[a_d\lambda_2\sqrt{1-k}] + \sin[a_d\lambda_2\sqrt{1-k}]\right] \quad (3.19.2)$$

Once the shear stress decreases to τ_r at $x = L$, debonding is initiated at the loaded end. As debonding propagates, the peak shear stress continues to move towards the embedded end. Thus there are three possible stress states within the bond length: the elastic state (state I), the softening state (state II) and the debonding state (state III) (Figure 3.32-e). The debonded length is denoted by d, the solution for the elastic-softening zones are still valid if L is replaced by $(L - d)$. The differential equation for the debonding zone can be obtained by substituting equation (3.13.3) into equation (3.14). The solution for the debonding region with $(L-d)\leq x\leq L$ is given by:

$$\delta = \frac{\delta_f}{2\lambda_1\lambda_2\sqrt{1-k}}\Big[\lambda_1\big[\lambda_2\sqrt{1-k}\big(2 + kd^2\lambda^2 + k\lambda^2(L-d)^2 - 2kd\lambda^2(L-x)\big) - 2\lambda^2(L-x-d)\sin\big(\lambda_2 a_d\sqrt{1-k}\big)\big] + 2\lambda^2\lambda_2\sqrt{1-k}(L-x - d)\cos\left(\lambda_2 a_d\sqrt{1-k}\right)tanh[\lambda_1(a_d + d - L)]\Big] \quad (3.20.1)$$

$$P = \frac{2\pi r_b\tau_f}{\lambda_2\sqrt{1-k}}\left[\frac{\lambda_2\sqrt{1-k}}{\lambda_1}cos\big(a_d\lambda_2\sqrt{1-k}\big)tanh[\lambda_1(L-d-a_d)] + sin\left(a_d\lambda_2\sqrt{1-k}\right)\right] + 2k\pi r_b\tau_f d \quad (3.20.2)$$

$$\Delta = \frac{\delta_f}{2\lambda_1\lambda_2\sqrt{1-k}}\Big[\lambda_1\big[\lambda_2\sqrt{1-k}(2 + kd^2\lambda^2 + 2\lambda^2 dsin\left(\lambda_2 a_d\sqrt{1-k}\right)\big] - 2\lambda^2\lambda_2\sqrt{1-k}cos\left(\lambda_2 a_d\sqrt{1-k}\right)tanh[\lambda_1(a_d + d - L)]\Big] \quad (3.20.3)$$

P reaches its maximum value when the derivative is zero with respect to *d*, or when:

$$tanh^2[\lambda_1(L-d-a_d)] = \frac{cos\big(a_d\lambda_2\sqrt{1-k}\big) - k}{cos\big(a_d\lambda_2\sqrt{1-k}\big)}$$

Solving for *d* at the ultimate load, denoted as d_{ult}, as:

$$d_{ult} = L - a_d - \frac{1}{\lambda_1}tanh^{-1}\sqrt{\frac{cos\big(a_d\lambda_2\sqrt{1-k}\big) - k}{cos\big(a_d\lambda_2\sqrt{1-k}\big)}} \quad (3.21.1)$$

$$P_{ult} = \frac{2\pi r_b\tau_f}{\lambda_2\sqrt{1-k}}\left[\frac{\lambda_2\sqrt{1-k}}{\lambda_1}\sqrt{cos\big(a_d\lambda_2\sqrt{1-k}\big)\big[cos\big(a_d\lambda_2\sqrt{1-k}\big) - k\big]} + sin\left(a_d\lambda_2\sqrt{1-k}\right)\right] + 2k\pi r_b\tau_f d_u \quad (3.21.2)$$

The above analysis shows that the full-range mechanical behaviour of rockbolts under tension consists of five distinct stages as depicted in Figure 3.32. The important points are point A(P_1,u_1) corresponding to the initiation of interface softening, point B(P_2,u_2) corresponding to the initiation of debonding, and point C(P_3,u_3) corresponding to the ultimate load. These three points may be identified from an experimental

load–displacement curve, and used to calibrate the parameters in the tri-linear bond-slip model (Figure 3.33).

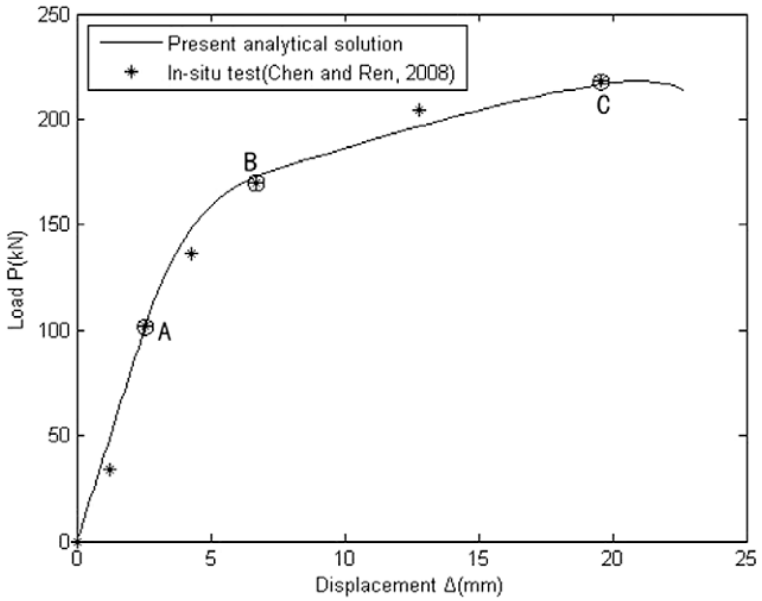

Figure 3.33 Comparison of theoretical result with pull out test (Ren *et al*, 2010)

The ISS model is a traditional approach of rockbolting mechanism. From Li and Stillborg (1995) to Ren *et al* (2010), this model has been advanced by many researches. Up-to-date, it is the biggest achievement of rockbolting mechanisms. However, it is not a cause-effect based approach. Parameters used in the model, such as shear stress - shear displacement behaviour in Li and Stillborg or tri-linear stress-strain relationships in Ren *et al*, must be calibrated from pullout tests. Any change of the elements in the rockbolting system, such as mechanical properties of the grout or surface profile of the bolt or presence of fracture in the rock, requires other pullout tests.

In addition, there are four bond-slip model parameters δ_1, δ_f, k and τ_f in the above analytical solution. Ren *et al* suggest finding P_1, u_1, P_2 and P_3 to solve these parameters and they use a software named 1stOpt in their study. It is recommended using P_1, u_1, P_3, u_3 to calculate those four parameters as point B is difficult to identify.

3.8 CONCLUSIONS

The following sections describe the main conclusions drawn from this chapter:

- The anchorage is affected by parameters such as resin annulus, grout strength, bolt profile characteristics, rock roughness, rock strength, and mechanical properties of the bolt.
- From the research studies in both pull and push tests it can be inferred that the bolt interacts with the rock via shear stress at the contact interfaces. Accordingly, the shear resistance of the interface is the key element in transferring the load from the bolt to the rock.
- It is commonly accepted that there are three components in bond strength: cohesion, friction and mechanical interlock.
- An exponential decay pattern of axial load and shear stress has been widely accepted in the elastic stage of rockbolting.
- There are two mechanical models to describe the bond behaviour of cable bolting. BSM focus on the dilational slip, and Hyett's model emphasises the friction and torsional effect.
- The ISS model is the significant achievement of rockbolting mechanisms study to date.

CHAPTER FOUR

LABORATORY STUDIES AND MATERIAL PROPERTIES

LABORATORY STUDIES AND MATERIAL PROPERTIES

4.1 INTRODUCTION

To investigate the load transfer mechanisms and failure modes in rock bolting, laboratory experiments were conducted. There were push tests from 100mm steel sleeves and pullout tests embedment length 200mm from concrete blocks. Double shear tests were undertaken to exanimate the influence of rib profile on rockbolting under shear load. Shear tests under CNS were also performed to investigate the role of the interlock strength component and failure modes in plane stress conditions. All tests were with an emphasis on the identification of failure modes and results were compared with previous studies.

The mechanical properties of the bolts, resin, and concrete were tested. Some data that were carried out in previous research (Jalalifar 2006, Aziz 2000-2012) were also considered. Parameters examined include UCS, shear strength, and modulus of deformation. These parameters are pertinent to the overall study of the load transfer mechanism of rockbolting.

4.2 MATERIAL PROPERTIES

4.2.1 Rock bolts

Table 4.1 shows different types of rock bolts. Rock bolts are classified into several groups according to their anchorage (Jalalifar, 2006). The first group represents mechanically anchored bolts that can be anchored by a slit-wedge mechanism or an expansion shell. The second group consists of fully grouted rock bolts anchored by cement or resin. The third group includes friction anchored rock bolts split set and swellex.

Table 4.1 Different bolt types (Jalalifar, 2006)

Bolt	Capacity (t)	Comments	Diagram
Point anchored (tensioned)	10-16t	● Inexpensive ● Possible immediate support ● Limited to use in soft rock ● Long-term stability affected by slippage	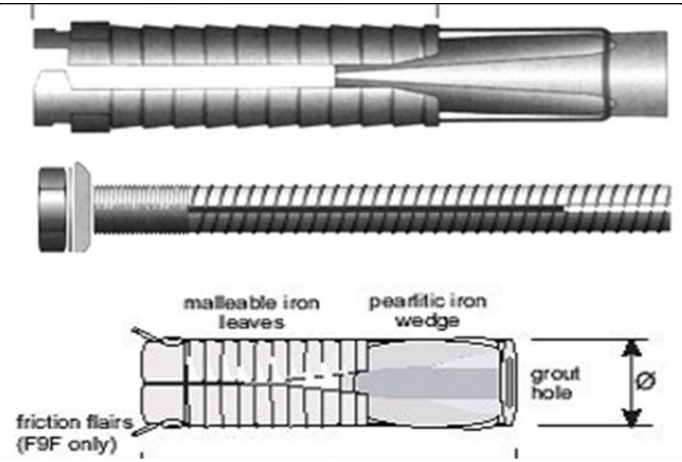
Fully grouted (untensioned)	15-25t	● High corrosion resistance ● Durable ● Consistent ● Long setting time of cement grout ● Installation is time critical ● More expensive than mechanical bolts	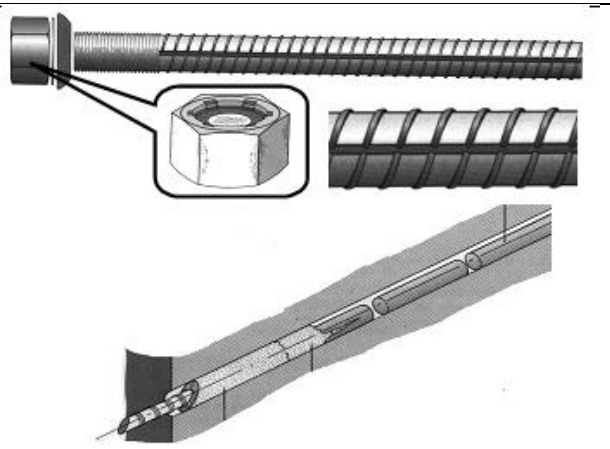

Roof trusses	Up to 20t	Suitable for mine roadway intersections and high stress areas	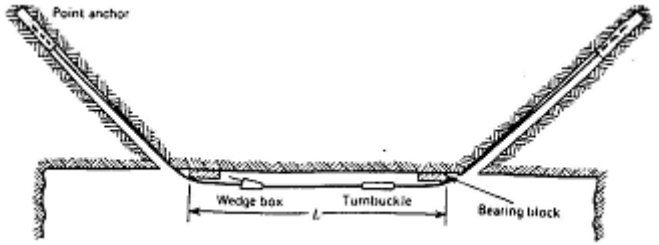
Grouted cables	Up to 15t	Up to 15m	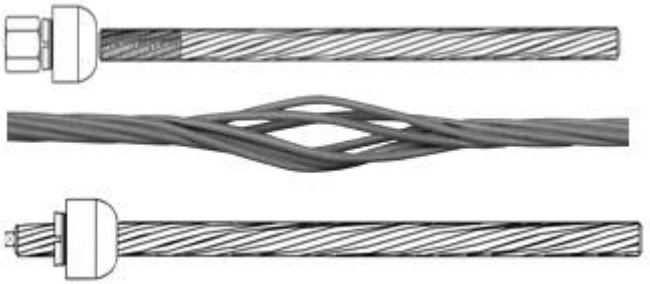
Threaded bolts	Up to 33t		
Cone bolts	Up to 20t	● Easy to install ● The anchor depends on grout specification	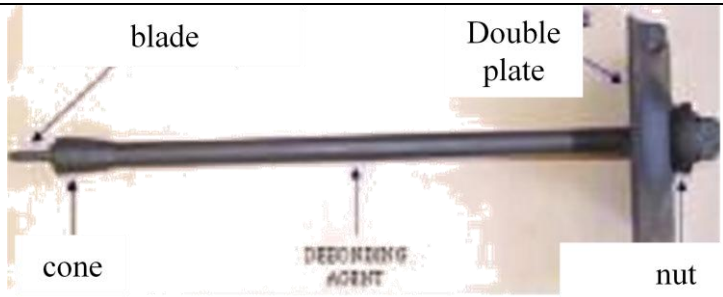

Figure 4.1 shows the photographs of four types of bolts which are popular and used widely by the Australian mining industry. The core sizes are similar, but they have different rib profiles. They were used to study the load transfer mechanism by Aziz (2002-2012), Jalalifar (2006) and also in this study. Table 4.2 lists their rib profile specifications, and the definition of rib profile of the bolts was shown in Figure 1.3 in Chapter one.

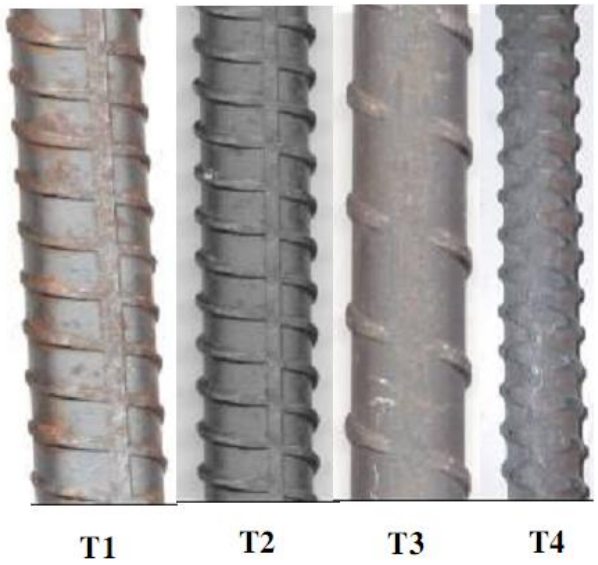

Figure 4.1 Bolts used widely by the Australian mining industry (Aziz, 2003)

Table 4.2 Specifications of different bolts (Aziz, 2003)

Bolt	Profile Spacing (mm)	Core Diameter (mm)	Profile Height (mm)	Profile Width (mm)	Profile Length (mm)
T1	11.5	21.7	1	3.2	32
T2	12	21.6	1.5	3.2	32
T3	24	21.8	1.2	4	28
T4	9.7	19.6	1.3	4.2	26

Tensile, bending, and shear strength of the steel bolt are important mechanical parameters that influence its behaviour when loaded axially and in shear. The yield strength is an important factor in determining tension. It should be noted that although a roof bolt of high yield strength is desirable, its use *in situ* should be avoided. Dynamic failure of a high strength bolt could cause severe injury by sudden failure (Peng 1984). Accordingly, bolts currently used in Australian mines are restricted to approximately 320kN. The value of the yield and ultimate failure loads of commonly used types of bolts are described in Table 4.3.

Table 4.3 Bolt tensile strength (Jalalifar, 2006)

Bolt	Yield Point (kN)	Tensile Strength (kN)	Yield stress (MPa)	Ultimate stress (MPa)
T1	260	328	683	862
T2	256	342	673	900
T3	210	358	552	942
T4	163	194	518	617

4.2.2 Resin grout

Epoxy and polyester resins are the most commonly used forms of chemicals used in rock bolt installation in Australian mines. Strength tests were carried out on resin, including uniaxial compression tests, double shear tests, direct shear tests and triaxial tests. These tests were carried out on slow setting (20 minutes) resin. A longer setting time was essential for the strength tests. The diameter of the prepared samples was different for different tests carried out.

The uniaxial compression test is the most common test performed on rock and other samples, in this case resin. As UCS is not the intrinsic property of the material, the samples were prepared in different diameters as 54, 30 and 20mm with the length to diameter ratio of 2.5:1. The samples were cast in a plastic mould and tests were accomplished with an Instron machine of 500kN capacity, as shown in Figure 4.2. A constant displacement rate of 1 mm/min was used to load the samples to failure. All results are summarised in Table 4.4. The average UCS values were 68.4±1.6 MPa which is in agreement with the manufacturer's specified strength of 71MPa.

Figure 4.2 UCS tested samples and loading machine.

Table 4.4 Resin UCS tests results

Ave. diameter	Test number	Ave. $\frac{\text{height}}{\text{diameter}}$	UCS (MPa)	S.D. (MPa)
54.2 mm	5	2.4:1	71.8	2.0
29.7 mm	6	2.4:1	66.7	1.2
20.7 mm	6	2.4:1	67.4	1.7
		Average=	68.4	1.6

Whenever conical failure was achieved (Figure 4.3), the failure angle was measured. The average failure angle was 64°. Accordingly, the internal friction angle of the resin can be estimated as 38°. In addition, according to:

$$\text{UCS} = \frac{2c\cos\phi}{1-\sin\phi} \qquad (4.1)$$

The cohesion of the resin can be estimated as 16.6MPa.

Figure 4.3 Resin fracture angle in uniaxial compressive tests.

Two 54mm diameter samples were tested in triaxial compression to obtain the failure envelope of the resin. A hydraulic pump was used to maintain constant confining pressure. An initial confining pressure of 1.0MPa was applied prior to any application of axial load. The peak and residual strengths were plotted in Figure 4.4.

From the results, in terms of principal stress the resin peak and residual strength envelope were:

Peak: $\sigma_1 = 67.27 + 7.863\sigma_3$ (4.2.1)

Residual: $\sigma_1 = 9.39 + 7.95\sigma_3$ (4.2.2)

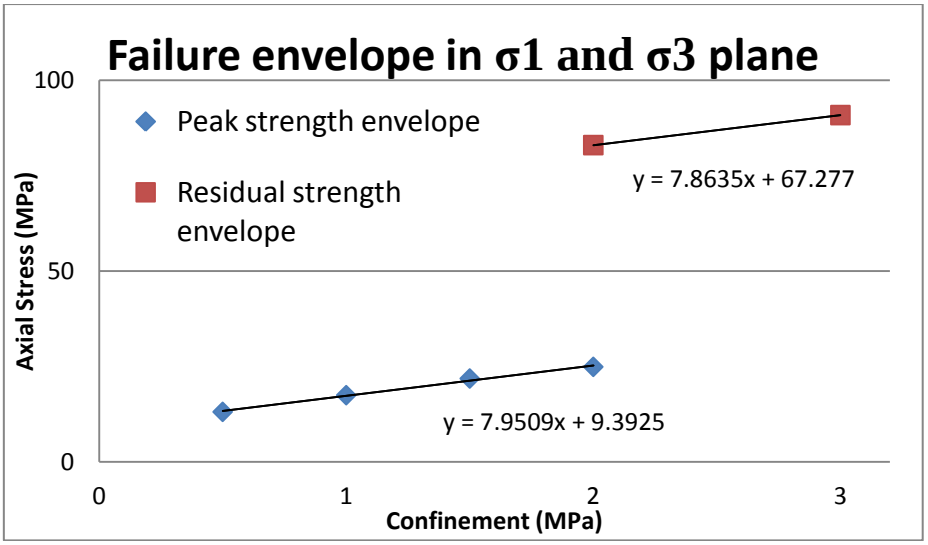

Figure 4.4 Triaxial compressive tests results

Consequently, the derived peak UCS was 67.3MPa. This result is in agreement with UCS tests. In terms of normal stress and shear stress, the peak and residual strength envelopes were:

$$\text{Peak: } \tau = 12.2 + \tan 50° \cdot \sigma_n \qquad (4.3.1)$$

$$\text{Residual: } \tau = 1.7 + \tan 50° \cdot \sigma_n \qquad (4.3.2)$$

The peak cohesive strength was found to be 12.2MPa, and both peak and residual frictional angles were approximately 50°, as shown in Figure 4.5.

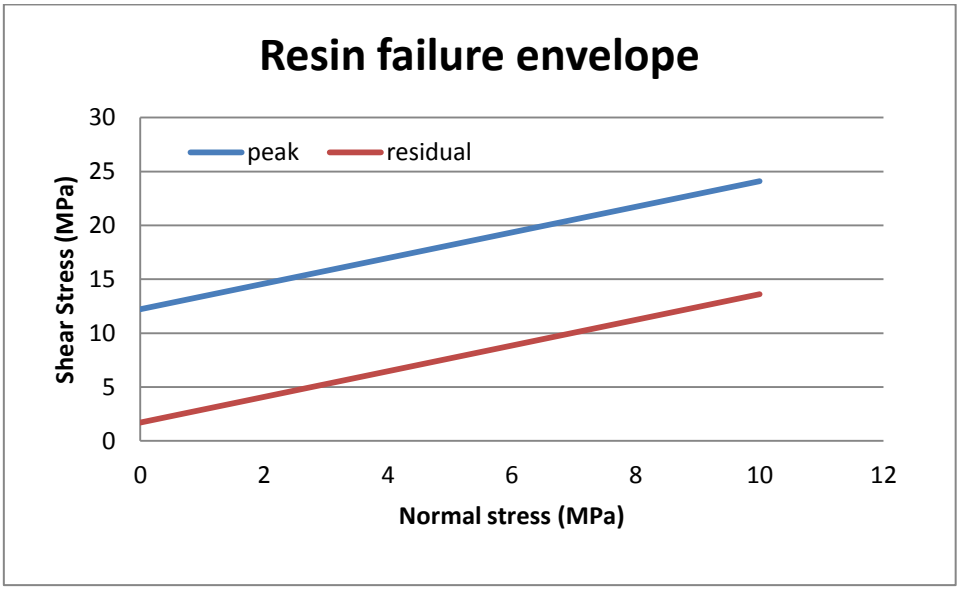

Figure 4.5 Resin failure envelope

The shear strength tests were also undertaken using double shear tests with a 50 tonne Avery machine. The samples were cast in specially prepared moulds 32 mm in diameter, fitting inside the double shear barrel, as shown in Figure 4.6. Three tests were carried out with the average shear strength of 11.4MPa.

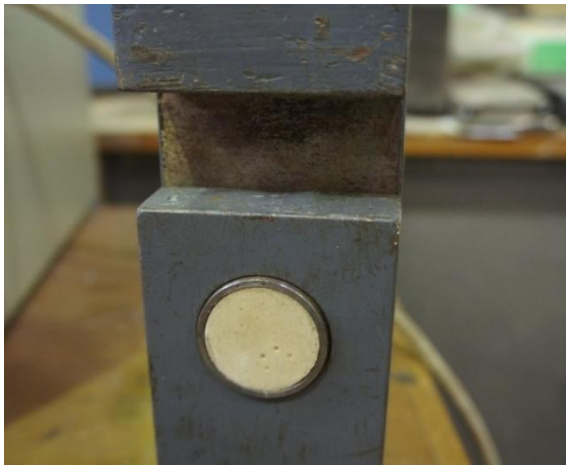

Figure 4.6 Resin double shear tests.

Two 32mm diameter resin samples were tested by direct shear to obtain the full range behaviour of the resin. The samples were prepared in a plastic mould and tested in direct shear box, as shown in Figure 4.7. It is believed that the post failure behaviour of the resin had great influence on the rockbolting performance.

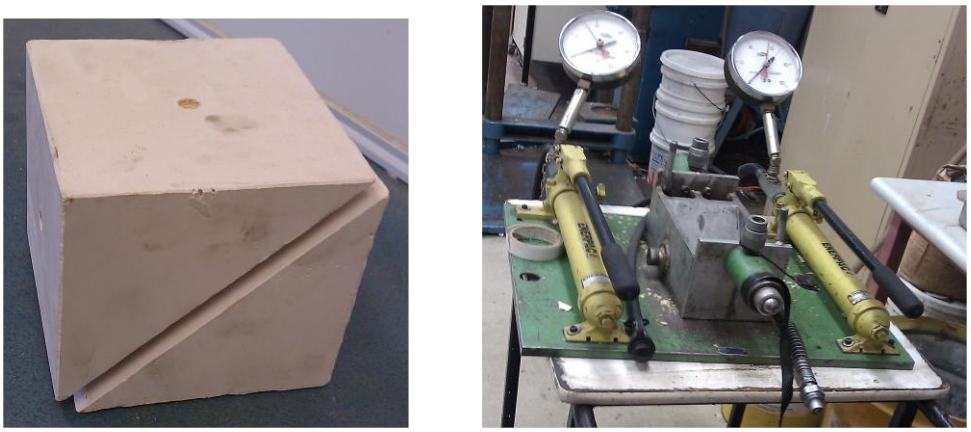

Figure 4.7 Resin direct shear tests

In the test, the normal forces were set to 3kN and 5kN respectively. The full range shear behaviour of the resin was presented in Figure 4.8. The real shear displacement in the tests was 5mm forward followed by 7mm backward, but expressed as from 0 to 12mm. The results were also interpreted as peak and residual shear strengths in terms of normal stress and shear stress, as shown in Figure 4.9.

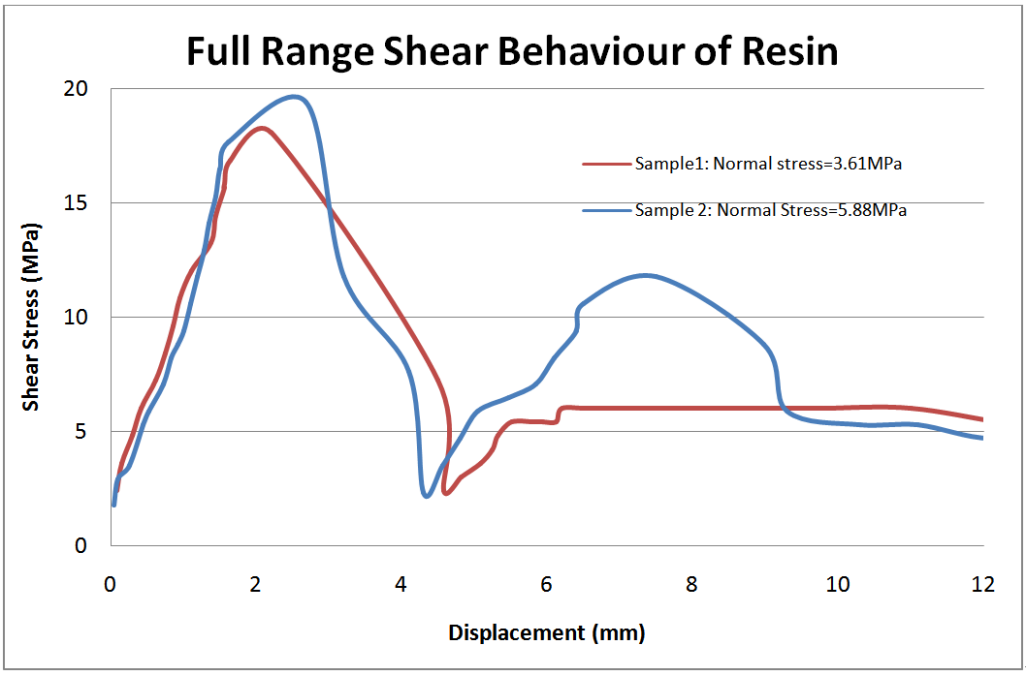

Figure 4.8 Full range shear behaviour of the resin obtained in direct shear tests

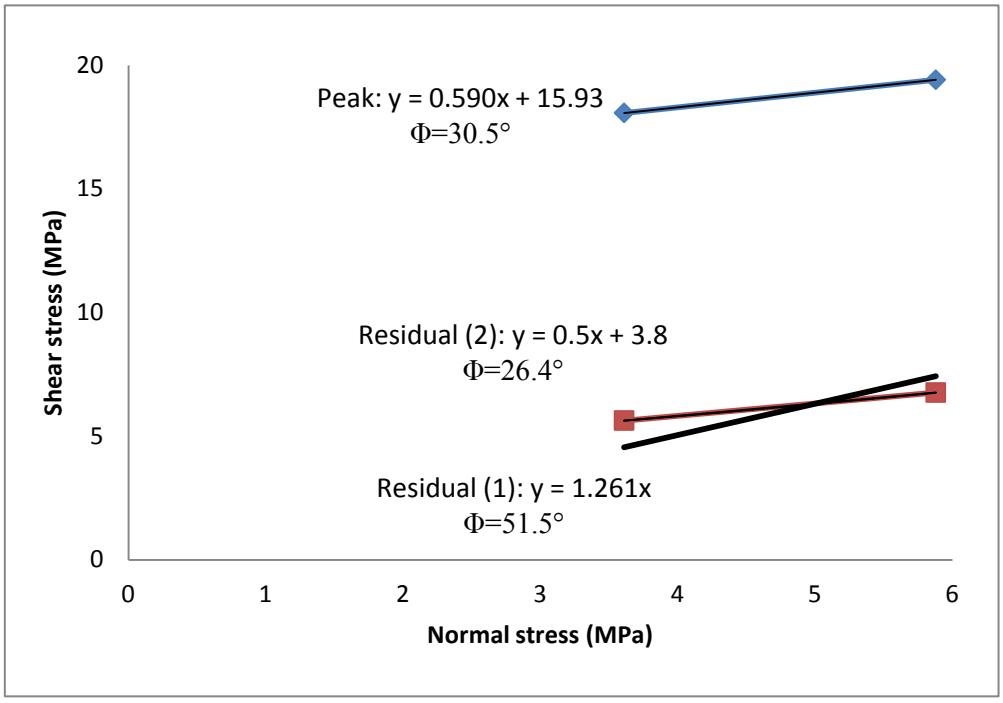

Figure 4.9 Peak and residual strengths obtained from direct shear tests

The peak cohesion was found to be 15.9MPa, very similiar to the value calculated from UCS tests. The peak internal frictional angle was approximately 31°. The residual strength description is an issue. As shown in Figure 4.9, there are two models to describe post failure behaviour of the resin:

(1) cohesion comes to zero immediately after failure, represented by black line *y=1.26x* in the diagram, or

(2) simultaneous mobilisation of cohesive and frictional strength components, which is described by the red line *y=0.497x+3.833* in Figure 4.9.

In research work (Oliveira, 2012) cited that the cohesional strength component could only be mobilised up to a stress level corresponding to the onset of micro-cracking. Beyond this stress level, there was a degradation of cohesion, i.e. softening, and mobilisation of the frictional strength component, which took place due to the development of micro fractures. This model is depicted in Figure 4.10 where ε_c^p marks the plastic shear strain beyond which there is only a residual cohesion and ε_f^p marks the plastic shear strain at which the frictional component is fully mobilised.

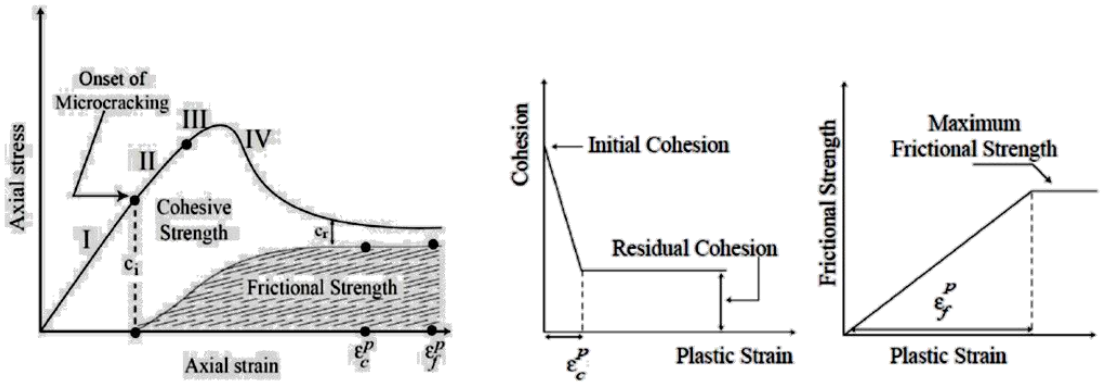

Figure 4.10 Mobilisation of the strength components (Oliveira, 2012)

In rockbolting and bond failure mechanism, mobilisation of cohesive and frictional strength components is complicated. It is considered that, both residual models are correct as they represent different situations. In the case of low confinement such as soft rock, dilational slip is the dominant failure mode. Once failure occurs, the cohesional strength will quickly decay to zero. In this case, residual model (1) closely describes the post failure behaviour of the resin. Figure 4.11 illustrates an element immediately after shear failure. The confinement is small thus dilational slip occurs and the mechanism is described by $s = Ntan(\phi + i)$.

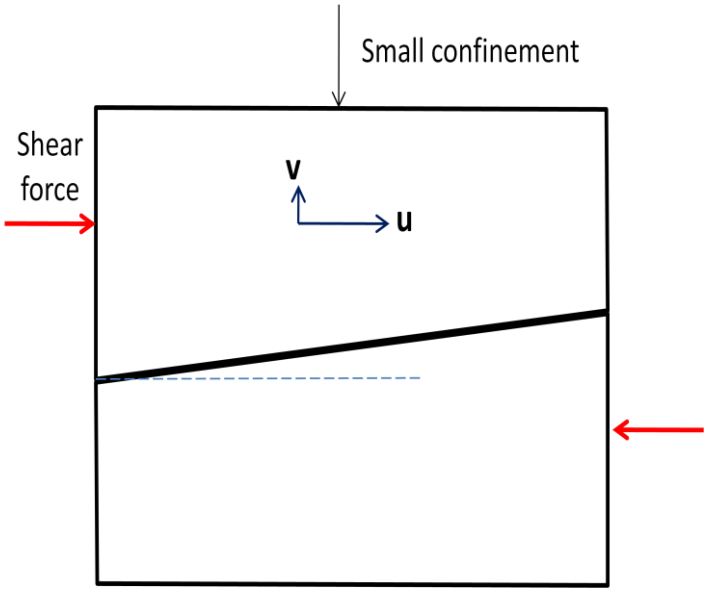

Figure 4.11 After shear failure, cohesion reduces to zero due to low confinement.

On the other hand, if the confinement is high such as in hard rock or a steel sleeve in the laboratory, the radial dilation is likely to be depressed. For example, in CNS tests (Aziz, 2002), the average dilation went to negative after the normal stress exceeded 3.5MPa for type I joints and 5MPa for type II joints. Similar results were obtained in cable bolt pullout tests (Hyett *et al*, 1995). Thus, it can be concluded that the cohesive strength component will gradually decay in case of high confinement. This concept is demonstrated in Figure 4.12. After the initial shear failure (Figure 4.12.1), the dilation is depressed by the high confinement pressure (Figure 4.12.2) after a very small displacement (*d*). In this situation, the material element is equivalent to an undamaged element (Figure 4.12.3) because no further displacement is allowed along the failure direction. Theoretically, this new element would recover 100% of its cohesion if thickness of the failure plane is zero. If the shear force continually exceeds the shear resistance, a new fracture will be established, represented by the dash-dot line in Figure 4.12.4, until all material around the slipping line is ground to powder to form a sheared band.

The residual cohesive strength model (2) can better describe the mechanism presented by this procedure. That is, the cohesion will gradually decay according to the shear displacement and introduced confining pressure. In addition, if the shear displacement of the element is d*w* in the initial shear failure, the theoretical residual cohesion can be found as:

$$c_{residual} = \frac{\mathrm{d}L - 2\mathrm{d}w}{\mathrm{d}L} \times c_{peak} \qquad (4.4.1)$$

With regard to the residual strength in direct shear test, it can be concluded that residual strength expression (1) in Figure 4.9, that is:

$$s_{residual} = Ntan(\phi + i) \qquad (4.4.2)$$

is suitable for low confinement. The general form of expression (2) in Figure 4.9:

$$s_{residual} = \mathrm{c}_{\mathrm{residual}} + Ntan\phi \qquad (4.4.3)$$

is proper expresion for high confinement. In reality, the post-failure behaviour of the resin is somewhere between these two equations. More accurate model is demanded to closely describe the residual strength of the resin specific for the rockbolting mechanism.

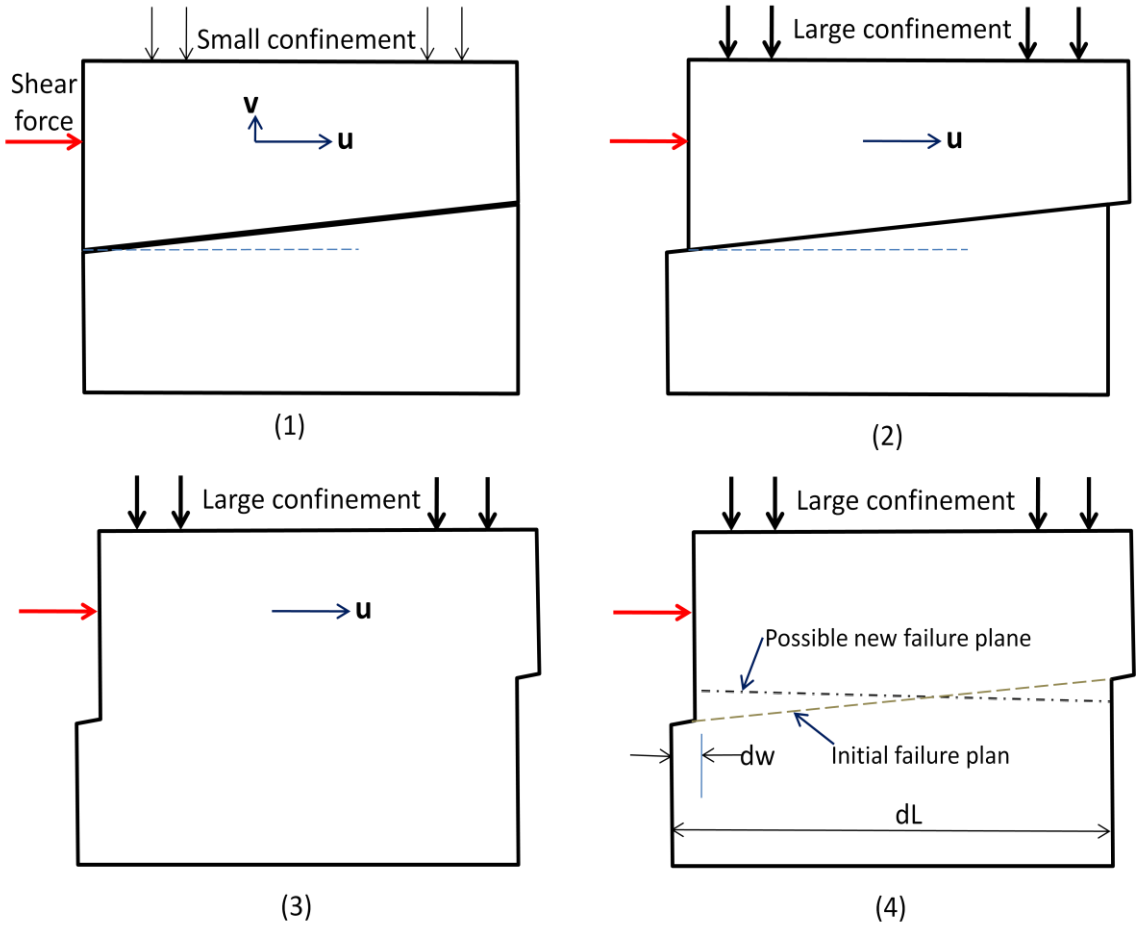

Figure 4.12 Concept of the residual cohesional strength in a material element

In this study, the confinements of laboratory pull/push tests were high as they were either 300mm concrete blocks or 10mm thick steel sleeves (refer to later section of this chapter). In these cases, the cohesion will not reduce to zero immediately after failure. Therefore, the model of gradual decaying of the cohesional strength was used to analyse the post failure behaviour in the tests.

Figure 4.13 shows the relationship between stress and strain in resin and displays the load versus displacement (Jalalifar, 2006). The elastic modulus was measured to be 10.5GPa and the Poisson's ratio was 0.26. Consequently, the bulk modulus and shear modulus are:

$$K = \frac{E}{3(1-2v)} = 7.3\ \text{GPa};\quad G = \frac{E}{2(1+v)} = 4.2\ \text{GPa}$$

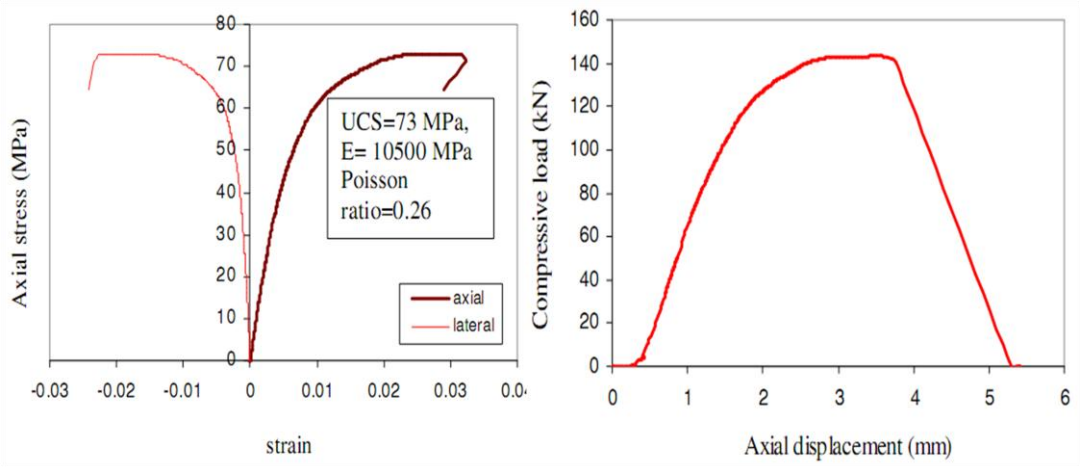

Figure 4. 13(a) stress strain curve for resin, and (b) load versus displacement

To sum up, the mechanical properties are tabulated in Table 4.5. These values were used in later analysis and computer simulation.

Table 4.5 Resin properties used in this thesis

UCS (MPa)	68	Residual frictional angle (°)	35
UTS (MPa)	13.5	Elastic modulus (GPa)	10.5
Peak cohesion (MPa)	13.5	Poisson's ratio	0.26
Internal friction angle (°)	35	Bulk modulus (GPa)	7.3
Residual cohesion (MPa)	1.7	Shear modulus (GPa)	4.2

4.2.3 Concrete properties

The nominated strength of 40MPa concrete was used in pullout and double shearing tests. Cylindrical samples from each concrete batch were cast to measure its ultimate strength of the concrete. Figure 4.14 shows the cast samples and the test machine. The results averaged UCS of 38.3MPa with standard deviation 2.3MPa. The internal frictional angle, estimated from failure angle, was around 38°. The cohesion was calculated as 9.3MPa.

Figure 4.14 Cast concrete samples and test machine.

The density of the concrete cylinder was also calculated to be 2200 kg/m^3. The typical value of Poisson's ratio specified by AS3600 is 0.2. The modulus of elasticity was calculated from the equation expressed in Australian Standard AS3600 (1994) as:

$$E = 0.043\rho^{1.5}\sqrt{\sigma_c} \qquad (4.5)$$

Where:

E = modulus of elasticity (MPa)

σ_c =UCS (MPa)

ρ= density (kg/m^3)

The mechanical properties of the concrete used in pull out tests and double shear tests are summarised in Table 4.6.

Table 4.6 Mechanical properties of the concrete block

UCS (MPa)	38.3
Elasticity modulus (GPa)	27.5
Poisson's ratio	0.2
Cohesion (MPa)	9.3
Internal friction angle (°)	38

4.3 PUSH AND PULL TESTS

4.3.1 Short Encapsulation Push Test (SEPT)

The push and pull tests help understand the effect of various parameters on the mechanical behaviour of a bolt system. There is large amount of push/pull test data regarding various variables in literature and in previous research conducted by Aziz and Jalalifar. However, there is very little concern with failure modes in the tests. The failure mechanism study based on failure modes is one of the objectives of this research work. As a result, SEPT was conducted to identify the failure mode. In addition, the data were compared with previous studies to ensure the consistency of the failure mode occurring in this test.

Push testing means pushing a bolt through hardened resin under normal load. Figure 4.15 shows the details of the short encapsulation push test cell. The cell is a 100mm long steel cylinder with an internal groove to hold the encapsulation medium and prevent premature failure between the internal surface and the resin. The test bolt was of the T2 type with 21.8mm diameter and 24mm profile spacing, it was encapsulated into test cells using PB1 Mix and Pour resin grout.

Figure 4.16 shows a bolt after the test and a tube surface inside. The failure mode can be identified as parallel shear failure as it occurred parallel to the bolt axis. The mechanism of this kind of failure mode is formulated in following chapters.

Jalalifar (2006) also reported on this kind of failure mode both in push and pull tests, as shown in Figure 4.17. It can be concluded that if the radial stiffness is large enough, the confinement will minimise dilation and parallel shear failure of the grout will be

the dominant failure mode of the bond.

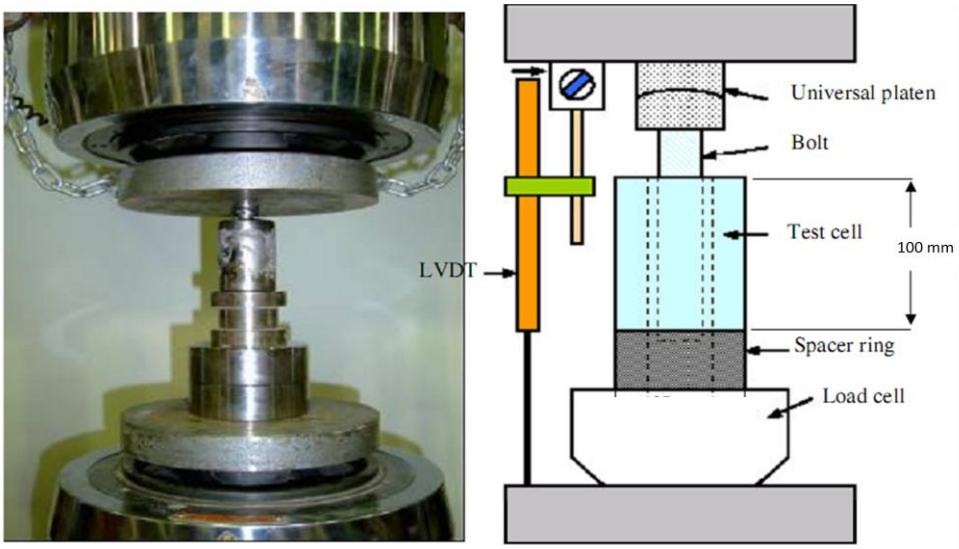

Figure 4.15 The push test configuration and the schematic of the test

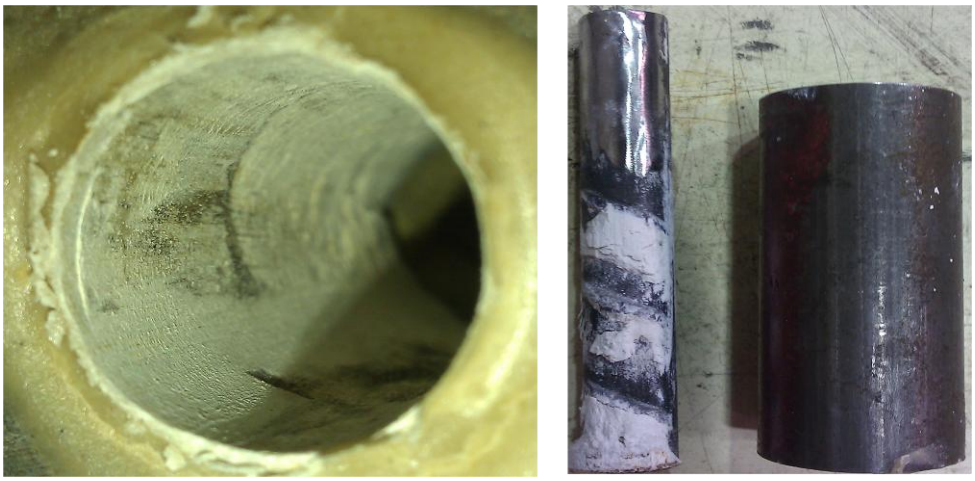

Figure 4.16 Post test bolt and grout annulus

Figure 4.17 Post-test sheared bolt out of steel cylinder (Jalalifar, 2006).

If the confinement is not strong enough, such as 4.2mm steel tube, dilational slip failure occurs, especially at the pulled end, as shown in Figure 4.18. Paint peeling off the tube surface indicates significant expansion and damage of the tube in the pullout tests, corresponding to the dilational slip failure of the bond.

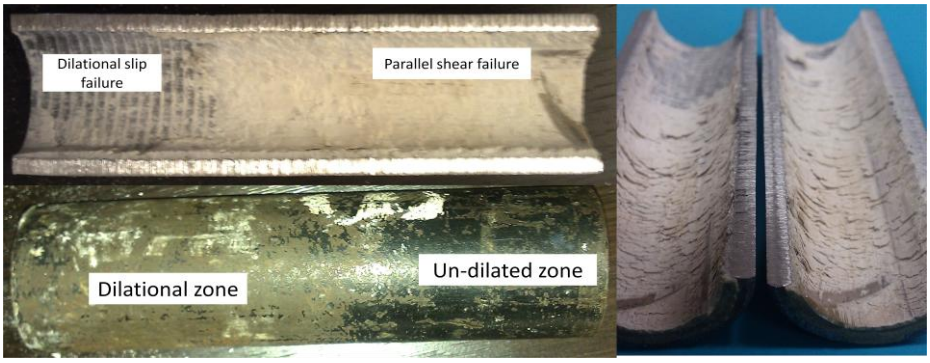

Figure 4.18 Post test of 4.2mm steel tube

Figure 4.19 shows a load displacement curve of the test. A comparison with Aziz and Webb (2003) and Jalalifar (2006) work is shown in Figure 4.20. It can be seen that all the profiles have an initial linear stage, a peak zone, and a post peak zone. The post peak load displacement profile was considered at the plastic stage because the bonding between bolt and resin failed. The load displacement relationship cannot be considered properly as an elasto-plastic relationship similar to loading a steel bar to failure because it involves separating one material from another.

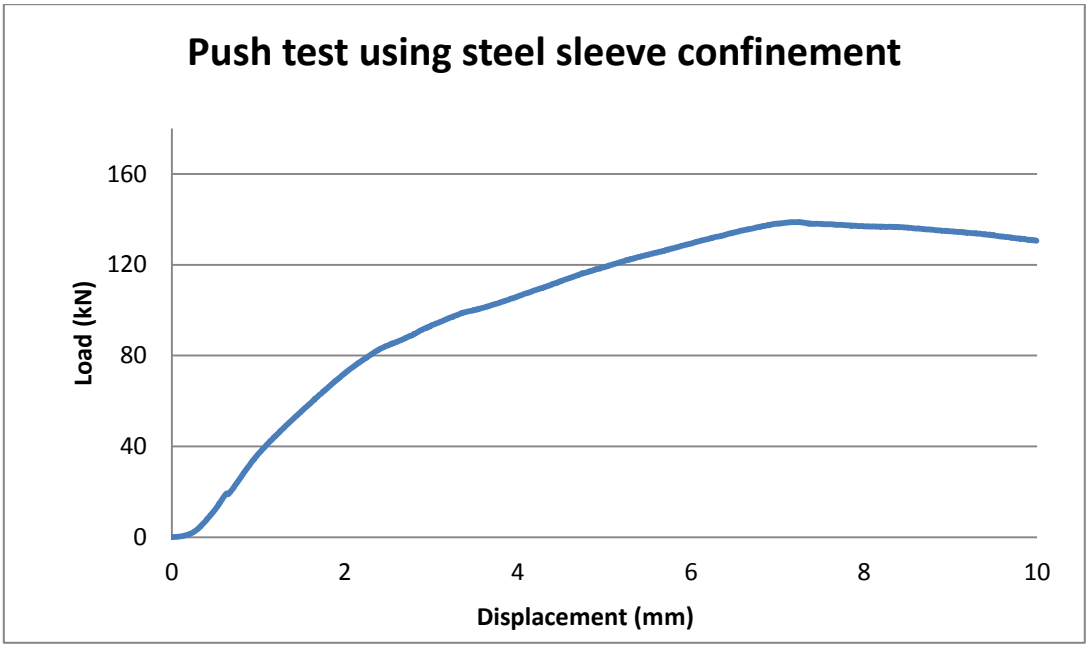

Figure 4.19 Load displacement curve of push test.

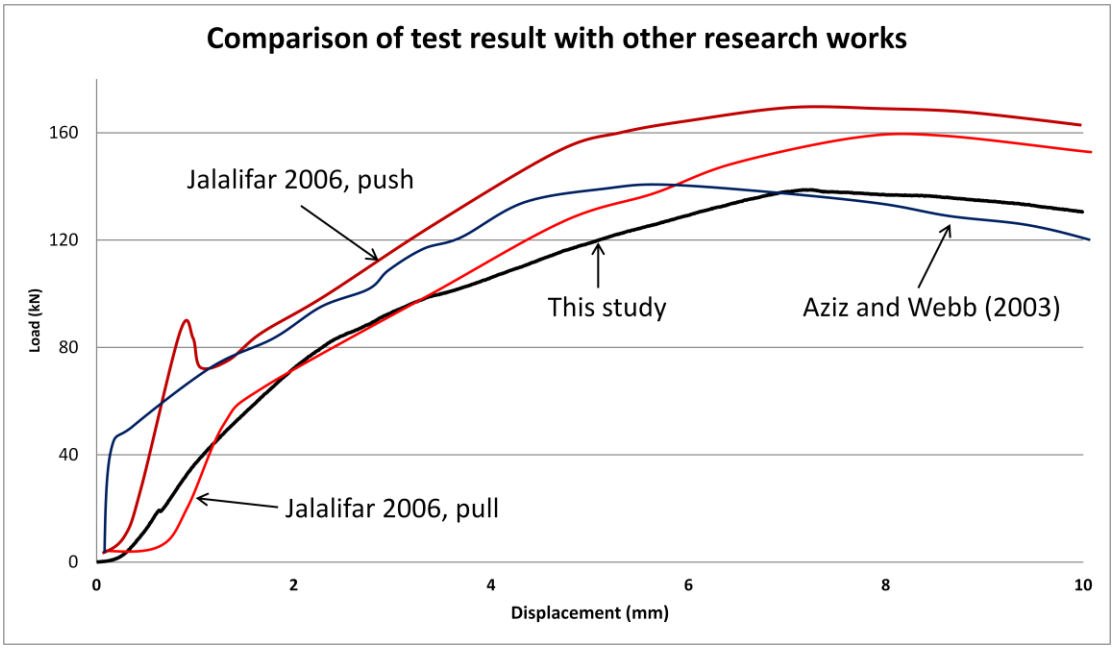

Figure 4.20 Comparison of Test result with other tests using similar experimental configuration.

4.3.2 Pullout tests using concrete blocks

It is difficult to observe the failure procedure in pull or push test using steel tube confinement. Accordingly, a series of pull out tests using T2 bolts were carried out in 300mm concrete blocks. The embedded bolt length was 200mm and the displacements due to pulling were monitored from both ends of the encapsulated bolt, as shown in Figure 4.21.

Figure 4.21 Pull out configuration and grouted bolt after test

Figure 4.22 shows the load displacement curves of the test. As the sample was not confined in steel frame, the failure was caused by fracture of the concrete block in both samples. Thus, the initial load-displacement profile (up to peak load) represented

the bond performance but the peak load is not the peak strength of the bond but rather the capacity of the confinement. In a similar test by William (2002), the peak load was found to be around 160kN for the same bolt while the embedded length was 260mm.

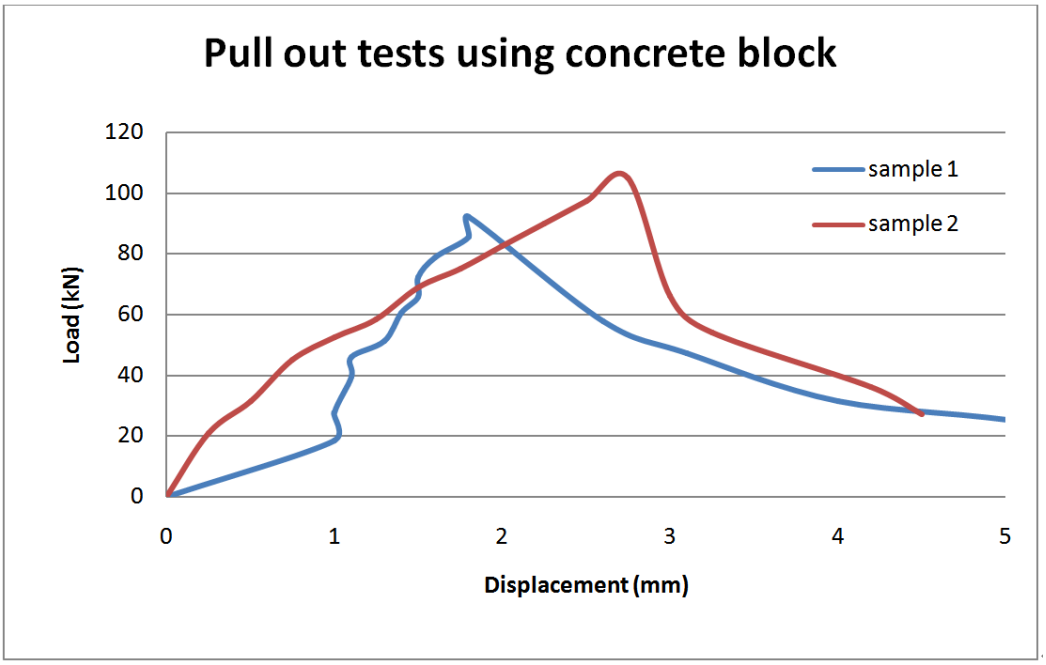

Figure 4.22 Load displacement curves in pull out tests.

Observation of the failure mode at the bolt-resin interface is one of the major objectives of this test. After failure, the concrete was removed and the failure mode at resin bolt contact was identified, as shown in Figure 4.23. The dominant failure mode was dilational slip, evidenced by the reminding resin powder in front of the profile. The mechanism of this kind of failure mode is studied in Chapter five.

Figure 4.23 Resin bolt interface in pull out tests

The displacement difference at two end of the bolt was also monitored as shown in Figure 4.24. The displacement of the loaded end is expressed by a dotted line as a

reference; the solid line is the displacement of the unloaded end and their difference is represented by the dashed line. From the diagram it can be identified that the free end begins to move when the loaded end has a displacement around 1.5mm, i.e. 70kN load. When loaded end had a displacement of 2mm, the displacement difference of the two ends remained to be a constant value about 1.2mm.

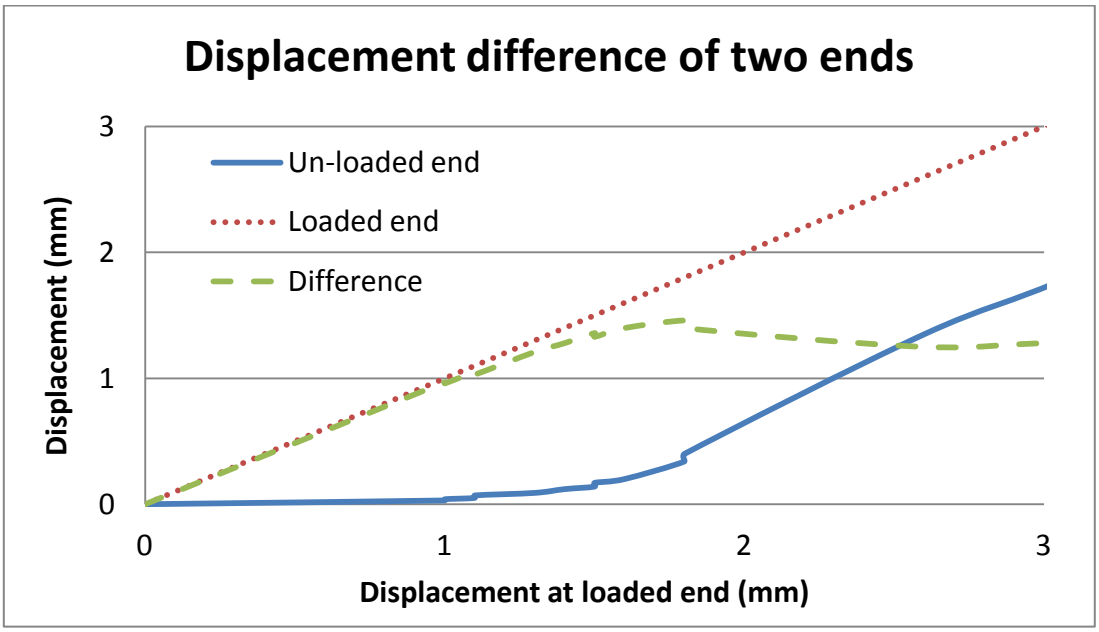

Figure 4.24 Displacement at two ends in pull out test

The initial stage of the load-displacement curve of the bond is normally proportional and often referred to as "elastic" in literature. However, linearity is not a sufficient condition to describe the elastic behaviour. To the best knowledge of the author, there is no research work to determine the elastic and plastic components in the initial linear stage of the bond. In this experiment, the linear stage of the bond performance is not elastic because the resin in front of the bolt profile has already had plastic deformation.

The linearity of the bond specifies that the unloaded end of the bolt remains intact (Nemcik and Aziz, 2012, via communication). In this experiment, it can be calculated that the elongation of the bolt stem outside the concrete block is approximately 0.2mm when the axial load is 70kN. It indicates that within 1.3mm of axial displacement, the bond is linear because the free end is still fixed. Once the free end of the bolt begins to move, the bond enters into a non-linear stage characterised by reduction of axial stiffness. Further controlled experiments are required to verify this

hypothesis.

4.4 DOUBLE SHEAR TESTS

Bolts installed in jointed rock undergo axial and shear loading. Figure 4.25 shows a typical bolt bending due to bedding displacement. To gain a better understanding of the load transfer mechanism and rockbolting failure, a series of laboratory based double shear tests were carried out. Using different types of bolts the study examined the influence of various parameters on the load transfer characteristics of bolts.

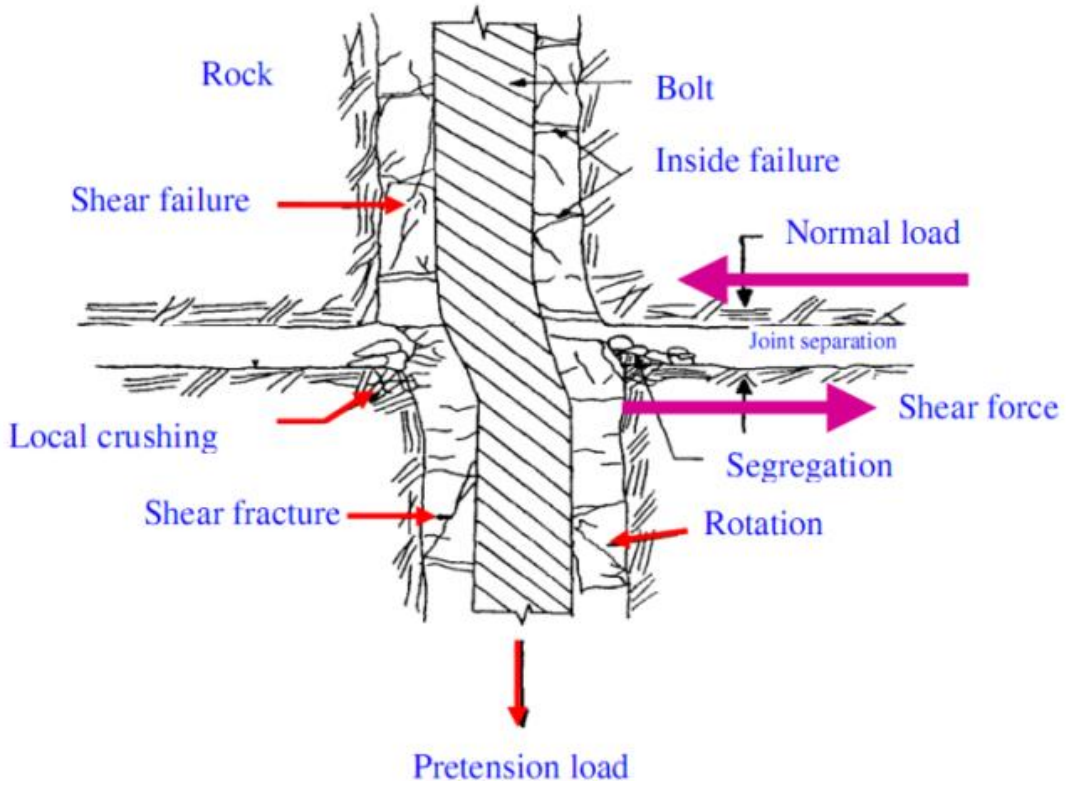

Figure 4.25 Bolt bending behaviour (cited from Indraratna *et al*, 2000)

Figure 4.26 shows the mechanical concepts of a reinforced joint subjected to shear load. The bar may fail in one of the two locations, the joint - bolt intersection (affected by the contribution of normal and transversal forces at point C or at point D, which is due to a combination of axial force and bending moment where the bending moment is maximum and shear force is zero (hinge point). Based on beam theory both the bending moment and curvature of the bolt at point C are zero. Both the axial and shear forces at this point reach a maximum.

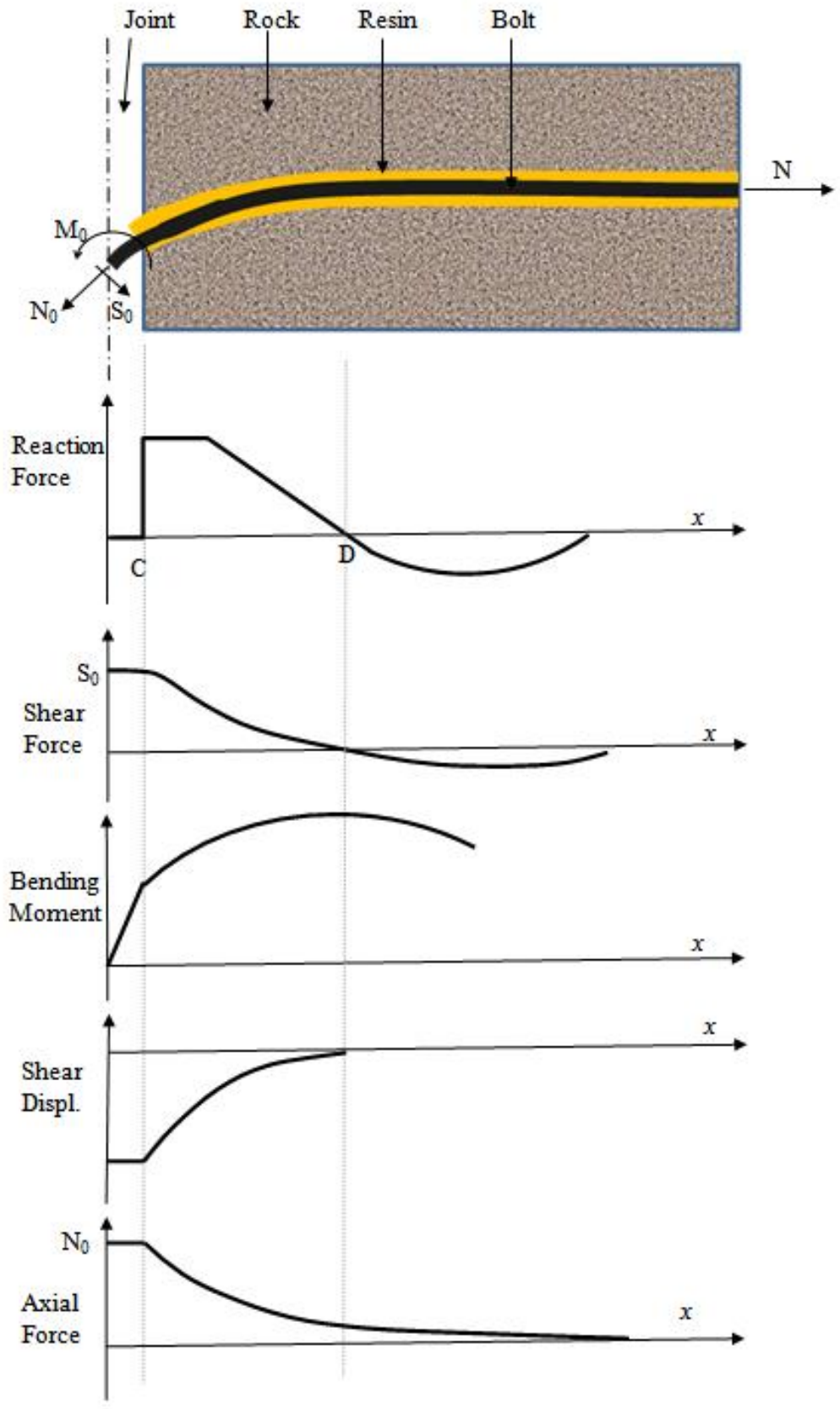

Figure 4.26 Concept of reinforced joint subjected to shear load

4.4.1 Experimental assemblage

Double jointed concrete blocks were cast for each double shearing test. The solid ingredients comprised mainly of sand and cement and the concrete blocks were cast to a strength of 40MPa. Once mixed, the concrete was poured into 1050mm x 300mm x 300mm steel moulds that were divided into three sections. A 24mm diameter length of plastic was set through the centre of the mould to create a hole for the bolt. Figure 4.27 shows a general view of the double shear mould set showing actual dimensions of the concrete blocks used. The concrete was left in the mould for 24 hours to set and stored in a humid environment for another 30 days to cure. The plastic conduit forming the hole was removed and the hole was riffled to a larger diameter for effective bolt anchorage. Rifling of the hole was achieved by a specially machined tip of a wing bit to mimic the rifling of the drill bits used underground.

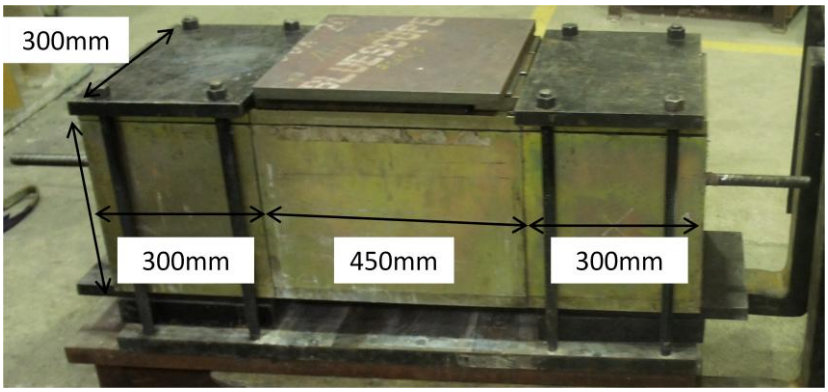

Figure 4.27 Double shear sample

A 1400 mm long bolt with 100 mm of thread on each end was fixed into the concrete specimen using resin grout. Prior to installation the blocks were placed upright and clamped together to ensure alignment. A series of rubber stoppers and steel plates were attached to the bottom of the hole to prevent resin seepage. The resin mix was 100 grams of resin and two grams of catalyst. Resin was poured into the hole and then the bolt was pushed through the stopper plates using 50mm wooden dowel mounted at the top of the bolt. More resin was used as required while the bar was rotated to reduce voids and fill the space between the bolt and the sides of the hole.

Figure 4.28 shows the sketch of the double shear box and the assembled shear box in 5000kN capacity Avery testing machine. A base platform that fitted into the bottom ram of the testing machine was used to hold the shear box between the loading plates.

Steel blocks about 75mm thick were placed beneath the two outer concrete blocks to allow for centre block vertical displacement when sheared. The two outer ends of the shear box were then clamped to the base platform so the blocks would not move during shearing. A pre-determined tensile load of 50kN was applied to the bolt prior to shear loading. This acted as a compressive confining pressure to simulate different forces on the joints within the concrete. Axial tensioning was accomplished by tightening the nuts on both ends of the bolt. The applied loads were monitored by two hollow load cells mounted on the bolt on either side of the block. During testing load cell readings were monitored. One of the unique features of this double shear system was that it was a symmetric system of load application and shearing of the bolt, which was particularly relevant when the bolt was subjected to axial loading.

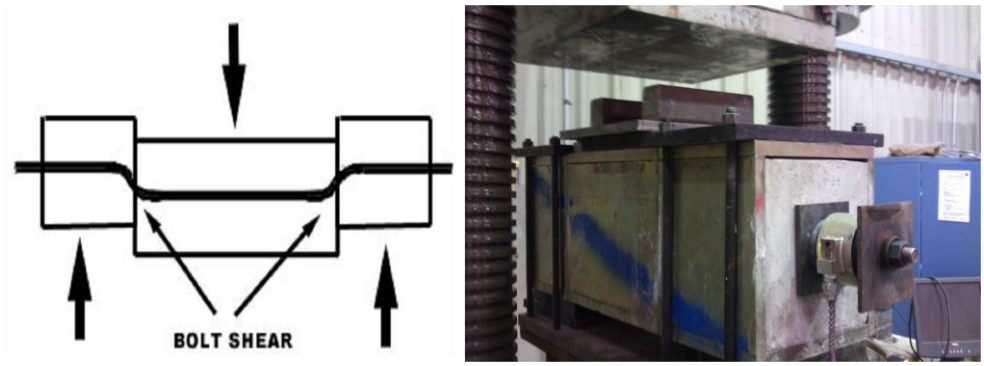

Figure 4.28 Sketch and experimental assembly of double shear test

4.4.2 Tests results

Figure 4.29 shows the general load-displacement curve of a double shearing test (Jalalifar, 2006). Three distinct load-displacement stages are shown which are named linear, non-linear, and plastic. Generally the profiles are similar, however the load build up and resultant displacements are influenced by the mechanical properties of each element, bolt profile configuration, concrete block size and axial pre-tension.

The initial part of the graph is associated with the linear behaviour of the bond. The surfaces start sliding against each other as the shear load is applied. This linear section is characterised by a rapid increase in shear load at a relatively small displacement. There is usually some minor fracturing of the grout and concrete, which cause a loss of bonding. The displacement level at the linear stage reduces as the pre-tension load increases. The transitional zone is characterised by decrease of shear stiffness after the

peak linear load (point P in Figure 4.29). Displacement at this stage is approximately the same magnitude to the linear stage section. Occasionally, a small drop in the shear load occurs beyond the yield point (P) due to axial fractures developing in the concrete. The plastic limit of the bolt is characterised by a low rate of shear loading at increased shear displacement, in other words, low stiffness in the system. Hinge points are created in the bolt on both sides of the shear joint plane because of reduced shear stiffness. The concrete and grout are completely damaged at the compression zones with excessive fracturing along the axis of the bolts in all three blocks.

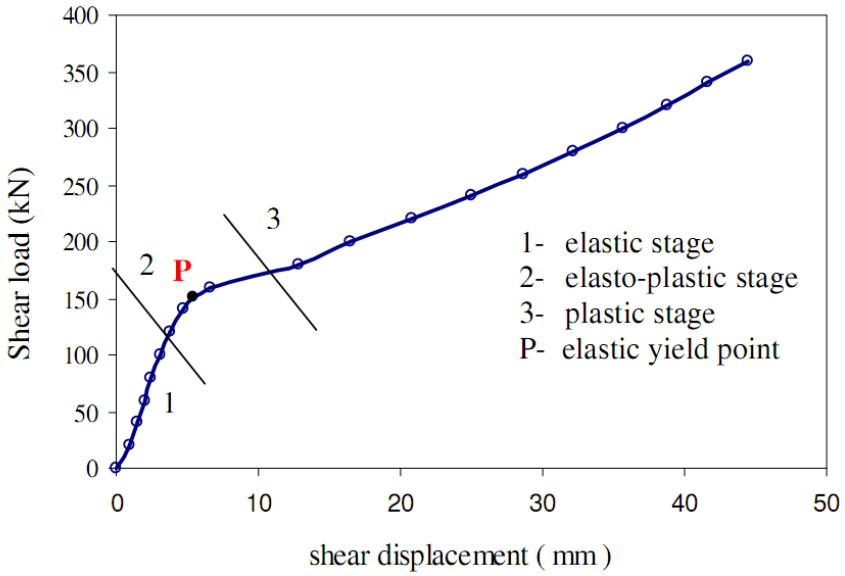

Figure 4.29 Typical shear load displacement profile stages of the sheared bolt (Jalalifar, 2006)

The tested bolts were T2 type bolts with rib profile spacing of 12.5, 25, 37.5, 50mm and plain with no rib profiles. The initial pretension was 50kN. The results are summarised in Table 4.7 and all load-displacements are plotted in Figure 4.30. The test results, for the same rib profile spacing, are shown in Figure 4.31. In the testing, the developed axial load was monitored by two load cells. A typical axial load versus shear displacement curve is shown in Figure 4.32. The average load difference between the two cells was small (< 6%). Therefore, the average value of the two load cells is used to represent the axial load developed in the tests. Table 4.8 shows the developed axial load in the tests, and Figure 4.33 shows the shear load and developed axial load with increasing shear displacement during the tests.

Table 4.7 Double shear result

Profile spacing (mm)	**Shear load at yield point (kN)**	**Shear displacement at yield point (mm)**	**Shear stiffness at linear stage (kN/mm)**	**Maximum shear load (kN)**	**Shear displacement at maximum shear load (mm)**	**Shear stiffness at maximum load (kN/mm)**	**Absorbed energy (kJ)**	**Average load capacity (kN)**	**Average absorbed energy (kJ)**
12.5	230	7	28	670	54	8.5	22.1	670	22.1
25	200	10	20	700	74	8.1	30.4	665	26.4
	220	10	20	630	59	8	22.3		
37.5	190	14	19	780	74	6.7	32.1	665	27.1
	150	10	20	550	67	8.1	22.1		
50	210	12	24	900	74	10	36.7	800	31.4
	220	11	24	700	63	8.5	26.1		
Plain	90	9	10	500	50	8.3	13.3	685	27.3
	300	8	30	870	70	6.5	41.2		
Ave=	234	10.1	21.7	700	65	8.1	27.4		

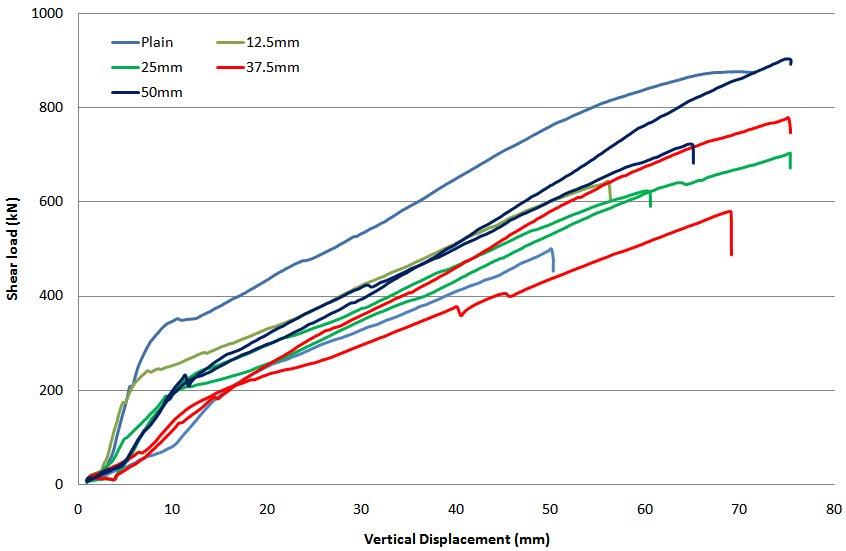

Figure 4.30 Double shear tests results

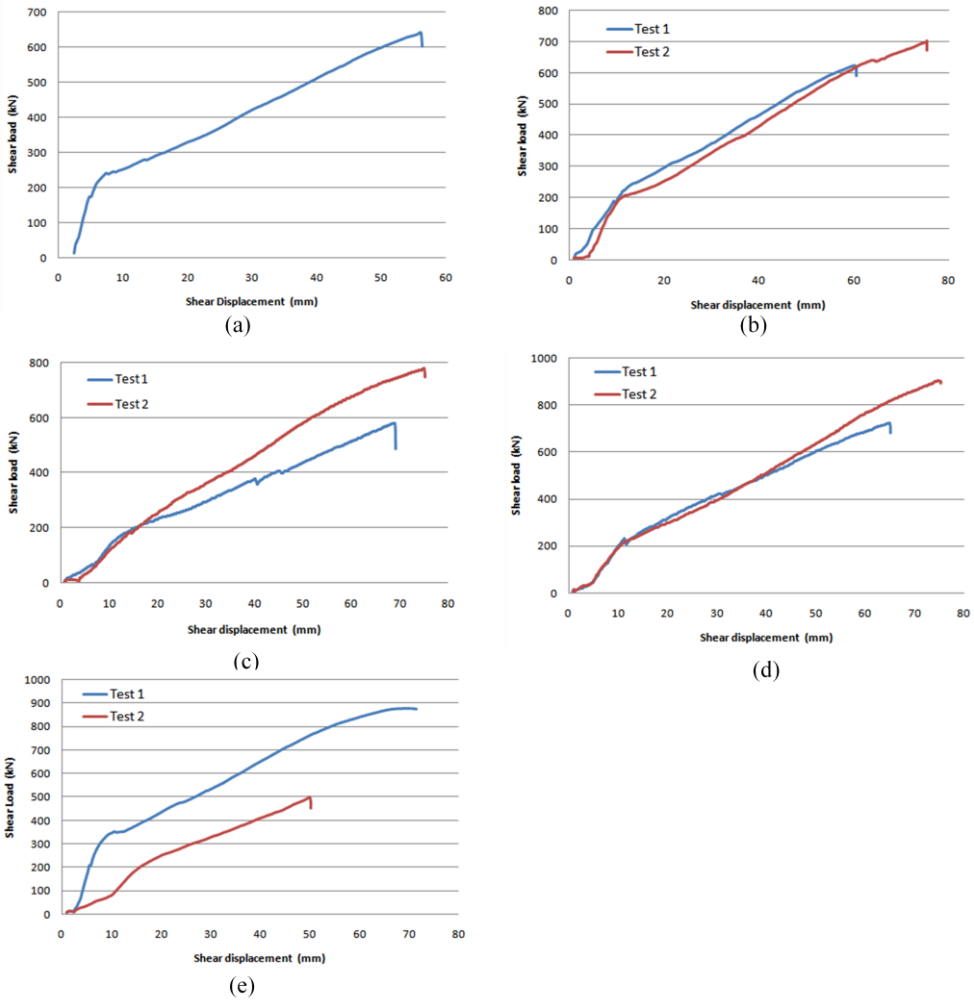

Figure 4.31 Double shear tests results respecting to different rib profile (a) 12.5mm spacing; (b) 25mm spacing; (c) 37.5mm spacing (d) 50mm spacing (e) smooth bolt.

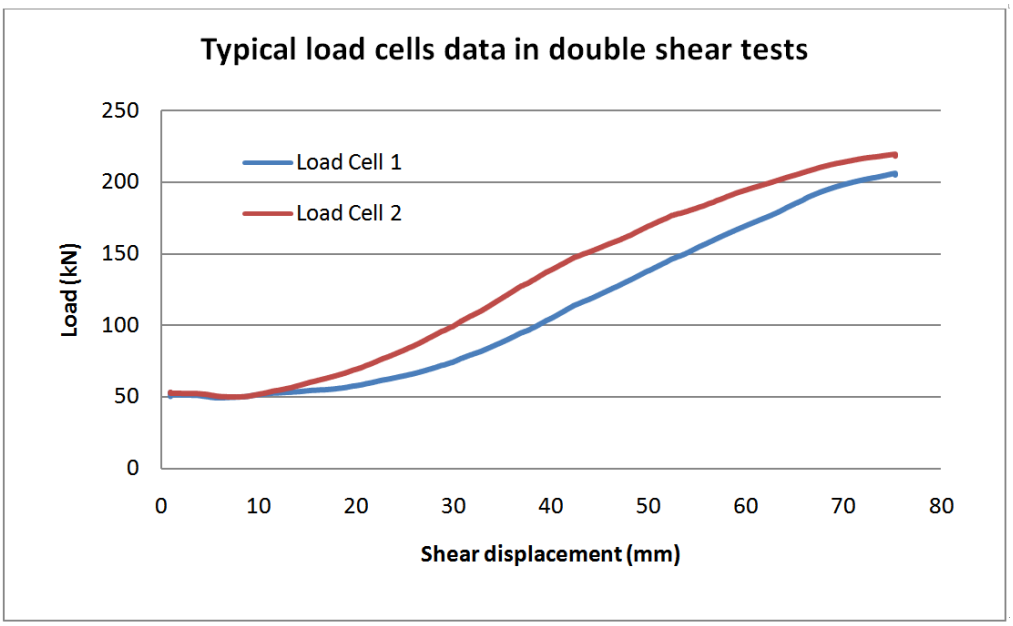

Figure 4.32 Typical axial load in double shear tests

Table 4.8 Axial load developed in the double shear tests

Profile spacing (mm)	Maximum shear displacement (mm)	Average maximum axial load (kN)
12.5	54	182
25	74	213
	59	199
37.5	67	211
	74	221
50	74	210
	63	202
Plain	50	129
	70	229
Ave=	65	200

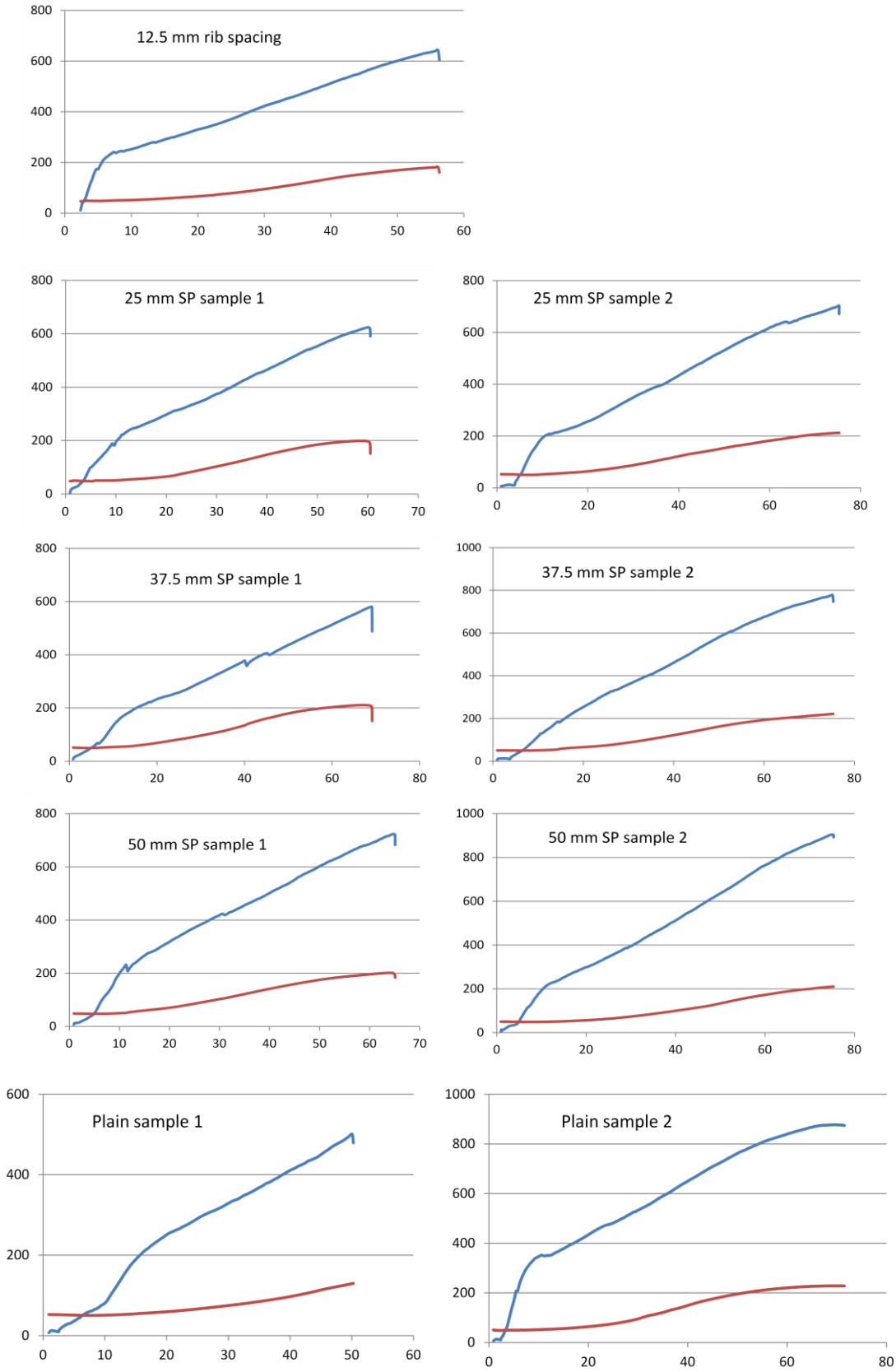

Figure 4.33 Shear (blue line) and axial (red line) load (kN) versus shear displacement (mm), SP=spacing.

The testing results are compared with a similar study by Jalalifar (2006). Figure 4.34 shows a comparison of 12.5mm rib spacing bolt with similar experiments conducted by Jalalifar (2006). The bolt, pre-tension load and concrete strength are the same but the cross section of the concrete block was 150x150mm in Jalalifar's test. It should be noted that the full curve of Jalalifar's test was not presented in his report. From the view point of shear stiffness the two results agree well.

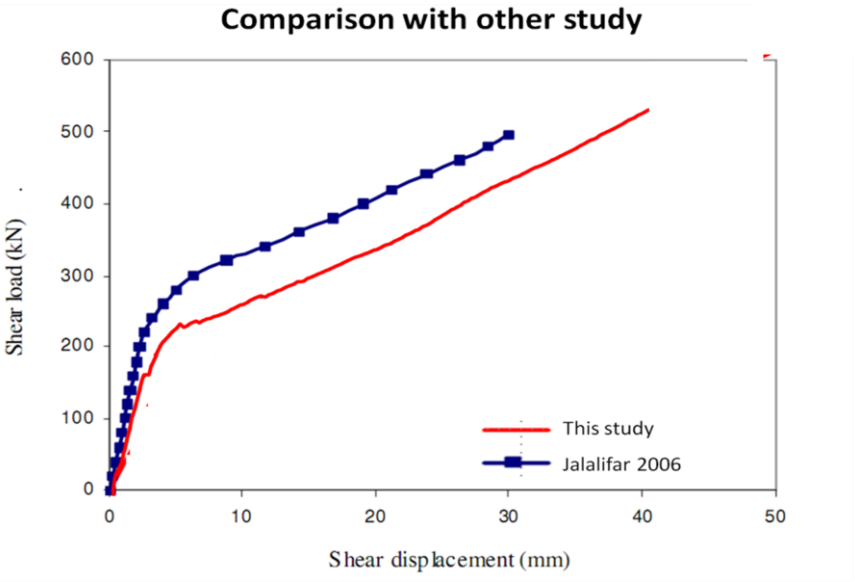

Figure 4.34 Comparison of 12.5mm rib spacing with the same bolt tested by Jalalifar (2006).

4.4.3 Discussion

(1) Shear capacity and energy absorption.

The maximum shear load is an important parameter indicating the shear capacity of the reinforcement, but it does not take into account the ductility of the reinforcement. The maximum absorbed energy due to shear resistance (F) with respect to displacement (s) is calculated by:

$$Energy = \int F\, ds \qquad (4.6)$$

For each test, the maximum shear load and absorbed energy were normalised with

respect to the average value of all tests. The normalised shear capacity and total energy absorption of the tests is presented in Figure 4.35. it should be noted that the plain bar offered comparable strength and energy absorption characteristics to other type of rebars.

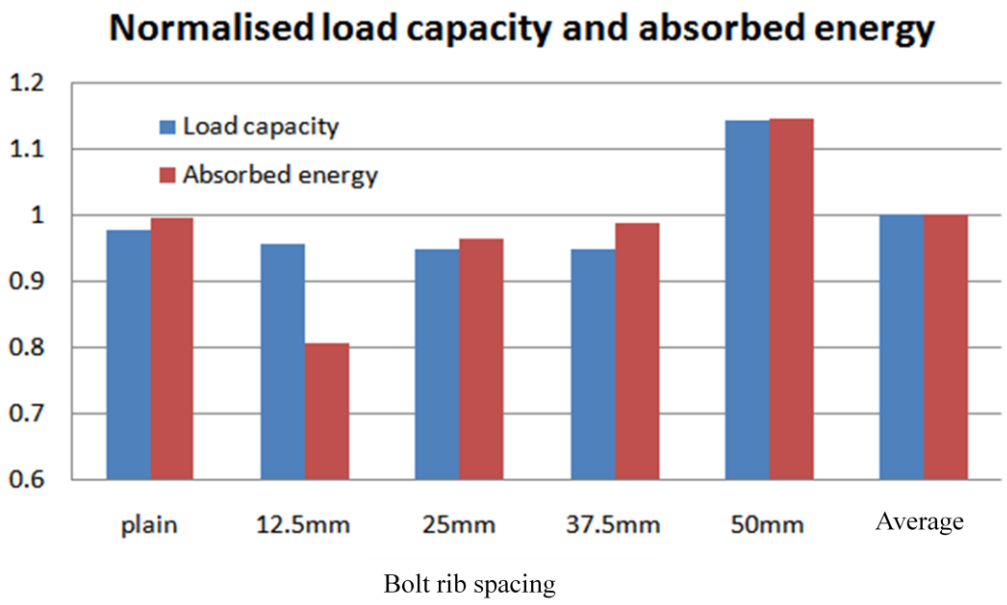

Figure 4.35 Normalised shear capacity and total energy absorption of the double shear rockbolt tests

(2) Pretension effect

There were a few experimental studies to evaluate the influence of bolt profile on shear resistance of rockbolting by using different bolts, such as Aziz *et al* (2003), Aziz *et al* (2005), Jalalifar (2006), Craig and Aziz (2010). There were no experimental tests conducted to evaluate the effect of bolt profile spacing on shear resistance under pre-tension loading. The rib space of the bolt is the only variable in this study. As discussed in previous chapters, the bolt rib profile has a great influence on the load transfer when bolts are subjected to axial loading. How the bolt profile affects the shear behaviour of reinforcement joint is the major concern of this study.

As shown in Figure 4.29, point P, charactered by a sharp drop of shear stiffness, is the peak load in the initial linear part of the shear load-displacement curve and

initialisation of the transitional zone. From then on, shear stiffness decreases towards the plastic range and the bolting system undergoes irreversible deformation. In double shear tests, it is found that point P is associated with the development of axial load.

Firstly, the shear load and developed axial load were normalised for each test. For example, the 12.5mm spacing bolt had a shear capacity 670kN and maximum axial load of 182kN, then:

$$\text{Normalised shear load} = \text{shear load}/670$$

$$\text{Normalised axial load} = \text{axial load}/182$$

The performances of the bolts are then re-plotted as Figure 4.36. The displacement at the turning point P was found to be 7.09mm and then the value Q in Figure 4.36 was calculated as 50.19kN. Comparing with its initial value 47.05kN, the increment of axial load

$$\%\Delta Q = \frac{50.19 - 47.05}{47.05} = 6.7\%$$

Figure 4.37 show the normalisation of all other tests. The calculated results of the value at point Q and the increment percentage are summarised in Table 4.9.

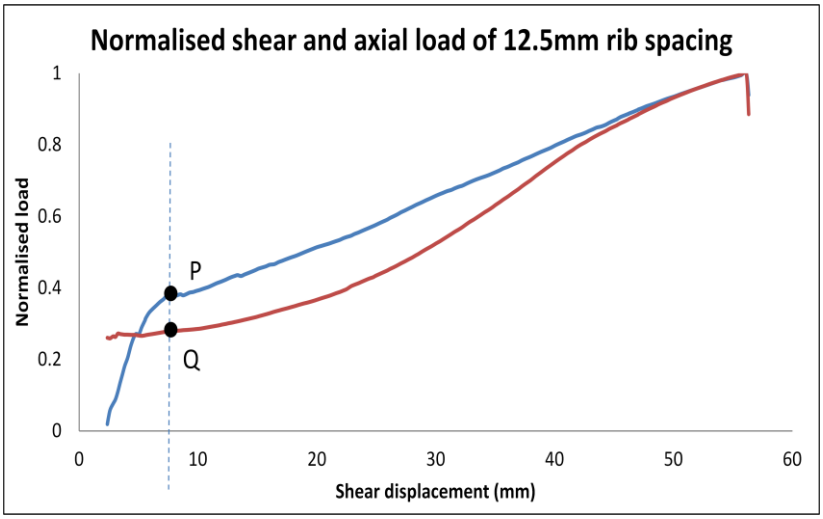

Figure 4.36 Normalised load-displacement curves of 12.5mm bolt.

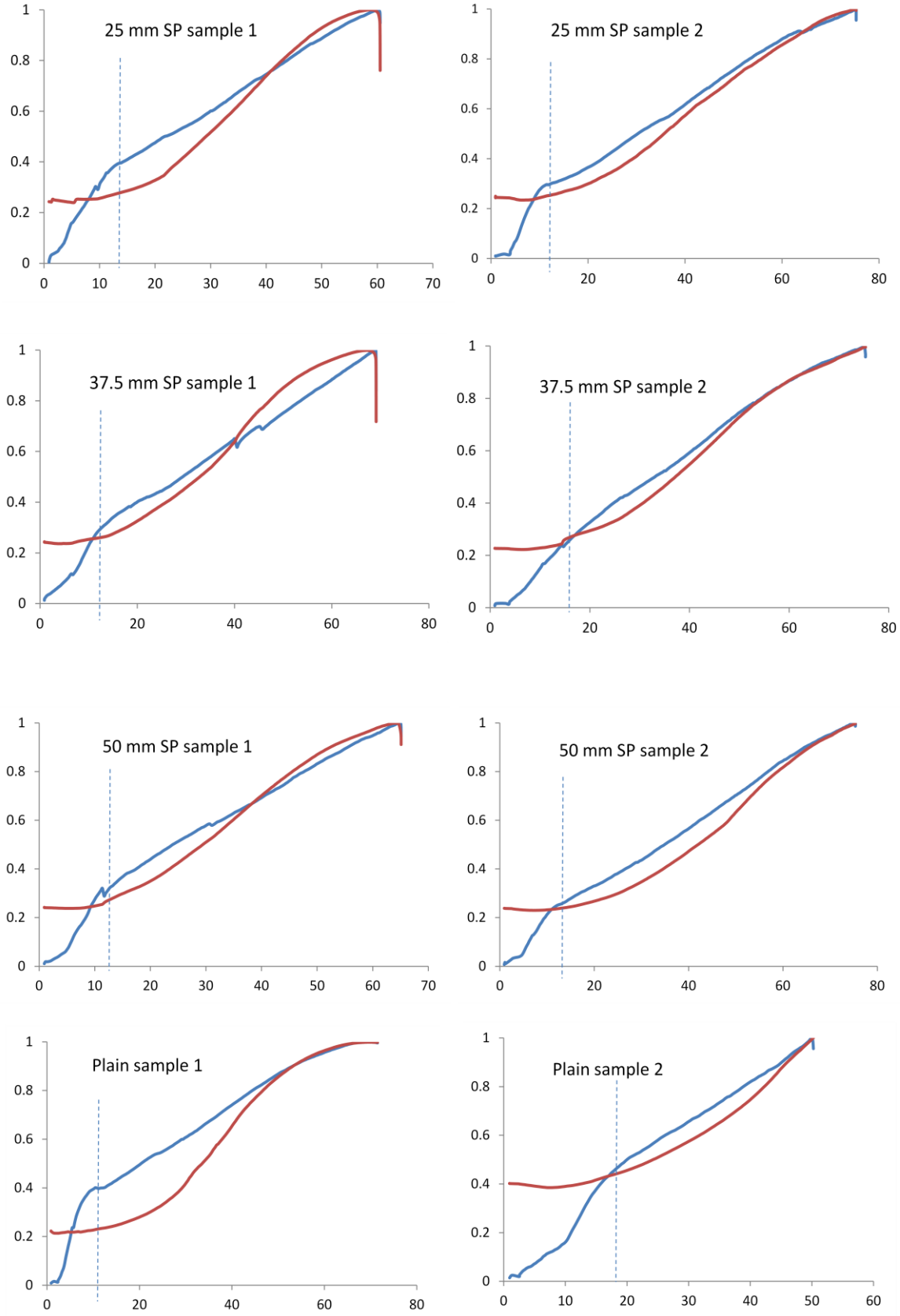

Figure 4.37 Normalised shear load and axial load (respect to their ultimate values) and shear displacement (mm) curves for 25, 37.5, 50mm rib spacing and plain bolts.

Table 4.9 Axial load and its percentage increment at upper elastic limit

Profile spacing (mm)	Displacement at Point P (mm)	Axial load at point Q (kN)	Initial axial load (kN)	Axial load increment (%)
12.5	7.086	50.19	47.05	6.7
25	12.69	54.17	48.20	12.4
	10.63	52.53	49.91	5.2
37.5	11.05	54.44	49.89	9.1
	13.96	53.72	49.38	8.8
50	11.06	51.20	48.11	6.4
	11.81	49.75	48.57	2.4
Plain	9.34	51.48	48.88	5.3
	---	---	---	---
Ave=	11.0	52.2	48.7	7.0

It should be noticed that the second sample of plain bolt did not follow the profile pattern shown in Figure 4.29. Point P on the curve is non-identifiable. Thus its result was ignored.

It can be seen that the increment of axial load is from 2.4% to 12.4% of pretension load with an average value of 7%. This range indicates the commencement of developing of axial load. Therefore, it can be supposed that the ending of the initial linear stage on the shear load-displacement curve (P) is most likely caused by the axial load exceeding pretension load. Accordingly, two conclusions can be drawn:

i. The end conditions (plate, no plate or pretension) of sheared joint would be the major factor of changing shear stiffness.
ii. The yield point (P) is likely to occur at an increased shear load with an increased pre-tension load.

Figure 4.38 shows result of double shear tests under different pretension loading conducted by Jalalifar (2006).

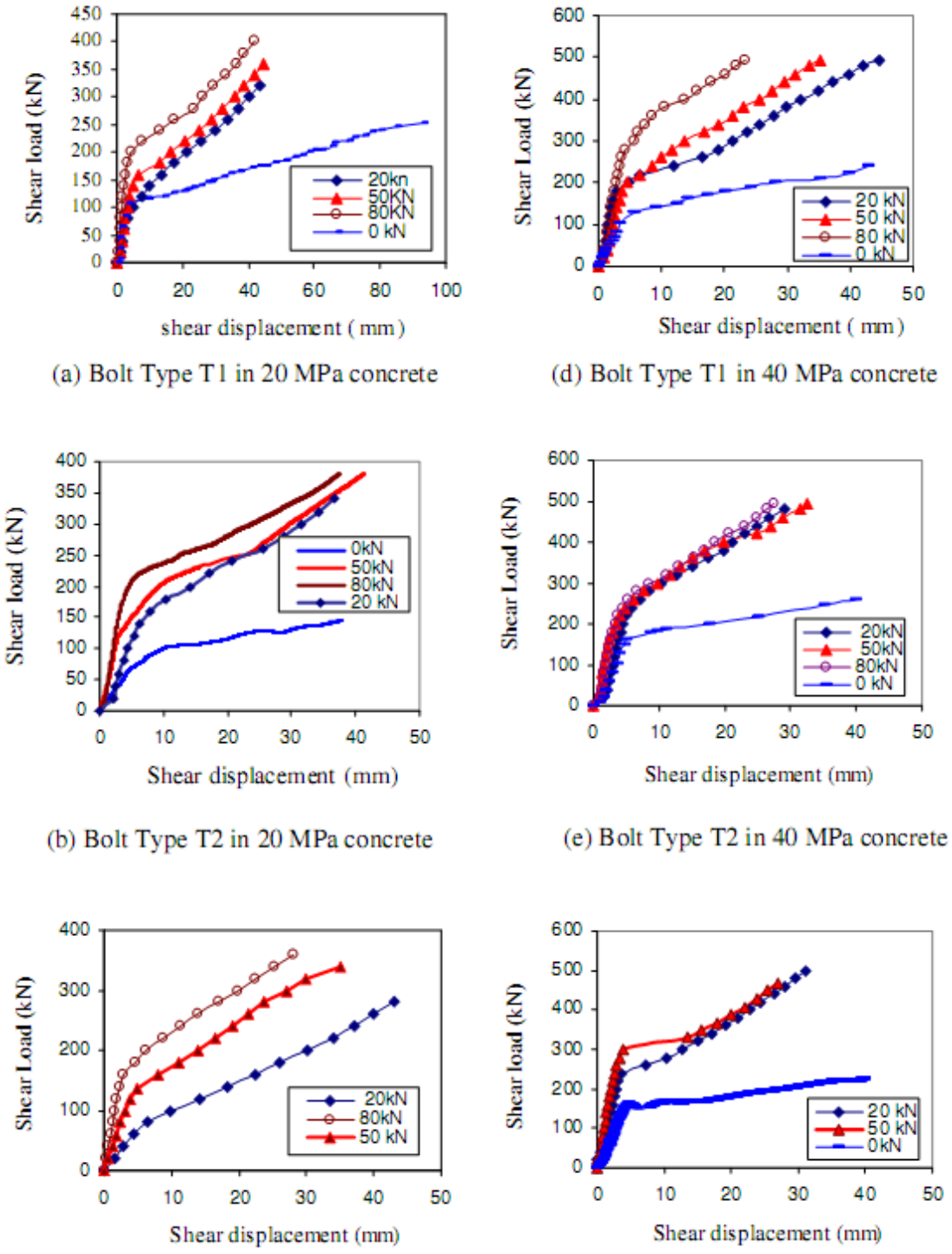

Figure 4.38 Double shear test results under different pretension (Jalalifar, 2006)

Nevertheless, a bolt under tension compresses the rock, which prevents bed separation and frictional forces developing between the layers, but this does not mean that more tension creates better stability (Peng and Guo, 1992). When a bolt is pre-tensioned it would influence the shear strength of the joint with forces acting both perpendicular

and parallel to the sheared joint.

(3) Failure modes

Identification of failure mode is one of the major aims of this test. Following each double shear test, the concrete blocks of each tested unit were broken and failure modes were observed. Figure 4.39 shows the joint surface after test. It is clear that tensile failure of the bolt is the major cause of the test. Radial fractures in the concrete block were developed. And the concrete powder was evidence of the development of shear dilation at the joint.

Figure 4.40 shows the front view of the sheared block. The compressive failure of the concrete around the sheared joint is clearly evident. The radial cracks were cone shaped. In the axial direction, the deformation can be roughly divided into three segments. In the section *L1* (≈150mm), the bolt displacement in sheared direction was negligible, hence only axial load was developed. *L2* (≈90mm) was a transition zone which indicated the developing of bending moment on the bolt. In the segment *L3* (≈60mm), the developed bending moment and axial load were the main factors affecting the joint performance.

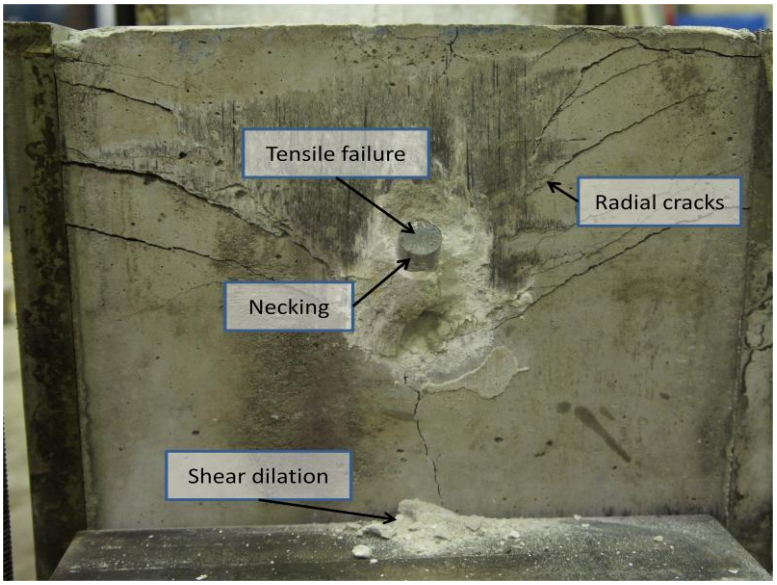

Figure 4.39 Failure modes at the joint

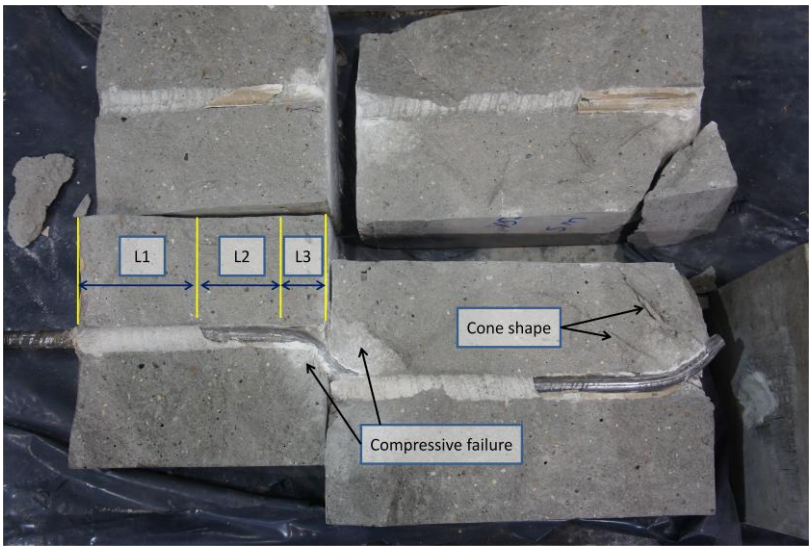

Figure 4.40 Front view of the sheared joint after test.

The deformation of the resin annulus is shown in Figure 4.41. In the transitional zone, dilational slip of the resin/bolt interface could be identified, supported by the resin powder lodged in front of the bolt ribs. The axial displacement decayed towards the fixed end (pretension), as the length of sheared resin becames smaller. At the fixed end, there was about 1mm axial displacement which can be considered as a system error of the test.

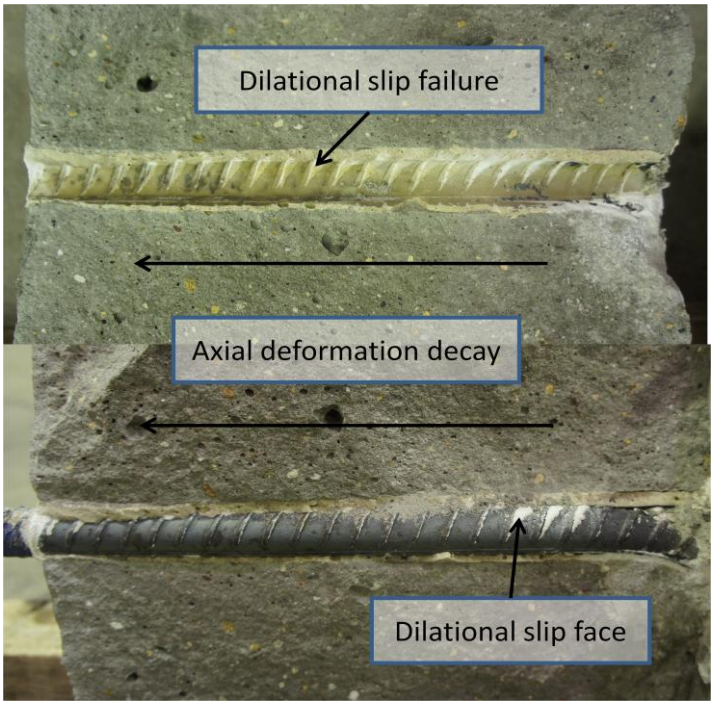

Figure 4.41 Deformation of the resin annulus in double shear test

4.5 CONSTANT NORMAL STIFFNESS (CNS) TESTS

The CNS shear apparatus built at the University of Wollongong consists of two steel boxes, one of size 250x75x150mm at the top, and another of size 250x75x100mm at the bottom. A series of springs were used to simulate the normal stiffness (k_n) of the surrounding rock mass: $k_n = dN/du_r$, where dN and du_r are the changes in normal load and radial displacement respectively. Therefore, the units of k_n are given in kN/mm. As shown in Figure 4.42, the top box can only move in the vertical direction along which the stiffness is constant. The bottom box is fixed on a grid base through bearings and can move only in the shear (horizontal) direction. The desired initial normal stress (σ_{n0}) is applied by a hydraulic jack, where the applied load is measured by a calibrated load cell. The maximum normal load capacity of the apparatus is 180kN. The shear load is applied to a strain-controlled unit. The applied shear load can be recorded via strain meters. The apparatus has a maximum shear load capacity of 120kN, and the rate of horizontal displacement can be varied between 0.35 and 1.70 mm/min. The dilation and the shear displacement of the joint are recorded by LVDTs mounted on the top of the specimen and in the horizontal (shear) direction, respectively.

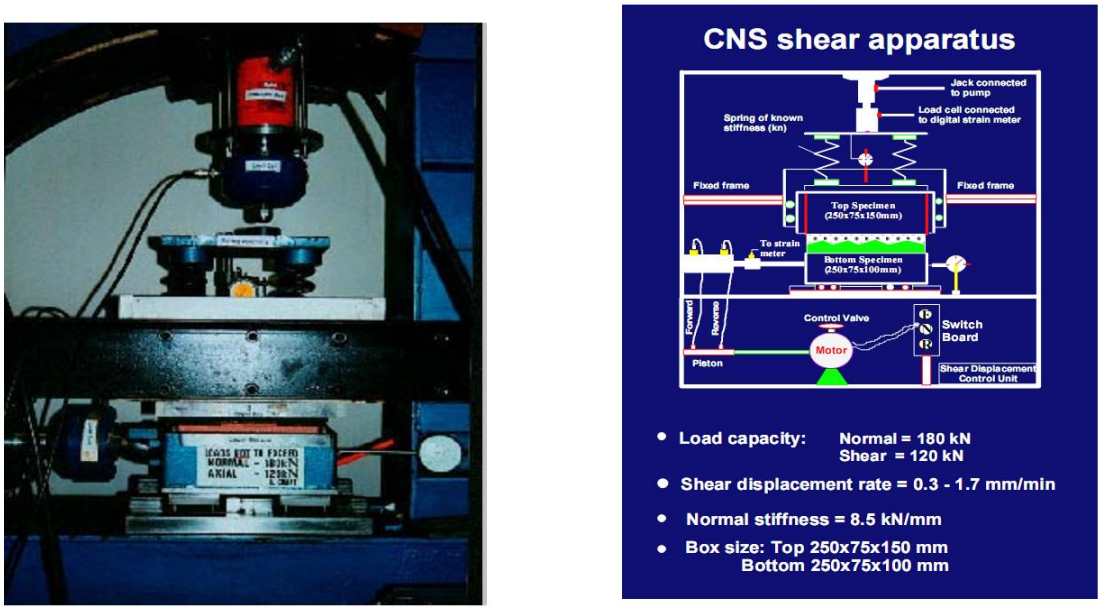

Figure 4.42 CNS apparatus

A 125mm length of a steel plate representing a round bolt opened onto a flat plane was used for CNS shear testing. The image in Figure 4.43 shows the bolt of 22.2mm in diameter opened onto a flat surface. The bolt profiles (ribs) have 25mm spacing with 1.2mm rib height, 4mm rib width and 90° rib face angle. The flattened surface of the bolt was then welded on the bottom plate of the direct shear testing.

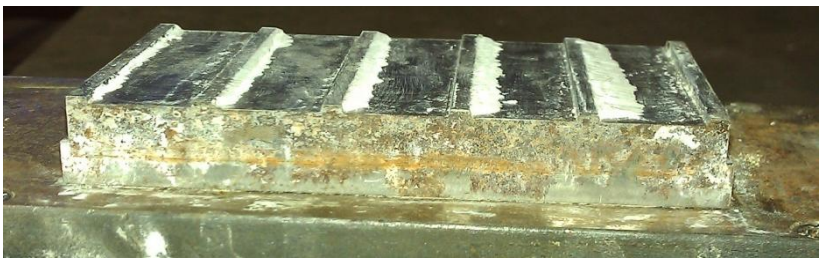

Figure 4.43 Steel plate representing bolt profile in CNS tests

The welded bolt surface on the bottom plate of the top shear box was used to print the image of the bolt surface onto the plaster and resin as shown in Figure 4.44. Two kinds of samples were cast and tested. The strong gypsum plaster ($CaSO_4.H_2O$ hemihydrates 98%) was used for the first two samples. The initial setting time of plaster was about 25 min when it was mixed with water, and its long term strength is independent of time once the chemical hydration is complete. The basic properties of the plaster material were determined as UCS 20MPa, tensile strength 6MPa and Young's modulus of 7.3 GPa. The samples three and four were cast in resin and the remainder cast in high strength casting plaster. The properties of the hardened resin after two weeks were: UCS = 68MPa, tensile strength=13.5MPa, and Young's modulus= 10.5GPa.

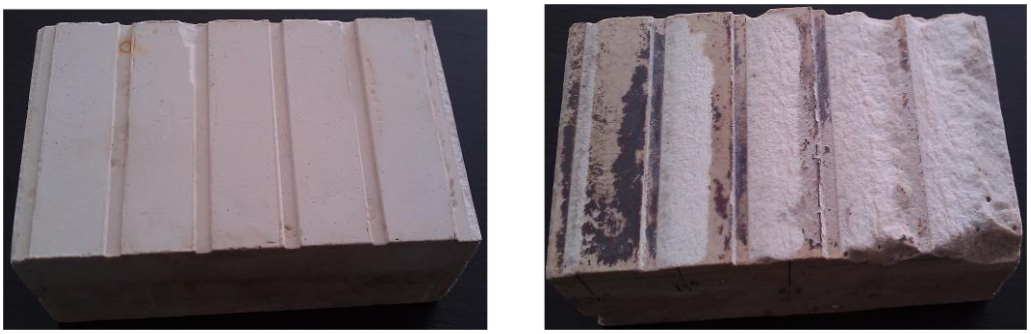

Figure 4.44 Sample specimen with the imprint of the bolt profile before and after test

The nominated vertical stiffness of the apparatus was 8.5 kN/mm, the measured value averaged 8.65 kN/mm with S.D.±0.3 kN/mm, as shown in Figure 4.45.

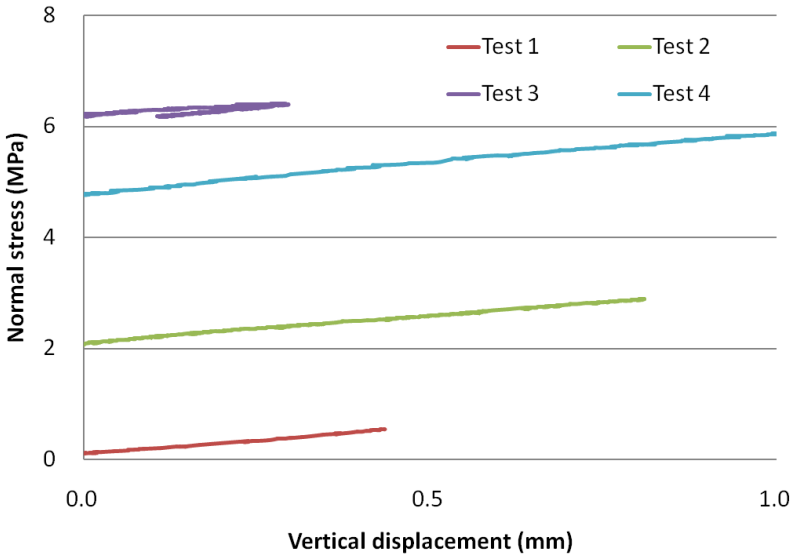

Figure 4.45 Radial stiffness in the tests

Figure 4.46 shows the shear stress profiles of the bolt-grout interface for selected normal stress conditions. Figure 4.47 shows the variation of dilation with shear displacement at various normal stresses. Figure 4.48 illustrated the shear load and normal load of each test.

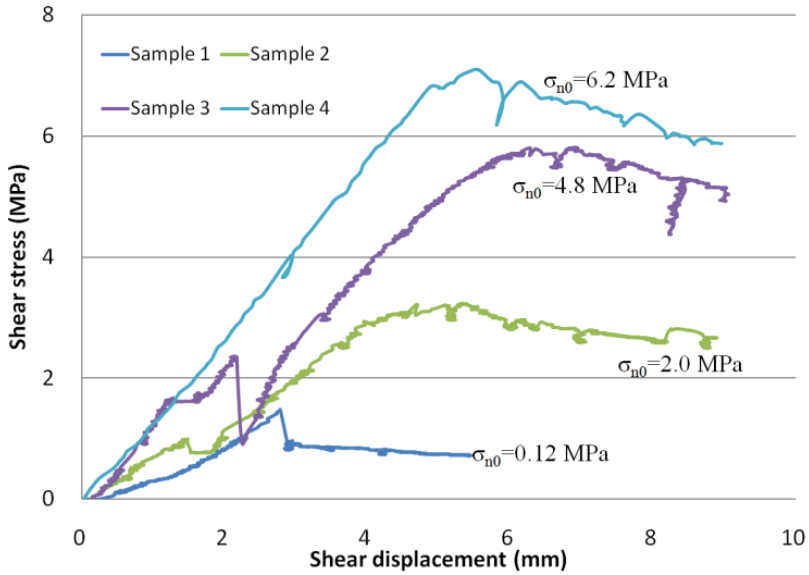

Figure 4.46 Shear stress profiles of the bolt-grout interface for different normal stress conditions

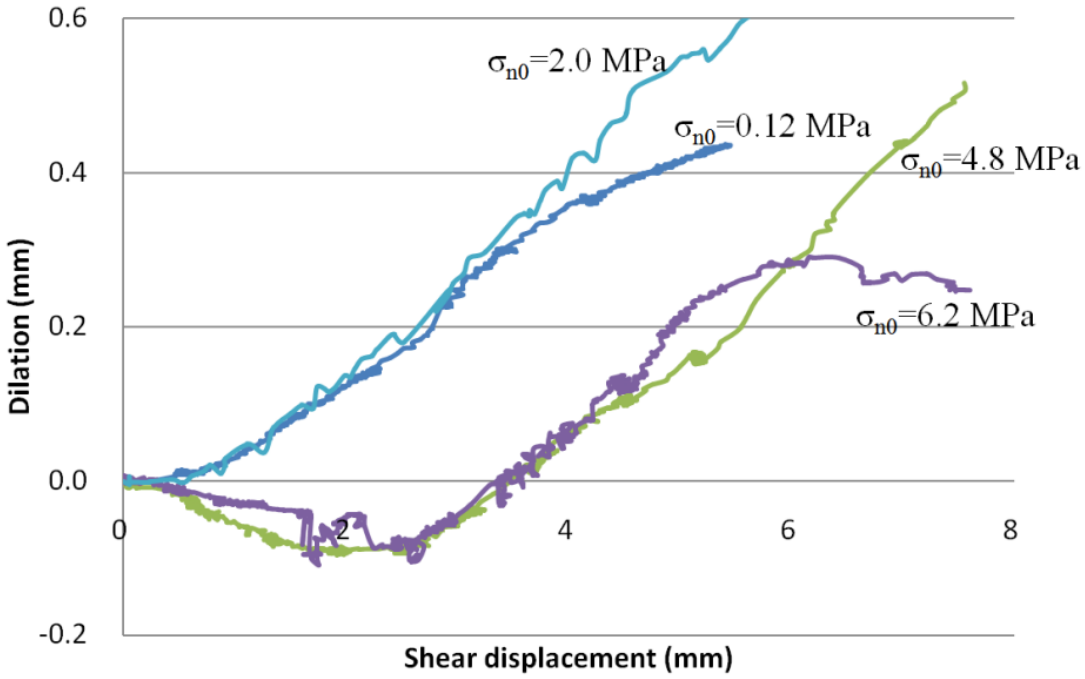

Figure 4.47 Dilational behaviour at various normal stresses

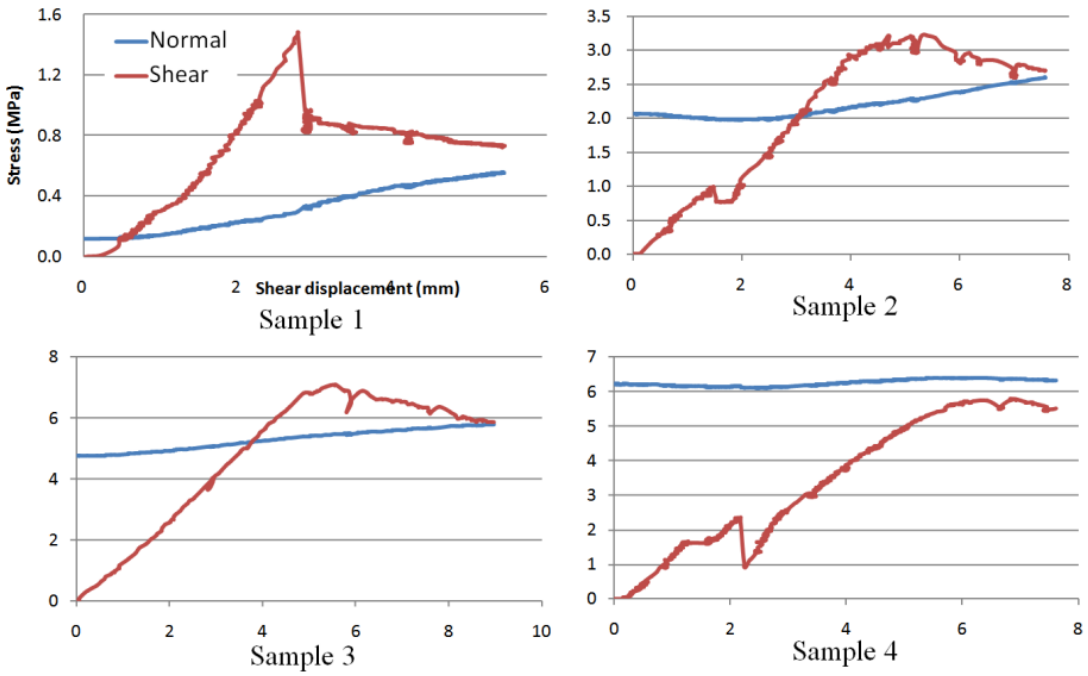

Figure 4.48 Shear load and developed normal load of each test

Investigation of failure modes was one of major aims of the tests. Figure 4.49 shows a typical failure procedure in the tests and Figure 4.50 shows samples after testing. It was found that the failure modes are different for different profiles even in one test. Parallel shear failure and dilational slip could be identified as a major factor of the

deformation. The radial cracks were not persistent, which can be attributed to the boundary effect rather than failure mode.

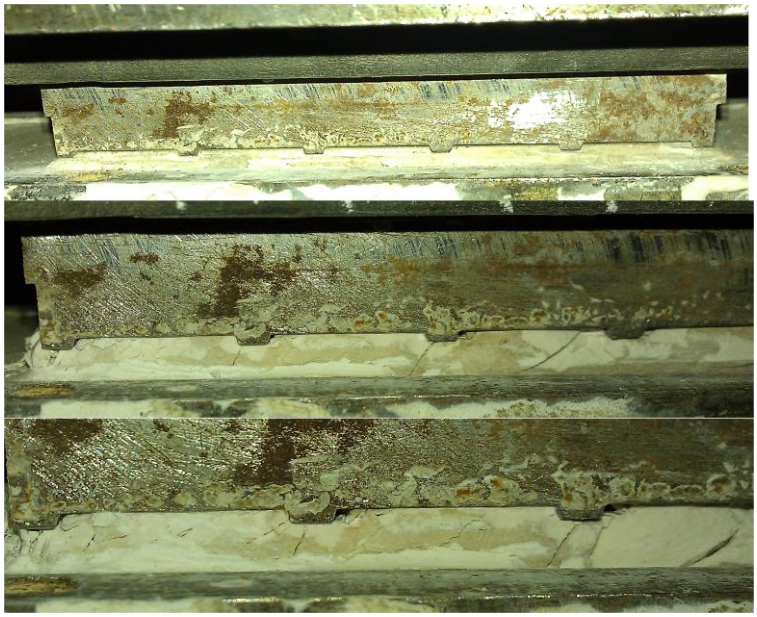

Figure 4.49 Failure procedure in CNS test

Figure 4.50 Sample after testing

4.6 SUMMARY

Form laboratory studies, it can be concluded that:

- Resin mechanical properties play an important role in load transfer of the rockbolting mechanism, especially when subjected to axial loading.
- There are two ways to describe the residual strength of the resin. If the confinement is low, the cohesional strength will diminish immediately after failure and dilational slip described by equation (4.4.2) dominates the post failure performance. If the confinement is sufficient large, the dilation will be ceased in an infinite displacement and the failure material will recover its cohesion.
- In the short encapsulated push test, the failure mode can be identified as parallel shear failure. This result is consistent whenever 8mm steel sleeve is used as the confining material.
- In pullout tests using a 300mm concrete block, dilational slip is observed to be the dominated failure mode.
- In pull tests it was observed that plastic deformation occurred at the bolt profile and resin annulus contact even in the linear stage of the bond performance. It was concluded that the initial stage of the bond performance is proportional but not elastic.
- The end point of the linear stage when rockbolting is subjected to axial loading is related to commencement of displacement of the unloaded end of the bolt.
- From the double shear test, it can be concluded that the bolt rib profile affects the shear behaviour of rockbolting.
- There is no conclusion on how different rib profiles generate different reactions at the joint surface. However, the rib profile will at least affect the rockbolting shear performance via axial load transfer.
- Another finding from the double shear tests is that the end of the linear stage (point P in Figure 4.29) is associated with the development of axial load at the end

plate.

- In CNS testing, shear failure of grouting materials and dilational slip of failure surfaces were observed. It confirmed that the rockbolting failure was a combination of these failure modes.

CHAPTER FIVE

FAILURE MODES ANALYSIS AND LOAD PREDICTION IN BOLT PULL OUT TESTS

FAILURE MODES ANALYSIS AND LOAD PREDICTION IN BOLT PULLOUT TESTS

5.1 INTRODUCTION

Steel bolts are an essential part of roadway support in coal mining roadways. The effectiveness of bolt reinforcement are a very well known subject however, little has been done in optimising the bolt profile that directly contributes to the load transfer between the bolt and the surrounding resin. To improve bolt load transfer through the steel rebar design, it is essential to understand the details of the influence of bolt profile. Analytical study done in this chapter provides the tools that enable a better understanding of the rebar profile role in increasing the shear resistance during the working life of bolts.

In traditional rockbolting mechanism analysis, the effect of mechanical interlocking is often integrated into the analytical models in various ways but do not concern the rib geometry. For example, Li and Stillborg (1999) developed an ISS model for predicting the behaviour of rock bolts in pullout tests, in uniformly deformed rock mass, when subjected to opened joints. The effect of mechanical interlock is included into the shear load displacement behaviour of the bolt-resin interface. More recently, a tri-linear bond-slip model with residual strength at the interface has been adopted and closed-form solutions were obtained for the prediction of full range behaviour of fully grouted rock bolts under axial load, Ren, *et al* (2009) and Martin (2011). In these cases, the deformation of surrounding materials is lumped into a zero thickness interface, which is assigned with specific stress-strain behaviour to simulate the mechanical interlocking observed in pullout tests. These are the most advanced achievements so far in rockbolting mechanisms when a single bolt is subjected to axial loading. However, they described the effect of the interaction between bolt, grout and rock

under axial loading but the profile configuration of a bolt and its influence on the bolting performance are ignored. The weakness of those approaches includes:

- All of them are not a cause-effect based approach;
- All of them must be calibrated by pullout tests for each application;
- Key parameter is not consistent in some models;
- Key point on the pullout curve are hard to identify in some models;
- They are rarely useful to achieve optimum bolt profile design;
- They are rarely useful to achieve optimum resin design

Moreover, they did not formulate the real interaction between the bolt and surrounding materials. For example, in ISS model the ribbed bar is conceptualised as a strength smooth bar. Figure 5.1 shows a computer simulation of the interfacial shear stress along a smooth bar and along a ribbed bar when both subjected to a same axial load within elastic range. The rib geometry of the rebar is the same for T2 bolt and its interface is defined as the cylinder just passing the rib tips.

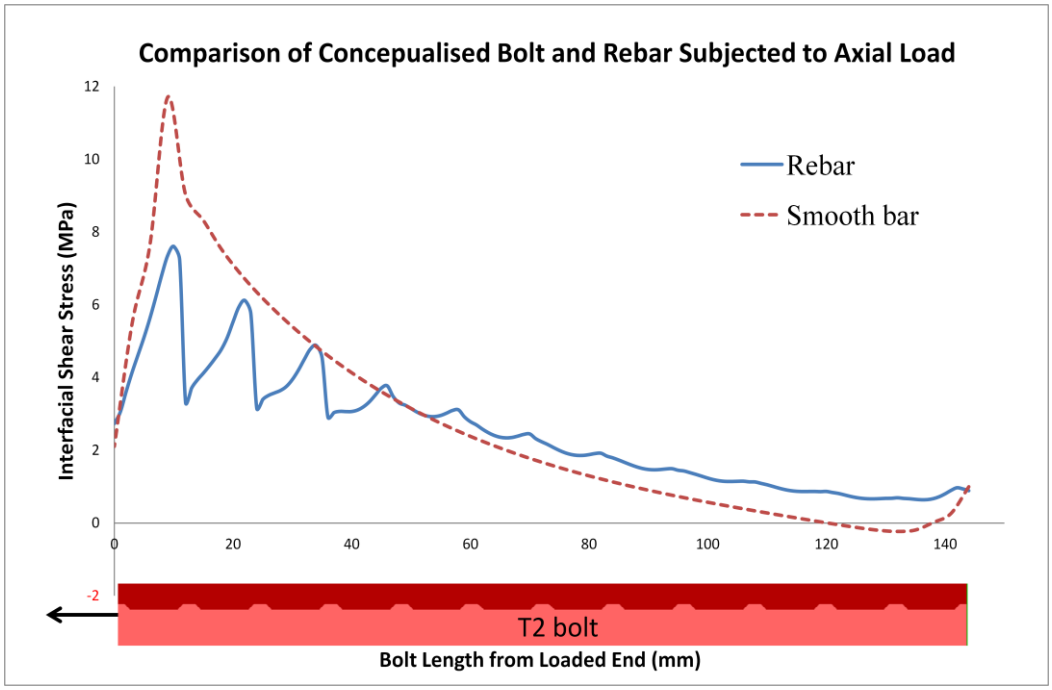

Figure 5.1 FLAC axisymmetric model to compare the shear stress distribution for a rebar and a smooth bar.

Investigations of load transfer between the bolt and resin indicates that the bolt profile shape and spacing plays an important role in improving the shear strength between the bolt and the surrounding mediums, Goto (1971), Tepfers (1973), Fabjanczyk and Tarrant (1992, 1998), Blumel (1996, 1997), Gray *et al* (1998), Ito *et al* (2001), Aziz and Dey (2002), Kilic *et al* (2002 a), Aziz and Webb (2003), Moosavi *et al* (2005), Aziz and Jalalifar (2005), Jalalifar (2006), Aziz *et al* (2006), Aziz *et al* (2008). The SEPT results indicate significant variations in load transfer with different bolt rib profile spacing. Other variables such as profile rib angle, and its shape and size are also important parameters contributing to the load transfer capacity of rock bolt system.

Empirical studies can match the graphs of physical tests however these methods cannot describe the exact reasoning why such behaviour occurs. The laboratory testing has its challenges as manufacturing of minute differences in bolt profile in the workshop is difficult. In addition, the whole procedure of rockbolting failure is difficult to observe. Therefore, a mathematical description of the bolt profile and its behaviour during the bolt pullout tests is desired to provide better understanding of the physical process that influence the shear strength of the loaded bolt.

The load transfer capacity of the bolt is governed by the shear strength developed between the rock/grout and the grout/bolt interfaces. Grout/rock interface failure can rarely occur in laboratory pullout tests and in practice due to the rifling effect during hole drilling. As a result the bonding strength at the grout/bolt interface dominates the effect on rockbolting, Aziz *et al* (2006, 2008). Bond may be defined as the gripping effect of the grouting annulus on the embedded steel bar (smooth, threaded or ribbed) to resist forces tending to slide the bar longitudinally. The properties of the steel bar as well as the grout material (for the annulus, compressive strength and confinement and for the bar, smoothness and the shape of indentations) play important roles in developing high or low values of bond capacity.

It is commonly accepted that the bonding strength has three components: cohesion,

friction and interlock. The mechanical interlock component plays an important role in bonding capacity and load transfer in the rockbolting system. In fact it is created by the bolt rib profile configuration. Moreover, the frictional component is also affected by the rib configuration because the radial pressure is mainly generated by the axial displacement of the bolt ribs.

It is important to distinguish between the two types of dilational slipping: volumetric dilation and roughness caused dilation. Traditionally, dilation means volume increase, such as powder will be generated when material is breaking or shear slipping of two surfaces (Figure 5.2 a and b). In this case, it is often theoretically described by adding a small angle (usually 10° in numerical simulation) to the internal frictional angle of the material or the discontinuity. In the other case, dilation may be generated by the surface roughness (Figure 5.2 c and d). Consequently, the slope angle will be the dilational angle. In bond slip problems of rockbolting, two kinds of dilation occur simultaneously. Dilation generated by the bolt rib geometry is the roughness caused dilation; and its apparent dilational angle is the bolt rib face angle. The dilation caused by increasing volume is neglected in this thesis.

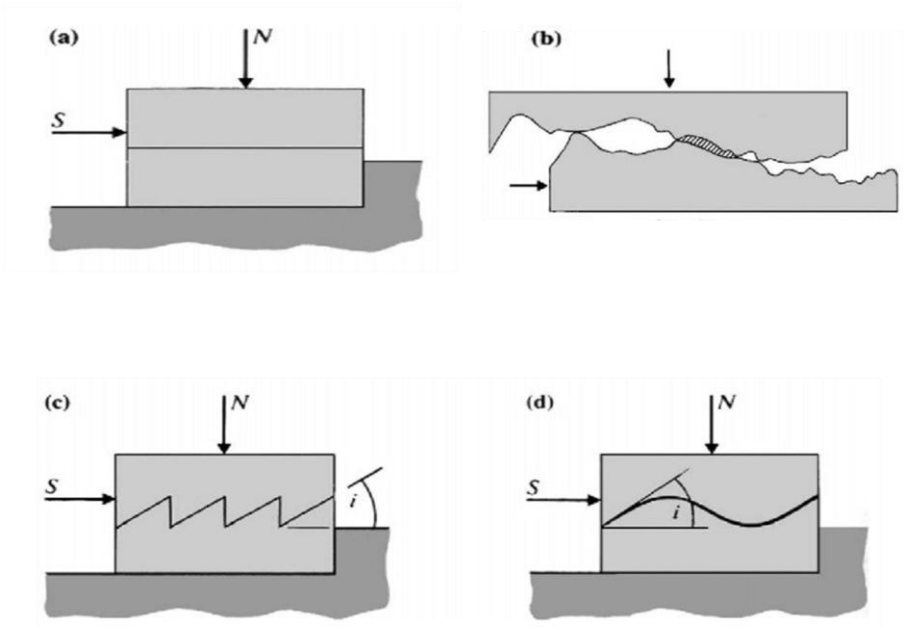

Figure 5.2 Dilations caused by (a) (b) Material volume increases after breaking or slipping; (c) (d) Surface roughness (Brady and Brown, 2005).

How the bolt profile interacts with the grout material under axial loading is the focus of this chapter. It is a structurally based approach to reasoning the performances of the rock bolt when pull tested. Another aim of the theoretical predictions is to provide an understanding of the initial grout failure and to offer a new tool for research into the best profile geometries to reach optimum shear strength between the bolt and the surrounding medium.

In this chapter, the thick walled cylinder theory is presented firstly as it is employed in the later analytical approach, followed by a summary of various failure criteria. After the literature review of research work which concerned with bolt profile, an analytical approach is conducted based on the failure modes study. The concepts of "parallel shear failure" and "dilational slip failure" are introduced and identified. Based on Mohr-Coulomb's failure criterion, the governing equations for several failure modes have been formulated. Then, application examples of optimum bolt design are offered. Finally, the performance of T2 bolts in SEPT is predicted and compared with experimental data.

5.2 THICK WALLED CYLINDER THEORY

5.2.1 Lame's equations

In rock bolting problems, the thick-walled cylinder theory is frequently employed by researchers, for example Tepfers (1973), Farmer (1975), Yazici and Kaiser (1992), Hyett *et al* (1995). Due to the nature of rock bolting, the grout annulus can be considered as a thick-walled cylinder surrounding the steel bolt. In addition, the behaviour of the confining tube in laboratory pullout tests can be also predicted using thick-walled cylinder theory. In the field, steel bolts are surrounded by rock with infinite radius; the elongation of the bore hole can be estimated via transforming the

infinite medium to an equivalent thick-walled cylinder, Yazici and Kaiser (1992), Hyett *et al* (1995). If the ribs of the bolt have a periodic formation along the bolt axis, then the rock bolting system can be treated as a two dimensional problem.

A thick-walled cylinder is an axisymmetric problem; neglecting body force gives the following equilibrium equation (Seed, 2000, Chapter 11):

$$\frac{\partial \sigma_{rr}}{\partial r} = \frac{\sigma_{\theta\theta} - \sigma_{rr}}{r} \qquad (5.1.1)$$

As the strain in *z* direction is independent of *r*, the following compatibility equation can be constructed:

$$\frac{d}{dr}(\sigma_{rr} + \sigma_{\theta\theta}) = 0 \qquad (5.1.2)$$

Various forms of boundary conditions can be prescribed. For example, if the resin annulus is considered as a thick-walled cylinder which undergoes internal and external pressures, as shown in Figure 5.3, the standard solution, known as Lame's equations, can be obtained:

$$\sigma_{rr} = \frac{a^2 p_1 - b^2 p_2}{b^2 - a^2} - \frac{a^2 b^2 (p_1 - p_2)}{b^2 - a^2}\frac{1}{r^2} \qquad (5.2.1)$$

$$\sigma_{\theta\theta} = \frac{a^2 p_1 - b^2 p_2}{b^2 - a^2} + \frac{a^2 b^2 (p_1 - p_2)}{b^2 - a^2}\frac{1}{r^2} \qquad (5.2.2)$$

The circumference stress is in tension. The maximum tension will occur at the outer wall and its magnitude can be found as

$$\sigma_{tension(\max)} = \sigma_{\theta\theta}(b) = \frac{2a^2 p_1 - (a^2 + b^2) p_2}{b^2 - a^2} \qquad (5.3)$$

If the cylinder material is taken to be isotropic and linearly elastic, then:

$$\varepsilon_{rr} = \frac{du_r}{dr} = \frac{1}{E}[\sigma_{rr} - v(\sigma_{\theta\theta} + \sigma_{zz})] \qquad (5.4.1)$$

$$\varepsilon_{\theta\theta} = \frac{1}{E}[\sigma_{\theta\theta} - v(\sigma_{rr} + \sigma_{zz})] \qquad (5.4.2)$$

$$\varepsilon_{zz} = \frac{1}{E}[\sigma_{zz} - v(\sigma_{\theta\theta} + \sigma_{rr})] \qquad (5.4.3)$$

Accordingly, the radial displacement is expressed as:

$$u_r = \frac{r}{E(b^2 - a^2)}\left[(1-2v)(p_1a^2 - p_2b^2) + \frac{(1+v)a^2b^2}{r^2}(p_1 - p_2)\right] \qquad (5.5.1)$$

For open cylinder $(\sigma_{zz} = 0)$, the radial displacement is

$$u_r = \frac{r}{E(b^2 - a^2)}\left[(1-v)(p_1a^2 - p_2b^2) + \frac{(1+v)a^2b^2}{r^2}(p_1 - p_2)\right] \qquad (5.5.2)$$

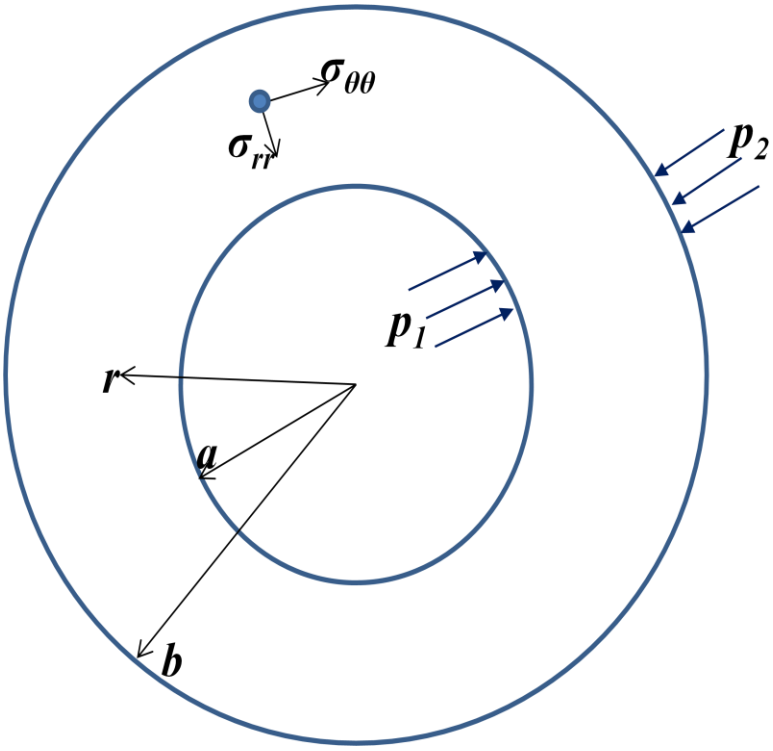

Figure 5.3 A thick-walled cylindrical vessel of inner radius *r* and outer radius *R* subject to internal and external pressure p_1 and p_2 respectively.

Equation (5.5.1) was used by Tepfers (1973). However, Yazici and Kaiser (1992) and Hyett *et al* (1995) used the following equation:

$$u_r = \frac{(1+v)(1-2v)}{E} \cdot \frac{p_1a^2 - p_2b^2}{b^2 - a^2} \cdot r + \frac{1+v}{E} \cdot \frac{(p_1 - p_2)a^2b^2}{b^2 - a^2} \cdot \frac{1}{r} \qquad (5.5.3)$$

Equation (5.5.3) is different from equation (5.5.1) or (5.5.2). Nevertheless, the open cylinder case, *i.e.* equation (5.5.2), is used in this thesis.

If the thick-walled cylinder is not confined, *i.e.* p_2=0, the displacement at the inner wall is:

$$u_{r=a} = \frac{a[(1-v)a^2 + (1+v)b^2]}{E(b^2 - a^2)}\, p_1 \qquad (5.6.1)$$

For $b \to \infty$, the radial displacement becomes:

$$\lim_{b\to\infty} u_r = \frac{a(1+v)}{E}\, p \qquad (5.6.2)$$

Equation (5.6.2) describes the radial displacement, induced by an internal pressure *p* in a circular hole of radius *r*, in an infinite medium.

5.2.2 Applications of single cylinder

In the laboratory SEPT and double shear tests as presented in Chapter 4, where:

- inner radius of the resin annulus *a* = 11.1mm
- outer radius of the resin annulus *b*=15.3mm
- mechanical properties of the resin v_g=0.26 and E_g=10500MPa

Then, according to equation (5.6.1), the radial displacement of the unconfined resin annulus is:

$$u_{r=a} = \frac{a[(1-v)a^2 + (1+v)b^2]}{E(b^2 - a^2)}\, p = 0.00368p \text{ (mm)}$$

In which the inner pressure *p* is in MPa. This represents the maximum radial displacement of the resin annulus in the elastic stage.

The concrete block used in pullout tests and double shear tests has block dimensions

300 x 300 x 300mm. It can be thought of as a cylinder with:

- inner radius a=15.3mm,
- outer radius *b*=150mm,
- concrete properties *v*=0.2 and *E*=27500 MPa,

Then the relationship of radial displacement with the confining pressure for the concrete block will be:

$$u_{r=a} = \frac{a[(1-v)a^2 + (1+v)b^2]}{E(b^2 - a^2)}\, p = 0.000679p \text{ (mm)}$$

If the concrete block is infinite, the property parameters can be placed into equation (5.6.2):

$$u_r = \frac{a(1+v)}{E} p \ = \frac{15.3(1+0.2)}{27500} p = 0.000667p \text{ (mm)}$$

The difference between the 300mm block and infinite rock mass is less than 2%, indicating that in the elastic stage, a 300mm concrete block is sufficient to represent an infinite medium.

In the laboratory push testing of T2 bolt (Chapter 4), the steel sleeve has

- inner radius a=15.3mm,
- outer radius *b*=24mm
- steel sleeve properties v_s=0.3 and E_s=200000MPa,

Then the radial displacement at the bolt-resin interface in the elastic stage is

$$u_{r=a} = \frac{a[(1-v)a^2 + (1+v)b^2]}{E(b^2 - a^2)}\, p = 0.000204\, p \text{ (mm)}$$

The radial stiffness of the steel sleeve is about 3.3 times more than the concrete block used in double shear tests.

5.2.3 Compound cylinders

In the laboratory SEPT, steel sleeve is frequently used as the confining tube. This system can be considered as compound thick-walled cylinders shown in Figure 5.4.

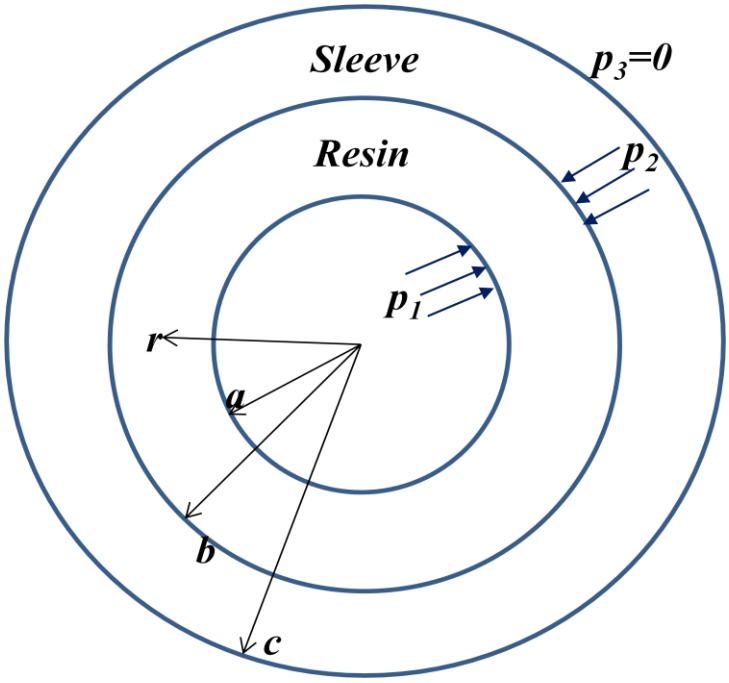

Figure 5.4 Compound cylinders.

For the resin annulus, the displacement at the contact between the resin and sleeve is calculated using $r=b$ in equation (5.5.2):

$$u_{r1}(b) = \frac{b}{E_g(b^2 - a^2)}\left[\left(1 - v_g\right)(p_1 a^2 - p_2 b^2) + \left(1 + v_g\right)a^2(p_1 - p_2)\right]$$

For the outer confinement cylinder, the outer pressure $p_3=0$. Using equation (5.6.1) the inner wall displacement of the confining cylinder will be:

$$u_{r2}(b) = \frac{b}{E_s(c^2 - b^2)}[(1 - v_s)p_2 b^2 + (1 + v_s)c^2 p_2]$$

The displacement at the contact will be the same value, therefore

$$u_{r1}(b) = u_{r2}(b)$$

Solving for p_2,

$$p_2 = \frac{2a^2}{\frac{E_g(b^2-a^2)}{E_s(c^2-b^2)}[(1-v_s)b^2+(1+v_s)c^2]+(1-v_g)b^2+(1+v_g)a^2}p_1 \quad (5.7)$$

The radial displacement at the inner wall of the smaller cylinders can be found by using $r=a$ in equation (5.5.2),

$$u_r(a) = \frac{a}{E_g(b^2-a^2)}\left[(1-v_g)(p_1a^2-p_2b^2)+(1+v_g)b^2(p_1-p_2)\right] \quad (5.8)$$

Where p_2 is the value calculated via equation (5.7)

In the SEPT of T2 bolt, the following is known:

- the inner radius of the resin annulus a = 11.1mm
- outer radius of the resin annulus b=15.3mm
- outer radius of the steel sleeve c=24mm
- mechanical properties of the resin v_g=0.26 and E_g=10500MPa
- and steel sleeve properties v_s=0.3 and E_s=200000MPa

Then the pressure at the contact can be found by equation (5.7):

$$p_2 = \frac{2a^2}{\frac{E_g(b^2-a^2)}{E_s(c^2-b^2)}[(1-v_s)b^2+(1+v_s)c^2]+(1-v_g)b^2+(1+v_g)a^2}p_1$$

$$= \frac{2\times 11.1^2}{\frac{10.5\times 110.9}{200\times 341.9}[0.7\times 15.3^2+1.3\times 24^2]+0.74\times 15.3^2+1.26\times 11.1^2}p_1$$

$$= 0.776p_1$$

Then the radial dilation can be calculated using equation (5.8):

$$u_r(a) = \frac{a}{E_g(b^2-a^2)}\left[(1-v_g)(p_1a^2-p_2b^2)+(1+v_g)b^2(p_1-p_2)\right]$$

$$= \frac{11.1}{10500 \times 110.9}[0.75(11.1^2 p_1 - p_2 \times 15.3^2) + 1.25 \times 15.3^2(p_1 - p_2)]$$

$$= 9.5 \times 10^{-6}[385p_1 - 468.2p_2] \qquad (where\ p_2 = 0.776p_1)$$

$$= 0.000207p_1(\text{mm})$$

The value indicates that the radial displacement or dilation during the elastic stage is very small.

For the pullout tests using concrete blocks, the parameters of the compound cylinders are a=11.1mm, b=15.3mm, c=150mm, v_c=0.2, v_g=0.26, E_c=27500MPa, E_g=10500MPa. Then:

$$p_2 = \frac{2a^2}{\frac{E_g(b^2 - a^2)}{E_c(c^2 - b^2)}[(1 - v_c)b^2 + (1 + v_c)c^2] + (1 - v_g)b^2 + (1 + v_g)a^2} p_1$$

$$= \frac{2 \times 11.1^2}{\frac{10.5 \times 110.88}{27.5 \times 22266}[0.8 \times 15.3^2 + 1.2 \times 150^2] + 0.74 \times 15.3^2 + 1.26 \times 11.1^2} p_1$$

$$= 0.648p_1$$

Then

$$u_r(a) = \frac{a}{E_g(b^2 - a^2)}\left[(1 - v_g)(p_1 a^2 - p_2 b^2) + (1 + v_g)b^2(p_1 - p_2)\right]$$

$$= \frac{11.1}{10500 \times 110.88}[0.74(11.1^2 p_1 - p_2 \times 15.3^2) + 1.26 \times 15.3^2(p_1 - p_2)]$$

$$= 0.000009534[386.13p_1 - 468.18p_2] \quad \ldots\ldots (substituting\ p_2 = 0.648p_1)$$

$$= 0.000789p_1\ (\text{mm})$$

The circumference of the resin annulus is in tension, and the maximum tensile stress of the resin annulus can be found using equation (5.3):

$$\sigma_{resin-tension(\max)} = \frac{2a^2p_1 - (a^2 + b^2)p_2}{b^2 - a^2}$$

$$= \frac{2 \times 11.1^2 p_1 - (11.1^2 + 15.3^2) \times 0.648 p_1}{110.88}$$

$$= 0.1343 p_1$$

For the concrete block:

$$\sigma_{concrete-tension(\max)} = \frac{2b^2p_2 - (c^2 + b^2)p_3}{c^2 - b^2}$$

$$= \frac{2 \times 15.3^2 p_2 - 0}{150^2 - 15.3^2} = 0.021 p_2$$

$$= 0.014 p_1$$

Therefore, it is sufficient to prevent concrete tensile failure if concrete tensile strength is greater than one-tenth of the resin tensile strength. The nominated tensile strength of the resin is 13.5MPa (Table 4.5). The estimated UTS of the concrete is above 3MPa. However, in the tests, sample failure was concrete tensile failure and there was no apparent tensile failure on the resin annulus (Figure 4.21 and 4.23). The possible reasons could be:

- The tensile strength of concrete is smaller than 1/10 of the resin strength.
- There are cracks in the concrete blocks.
- Boundary effect. The length of the concrete block is only 300mm, far less than an open cylinder assumed in the thick walled cylinder theory.

5.2.4 Yield criteria of thick walled cylinder

Failure of a thick walled cylinder made of ductile materials may be initiated as the result of inelastic deformation, and is predicted by either the maximum shear-stress criterion or the maximum octahedral shear-stress criterion (Hearn, 1997). When Tresca criterion

is used, the maximum shear stress in the cylinder wall is associated with the maximum shear stress at yield in simple tension as $\tau_{max} = \sigma_y/2$. Consequently, for p_2=0 the internal pressure at initial yield is:

$$p_1 = \frac{\sigma_y}{2b^2}(a^2 - b^2) \qquad (5.9.1)$$

For complete plastic collapse of the cylinder:

$$\sigma_{rr} = \sigma_y ln\frac{a}{b} \qquad (5.9.2)$$

Another failure criterion is maximum octahedral shear-stress. The yield stress σ_y is obtained by setting the maximum octahedral shear stress in the cylinder equal to the octahedral shear stress that occurs in a tensioned specimen made of the same material when the tension specimen axial stress is σ_y. The octahedral shear stress in the tensioned specimen is given by the relationship:

$$\tau_{oct} = \frac{1}{3}\sqrt{(Y-0)^2 + (0-0)^2 + (0-Y)^2} = \frac{\sqrt{2}Y}{3} \qquad (5.10)$$

If a thick-wall cylinder is made of a brittle material, the material property associated with fracture is the ultimate tensile strength σ_t. At the failure loads, the maximum principal stress (either the circumferential stress or axial stress) in the cylinder is equal to σ_t. If the cylinder is loaded so that the magnitude of the maximum compressive principal stress is appreciably larger than σ_t, the criterion of failure is uncertain.

5.3 FAILURE CRITERIA

A complete plasticity theory has three components: a yield criterion that defines the initial inelastic response of the material, a flow rule that relates the plastic strain increments to the stress increments after initiation of the inelastic response, and a

hardening rule that predicts changes in the plastic strain (Noresi, 1993). This section considers the first component of plasticity theory: the yield criterion.

In general, failure occurs through either yielding or fracture. It is postulated that yielding is initiated in a multi-axial stress state when this effective stress reaches a limiting value. The same concept may be used to predict failure by fracture, provided that an appropriate failure criterion can be established.

A yield criterion is usually expressed in mathematical form by means of a yield function $f(\sigma, Y)$, where σ defines the state of stress and Y is the yield strength. The yield function is defined such that the yield criterion is satisfied when $f=0$. When $f<0$, the stress is elastic. Various failure criteria are summarised in Table 5.1 according to Richards (2001), Noresi *et al* (1993) and Seed (2000).

The initiation of yield in ductile metal can be predicted reasonably well by either the maximum shear stress criterion or the maximum octahedral shear stress criterion. Hence it is often employed for bolt failure in shear tests. Unfortunately, no single yield criterion has been established to accurately predict yielding or fractures for resin or rock materials. The most frequently used Mohr-Coulomb's failure criterion is chosen in this study.

Table 5.1 Summary of Failure criteria

Name	**Yield function**	**Applicable material**	**Comments**
Rankine (maximum principal stress)	$f = max(\|\sigma_1\|, \|\sigma_2\|, \|\sigma_3\|) - Y$	Brittle	Used in conjunction with other criteria
St. Venant (maximum principal strain)	$f = max\|\sigma_i - v\sigma_j - v\sigma_k\| - Y$	Brittle	
Beltrami (strain energy density)	$f = \sigma_1^2 + \sigma_2^2 + \sigma_3^2 - 2v(\sigma_1\sigma_2 + \sigma_1\sigma_3 + \sigma_2\sigma_3) - Y^2$		
Tresca (maximum shear stress)	$f = max(\|\sigma_1 - \sigma_2\|, \|\sigma_1 - \sigma_3\|, \|\sigma_2 - \sigma_3\|) - Y$	Ductile	Conservative in pure shear
Von Mises (distortional energy density)	$f = \frac{1}{3}(\sigma_2 + \sigma_2 + \sigma_3) - \frac{\sqrt{2}}{3}Y$		Accurate in pure shear; preferred in plasticity studies
Mohr-Coulomb (shear in normal stress)	$f = (\sigma_1 - \sigma_3) + (\sigma_1 + \sigma_3)sin\phi - 2c \cdot cos\phi$	Soil, rock and concrete	
Drucker Prager (energy in hydrostatic stress)	$f = \alpha I_1 + \sqrt{J_2} - K$		Outer bound of the Mohr-Coulomb; reduces to the Von Mises for a frictionless material

5.4 PREVIOUS STUDIES ON BOLT PROFILE

Studying the reinforced concrete beam in civil engineering, Goto (1971) experimentally demonstrated the bond action between concrete and deformed steel bars. The test specimens were axially loaded with a bar embedded in a concrete beam. The pullout force was applied through the free ends of the bar and cracks were observed at the surface.

Numerous internal cracks formed around the deformed bars. At bolt stresses less than 100MPa, these internal cone-shaped cracks were initiated around the ribs close to the primary cracks. When bolt stresses were increased, the internal cracks developed further from the primary cracks at almost every rib profile. The internal cone-shaped cracks were formed with their apexes near the bar lugs and with their bases generally directed towards the nearest primary cracks, as shown in Figure 5.5.

The angles of the internal cracks were seen to be ranging from 45° to 80° being larger further away from the primary crack. This indicated that the compressive forces across each inclined crack diminish with the distance from the primary crack and dissipate into the surrounding concrete. The angle also depended on rib profile geometry and the type of anchorage of the test specimen.

Goto also observed longitudinal splitting cracks, which were initiated near the bar at the faces of the primary cracks and extending towards the outside of the specimen. The major causes of longitudinal cracks could be both the action on the bolt ribs and deformation of the comb-like mechanism formed by the cone-cracked material. The latter cause would indicate that cone-shaped cracks develop before longitudinal splitting cracks, and that the splitting cracks were controlled by geometrical non-linearities.

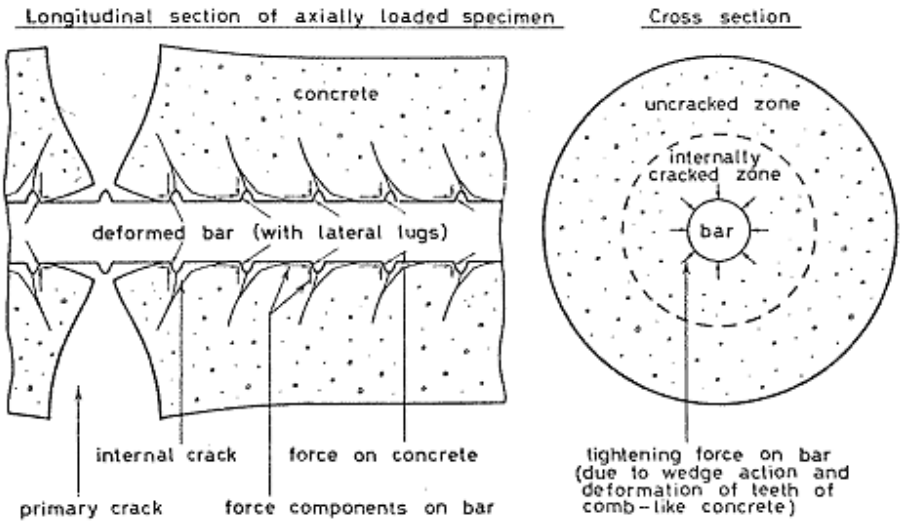

Figure 5.5 Deformation of concrete around steel reinforcing bar after formation of internal cracks (Goto, 1971)

Goto's work was improved by later researchers such as Tepfers (1973, 1979). Tepfers pointed out that the ribs with a face angle between 40° and 105° produced about the same movement. For bars with a face angle less than 30° the bonding action was different. When concrete was crushed to a compacted powder, it became lodged in front of the ribs (Figure 5.6). This in effect produced ribs with a face angle of 30° to 40°.

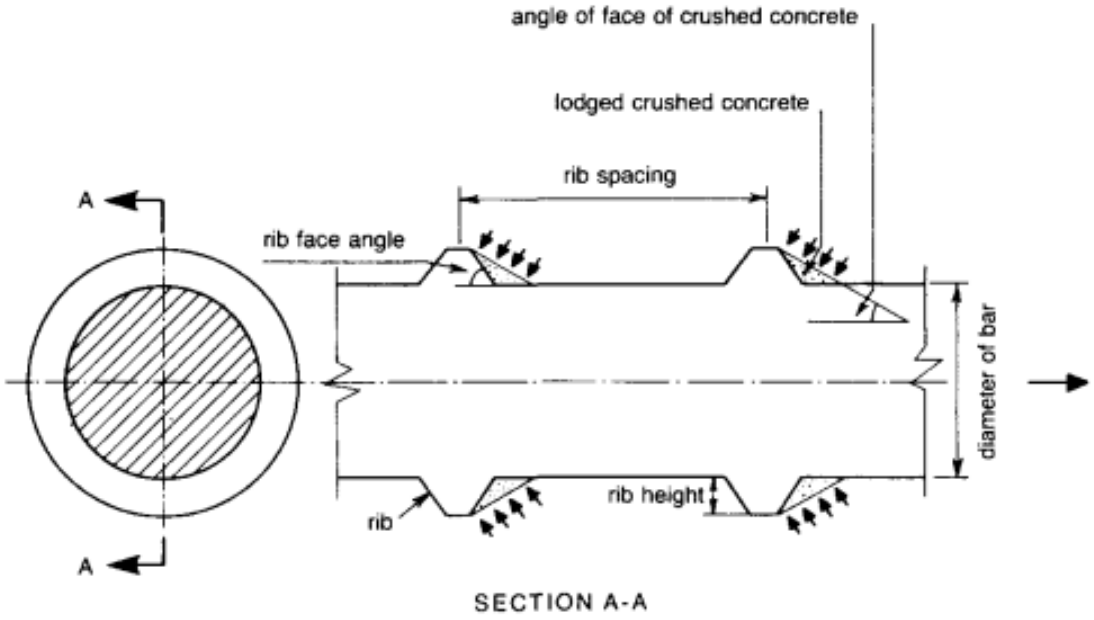

Figure 5.6 The geometry of a deformed reinforcing bar and the mechanical interaction between the bar and the concrete (Tepfers, 1973).

In an analytical model Tepfers (1979) assumed that the radial components of the bond forces can be regarded as a hydraulic pressure acting on a thick-walled concrete ring surrounding the reinforcing bar. The shear stress at the interface distributes into the surrounding material by compression under a certain angle (angle of the cone shaped crack) and is balanced by tensile stress rings in the concrete. However, in this model the rib geometry is ignored.

It should be noted that the rib face angle is different to the "angle of face of crushed concrete" (Figure 5.5) which is the real slipping direction of the rebar when dilational slip failure occurs. In this study, it is termed "slip face angle" from now on, to be distinguished from the term "bolt rib face angle".

Fabjanczyk and Tarrant (1992) investigated the load transfer mechanism in pushout tests. They found that bolts with a lower profile height had smaller stiffness (Figure 5.7) and concluded that the load transfer was a function of parameters such as hole geometry, resin properties, and bar surface configuration.

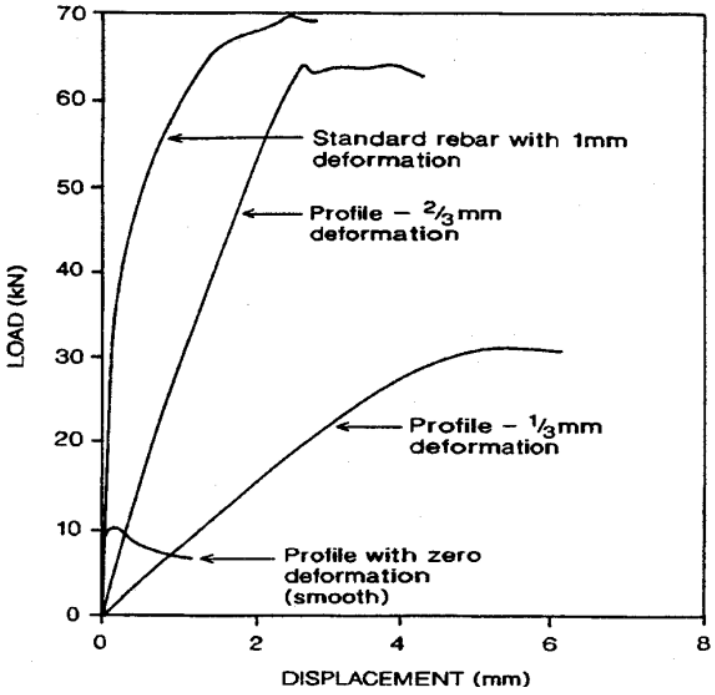

Figure 5.7 Load-displacement curves for rebar with various amounts of bar deformation removed (Fabjanczyk and Tarrant, 1992).

Ito *et al* (2001) used an X-ray CT scanner to visualise the patterns of failure in a pullout tests. The tests were conducted on four types of bolts (Table 5.2), grouted into an artificial rock with cement paste (Table 5.3) in the laboratory. The artificial rock was made of concrete, dimensions 1000x500x500 mm. The hole diameter was drilled at 65mm and the embedded length of a bolt was 350mm.

Table 5.2 Rockbolts and cable bolts used in the Ito's pull-out test, 2001

	Name	**Diameter (mm)**	**Yield Strength (kN)**	**Ultimate Strength (kN)**
	Deformed bolt	25	174	248
	Twist bolt	24	227	308
	Plain cable	15.2	222	261
	Bulb cable	15.2	222	261

Table 5.3 Mechanical properties of artificial rock and cement grout, Ito *et al* (2001).

	Density (kg/m^3)	**UCS (MPa)**	**UTS (MPa)**	**E (GPa)**	***v***
Concrete	2410	82.3	4.83	35.1	0.22
Grout (cement)	2060	98.7	3.59	21.2	0.25

Figure 5.8 shows the load displacement curves for all the cases. The results show the strong influence of bolt type on the deformational behaviour. In case 1 and case 2, the bolts were not pulled out until at the end of the test, but the part of the screw for holding

the bolt with a nut yielded. Case 3 and case 4 showed ductile behaviour. The difference in load displacement curves appeared to result from the mechanism of the bond failure.

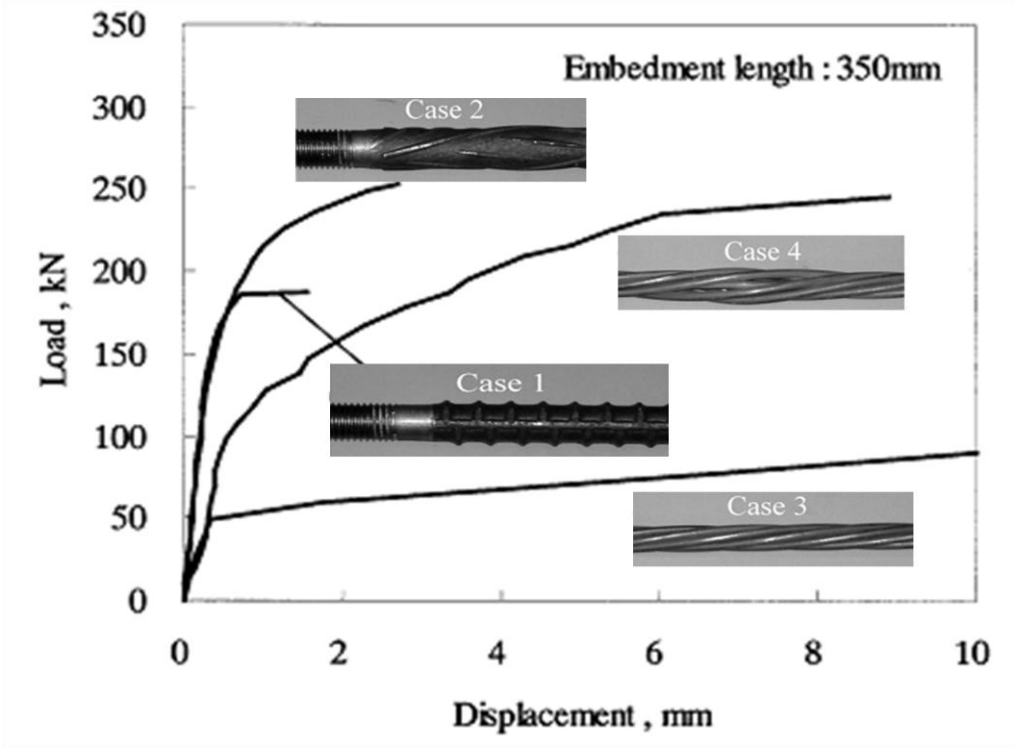

Figure 5.8 Load displacement curves of four cases in the pull-out tests (Ito *et al*, 2001).

Figure 5.9 shows the cross sectional images of the bolts at intervals of 10mm along the bolt axis. Results suggest that the failure mechanism is dependent on the type of bolts, namely the rib profile of the bolt. In case 2, the lugs of the twist bolt were spiral. Therefore, the failure mode within the grout was spiral with the twist. On the other hand, the failure modes in case 3 and 4 showed the radial splitting mechanism and hence were dominated by the inner pressure.

However, in pullout tests of cases 1, 2 and 4, the ultimate pullout forces have reached or exceeded the yield strength of the tested bolts (yield strength is listed in Table 5.2 and pullout curves are presented in Figure 5.8). Thus, the load-displacement curves for the load in excess of 220kN were affected by a combination of bond failure and the bolt yielding.

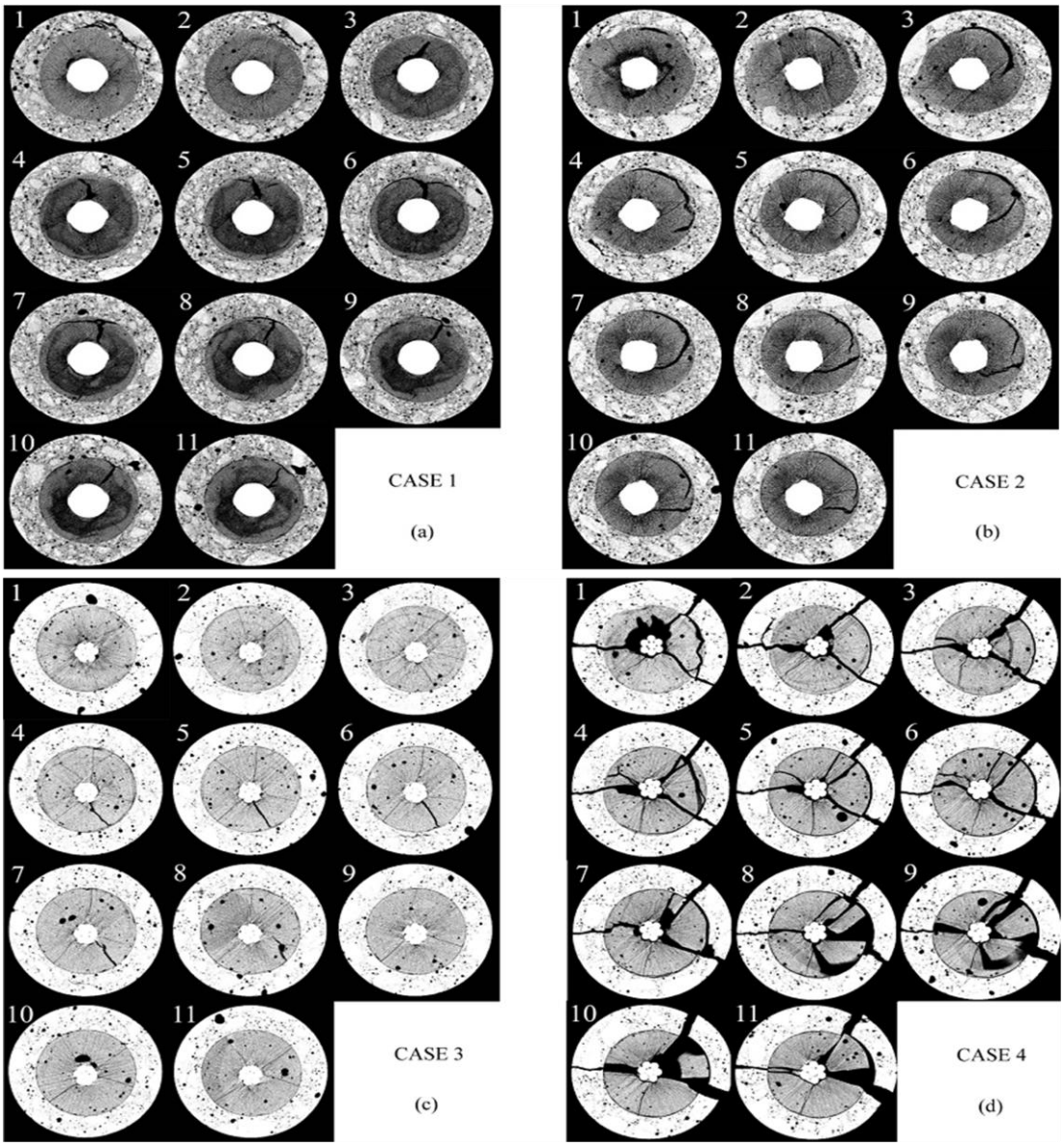

Figure 5.9 The cross sectional images at every 10mm from 10mm to the bottom of specimen below the upper surface of the artificial rock (Ito *et al*, 2001).

Kilic *et al* (2002 a) studied the effects of different shape of ribs of the 14mm diameter steel bolt by pullout tests. These were smooth surface bars, ribbed bars, single conical profile bars, double conical profile bars and triple conical profile bars. The tests were catalogued into four groups. Schematic illustration of tests in Group II and IV are shown in Figure 5.10.

The experimental results showed that there was a strong influence of the bolt profile on the load bearing capacity and deformational behaviour, shown in Figure 5.11. All bars

in the first three cases and some of bars in the last case were pulled out by shearing at the bolt grout interface (grout failure). But in final case, 15°, 30° and 45° triple conical profile surface bolts could not be pulled out, because the bolt stem failure (steel failure) occurred before shearing of the bolt-grout interface. The bond strength of a ribbed bar was 5.5 times greater than that of a smooth bar, and the bond strength of a conical profile bolt was 27% greater than that of a ribbed bar.

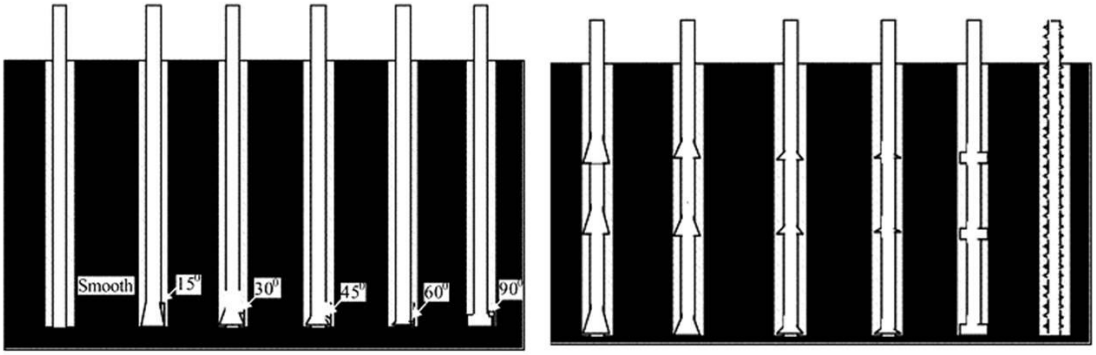

Figure 5.10 Left: Single conical profile bolts used in case II; Right: triple conical profile bolts used in case IV (Kilic *et al*, 2002 a)

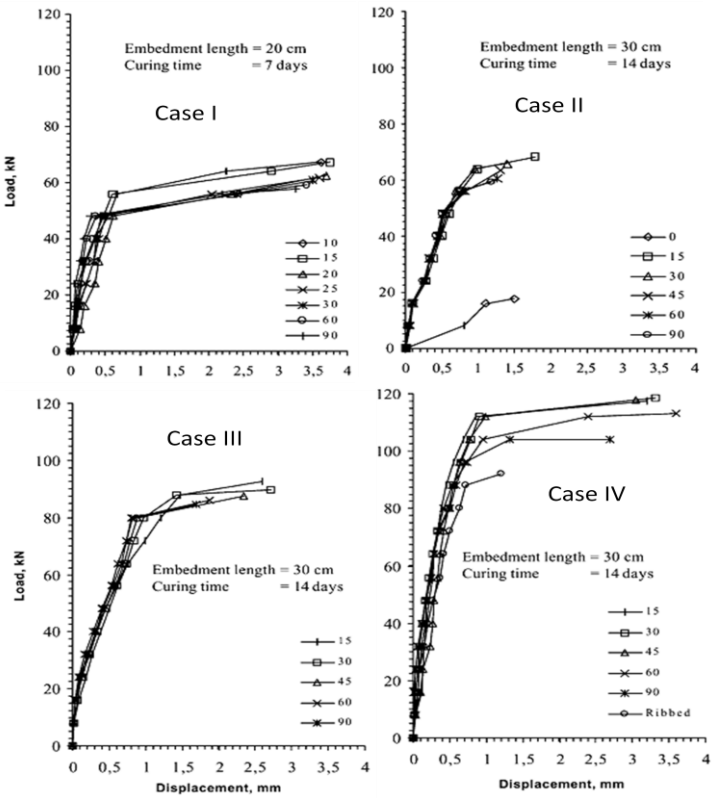

Figure 5.11 Load displacement curves of pullout tests (Kilic *et al* 2002 a).

Blumel (1996) reported on the influence of profile spacing on load transfer capacity of the bolt. Pull-out testing of equal diameter bolts with different profile spacing was carried out on bolts of 13.7 mm, 27.4 mm and 54.8 mm profile spacing. Blumel found that widening of the spacing between the profiles enhanced the load transfer capacity of the bolting system installation. Later, Blumel *et al* (1997) reported on the finite element modelling of the bolts with different profile spacing. Their study supported the experimental laboratory findings clearly demonstrating that higher stresses with more significant peaks being developed in the bolt with wider spaced ribs as compared to the small rib distance.

Aziz and Dey (2002) studied bolt profile spacing and load transfer conditions under CNS conditions and under different confining pressures. The study confirmed the existence of changes in the load-displacement profiles with respect to bolt surface profile configurations. Aziz and Webb (2003) studied profile configurations that included push testing of bolts installed in cylindrical steel tubes, 75 mm long and 27 mm in internal diameter. The tests were made using chemical resin instead of cement. Moosavi *et al* (2005) also studied the profile configurations in cementitious grout, leading to similar conclusions. Aziz *et al* (2005, 2006) extended this study to include both push and pull-out tests. Longer steel sleeve lengths, greater than 75 mm, were also used. 75 mm long steel sleeves were found to be of insufficient length to accommodate adequate number of profiles encapsulated in the tube, to allow credible and meaningful test results. Further studies undertaken by Aziz, *et al* (2008) indicated that increased profile spacing contributed to improvement in bolt anchorage stiffness (Figure 5.12).

The performances of T2 bolts with 12.5mm profile spacing of this literature are used as an illustrated example to analyse the failure modes of rock bolting in pullout in section 7 of this chapter. The failure mode of large profile spacing bolts (37.5 or 50mm) is more complicated than small spacing of 12.5mm. In addition, the ultimate strength of tested bolts is also around the yielding strength of the steel bolt (256 kN).

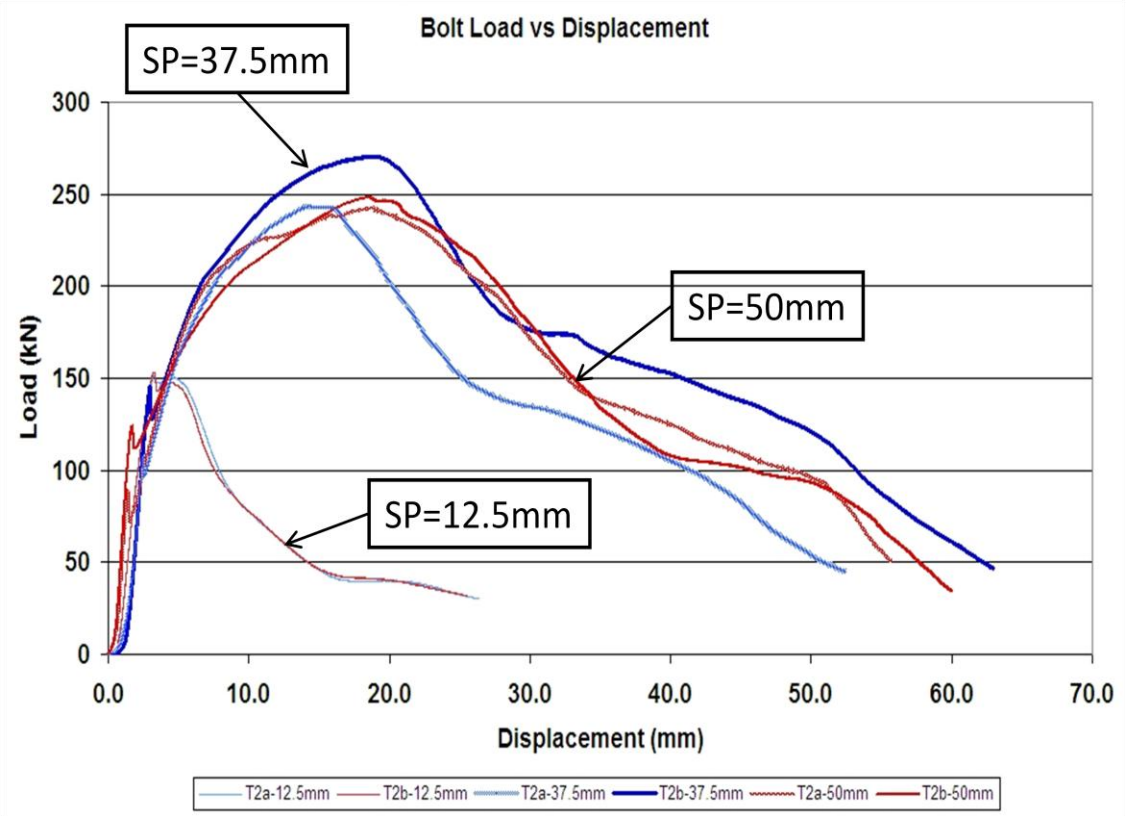

Figure 5.12 Laboratory studies of steel bolt pullout tests showing the maximum load for various spacing of the bolt profile (Aziz *et al*, 2008).

How the bolt profile interacts with the grout material under axial loading is the focus of this chapter. The aim of the theoretical predictions is to provide understanding of the initial grout failure and to offer a new tool for research into the best profile geometries to reach optimum shear strength between the bolt and the surrounding medium.

One bolt rib profile, shown in Figure 5.13, is the subject of discussion. The load F is a resultant force in the axial direction; r is the core radius of the steel bolt; R equals to r plus rib height; L is the spacing between the ribs; the dotted line indicates the parallel shear failure surface; dashed line indicates the dilational slipping surface and the angle i is the slipping face angle.

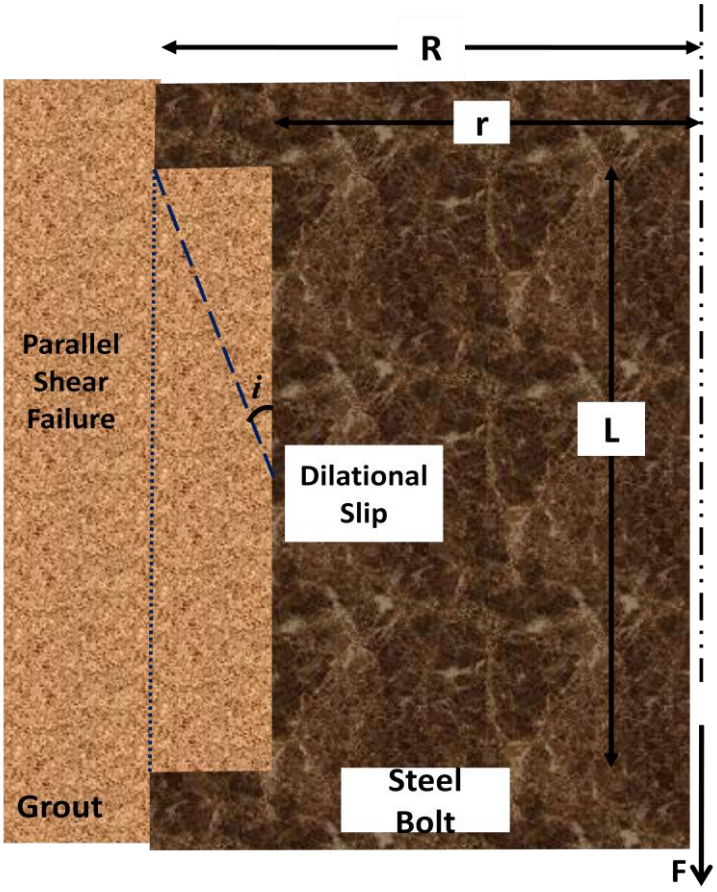

Figure 5.13 Schematic diagram of one bolt segment.

5.5 PARALLEL SHEAR FAILURE

Failure modes of rock bolting subjected to axial loading are the major concern for understanding the load transfer mechanism. Two failure modes were identified via laboratory studies, namely parallel shear failure and dilational slip failure.

5.5.1 Direct parallel shear failure

Direct parallel shear failure is defined by a cylindrical failure surface. It is a characteristic failure pattern, which occurs for smooth surface bar (without profiles) along the bolt-grout contact, and for very closely spaced rebar (similar to a screw profile) along the profile tips of the bar. For a smooth bolt, the resultant axial load can be expressed as:

$$F = \int \tau \, dA \tag{5.11}$$

Where:

F = the resultant force in the axial direction;

A = the failure surface area (bolt-resin interface);

τ = the shear stress at the interface

Once failure occurs, the shear stress can be calculated via Mohr-Coulomb's failure criterion as:

$$\tau = c + p \cdot tan\phi \tag{5.12}$$

Where:

c and ϕ are grout/steel interface properties

p = the confining pressure when failure occurs.

If a bolt has closely spaced ribs (Figure 5.14), parallel shear failure between the rib peaks will always occur just as for the smooth surface bar. It can be found that during such failure, the grout between the profiles (shaded area in Figure 5.14) will remain as if it was part of the steel bar. In fact, a closely spaced bar can be thought of as a smooth bar of a little larger diameter. The mechanical behaviour of the threaded bar can be expressed using similar equations:

$$F = \int \tau_{bolt-grout} \, dA_{bolt-grout} + \int \tau_{grout} \, dA_{grout} \tag{5.13}$$

Once failure occurs:

$$\tau_{bolt-grout} = c_{bolt-grout} + p \cdot tan\phi_{bolt-grout} \tag{5.14}$$

$$\tau_{grout} = c_{grout} + p \cdot tan\phi_{grout} \tag{5.15}$$

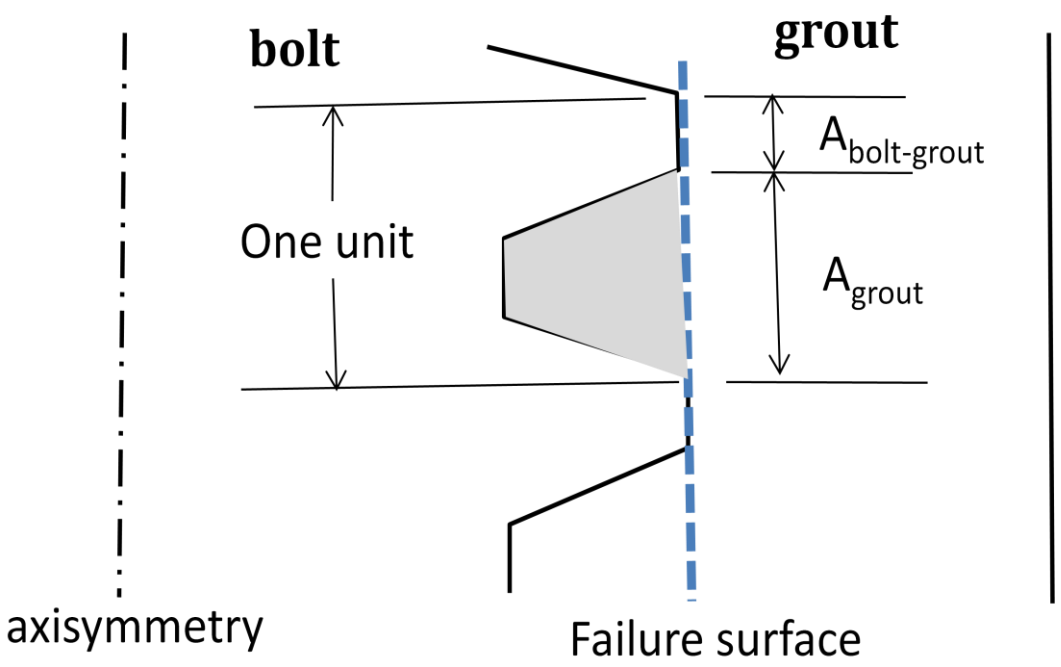

Figure 5.14 Schematic diagram of the rib profile of closely spaced bolt.

The load capacity of direct parallel shear failure is lower if compared with ribbed steel bar of the same core diameter (Aydan 1989; Ito *et al* 2001; Aziz *et al* 2008; Kilic *et al* 2002).

Moosavi *et al* (2005) conducted a series of laboratory tests to study the effect of confining pressure on the bond capacity of different rebar. A modified triaxial Hoek cell was used to facilitate application of a constant radial confining pressure to the grouted sample while pulling the bolt axially through the cement annulus. The results showed a non-linear relationship between the increase of bond capacity and confining pressure. The radial dilation was quantified also as a function of confining pressure.

Diameter 22mm and 28mm threaded rock bolts (called rebar P22 and P28 in Moosavi paper) were tested, as shown in Figure 5.15 (a). It can be seen that the profiles of the bar is closely spaced. An enlarged picture is used to obtain the geometric parameters of the rib as they were not provided in the paper. Measurements indicate that the rib width of the threaded bar is approximately 23% of the rib spacing (Figure 5.15 b).

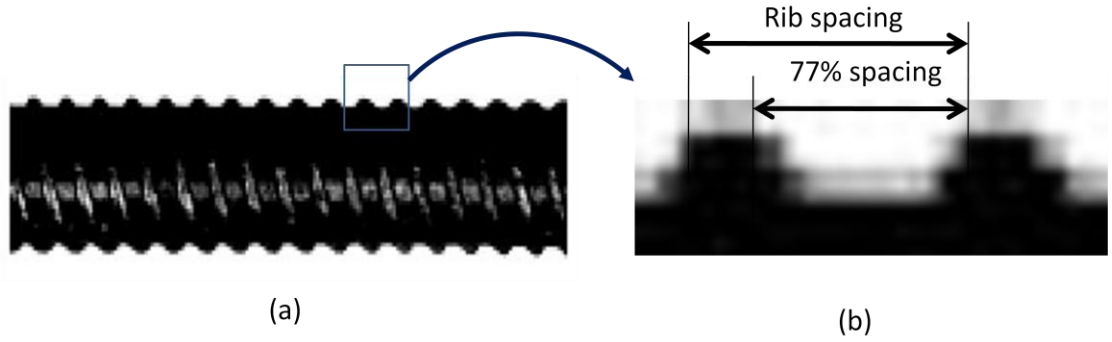

Figure 5.15 (a) Deformed bar used in experiment, after Moosavi *et al* (2005). (b) Measured rib parameter via enlarged picture.

The test results provided in the research article for threaded bars are shown in Figure 5.16. The dilation diagrams show that the dilation is very small at confining pressures of 3.2, 4.8 and 6.4MPa for P28 bolts, and also the confining pressure of 3.5 and 5MPa in cases of P22 bolts. The diagrams also indicate that the failure mode is direct parallel shear failure of the grout for these cases. As a result, the shear stress in the failure surface should be predicted via equations (5.13), (5.14) and (5.15).

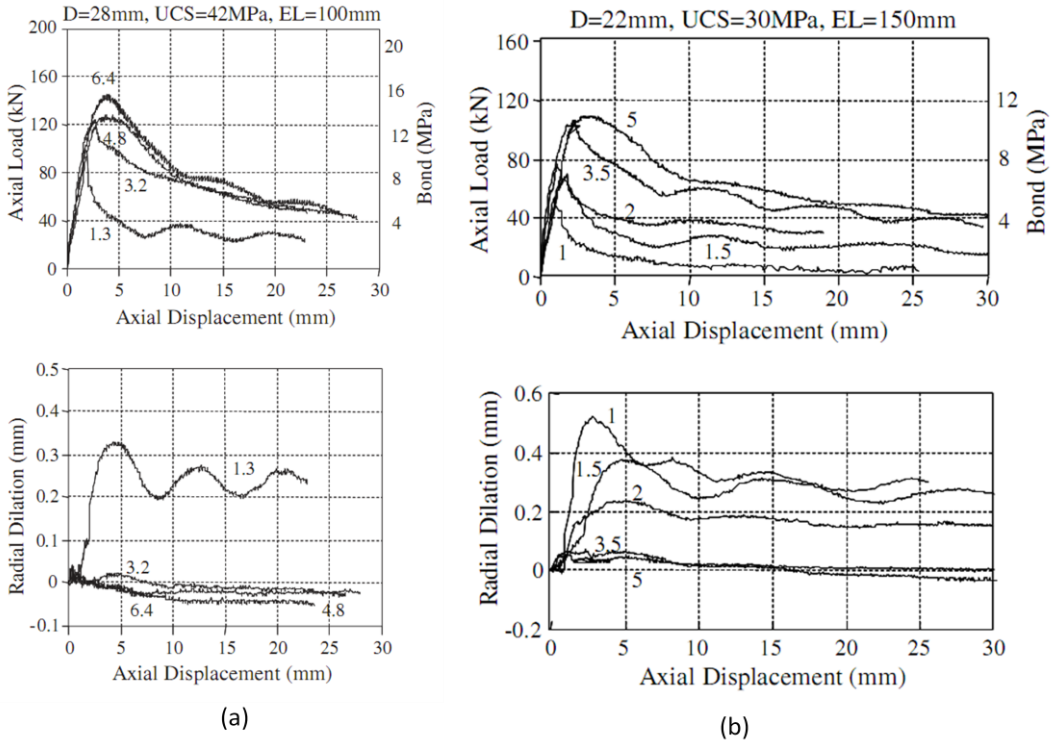

Figure 5.16 Results of pull test (a) P28 bolt with UCS=42MPa grout and (b) P22 bolts with UCS=30MPa grout (Moosavi *et al*, 2005).

Before predicting the axial bolt loading capacity, the mechanical properties of the grout and steel-grout contact should be determined. The type 1 Portland cement mix of the grout used a water to cement ratio of 0.4, only the UCS values were provided in the paper. Assuming the internal friction angle of the grout is 35°, then according to equation (4.1) the cohesion can be estimated from the provided UCS data as 10.9MPa and 7.8MPa for 42MPa and 30MPa of concrete respectively.

A sensitivity study has been conducted on different friction angles ranging from 30° to 40°. It showed that, the difference of shear strength was less than 5% in tested confining stress and UCS ranges. So the assumption that $\phi = 35°$, will not affect the results significantly with respect to shear strength expressed in equation (5.15).

In addition, the grout to steel adhesion is simply assigned as 4MPa and their frictional angle as 28°. Then, the axial load capacity can be calculated by combining Equations (5.13), (5.14), (5.15) and (4.1). As an example of calculation, considering P28 bolt with grout UCS=42MPa and the cohesion of the grout as determined according to equation (4.1):

$$c = \frac{UCS\ (1 - sin\phi)}{2 \cdot cos\phi} = \frac{42\ (1 - \sin 35)}{2 \cdot \cos 35} = 10.9\ \text{MPa}$$

In case of confining pressure p=3.2MPa, the shear resistance of the grout can be determined by equation (5.15):

$$\tau_{grout} = c_{grout} + p \cdot tan\phi_{grout} = 10.9 + 3.2tan35 = 13.2\ MPa$$

The shear resistance caused by rib profile is determined by equation (5.14):

$$\tau_{grout-steel} = c_{grout-steel} + p \cdot tan\phi_{grout-steel} = 4 + 3.2(tan28) = 5.7\ MPa$$

Figure 5.15 shows that the grout shear failure surface was around 77% of the bolt surface area, and the embedded length=100mm. Consequently, using Equation (5.13),

the predicted load capacity is:

$$F = A_{grout-steel}\tau_{grout-steel} + A_{grout}\tau_{grout}$$

$$= 2\pi \times 0.014(100 \times 77\% \times 13.2 + 100 \times 23\% \times 5.7)$$

$$= 101\ kN$$

Using the selected cases, the calculations of the axial loads were performed and the results are summarised in Table 5.5. The average differences between the measured and theoretical axial loads are -14% and -6% for P28 and P22 bolts respectively. This variation may be attributed to the inaccurate data of material properties, and/or increasing grout volume due to slipping.

The last row in Table 5.5 is a demonstration of variation in failure modes. Due to lower confinement and resin dilation (Figure 5.16), failure mode in this test is changed to dilational slip, hence formulas used for direct parallel shear failure mode will no longer be applicable.

Table 5.4 Comparison of predicted axial load capacity with experiment data.

Bolts	**Confinement (MPa)**	**Calculated Axial loads (kN)**	**Experiment results (kN)**	**Difference %**
P28	3.2	101	118	-14
	4.8	110	124	-11
	6.4	119	142	-16
			Average=	-14
P22	3.5	96	105	-8.5
	5	106	110	-3.6
			Average=	-6
	1.5	82	70	+17

5.5.2 Parallel shear failure after dilation

When profiled bar is installed in a rock mass, any axial slip will generate some radial dilation depending on the roughness and geometry of the ribs. This lateral movement is restricted by the rock mass stiffness which surrounds the rebar. If the rock mass has a high stiffness (hard rock with no joints), the dilation will generate lateral confining pressure which results in high bond capacity of the reinforcement. On the other hand, soft rock masses specially when jointed, have low radial stiffness and would not generate high confining pressures in response to the dilation. This mechanism emphasises the importance of dilation and confining pressure when studying bond capacity of a grouted deformed bar.

Once dilation occurs, the initial stress field will be distorted. The confining pressure will become concentrated in the area along the slip, and stress in other sections of the bolt will be gradually released. If separation of the contact occurs, the confinement in that area will reduce to, approximately, zero (Figure 5.17). In this case, the parallel shear failure may also occur. The failure criterion is similar with direct parallel shear failure but with some modification of the confinement area. As shown in Figure 5.17, the confinement acting length $= (R - r)/\tan(i)$, Hence, the shear resistance can be described by:

$$F = 2\pi RLc + 2\pi R \cdot \frac{R - r}{tan\,(i)} \cdot p \cdot tan\phi \qquad (5.16)$$

This equation can be re-arranged to

$$F = 2\pi RL\left(c + \frac{R - r}{Ltan(i)} p \cdot tan\phi\right) \qquad (5.17)$$

Where

L=length of failure surface

c and φ are grout properties

p = the pressure acting on the slipping area

i = the slip angle, which is different to the rib face angle θ

R and r are rib geometry

The features of this kind of parallel shear failure are:

(1) The confinement is concentrated on the slipping area;

(2) Part of the bolt core is, or is nearly, separated from the grout material; and

(3) The radial stiffness is high or the rib height is large.

If the rib spacing is large, then the longer smooth bolt core separation from the surrounding material would be minimised, especially at high confinement and for ductile grout. If the radial stiffness is low, dilation will be large, decreasing the possibility of parallel shear failure, especial for small rib height. The T2 bolt meets the characteristics of this failure mode under high confining stiffness (Figure 4.16 and 4.23). Its pull out performance measured by Aziz (2008), shown in Figure 5.12, is used as an example to analyse the mechanism of this kind of failure mode, and is provided in section 7 of this chapter following the discussion of dilational slip angle.

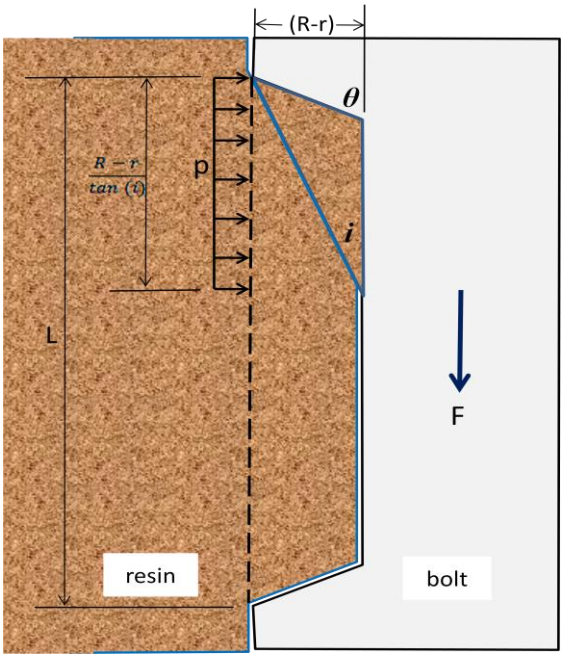

Figure 5.17 Parallel shear failure (dashed line) after dilational slip.

5.6 COMMENCEMENT OF DILATIONAL SLIP FAILURE

5.6.1 Problem description and assumptions

As discussed, the direct parallel shear failure can rarely occur without any dilatation for a common rebar bolt. That is, under normal circumstances dilatation will always occur, more or less, around the rebar bolt surface. If the confinement material is stiff, such as hard rock, the developed dilation will be ceased by the increased confinement pressure. In some cases where rock is very soft, the bolt rib will push the surrounding material radially outwards allowing for a profile slip out from its initial position. As a result, the mechanism of dilational slip failure is the major concern of the rebar bolting system.

Dilational slip failure is initialised by propagation of micro-cracks along a specific surface. Once the shear stress along this surface reaches a critical value, relative movement will take place. At this stage the rock bolting system enters a post-failure mode. The post-failure behaviour of ribbed bar is complicated due to the plastic deformation of grouting material as well as the re-distribution of the confining pressure, and is discussed in the later section of this chapter. Here, the emphasis is on the commencement of the dilational slip failure.

Firstly, the folowing assumptions are made;

(1) Mohr-Coulomb failure criterion is used to locate the failure surface within the grout material
(2) The initial confining pressure, p, is compressive and universal.

5.6.2 Dilational slip failure of rock bolting

Before slip failure occurs, the axial force, *F,* cannot affect the initial radial stress field because they are perpendicular. That is, *p* will keep its magnitude while *F* increases until relative axial movement takes place. In this procedure (shown in Figure 5.18):

$$\sigma_n = p\cos(i) - \frac{F}{A}\sin(i) \tag{5.18.1}$$

$$\tau = \frac{F}{A}\cos(i) - p\sin(i) \tag{5.18.2}$$

Where:

The conical area of the failure surface $A = \dfrac{\pi(R^2 - r^2)}{sin\ (i)}$ (5.18.3)

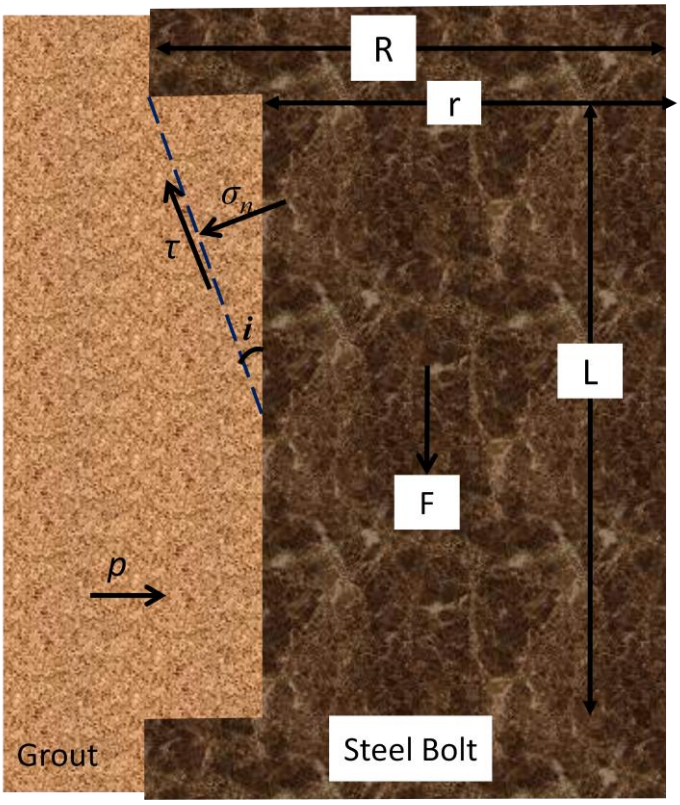

Figure 5.18 Dilational slip failure occurs along the dashed line

Once relative movement along the failure surface takes place, according to the assumption (1) made in last section, the dilational slip failure follows:

$$\tau = c + \sigma_n \cdot tan\phi \quad (5.19)$$

5.6.3 Maximum dilational slip face angle

Equations (5.18.1) and (5.18.2) can be re-arranged as follows:

$$F/A = \sigma_n \sin(i) + \tau \cos(i) \quad (5.20.1)$$

$$p = \sigma_n \cos(i) - \tau \sin(i) \quad (5.20.2)$$

Substituting equation (5.19) into equation (5.20.2):

$$p = \sigma_n \cos(i) - (c + \sigma_n tan\phi) \sin(i)$$

This is the expression of the initial confining pressure. The confining pressure is always positive (compression), therefore:

$$\sigma_n \cos(i) - (c + \sigma_n \cdot tan\phi) \sin(i) \geq 0$$

Re-arranging to:

$$\sigma_n \left(\frac{\cos(i)}{\sin(i)} - tan\phi \right) \geq c$$

As $c \geq 0$, hence:

$$\frac{\cos(i)}{\sin(i)} - tan\phi \geq 0$$

It can be solved as:

$$i \leq \frac{\pi}{2} - \phi \quad (5.21)$$

This is the expression of the upper limit of the dilational slip face angle. It demonstrates that the maximum slip face angle is solely dependent on the grout internal friction

angle. For example, if the resin internal friction angle ϕ=35°, then the dilational slip face angle must be less than 55°, no matter what the bolt rib face angle is.

The dilational slip face angle reaches its maximum value $(\pi/2-\phi)$ when c=0 and p=0. This is obviously not real for a rockbolting system. Thus the slip angle will always be less than this upper limit.

In reality, the rib face angle is normally greater than the upper limit of dilational slip face angle. If dilational slip failure occurs, the grouting material between the two angles will always be coupled with the bolt profile because there is no relative movement between them. In other words, grout material in this area will become part of bolt profile, and in most cases, permanently. For example, T2 bolts used in laboratory studies have a rib face angle approximately 70º, which is greater than the upper boundary of slip face angle 55º, therefore some resin has to stay in front of the bolt ribs once dilational slip occurs. This theoretical prediction has been evidenced by Figure 4.16, 4.23 and 4.41. In addition, equation (5.12) is also valid for plane stress because it is independent with the failure surface area, A, described by equation (5.18.3). Therefore, it also explains the existence of grout remaining in front of the ribs in CNS tests, shown in Figure 4.43 and 4.50.

As mentioned in section four of this chapter and shown in Figure 5.6, Tepfers (1973) stated that a rib with a face angle between 40° and 105° produced about the same movement. In addition, when concrete was crushed to a compacted powder, it became lodged in front of the ribs. However, Tepfers did not provide further explanation of this phenomenon. The theory of upper limit of dilational slip face angle derived in this section can explain Tepfers' experimental observations. That is, if the internal friction angle of the concrete is about 38°, then the bolt with face angle greater than 52° will produce approximately the same movement.

Kilic *et al* (2002) studied the effect of different shape of lugs (conical profiles) of the

steel bolt by pullout tests. Two groups of their tests are shown in Figure 5.19; and the result of these tests is shown in Table 5.5.

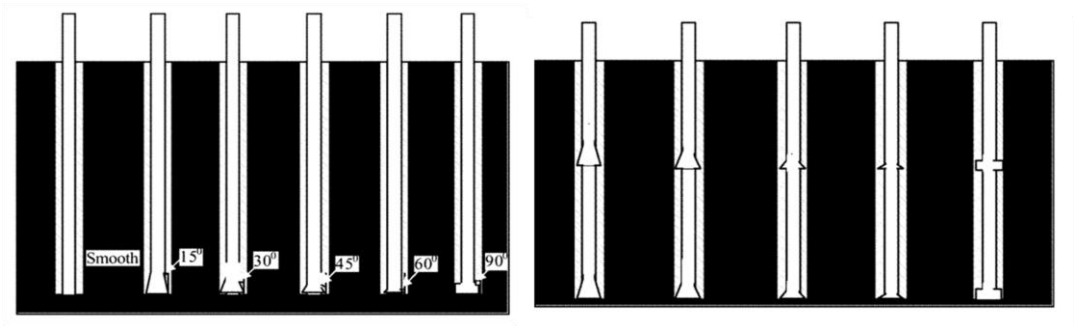

Figure 5.19 Schematic illustration of two groups tests conducted by Kilic *et al* (2002).

Table 5.5 Pull out test results for different rock bolt types (Kilic *et al*, 2002)

Bolt type	Yield load (kN)	Elastic displacement (mm)	Failure load (kN)
10° Single conical[a]	56	0.67	67.2
15° Single conical[a]	56	0.60	65.5
20° Single conical[a]	48	0.62	62.4
25° Single conical[a]	48	0.51	61.7
30° Single conical[a]	48	0.43	60.8
60° Single conical[a]	48	0.36	59.1
90° Single conical[a]	48	0.29	57.6
Smooth surfaces[b]	16	1.10	17.6
15° Single conical[b]	64	0.99	68.4
30° Single conical[b]	64	0.95	65.8
45° Single conical[b]	56	0.82	63.5
60° Single conical[b]	56	0.78	60.5
90° Single conical[b]	56	0.74	59.3
15° Double conical[b]	88	1.48	92.8
30° Double conical[b]	88	1.42	89.7
45° Double conical[b]	80	0.88	87.7
60° Double conical[b]	80	0.82	86.1
90° Double conical[b]	80	0.80	84.6

Their experimental results, highlighted in Table 5.6, show that the bolts with 60° conical profiles are very close in performance with the 90° conical profile bolts. These results can be explained by the upper limit of dilational slip angle theory.

5.6.4 Domain of dilational slip face angle for a known rebar bolt

According to analysis in last section, the theoretical upper limit of the slip face angle is

independent of bolt profile. In other words, it is universal whenever dilational slip failure occurs. For a known bolt, the range of dilational slip face angle can be further narrowed.

By combining Equations (5.18.1), (5.18.2) and (5.19) and eliminating σ_n and τ, the axial resultant force which causes dilational slip failure can be calculated by:

$$F_{dila} = \frac{\pi(R^2 - r^2)}{\sin(i)}\left[\frac{cos\phi}{cos(i+\phi)}c + ptan(i+\phi)\right] \qquad (5.22)$$

The axial load capacity of one bolt profile for the direct parallel shear failure is expressed in equation (5.13). Substituting equations (5.14) and (5.15) into (5.13), leads to

$$F = \int (c_{bolt-grout} + p \cdot tan\phi_{bolt-grout})\, dA_{bolt-grout} + \int (c + p \cdot tan\phi)\, dA_{grout}$$

As assumed the initial confining pressure, *p*, is evenly distributed, and neglecting the grout-steel contact, this equation becomes:

$$F_{shear\ failure} = 2\pi RL(c + ptan\phi) \qquad (5.23)$$

If dilational slip does occur, the condition expressed in the following equation will always apply:

$$F_{shear\ failure} \geq F_{dila}$$

Substituting (5.22) and (5.23), obtains:

$$2\pi RL(c + ptan\phi) \geq \frac{\pi(R^2 - r^2)}{sini}\left[\frac{cos\phi}{cos(i+\phi)}c + ptan(i+\phi)\right] \qquad (5.24)$$

To avoid cumbersome mathematical manipulations, we let *p*=0, equation (5.24) is simplified to:

$$2\sin i\cos(i+\phi) \geq \frac{(R^2-r^2)}{RL}\cos\phi$$

Further simplification leads to:

$$\sin(2i+\phi) - \sin\phi \geq \frac{(R^2-r^2)}{RL}\cos\phi$$

That is:

$$\sin(\phi+2i) \geq \frac{R^2-r^2}{RL}\cos\phi + \sin\phi \qquad (5.25)$$

The domain which satisfies equation (5.25) will be the theoretical slipping angle range for the specified bolt profile.

The bolt T2 is a popular bolt with an average rib spacing of 12.5mm and core diameter 21.7mm. After taking the average of the rib cross section, the average ribs height is found to be 1.2mm and average ribs width is 2.75mm. Accordingly, the rib geometry is *R*=12.1mm, *r*=10.9mm *L*=9.75mm. If ϕ =35°, then equation (5.25) becomes:

$$sin(35° + 2i) \geq \frac{12.1^2 - 10.9^2}{12.1 \times 9.75} cos35° + sin35° = 0.765$$

resulting in:

$$7° \leq i \leq 47°$$

Therefore, the possible dilational slip directions for T2 bolts are restricted to [7°, 47°], as shown in Figure 5.20. Consequently, the resin within two bolt ribs can be divided into three categories with regard to dilational slip failure. The resin above slip face angle 47°, indicated as (I) in Figure 5.20, will move with the bolt and can be thought of as part of the bolt profile. Section (II) is the shear failure band; hence micro-cracks will be developed in this area. The resin below 7° (section III) will remain intact in the procedure of failure.

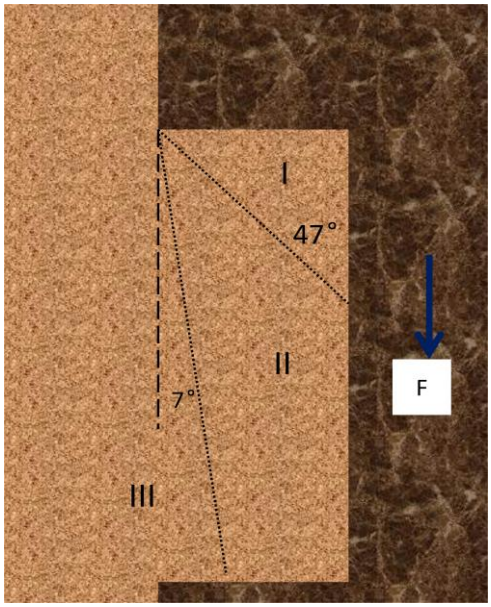

Figure 5.20 The slip face angle ranges of T2 bolt.

The derivation of the domain of the slip face angle is under assumption: p=0. To investigate the influence of confining pressure p, we transform equation (5.24) to:

$$Y = \frac{2\pi RL}{\pi(R^2 - r^2)}(c + p \cdot tan\phi) - \left[\frac{cos\phi}{\sin(i) \cdot cos(i+\phi)} \cdot c + \frac{tan(i+\phi)}{\sin(i)} \cdot p\right] \quad (5.26)$$

Inserting geometric parameters of T2 bolt, the Y values versus i were plotted for different p values as shown in Figure 5.21.

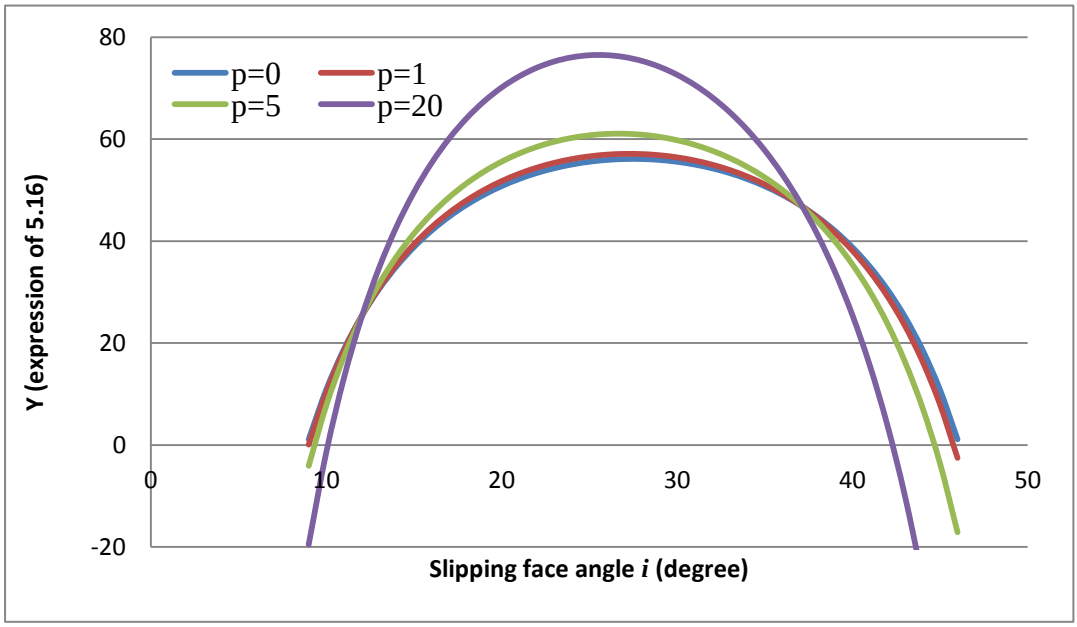

Figure 5.21 Equation (5.26) - plot for different confinement p.

The graphs suggest that the larger confining pressures result in the smaller domain of slip face angle. Therefore, The greatest domain of slip face angle is [7°, 47°], which occurs at *p*=0.

5.7 PARALLEL SHEAR FAILURE AFTER DILATION

5.7.1 Governing equation of dilational slip

As mentioned in section 5.6.2 and referring to Figure 5.18, the dilational slip equations are (5.18.1), (5.18.2) and (5.19). Eliminating τ and σ_n, yields:

$$\frac{F}{A}\cdot\cos(i) - p\cdot\sin(i) = c + \left(\frac{F}{A}\cdot\sin(i) + p\cdot\cos(i)\right)\tan\phi$$

where $A = \dfrac{\pi(R^2 - r^2)}{\sin(i)}$ is the conical surface area.

Rearranging to an *F*-*p* relationship:

$$\frac{F}{A} = \frac{c}{\cos i - \sin i\cdot\tan\phi} + \frac{\cos i\cdot\tan\phi + \sin i}{\cos i - \sin i\cdot\tan\phi}p$$

Noticing that:

$$\cos(i)\cdot\tan\phi + \sin(i) = \frac{\cos(i)\cdot\sin\phi + \sin(i)\cdot\cos\phi}{\cos\phi} = \frac{\sin(i+\phi)}{\cos\phi}$$

$$\cos(i) - \sin(i)\cdot\tan\phi = \frac{\cos\phi\,.\cos(i) - \sin(i)\cdot\sin\phi}{\cos\phi} = \frac{\cos(i+\phi)}{\cos\phi}$$

Then,

$$\frac{F}{A} = \frac{c + \dfrac{\sin(i+\phi)}{\cos\phi}p}{\dfrac{\cos(i+\phi)}{\cos\phi}}$$

Re-arranging to:

$$\frac{F}{A} = \frac{cos\phi}{cos(i+\phi)} \cdot c + p \cdot tan(i+\phi)$$

In case of cohesion c=0, the above equation reduces to:

$$\frac{F}{A} = p \cdot tan\,(i+\phi)$$

That is the Patton's equation of inclined discontinuity slipping (Figure 5.1 c d).

Substituting equation (5.18.3) into the original equation yields:

$$\frac{F \cdot sin\,(i)}{\pi(R^2 - r^2)} = \frac{cos\phi}{cos(i+\phi)} \cdot c + p \cdot tan(i+\phi)$$

Re-arranging and obtaining the dilational slip failure equation as:

$$F_{dilation} = \pi(R^2 - r^2)\left[\frac{cos\phi}{sin\,(i) \cdot cos(i+\phi)} \cdot c + \frac{tan\,(i+\phi)}{sin\,(i)} \cdot p\right] \qquad (5.27)$$

It can be seen that when dilational slip occurs, the axial force has to overcome two resistances, one is generated by cohesion and another is generated by confining pressure.

The governing equation of dilational slip failure composes of five aspects:

- Bolt axial load $F_{dilation}$
- Bolt rib profile R and r
- Resin mechanical properties ϕ and c
- Dilational slip face angle i
- Redial confinement p

The influence of resin properties is not the major concern of this study, hence can be evaluated as constants at c=16MPa and $\phi = 35°$. As discussed previously, the

confining pressure, *p*, is the initial installation pressure, it can be estimated as 5MPa in laboratory pullout tests or $(\sigma_1 + \sigma_2)/2$ in the field. Therefore, once the dilational slip face angle i is acknowledged, the influence of the bolt rib profile can be estimated.

5.7.2 The most vulnerable slipping surface

To investigate the role of the bolt rib profile in dilational slip failure of rock bolting, the dilational slip face angles i must be acknowledged, or at least narrowed down. In section 5.6, it has been derived that the maximum dilational slip face angle is the complementary angle of the internal friction angle of the resin regardless of bolt rib profile (equation 5.21). In addition, the dilational slip face angle can be further narrowed down using equation (5.25) for a given bolt.

For variable i, equation (5.27) is continuous in the domain of $[0,\ \pi/2 - \phi]$, hence the stationary points on the curve can be found using:

$$\frac{dF}{di} = 0$$

The dilational slip face angle, at which the axial force reaches its minimum value, is the most vulnerable surface of dilational slip failure of rock bolting.

For engineering applications, the most vulnerable slip face angle can be estimated using graphic method. Figure 5.22 shows $F/[\pi(R^2-r^2)]$ versus slip face angle *i* in the domain of [7°, 47°] at different confinements.

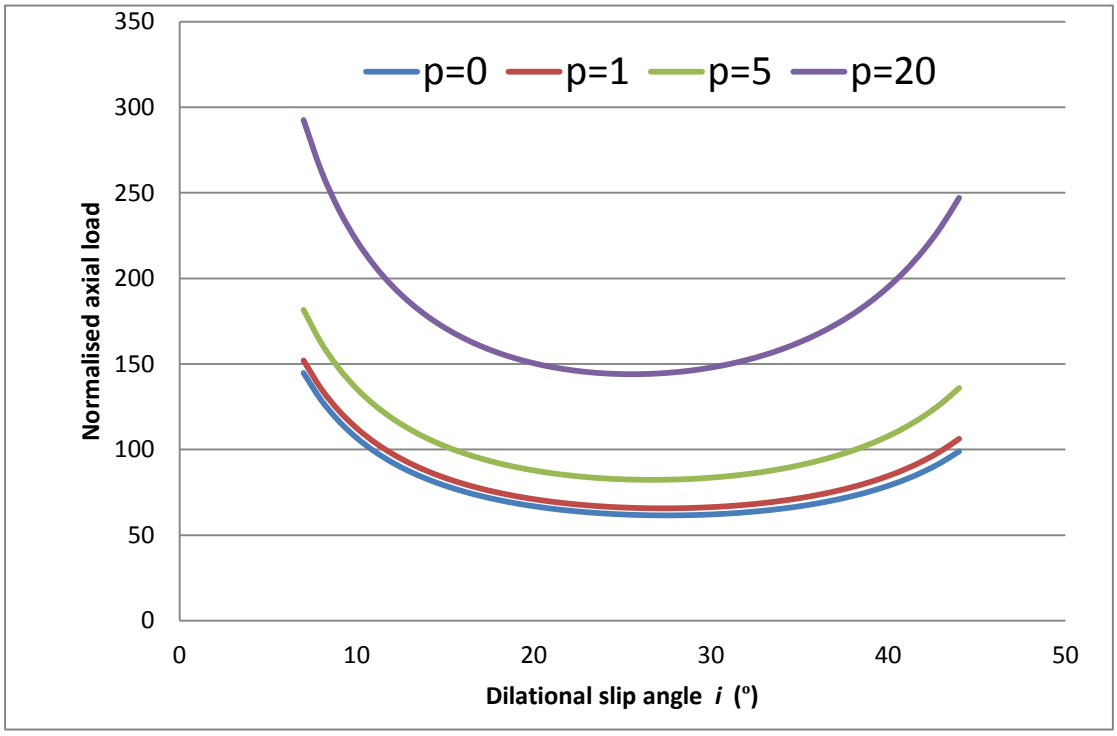

Figure 5.22 Schematic of normalised axial load at different slip face angles for different confinement pressures when dilational slip failure occurs.

Results suggest that, no matter what the value of the confining pressure is, there is one stationary point at which dilational slip failure commences by a minimum axial loading. Hence, this direction is the most vulnerable slip surface of the rockbolting when subjected to axial load.

According to Figure 5.22, the most vulnerable slip face angle of the T2 bolts grouted in resin annulus is approximately 28° at low confinements and approximately 25° if initial confinement pressure is 20MPa. From a view point of engineering applications, there is no difference. Therefore, it is reasonable to assume that the most vulnerable dilational slip face angle of T2 bolt is 27° under normal conditions.

Therefore, the parameters of T2 bolt can be summarised as:

- Core radius r=10.9mm,
- Core plus rib height R=12.1mm,
- Resin cohesion c=16MPa, and

- Resin frictional angle ϕ=35°
- Dilational slip face angle *i*=27°,

Then the axial load for dilational slip failure described by equation (5.27) is:

$$F_{dilation} = \pi(R^2 - r^2)\left(\frac{cos\phi}{cos(\phi + i) \cdot sin\,(i)}\, c + \frac{tan(\phi + i)}{sin\,(i)}\, p\right)$$

$$= 0.0000867\left(\frac{cos35°}{cos(35° + 27°) \cdot sin27°}\, c + \frac{tan(35° + 27°)}{sin27°}\, p\right)$$

$$= 5.33 + 0.359p\ (kN)$$

Where *p* is in MPa.

This is the dilational slipping failure criterion on the most vulnerable surface of fully grouted T2 rock bolting.

5.7.3 Design Application Using Slip Face Angle Solution

This section presents an application of the bolt profile design using the most vulnerable dilational slip face angle theory.

In section 5.7.2, the domain of dilational slip face angle for T2 bolt has been determined via $F_{shear\ failure} \geq F_{dilational\ slip}$. However, if direct parallel shear failure is probable rather than dilational slipping, what will the bolt rib parameters be? In other words, what profile geometry will lead to $F_{shear\ failure} \leq F_{dilational\ slip}$? When neglecting the grout-steel contact, this problem leads to:

$$2\pi RL(c + p\ tan\phi) \leq \frac{\pi(R^2 - r^2)}{sin(i)}\left[\frac{cos\phi}{cos(i + \phi)}c + p\ tan\,(i + \phi)\right] \qquad (5.28)$$

This equation concerns with grout properties as well as the rib geometry. If resin properties are used, and based on the previous discussion, the most vulnerable slip face angle is approximately 27°, equation (5.28) leads to:

$$2RL(16 + ptan35°) \leq \frac{R^2 - r^2}{sin27°}\left[\frac{cos35°}{cos(27° + 35°)}16 + ptan\,(27° + 35°)\right]$$

Rearranging:

$$2RL(16 + 0.7p) \leq (R^2 - r^2)(61.5 + 4.14p\,)$$

This equation requires knowledge of the initial confining pressure. In the field, the initial confinement can be estimated as the average of σ_1 and σ_2 stress. In the computer simulation, the initial confinement is often assigned as 5MPa. If *p*=5MPa, then a rib geometric equation can be established as:

$$39RL \leq 82.3(R^2 - r^2)$$

The equation can be solved with various rib parameters. For example, if the bolt is required to have the same core radius *r*=10.9mm, average rib width=2.75 mm and rib spacing SP=12.5mm, then:

$$39(10.9 + h)(12.5 - 2.75) \leq 82.3[(10.9 + h)^2 - 10.9^2]$$

$$i.e.\ h^2 + 17.2h - 50.4 \geq 0$$

Where: *h* is the bolt rib height.

Solving:

$$h \geq 2.55\,mm$$

Thus, if the rib height of T2 bolt is doubled, then during the laboratory pullout tests the direct parallel shear failure of the resin grout will most likely occur. If the embedded length is 115mm, i.e. 9 bolt rib profiles, the load capacity can be found via:

$$F \approx 2\pi RL(c + ptan\phi) \cdot n$$

$$= 2\pi \times (2.55 + 10.9) \times 9.75 \times (16 + 5 \times tan35) \times 9$$

$$= 145\ kN$$

Similarly, the minimum initial confining pressure to commence direct parallel shear failure can also be found.

5.7.4 Prediction of axial load capacity of T2 bolts

The following is a comprehensive case of axial load capacity prediction using a failure modes analysis method.

Three kinds of failure mode have been identified in previous sections of this chapter, namely *direct parallel shear failure* (equation 5.13), *dilational slip failure* (equation 5.27) and *parallel shear failure after dilation* (equation 5.17). For T2 bolt, the rib parameters have been identified as *R*=12.1mm, *r*=9.75mm SP=12.5mm and *L*=10.9mm. In addition, the mechanical properties of resin are assigned as *c*=16MPa and $\phi = 35°$. Therefore, when an axial load is applied to a short embedded length, the likelihood of direct parallel shear failure of the resin and the load at failure can be deduced from equation (5.13):

$$F1 = 2\pi RL(c + p\ tan\phi)$$

$$= 11.9 + 0.519p \text{ (kN)} \qquad (5.A)$$

The failure criterion of dilational slip (equation 5.27) was solved in section 5.7.2 as:

$$F2 = \frac{\pi(R^2 - r^2)}{\sin(i)}\left[\frac{cos\phi}{cos(i+\phi)}c + p\ \tan(i+\phi)\right]$$

$$= 5.33 + 0.359p \text{ (kN)} \qquad (5.B)$$

Comparing solutions (5.A) and (5.B), it can be found that *F1*<*F2* when *p*<41MPa,

which indicates that dilational slip will occur if initial confining pressure is less than 41MPa..

If the radial stiffness of bolting system is large and the rib spacing is not too wide, the increasing confining pressure will concentrate on the slipping area. Once the resin-steel contact is nearly separated (Figure 5.12), the parallel shear failure criterion will be:

$$F3 = 2\pi RL\left(c + \frac{R-r}{Ltan(i)}p \cdot tan\phi\right)$$

$$= 11.9 + 0.126p \text{ (kN)} \qquad (5.C)$$

Letting *F2=F3*, and solving: *p*=28.2 MPa. This pressure is not large in comparison with the compressive strength of the resin. Once the concentrated compressive stress reaches this value, parallel shear failure will occur. At this moment, *F2=F3*=15.5kN being the load capacity of one bolt profile. Thus, if the embedded section is 115mm, the ultimate load is calculated to be:

$$\mathrm{F_{ultimate}} = 15.5 \times (115 \div 12.5) = 140 \text{ kN}$$

The residual strength will be:

$$F_{residual} = 0.126p \times 8 = 0.126 \times 28.2 \times 8 = 28 \text{ (kN)}$$

It should be noted that if the calculated confining pressure, *p,* is higher than the compressive strength, then resin annulus failure may occur and the failure mode will possibly be different.

According to discussion of the resin residual strength in section 4.2.2 Chapter four, the post failure behaviour of the resin is modelled as cohesional strength decaying. Supposing that the cohesion keeps its original value for 15% of rib spacing after failure, and decays to zero after passing through one rib spacing, the predicted full

range load displacement curve of T2 bolt can be achieved, as shown in Figure 5.23.

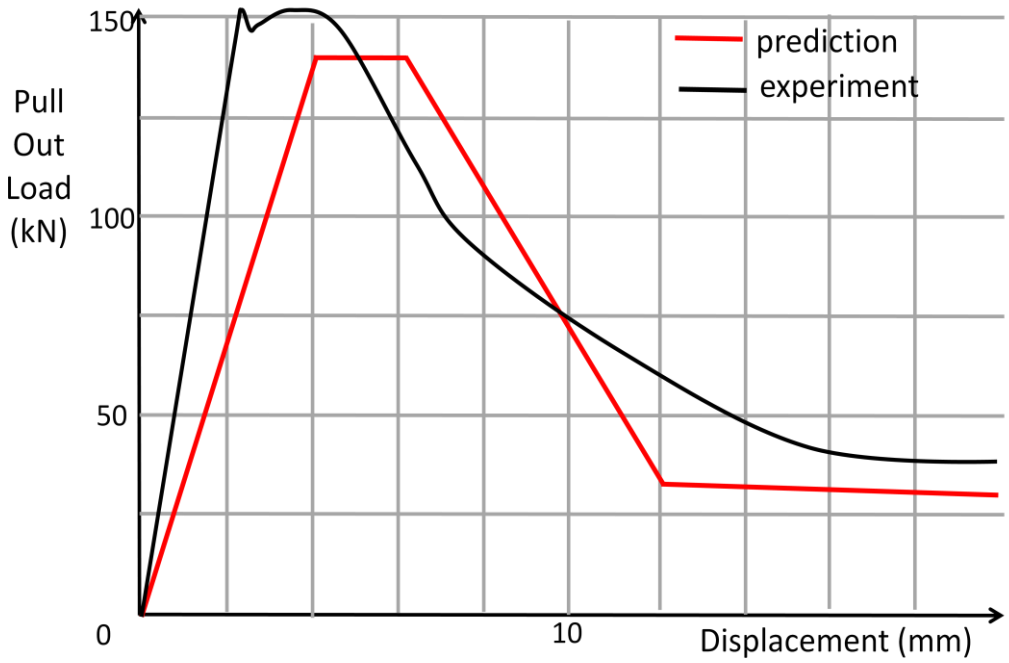

Figure 5.23 Comparison of predicted load displacement curve of T2 bolt with experimental performance.

5.8 DISCUSSIONS AND FURTHER WORK

5.8.1 Other failure modes

There are also other failure modes of rock bolting in addition to the identified failure modes. Firstly, if the bolt rib spacing is larger or confining material is ductile, the rebar stem will separate to the resin thoroughly. In this case, a pressure profile will be established (Figure 5.24).

Secondly, the confining pressure can increase locally to exceed the compressive strength of the grout, such as large rib spacing bolts. As compressive failure occurs in this situation, the failure mechanism is complicated. For example, using the same calculation procedure as done for T2 SP=12.5mm bolt, the confining pressure will be

beyond 200MPa if the parallel shear failure would commence for T2 SP=37.5mm bolt. It indicates that compressive failure of the resin annulus will occur prior to shear failure.

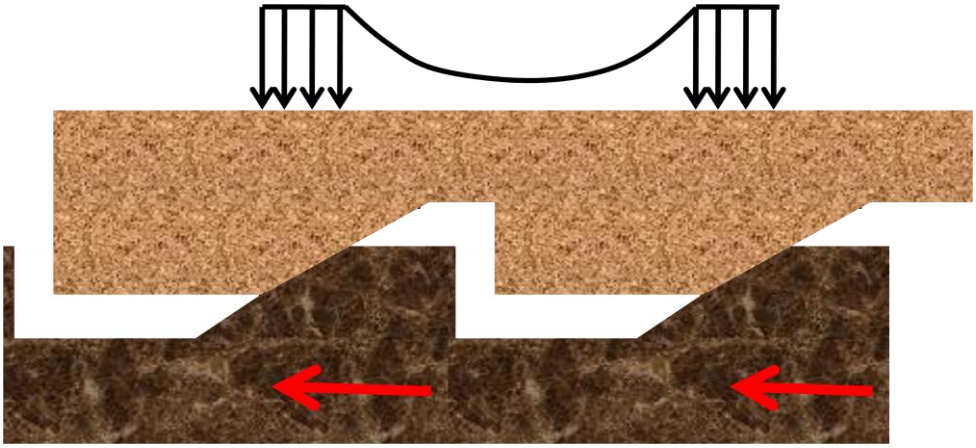

Figure 5.24 Pullout in ductile confinement material.

Thirdly, as demonstrated in Figure 5.17 and equation (5.27), the higher confining pressure the smaller the most vulnerable dilational slip angle. The dilational slip failure may occur multiple times as shown in Figure 5.25. In this case, the slipping angle will be less than 27°. The half space theory may be suitable to determine the secondary slip angle for this situation, and/or iterating calculations may be employed.

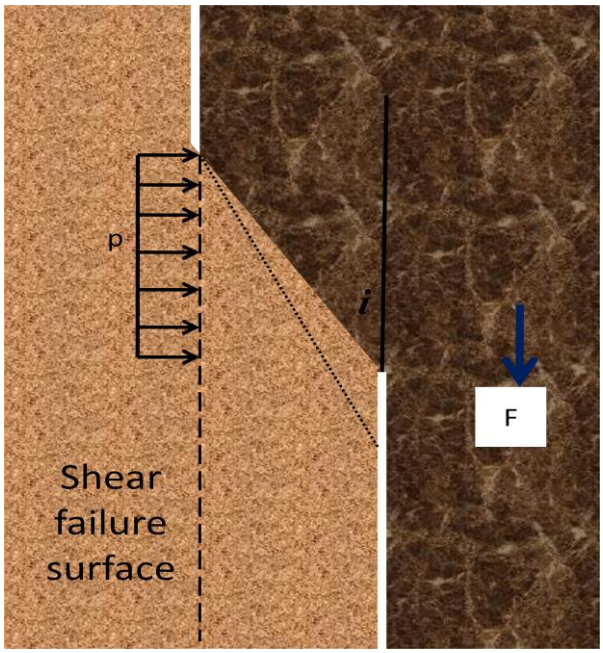

Figure 5.25 Secondary dilational slip failure of the grout material (dotted line).

There may be other failure modes. However, from a practical point of view, dilational slip failure and parallel shear failure are the major modes of rock bolting failure. They are persistently identified in the laboratory and in the field (Figures 4.16, 4.17, 4.18, 4.23, 4.41, 4.43, 4.44, 4.50 5.26 and 5.27).

Figure 5.26 Dilational slip in pullout tests using concrete block confinement.

Figure 5.27 CNS tests show that dilational slip is common at low confinement stress while parallel shear failure is observed at high confinement (Aziz, 2002).

5.8.2 Pullout stages of T2 bolts and associated mechanics

Aided with derived equations presented in this chapter, the pullout procedure of T2 bolt can now be better understood. The load displacement curve can be divided into six stages, as shown in Figure 5.28.

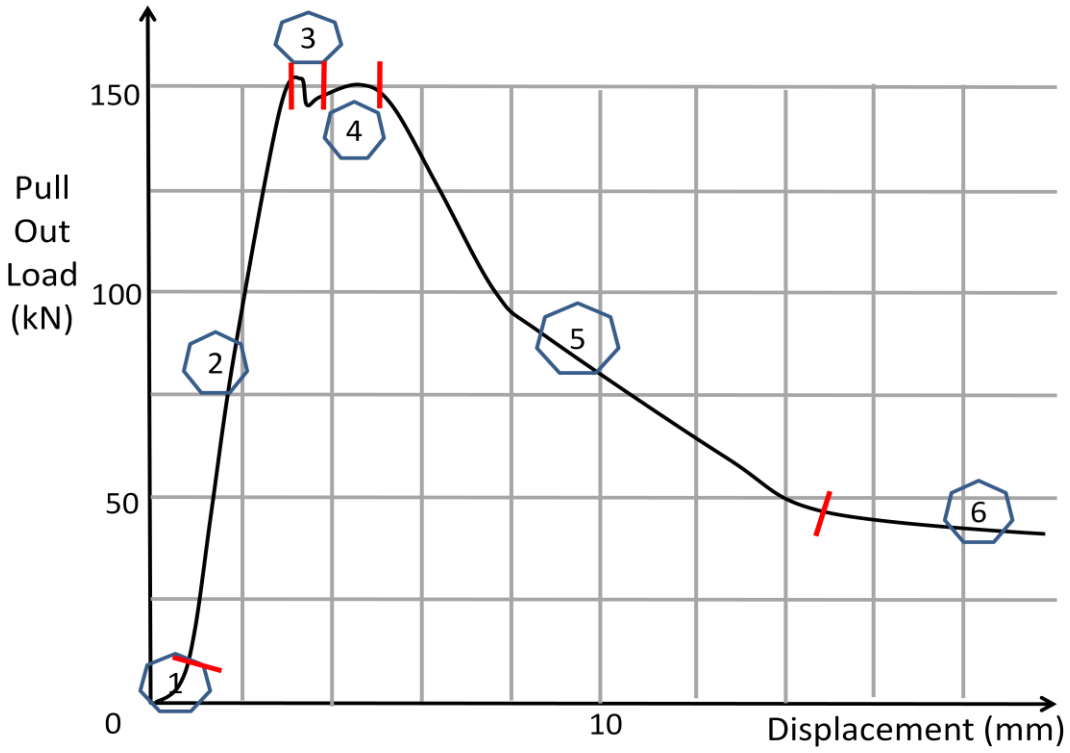

Figure 5.28 Pull out stages of T2 bolt.

Stage 1 is characterised by low axial load but large displacement compared with the later linear stage. It is reasonable to assume that it is caused by the movement of machine/bolting loading assembly rather than the bond. Hence, it is eliminated from the graph and the modified graph is shown in Figure 5.29.

Stage 2 is the initial linear stage, and is often called as “elastic stiffness” of the bond. To the best knowledge of the author, there is no literature showing the composition of the bond stiffness. A preliminary analysis is provided in the next section however, how to determine the magnitude of the initial stiffness of rock bolting is still unknown.

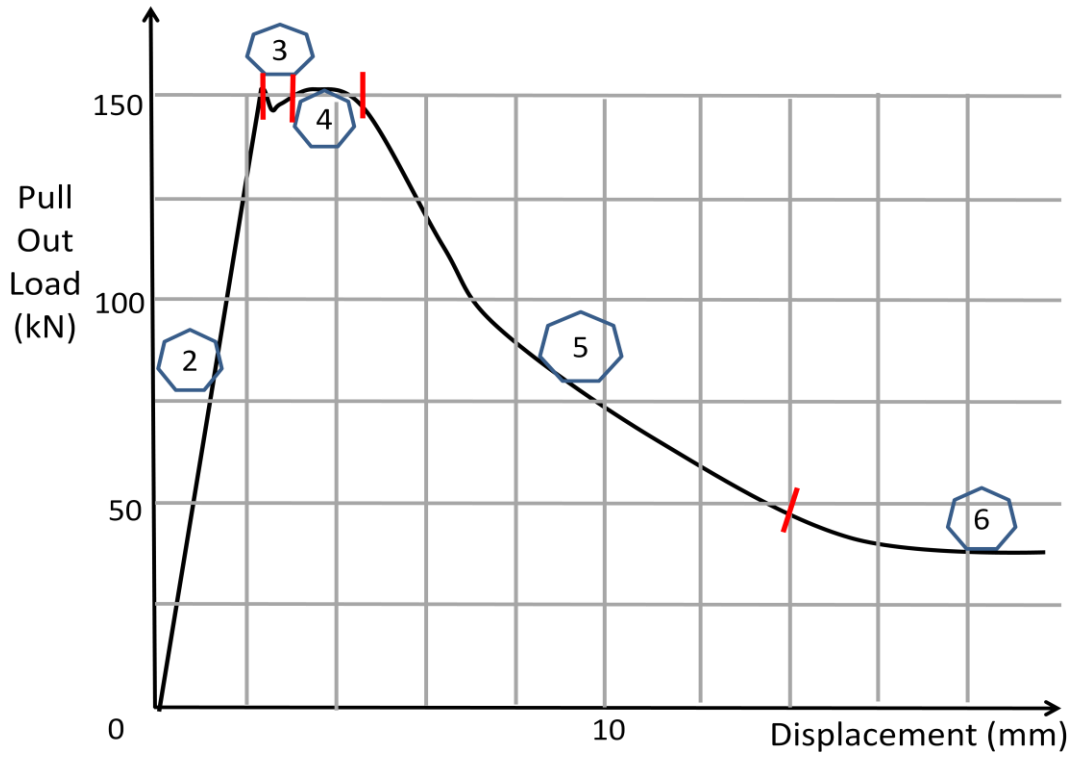

Figure 5.29 The bond behaviour of T2 bolt during pullout test.

Nevertheless, dilational slip has been started in this stage. During dilation, the resin annulus tends to separate from the bolt core and the initial confining pressure is disturbed. As the spacing of the bolt surface profile is not large, the pressure around the bolt stem will be close to zero. Consequently, equation (5.17) is established as failure criterion in this situation.

Stage 3 is characterised by sudden strain release, indicating commencement of displacement of the unloaded end of the bolt (as discussed in 4.3.2). It is presumed that the cohesion of the grout along the slipping direction drops to zero. However, the strength along directions other than the dilational slipping surface is not affected by the failure. As a result, the resistant force is recovered after slipping (as discussed in section 4.2.2).

Stage 4 is the immediate post failure phase. The failure direction is aligned to the axial direction. The cohesion along the axial failure is still at its full strength, and the

confining pressure is presumed to be gradually re-distributing to an even state.

Stage 5 is the process of cohesion decaying. It should last for approximately one rib spacing from stage 3. And in stage 6, the bond has only residual frictional strength.

5.8.3 Preliminary study on initial bond stiffness

It is necessary to clarify the initial linear bond stiffness for predicting the bond behaviour accurately. The relationship between the shear force τ_b and the displacement u is often simplified as $\tau_b=ku$ where k is the tangential stiffness of the interface. In order to satisfy the pullout test results, k can be idealised by specific bilinear, trilinear or hyperbolic curves. However, the accurate determination of the initial bond stiffness is not easy because the shear stress along the rock bolt is not uniform in a general pullout test. In addition, the shear deformation along the interface comprised both an inelastic deformation of the surrounding materials before slipping, and a relative displacement at the interface during slipping.

- **Radial strain of resin**

From section 5.7.4, the internal radial stress is 28.2 MPa during the bond failure. Using wedge theory, for the resin annulus radial displacement is:

$$\mathrm{u}_{\mathrm{resin-radial}} = \varepsilon L = \frac{p}{E} \cdot L = \frac{28.2}{10500} \cdot 4.2 = 0.011 \text{ mm}$$

In which the annulus thickness $L = 4.2$mm and Resin $E = 10500$MPa.

- **Radial expansion of the sleeve**

In the thick walled cylinder theory (section 5.2.2), the relationship of internal pressure and radial displacement of the steel sleeve have been derived as:

$$u_{r=a} = 0.000204\, p_1 \text{ (mm)}$$

The pressure p_1, can be determined via wedge theory as:

$$r \cdot p = R \cdot p_1$$

$$\therefore p_1 = \frac{r \cdot p}{R} = \frac{11.1 \times 28.2}{15.3} = 20.5\ MPa$$

where: r, R are inner and outer radius of the resin annulus

Consequently,

$$u_{sleeve-radial} = 0.000204 \times 20.5 = 0.04 \text{ (mm)}$$

The total radial displacement of the bond is the sum of resin compression (A) and sleeve expansion (B), that is:

$$u_r = 0.011 + 0.04 = 0.05 \text{ (mm)}$$

If slip angle *i*=27°, the axial displacement caused by the dilation will be:

$$u_{a1} = \frac{u_r}{\tan 27°} = \frac{0.05}{\tan 27°}$$

$$= 0.1 \text{ mm}$$

Therefore, the internal pressure can increase very quickly to a high value in the elastic stage if dilational slip occurs.

- **Shear displacement of resin**

Shear strain of the resin can be expressed as:

$$\gamma = \tau/G\ , \gamma = tan\gamma = u_a/t \quad \text{and} \quad \tau = F/A$$

where:

$\tau =$ shear stress,

$G =$ shear modulus,

$\gamma =$ shear strain,

$t =$ annulus thickness,

$F =$ axial load and

$A =$ shear area

Thus, the axial displacement caused by shear is:

$$u_{a2} = \frac{F \cdot t}{A \cdot G}$$

$$= \frac{F \cdot t}{2\pi RL \cdot \frac{E}{2(1+v)}} = \frac{15500 \times 4.2}{744 \times \frac{10500}{2(1+0.3)}}$$

$$= 0.022 \text{ mm}$$

- **Bolt elongation**

The elongation of one embedded bolt profile can be calculated using:

$$u_a = \frac{FL}{AE}$$

Where:

F=axial load,

A=bolt cross section,

L=length of bolt spacing and

E=elasticity.

Thus:

$$u_a = \frac{FL}{AE} = \frac{16400 \times 12.5}{387 \times 200000} = 0.00265 \text{ mm}$$

Total elongation of embedded bolt is:

$$u_{a3} = 0.00265 \times 115/12.5 = 0.024 \text{ mm}$$

The free bolt, approximately 300mm, used to conduct experiment is also loaded, therefore:

$$u_{a4} = \frac{FL}{AE} = \frac{150000 \times 300}{387 \times 200000} = 0.58 \text{ mm}$$

In the elastic stage, the sum of the axial displacement will be:

$$u_a = u_{a1} + u_{a2} + u_{a3} + u_{a4} = 0.1 + 0.022 + 0.024 + 0.58 = 0.73 \text{ mm}$$

The experimental data showed that the displacement during the linear stage of loading is about 2.2 mm. It means that, around 1.5mm of axial displacement is generated from plastic deformation. Further loading-unloading tests during the initial linear stage, are required to determine the components of true stiffness and plastic deformation.

5.9 CONCLUSIONS

The following conclusion can be draw:

- Parallel shear failure and dilational slip are two major failure modes when an axial load is applied to cause failure of the rock bolt.
- Direct parallel shear failure is the simplest failure mode, which always occurs on smooth bars and closely spaced rebars. After introducing Mohr-Coulomb's shear failure criterion, this failure mode can be described by equations (5.11) to (5.15). The theoretical prediction was compared with experimental data and shows good agreement.
- For dilational slip failure, the dilational slip face angle is different to the rib face angle.

- A universal upper limit of dilational slipping face angle can be calculated as the complementary angle of the internal friction angle of the grouting material.
- For a known bolt, the domain of the dilational slip face angle can be further narrowed using equation (5.25). Consequently, the grouting material between the bolt profiles can be divided into three parts, one will be part of the bolt profile moving along with the bolt, one will undergo shear failure and the rest will remain unaffected.
- The most vulnerable dilational slip face angle for a known bolt can be found by graphical method demonstrated in section 5.7.2.
- The governing equation of dilational slip failure has been derived under Mohr-Coulomb's failure criterion (equation 5.27). Application example of optimum bolt design is offered.
- The failure mode of T2 bolt in pullout tests is predicted as parallel shear failure after dilation. The predicted pullout load displacement curve shows good agreement with experimental results.
- For moderate rib spacing bolt similar to T2 bolts, the mechanism associated with each pullout stage is identified.
- A preliminary study of initial linear stiffness is conducted. It is found that plastic deformation is the dominant component in this stage.

CHAPTER SIX

BOLT PROFILE ANALYSIS USING THE HALF SPACE METHOD

BOLT PROFILE ANALYSIS USING THE HALF-SPACE METHOD

6.1 INTRODUCTION

The anchorage capacity of fully grouted rock bolts has been studied for many years, however the bolt rib profile and its effect on bolt shear resistance is poorly understood. In most cases, rockbolting failure is not due to the excessive tension in the bar; rather it is related to slip. Therefore bond is recognised as a critical parameter in reinforced rock design. To improve bolt loading capacity through the steel bolt profile design, it is necessary to have an understanding of the interaction between the rock bolt and the surrounding mediums.

In Chapter five, the failure modes of rockbolting subjected to axial loading have been categorised into parallel shear failure of the grouting material and dilational slip at the bolt-grout interface. The mechanisms of failure, namely “direct parallel shear failure”, “dilational slip failure” and “parallel shear failure after dilation”, were identified and formulated by modes. To improve these models, as well as to get a better understanding of the interactions of each element in rockbolting, it is necessary to investigate the stress field around the bolt when subjected to axial loading.

Furthermore, as demonstrated in Chapter four and Chapter five, radial dilation always occurs, more or less, when a rock bolt is subjected to axial load. When the axial load of the bolt increases, the radial displacement of the grout material commences causing the majority of the bolt-resin interface to tend to separate, as shown in Figure 5.12. This situation can be represented by uniformly distributed load acting on the half-space surface. Hence, the stress field introduced by axial load of the bolt can be evaluated by half-space theory.

Boussinesq derived fundamental solutions for vertical loading on infinite or semi-infinite elastic media. Cerutti determined solutions for horizontal tractions (cited by Poulos and Davis, 1974). While loading an infinite strip on the surface of a semi-infinite mass (Figure 6.1), by integration of Boussinesq's results, the stress tensor within the media can be calculated as a function of the load, location and material properties.

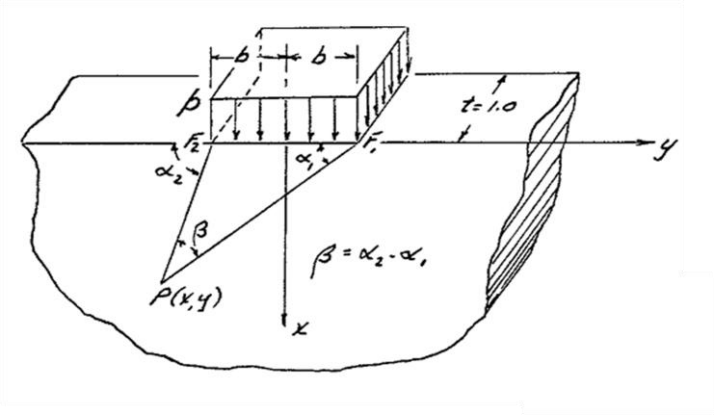

Figure 6.1 Uniform strip load on half space (Richards, 2001).

In this chapter, the equations of elastic half-space are presented as they are the governing equations of the proposed approach. Accordingly, the stress field around the bolt can be evaluated using several assumptions. A weakness plane which is spanning the tips of the bolt rib profiles is proposed, followed by a study of the weakness plane using Mohr-Coulomb's failure criterion. The derived mathematical expressions consist of the axial load of the bolt, mechanical properties of the grout material and the bolt rib geometry. A parametric study of the rib profile was conducted to investigate the influence of bolt profile on load transfer of the rockbolting system. Finally, a brief discussion on limitations of this approach is provided.

6.2 HALF-SPACE THEORY

6.2.1 Boussinesq's problem

The coordinate system and symbol signs are often different from text to text, which leads to different formula expressions for the same problem. In this study, the half-space coordinates and symbols used by Poulos and Davis (1974) are adopted. A positive stress indicates compression and a positive shear stress indicates that the shear stress acts on the positive surface towards positive direction.

For a point load, *P*, applied on the surface of a semi-infinite mass (shown in Figure 6.2), the stress field was expressed by Poulos and Davis (1974):

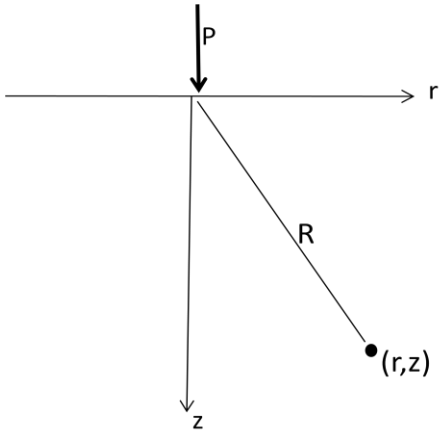

Figure 6.2 Point load applied on the surface of a semi-infinites mass (Boussinesq's problem)

$$\sigma_{zz} = -\frac{3Pz^3}{2\pi R^5} \tag{6.1}$$

$$\sigma_{rr} = -\frac{P}{2\pi R^2}\left[\frac{-3r^2 z}{R^3} + \frac{(1-2v)R}{R+z}\right] \tag{6.2}$$

$$\sigma_{\theta\theta} = -\frac{(1-2v)P}{2\pi R^2}\left[\frac{z}{R} - \frac{R}{R+z}\right] \tag{6.3}$$

$$\theta = \frac{(1+v)Pz}{\pi R^3} \tag{6.4}$$

$$\sigma_{rz} = \frac{3Prz^2}{2\pi R^5} \tag{6.5}$$

$$u_z = -\frac{P(1+v)}{2\pi ER}\left[2(1-v) + \frac{z^2}{R^2}\right] \tag{6.6}$$

$$u_r = -\frac{P(1+v)}{2\pi ER}\left[\frac{rz}{R^2} - \frac{(1-2v)r}{R+z}\right] \tag{6.7}$$

6.2.2 Cerutti's problem

For a horizontal point load acting along the surface of a semi-infinite mass, shown in Figure 6.3, the stress tense can be expressed as (Poulos and Davis, 1974):

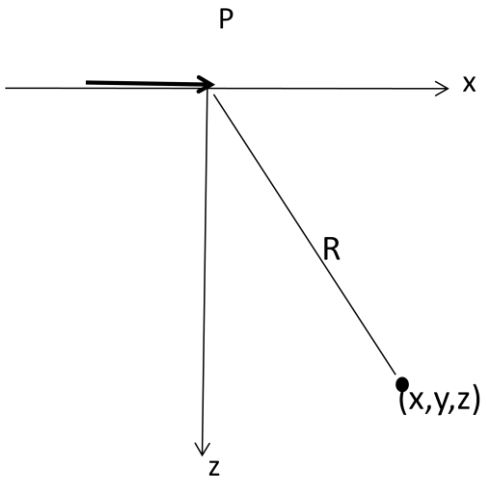

Figure 6.3 Horizontal point load acting along the surface of a semi-infinite mass (Cerutti's problem)

$$\sigma_{zz} = -\frac{3Pxz^2}{2\pi R^5} \tag{6.8}$$

$$\sigma_{xx} = -\frac{Px}{2\pi R^3}\left[\frac{-3x^2}{R^2} + \frac{1-2v}{(R+z)^2}\left(R^2 - y^2 - \frac{2Ry^2}{R+z}\right)\right] \tag{6.9}$$

$$\sigma_{yy} = -\frac{Px}{2\pi R^3}\left[\frac{-3y^2}{R^2} + \frac{1-2v}{(R+z)^2}\left(R^2 - x^2 - \frac{2Rx^2}{R+z}\right)\right] \tag{6.10}$$

$$\theta = \frac{(1+v)Px}{\pi R^3} \tag{6.11}$$

$$\sigma_{xy} = -\frac{Py}{2\pi R^3}\left[\frac{-3x^2}{R^3} + \frac{1-2v}{(R+z)^2}\left(-R^2 + x^2 + \frac{2Rx^2}{R+z}\right)\right] \quad (6.12)$$

$$\sigma_{yz} = \frac{3Pxyz}{2\pi R^5} \quad (6.13)$$

$$\sigma_{xz} = \frac{3Pzx^2}{2\pi R^5} \quad (6.14)$$

$$u_z = \frac{P(1+v)}{2\pi ER}\left[\frac{xz}{R^2} + \frac{(1-2v)x}{R+z}\right] \quad (6.15)$$

$$u_x = \frac{P(1+v)}{2\pi ER}\left[1 + \frac{x^2}{R^2} + (1-2v)\left(\frac{R}{R+z} - \frac{x^2}{(R+z)^2}\right)\right] \quad (6.16)$$

$$u_y = \frac{P(1+v)}{2\pi ER}\left[\frac{xy}{R^2} - \frac{(1-2v)xy}{(R+z)^2}\right] \quad (6.17)$$

6.2.3 Uniformly distributed load

By integration of solutions of Boussinesq's problem, it is found that for uniformly distributed load on the surface of a semi-infinite mass, if loading is vertical on an infinite strip, shown in Figure 6.4.1, then stresses yield:

$$\sigma_z = \frac{p}{\pi}[\alpha + sin\alpha \cos(\alpha + 2\delta)] \quad (6.18)$$

$$\sigma_x = \frac{p}{\pi}[\alpha - sin\alpha \cos(\alpha + 2\delta)] \quad (6.19)$$

$$\tau_{xz} = \frac{p}{\pi}[sin\alpha \sin(\alpha + 2\delta)] \quad (6.20)$$

If loading is horizontal on an infinite strip (Figure 6.4.2), by integration of solutions of Cerutti's problem, the stress tensor is described as:

$$\sigma_z = \frac{q}{\pi}[sin\alpha \sin(\alpha + 2\delta)] \quad (6.21)$$

$$\sigma_x = \frac{q}{\pi}\left[ln\frac{R_1^2}{R_2^2} - sin\alpha \sin(\alpha + 2\delta)\right] \quad (6.22)$$

$$\tau_{xz} = \frac{q}{\pi}[\alpha - sin\alpha \cos(\alpha + 2\delta)] \qquad (6.23)$$

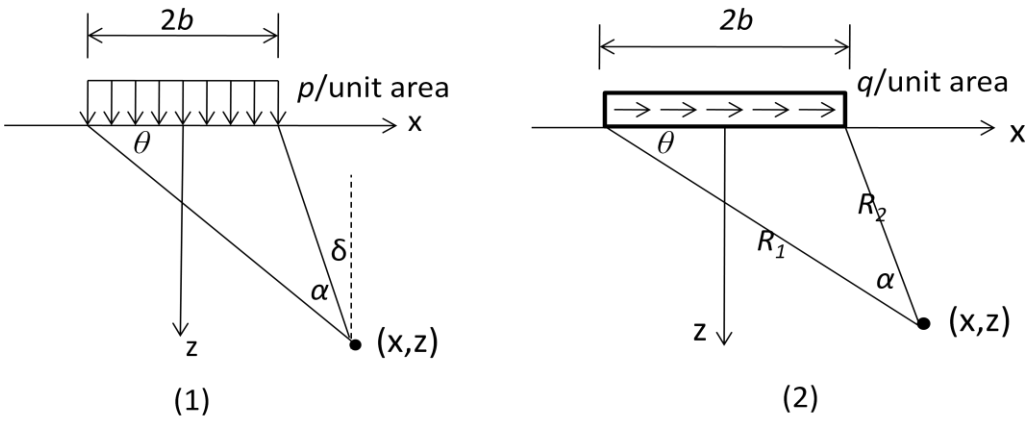

Figure 6.4 Uniformly distributed (1) vertical load *p* and (2) horizontal load *q* on the surface of a semi-infinite mass

6.3 METHODOLOGY AND GOVERNING EQUATIONS

Clearly, the mathematical description of the physical interaction between the bolt rib profile and the surrounding resin enables a thorough understanding of the bolt profile behaviour and together with parametric studies provide a method to improve the bolt rib profile configuration which is the subject of this thesis.

To investigate the influence of bolt rib profile on the load transfer system of rock bolting, a single spacing between two bolt ribs is examined. The bolt rib profile geometry is described using the variables (Figure 6.5):

- *a* = half rib tip width
- *b* = rib face length
- *c* = bolt stem length
- *L* = distance between two rib tips (equal to profile spacing – rib top width)

- θ = rib face angle

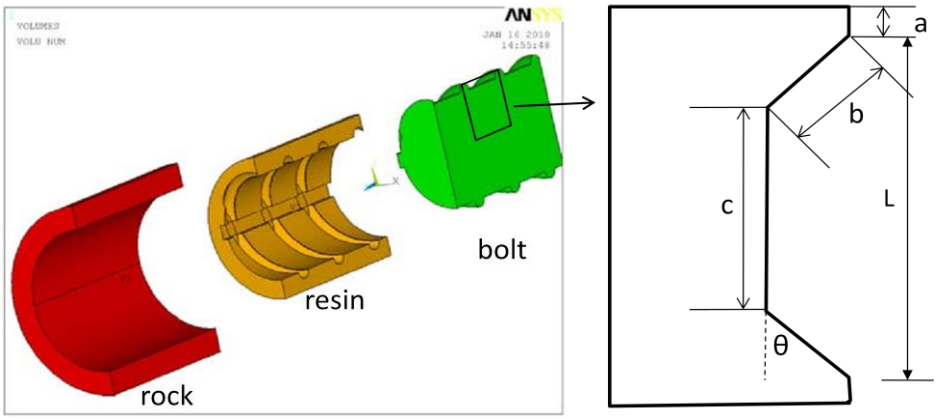

Figure 6.5 Rockbolting system and rib parameters of one bolt profile used in this study.

The rockbolt problem is often studied as an axisymmetric problem in 3-dimensions. When the bolt is subjected to an axial force, each bolt segment will experience a net axial load. This resultant force is then transferred into the resin via the rib profile. The stress distribution within the resin can be calculated according to solutions of half-space theory. In the resin, various weakness planes can be assumed as shown in Figure 6.6. For each proposed weakness plane, critical load can be calculated according to a nominated failure criterion. By comparing the sustainable load on each plane, the weakest plane would most likely commence the bond failure.

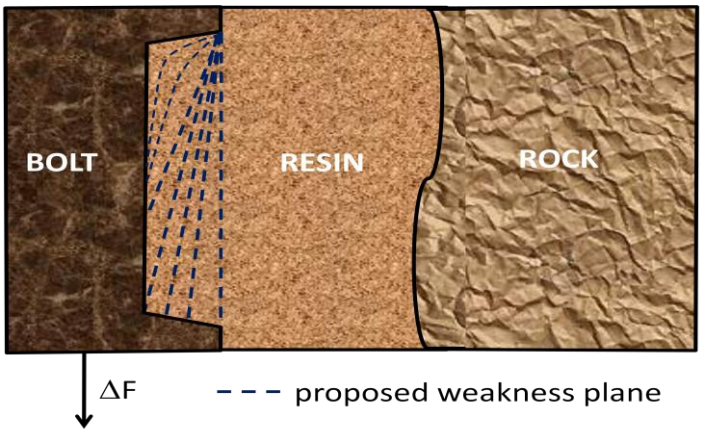

Figure 6.6 A schematic drawing of a single spacing and proposed weakness planes.

It is essential to test a large number of weakness planes to establish the failure plane

that would most likely fail. It is also necessary to confirm the theoretical calculation with experiments. However, to observe the commencement of the resin failure in the laboratory is rather difficult. Aziz (2002) used the flattened surface of a real bolt to examine the resin shear failure under CNS conditions in the laboratory, as shown in Figure 6.7-a. The failure mode of the resin covered on this flattened plate which contains all surface features of the bolt is relatively easy to identify. This technique is introduced in this study (Figure 6.7-b), whereby the axisymmetric rockbolting problem is reduced to a plane stress problem so that the theoretical solutions of half space are applicable and controlled experiments may be achievable.

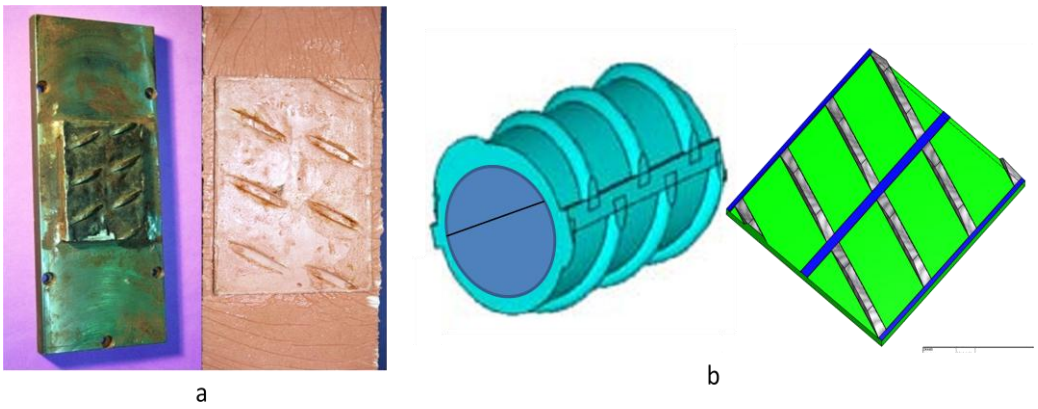

Figure 6.7 (a) Flattened real bolt profile. (b) Designed experimental plate with all bolt rib features.

Stress analysis on this flattened plate is a half-space problem. Hence, the stress tensor within the resin can be calculated using equation (6.18) to (6.23) if the load is uniformly distributed. In addition, according to geometry shown in Figure 6.4.1, it is found that:

$$\alpha + \delta + \theta = \frac{\pi}{2} \tag{6.24}$$

By eliminating δ, equations (6.18) to (6.20) can be simplified to:

$$\sigma_z = \frac{p}{\pi}[\alpha - \sin\alpha\cos(\alpha + 2\theta)] \tag{6.25}$$

$$\sigma_x = \frac{p}{\pi}[\alpha + \sin\alpha\cos(\alpha + 2\theta)] \quad (6.26)$$

$$\tau_{xz} = \frac{p}{\pi}\sin\alpha\sin(\alpha + 2\theta) \quad (6.27)$$

Equations (6.21) to (6.23) can be simplified to:

$$\sigma_z = \frac{q}{\pi}\sin\alpha\sin(\alpha + 2\theta) \quad (6.28)$$

$$\sigma_x = \frac{q}{\pi}\left[ln\frac{R_1^2}{R_2^2} + \sin\alpha\sin(\alpha + 2\theta)\right] \quad (6.29)$$

$$\tau_{xz} = \frac{q}{\pi}[\alpha + \sin\alpha\cos(\alpha + 2\theta)] \quad (6.30)$$

The equations (6.25) to (6.30) are the governing equations of this approach.

6.4 STRESS ANALYSIS OF A BOLT SUBJECTED TO AXIAL LOADING

6.4.1 Problem description and assumptions

When the bolt is loaded, the load is transferred to the resin as shown in Figure 6.8. The direction of the load is dependent on the bolt profile, while the magnitude depends on both the bolt profile and the material properties. To investigate the failure of the resin between two bolt ribs, a plane of weakness spanning between the bolt profile tips is assumed as shown in Figure 6.8.

During bolt loading, the distributed loads within the bolt can be represented as shear forces and normal forces. Assuming that the initial bonding shear forces *S1, S3, S4* and *S5* between the bolt and the resin are small and the tensile stress between the bolt and resin is also small, then:

- *S1* = *S3* = *S4* = *S5* ≈ 0
- *N* (tension) ≈ 0

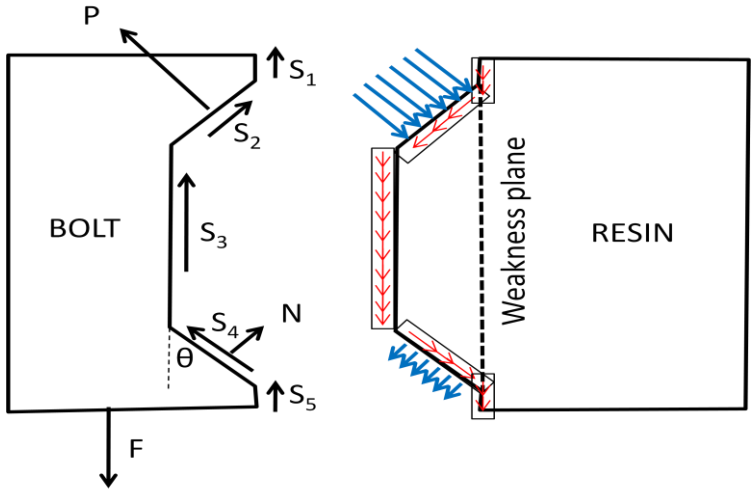

Figure 6.8 Load transfer between the steel bolt and the fully encapsulated resin.

Under these assumptions, the free body diagram of the bolt can be simplified as shown in Figure 6.9, where only one normal force and one shear force to the inclined bolt profile remains. In most cases these stress components play a major role in stress distribution within the resin.

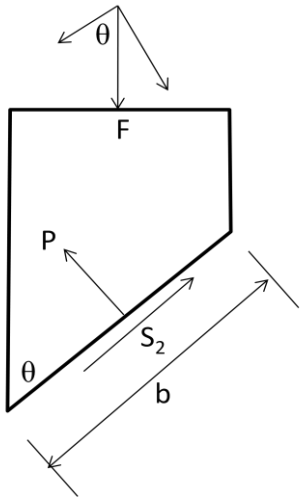

Figure 6.9 Free body diagram of the bolt after approximation

Assuming the stresses along the bolt profile face are evenly distributed (Figure 6.8), for static equilibrium of the bolt (Figure 6.9), the normal and shear stresses at the rib face can be obtained as:

$$p = \frac{F sin\theta}{b} \quad and \quad s_2 = q = \frac{F cos\theta}{b} \tag{6.31}$$

Where:

F = Net axial force on one bolt profile

θ = bolt rib face angle

b = bolt rib face length (Figure 6.5)

p = Normal load on bolt face b

s_2= q=Shear load on bolt face b

Both Boussinesq's and Cerutti's problems are for the half-space problems. However, the contact of bolt and resin is not an exact half-space because of irregularities of the rib profile. A FLAC simulation was conducted to validate the boundary simplification. The model simulated a section of the steel bolt shown in Figure 6.10-a with the rib face angle θ = 45˚. The axial force was applied to the bolt and the modelled shear stress contours were plotted as shown in Figure 6.10-a. The modelled contours were compared with the shear stress calculated using the Boussinesq's and Cerutti's equations (Figure 6.10-b). Both the calculated and modelled contours were in reasonable agreement indicating that the numerical assumptions can be used. Properties used in the calculations and in the FLAC model are shown in Table 6.1.

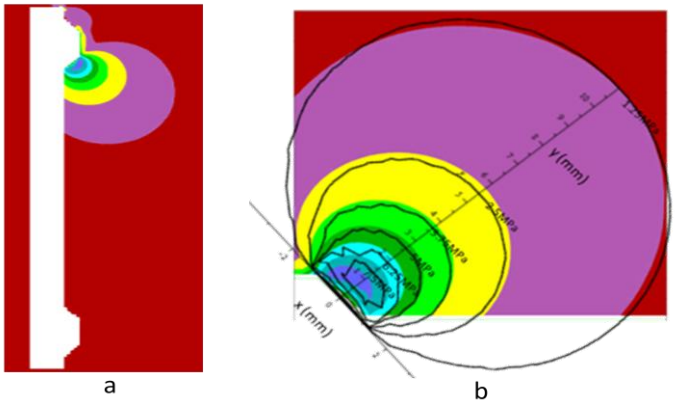

Figure 6.10 (a) Shear stress distribution in FLAC model. (b) Comparison of calculated and modelled shear stresses

Table 6. 1 Material properties used in calculations and FLAC model

UCS (MPa)	70
Shear strength (MPa)	16
E (GPa)	10.5
Poisson's ratio	0.25

The resin and the rock are two materials with a common boundary. Study of rock and resin stiffness and resin failure near the bolt indicates that they are of comparable stiffness. Therefore, for the purpose of stress analysis, the resin and the rock can be considered as being one material. In practice the resin-rock boundary is invariably rifled due to drilling with a wing bit, as shown in Figure 6.11. The analysis can be simplified by extending the resin boundary to infinity as failure along the resin-rock interface due to rifling effect is unlikely to occur.

Figure 6.11 Rifled bolt hole images (Aziz, 2004).

Three different failure criteria can be used in the calculations. These are the shear failure, the Mohr-Coulomb and the distortional energy (Von Misses) failure criteria. From the three methods or models the Mohr-Coulomb criterion of failure is chosen for this study. Accordingly, the normal and shear stresses to the chosen weakness plane must be calculated.

6.4.2 Stresses on the assumed failure plane due to normal load

To apply Boussinesq's equations in calculations of the normal and shear stress along the studied failure plane, the resin section is rotated as shown in Figure 6.12 so that the load (*p*) becomes vertical. Solid line PQ represents the assumed plane of failure connecting two corners of the bolt ribs, and the bolt rib face angle θ that is between the line of load application and line PQ. Point A represents any point on the plane of weakness, and the variable (*h*) indicates its distance from point P, i.e. *h*=|AP|.

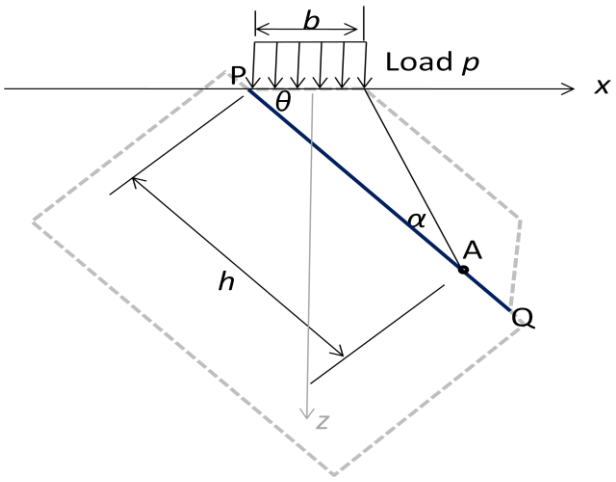

Figure 6.12 Schematic of the loading diagram with the assumed failure plane

For convenience, line PQ is rotated around the x-axis and coordinate system is re-set as shown in Figure 6.13.

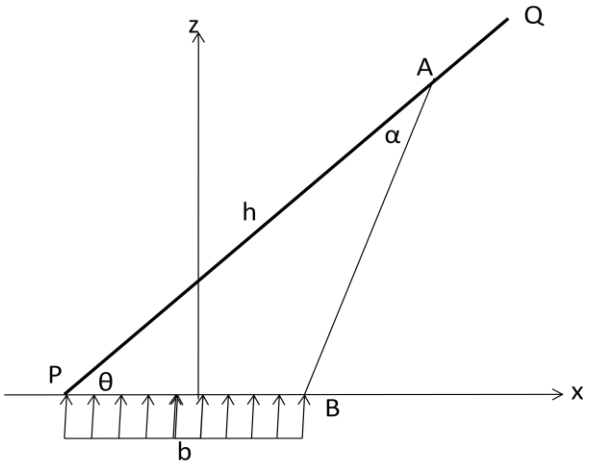

Figure 6.13 Further rotation of the loading diagram with the assumed plane of failure

The location parameters in the governing equations α, R_1 and R_2 have to be substituted by the rib geometry which is described by parameters b, h and θ. In ΔAPB:

$$\mathrm{AP} = R_1 = h \tag{6.32}$$

By cosine rule:

$$\mathrm{AB} = R_2 = \sqrt{b^2 + h^2 - 2bhcos\theta} \tag{6.33}$$

And by sine rule:

$$\frac{sin\alpha}{b} = \frac{sin\theta}{\mathrm{AB}}$$

Therefore:

$$\sin\alpha = \frac{b\sin\theta}{\sqrt{b^2 + h^2 - 2bh\cos\theta}} \tag{6.34}$$

It can be found that:

$$\cos\alpha = \frac{h - b\cos\theta}{\sqrt{b^2 + h^2 - 2bh\cos\theta}} \tag{6.35}$$

Hence:

$$\alpha = \tan^{-1}\frac{b\sin\theta}{h - b\cos\theta} \tag{6.36}$$

In addition,

$$\mathrm{PQ} = L = c + 2b\cos\theta \tag{6.37}$$

Where:

b, c, L and θ are rib geometrical parameters shown in Figure 6.5;

α, R_1 and R_2 are positioning parameters used in the governing equations shown in Figure 6.4 and 6.13.

h is variable

6.4.3 Stress transformation to supposed failure surface

The stress tensor calculated using the Boussinesq and Cerruti's equations are used to calculate the shear and normal stress along the plane of proposed weakness. Since the final solutions need to calculate stress parallel and perpendicular to the failure plane, to simplify the calculations, the plane stress vector needs to be transformed to a coordinate system parallel to the plane of failure. Stress transformation is performed as shown in Figure 6.16 by using equations:

$$\sigma_{XX} = \frac{1}{2}(\sigma_{xx} + \sigma_{yy}) + \frac{1}{2}(\sigma_{xx} - \sigma_{yy})cos2\theta + \tau_{xy}sin2\theta$$

$$\sigma_{YY} = \frac{1}{2}(\sigma_{xx} + \sigma_{yy}) - \frac{1}{2}(\sigma_{xx} - \sigma_{yy})cos2\theta - \tau_{xy}sin2\theta$$

$$\tau_{XY} = -\frac{1}{2}(\sigma_{xx} - \sigma_{yy})sin2\theta + \tau_{xy}cos2\theta$$

Accordingly, the normal and shear stress to the failure plane would be:

$$\sigma_n = \frac{1}{2}(\sigma_x + \sigma_z) - \frac{1}{2}(\sigma_x - \sigma_z)cos2\theta - \tau_{xz}sin2\theta \quad (6.38)$$

$$\tau = -\frac{1}{2}(\sigma_x - \sigma_z)sin2\theta + \tau_{xz}cos2\theta \quad (6.39)$$

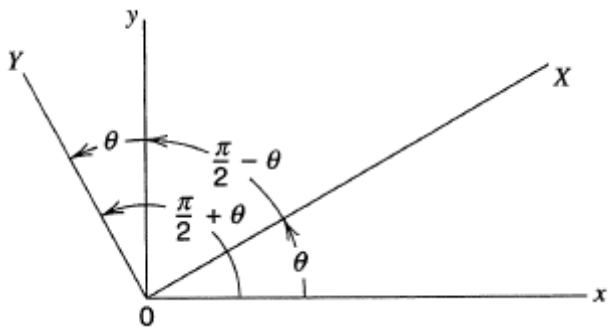

Figure 6.14 Stress transformation diagram (Boresi *et al*, 1993)

6.4.4 Calculations of resultant stresses caused by the normal load

The normal stress, which is introduced by axial stress component *p*, to the assumed failure plane is calculated. Substituting equations (6.25), (6.26) and (6.27) into equation (6.38) yields:

$$\int \sigma_{n-p} dh = \int \left[\frac{p}{\pi}\alpha - \frac{p}{\pi}\sin\alpha\cos(\alpha+2\theta)\cos 2\theta - \frac{p}{\pi}\sin\alpha\sin(\alpha+2\theta)\sin 2\theta\right] dh$$

$$= \frac{p}{\pi}\int [\alpha - \sin\alpha\,(\cos(\alpha+2\theta)\cos 2\theta + \sin(\alpha+2\theta)\sin 2\theta)]dh$$

$$= \frac{p}{\pi}\int [\alpha - \sin\alpha\cos\alpha]dh \qquad (6.40)$$

In a similar manner, the shear stress on the weakness plane is obtained by substituting equations (6.25) to (6.27) into equation (6.39):

$$\int \tau_p\, dh = \int \left[-\frac{p}{\pi}\sin\alpha\cos(\alpha+2\theta)\sin 2\theta + \frac{p}{\pi}\sin\alpha\sin(\alpha+2\theta)\cos 2\theta\right] dh$$

$$= \frac{p}{\pi}\int \sin\alpha\,[\sin(\alpha+2\theta)\cos 2\theta - \cos(\alpha+2\theta)\sin 2\theta]\,dh$$

$$= \frac{p}{\pi}\int \sin^2\alpha\, dh \qquad (6.41)$$

To solve $\int \sigma_{n-p} dh$ and $\int \tau_p\, dh$ further we need to calculate $\int \alpha\, dh$, $\int sin\alpha\, cos\,\alpha\, dh$ and $\int sin^2\alpha dh$.

6.4.5 Calculations of resultant stresses caused by the shear load

The stress calculations due to the shear load are similar to the normal load calculations presented in section 6.4.4.

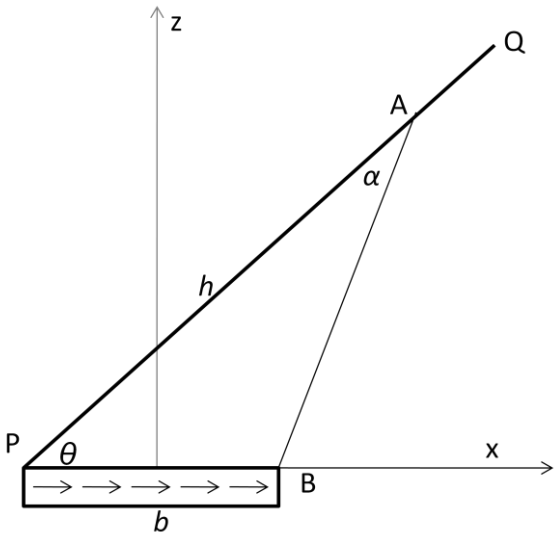

Figure 6.15 Shear load and the assumed plane of failure PQ.

The normal and shear stresses at the weakness plane due to load q can be calculated using equation (6.38) and (6.39). Substituting equations (6.28), (6.29) and (6.30) into equation (6.38), yields:

$$\int \sigma_{n-q} dh = \int \left(\frac{q}{2\pi} \left[ln \frac{R_1^2}{R_2^2} + 2 \sin\alpha \sin(\alpha + 2\theta) \right] - \frac{q}{2\pi} ln \frac{R_1^2}{R_2^2} \cos 2\theta - \frac{q}{\pi} [\alpha + \sin\alpha \cos(\alpha + 2\theta)] \sin 2\theta \right) \mathrm{d}h$$

$$= \frac{q}{2\pi} \int \left[(1 - \cos 2\theta) ln \frac{R_1^2}{R_2^2} + 2 \sin\alpha \sin(\alpha + 2\theta) - 2\alpha \sin 2\theta - 2 \sin\alpha \cos(\alpha + 2\theta) \sin 2\theta \right] \mathrm{d}h$$

$$= \frac{q}{\pi} \int \left[\sin^2\theta ln \frac{R_1^2}{R_2^2} - \alpha \sin 2\theta + \sin\alpha \, (\sin\alpha\cos 2\theta + \cos\alpha\sin 2\theta) - \sin\alpha \sin 2\theta \, (\cos\alpha\cos 2\theta - \sin\alpha\sin 2\theta) \right] dh$$

$$= \frac{q}{\pi} \int \left[\sin^2\theta ln \frac{R_1^2}{R_2^2} - \alpha \sin 2\theta + (\cos 2\theta + \sin^2 2\theta) \sin^2\alpha + \sin 2\theta (1 - \cos 2\theta) \sin\alpha \cos\alpha \right] dh \qquad (6.42)$$

Substituting equations (6.28), (6.29) and (6.30) into equation (6.39), yields

$$\int \tau_q \, dh = \int \left(-\frac{q}{2\pi} ln \frac{R_1^2}{R_2^2} \sin 2\theta + \frac{q}{\pi} [\alpha + \sin\alpha \cos(\alpha + 2\theta)] \cos 2\theta \right) dh$$

$$= \frac{q}{\pi} \int \left[-\frac{\sin 2\theta}{2} ln \frac{R_1^2}{R_2^2} + \alpha \cos 2\theta + \cos 2\theta \sin\alpha \cos(\alpha + 2\theta) \right] dh$$

$$= \frac{q}{\pi} \int \left[-\frac{\sin 2\theta}{2} ln \frac{R_1^2}{R_2^2} + \alpha \cos 2\theta + \cos 2\theta \sin\alpha \, (\cos\alpha \cos 2\theta - \sin\alpha \sin 2\theta) \right] dh$$

$$= \frac{q}{\pi} \int \left[-\frac{sin2\theta}{2} ln \frac{R_1^2}{R_2^2} + \alpha cos2\theta + \cos^2 2\theta \sin\alpha\cos\alpha - \sin 2\theta cos2\theta \sin^2\alpha \right] dh$$

…… (6.43)

6.4.6 Superposition of stress vector on the failure plane

Through superposition, equations (6.40), (6.41), (6.42) and (6.43) are combined and yield the final expression of the normal and shear stress on the plane of weakness:

$$\int \sigma_n dh = \int \sigma_{n-p} dh + \int \sigma_{n-q} dh$$

$$= \frac{p}{\pi} \int [\alpha - sin\alpha cos\alpha] dh + \frac{q}{\pi} \int \left[\sin^2\theta ln \frac{R_1^2}{R_2^2} - \alpha \sin 2\theta + (\cos 2\theta + \sin^2 2\theta) \sin^2\alpha + \sin 2\theta (1 - \cos 2\theta) \sin\alpha \cos\alpha \right] dh$$

…… $Substituting \;\; equation$ (6.31)

$$= \frac{F sin\theta}{\pi b} \int [\alpha - sin\alpha cos\alpha] dh + \frac{F cos\theta}{\pi b} \int \left[sin^2\theta ln \frac{R_1^2}{R_2^2} - \alpha sin2\theta + (\cos 2\theta + sin^2 2\theta) sin^2\alpha + sin2\theta (1 - \cos 2\theta) sin\alpha \cos\alpha \right] dh$$

$$= \frac{F}{\pi b}\int \Bigg[(\alpha - sin\alpha cos\alpha)sin\theta + \Bigg[sin^2\theta ln\frac{R_1^2}{R_2^2} - \alpha sin2\theta + (\cos 2\theta + sin^2 2\theta)sin^2\alpha + sin2\theta(1-\cos 2\theta)sin\alpha\cos\alpha\Bigg]cos\theta\Bigg]dh \quad (6.44)$$

For the shear stress expression, yields:

$$\int \tau\, dh = \int \tau_p\, dh + \int \tau_q\, dh$$

$$= \frac{p}{\pi}\int sin^2\alpha\, dh - \frac{q}{\pi}\int \left[\frac{sin2\theta}{2} ln\frac{R_1^2}{R_2^2} - \alpha cos2\theta - \cos^2 2\theta \sin\alpha\cos\alpha + \sin 2\theta cos2\theta \sin^2\alpha\right] dh$$

$$\ldots\ldots Substituting\ equation\ (6.31)$$

$$\int \tau\, dh = \frac{Fsin\theta}{\pi b}\int sin^2\alpha\, dh - \frac{Fcos\theta}{b\pi}\int \left[\frac{sin2\theta}{2} ln\frac{R_1^2}{R_2^2} - \alpha cos2\theta - \cos^2 2\theta \sin\alpha\cos\alpha + \sin 2\theta cos2\theta \sin^2\alpha\right] dh$$

$$= \frac{F}{\pi b}\int \Bigg[sin\theta sin^2\alpha - cos\theta\left[\frac{sin2\theta}{2} ln\frac{R_1^2}{R_2^2} - \alpha cos2\theta - \cos^2 2\theta \sin\alpha\cos\alpha + \sin 2\theta cos2\theta \sin^2\alpha\right]\Bigg] dh \quad (6.45)$$

6.4.7 Integration and simplification

To calculate equations (6.44) and (6.45), the relationship of rib geometric parameters must be incorporated. Defining *I1* to *I4* as:

$$I1 = \int sin^2\alpha dh,$$

$$I2 = \int sin\alpha\, cos\,\alpha\, dh,$$

$$I3 = \int \alpha\, dh$$

$$I4 = \int ln\frac{R_1}{R_2} dh$$

Substituting equation (6.34) in *I1*, yields:

$$I1 = \int \left(\frac{bsin\theta}{\sqrt{b^2 + h^2 - 2bhcos\theta}}\right)^2 dh$$

$$= bsin\theta\, tan^{-1}\frac{h - bcos\theta}{bsin\theta}$$

The definite integral of *I1* is:

$$\mathrm{I1} = \int_0^{\mathrm{L}} \sin^2\alpha\, \mathrm{dh} = b\gamma sin\theta \qquad (6.46)$$

where:

$$\gamma = tan^{-1}\left(\frac{m - cos\theta}{sin\theta}\right) + \frac{\pi}{2} - \theta \qquad (6.47)$$

$$m = \frac{L}{b} \qquad (6.48)$$

Substituting equations (6.34) and (6.35) to *I2*, yields:

$$I2 = \int \frac{bsin\theta}{\sqrt{b^2 + h^2 - 2bhcos\theta}} \times \frac{h - bcos\theta}{\sqrt{b^2 + h^2 - 2bhcos\theta}} dh$$

$$= \frac{1}{2} bsin\theta ln(b^2 + h^2 - 2bhcos\theta)$$

The definite integral of *I2* is:

$$\mathrm{I2} = \int_0^{\mathrm{L}} sin\alpha\, cos\,\alpha\, \mathrm{dh} = bksin\theta \qquad (6.49)$$

where $k = ln\sqrt{m^2 - 2mcos\theta + 1}$ (6.50)

Substituting equation (6.36) in *I3*, yields:

$$I3 = \int tan^{-1}\left(\frac{b\sin\theta}{h - bcos\theta}\right) dh$$

Using integration by parts (IBP), solution can be found as:

$$I3 = h\, tan^{-1}\left(\frac{bsin\theta}{h - bcos\theta}\right) + bsin\theta ln\sqrt{h^2 - 2bhcos\theta + b^2} + bcos\theta\, tan^{-1}\left(\frac{h - bcos\theta}{bsin\theta}\right)$$

The result can be verified via reverse differentiation.

Therefore, for definite integral:

$$I3 = \int_0^L \alpha\, dh = \left[h\, tan^{-1}\left(\frac{\mathrm{b}\sin\theta}{h - bcos\theta}\right) + bsin\theta ln\sqrt{h^2 - 2bhcos\theta + b^2} + bcos\theta\, tan^{-1}\left(\frac{h - bcos\theta}{bsin\theta}\right)\right]_0^L$$

$$= bm(\pi - \theta - \gamma) + bksin\theta + b\gamma cos\theta \qquad (6.51)$$

In the procedure of simplification, it should be noted that:

$$tan^{-1}\left(\frac{\mathrm{b}\sin\theta}{L - bcos\theta}\right) = \pi - \theta - \gamma$$

$$ln\frac{\sqrt{L^2 - 2bLcos\theta + b^2}}{L} = k - lnm$$

Substituting equations (6.32) and (6.33) into *I4* component:

$$I4 = \int ln\frac{h}{\sqrt{b^2 + h^2 - 2bhcos\theta}}\, dh$$

$$= (h - bcos\theta)\, ln(h^2 - 2bhcos\theta + b^2) - 2(h - bcos\theta) + 2bsin\theta\, tan^{-1}\left(\frac{h - bcos\theta}{bsin\theta}\right)$$

This solution can also be verified via reverse differentiation, for definite integral:

$$I4 = \int_0^L ln\frac{R_1}{R_2}\, dh$$

$$= \left[(h - bcos\theta)\, ln(h^2 - 2bhcos\theta + b^2) - 2(h - bcos\theta) + 2bsin\theta\, tan^{-1}\left(\frac{h - bcos\theta}{bsin\theta}\right)\right]_0^L$$

$$= bkcos\theta - bkm + bm\, lnm - b\gamma sin\theta \qquad (6.52)$$

Finding the solutions of *I1* to *I4*, the equation (6.44) becomes:

$$\int \sigma_n dh = \frac{F}{\pi b}\int \left[(\alpha - sin\alpha cos\alpha)sin\theta + \left[sin^2\theta ln\frac{R_1^2}{R_2^2} - \alpha sin2\theta + (\cos2\theta + sin^2 2\theta)sin^2\alpha + sin2\theta(1 - \cos2\theta)sin\alpha\cos\alpha\right]\right] dh$$

$$= \frac{F}{b\pi}[sin\theta(I3 - I2) + 2sin^2\theta I4 - sin2\theta I3 + (\cos2\theta + sin^2 2\theta)I1 + sin2\theta(1 - \cos2\theta)I2]$$

$$= \frac{F}{b\pi}[2sin^2\theta(bkcos\theta - bkm + bm\, lnm - b\gamma sin\theta) + (sin\theta - sin2\theta)[bm(\pi - \theta - \gamma) + bksin\theta + b\gamma cos\theta] + (\cos2\theta + sin^2 2\theta)b\gamma sin\theta + bksin\theta(sin2\theta - sin\theta - sin2\theta\cos2\theta)]$$

$$= \frac{G_1}{\pi}F \qquad (6.53)$$

Where:

$$G_1 = 2sin^2\theta(kcos\theta - km + m\,lnm - \gamma sin\theta) + (sin\theta - sin2\theta)[m(\pi - \theta - \gamma) + ksin\theta + \gamma cos\theta] + (\cos2\theta + sin^2 2\theta)\gamma sin\theta + ksin\theta(sin2\theta - sin\theta - sin2\theta\cos2\theta)$$

For shear force, the equation (6.45) can be calculated as:

$$\int \tau\, dh = \frac{F}{\pi b}\int \left[sin\theta sin^2\alpha - \left(\frac{sin2\theta}{2} ln\frac{R_1^2}{R_2^2} - \alpha cos2\theta - \cos^2 2\theta \sin\alpha\cos\alpha + \sin2\theta cos2\theta \sin^2\alpha\right)\right] dh$$

$$= -\frac{F}{b\pi}[sin2\theta cos\theta I4 - cos2\theta I3 - \cos^2 2\theta I2 - (\sin\theta - \sin2\theta cos2\theta)I1]$$

$$= -\frac{F}{b\pi}[sin2\theta cos\theta(bkcos\theta - bkm + bm\,lnm - b\gamma sin\theta) - cos2\theta[bm(\pi - \theta - \gamma) + bksin\theta + b\gamma cos\theta] - bksin\theta\cos^2 2\theta - b\gamma sin\theta(\sin\theta - \sin2\theta cos2\theta)]$$

$$= \frac{G_2}{\pi}F \qquad (6.54)$$

Where:

$$G_2 = -[sin2\theta cos\theta(bkcos\theta - bkm + bm\,lnm - b\gamma sin\theta) - cos2\theta[bm(\pi - \theta - \gamma) + bksin\theta + b\gamma cos\theta] - bksin\theta\cos^2 2\theta - b\gamma sin\theta(\sin\theta - \sin2\theta cos2\theta)]$$

6.4.8 Failure study on the supposed surface using derived model

For this study, the Mohr-Coulomb's failure criterion is selected. Two combined stress fields are considered within the resin. The first one is the pre-loading stress field and the

second is the bolt load induced stress field. Thus, the failure criterion (*f*) is expressed as net resistant force that can be summed together:

$$f = T_0 + T = (c_w + tan\phi\ \sigma_{n0} - \tau_0)L + \left(tan\phi \int \sigma_n dh\ - \int \tau\ dh\right) \qquad (6.55)$$

Where:

f = failure criterion

T_0 = pre-loading shear resistance at the failure plane

T = bolt induced shear load at the failure plane

$L = c + 2bcos\theta$ = resin failure length

h = distance from any chosen point along the weakness plane

ϕ = internal frictional angle of the resin

σ_{n0} = initial normal stress on the weakness plane

c_w = resin cohesion

τ_0 = initial shear stress

σ_n = normal stress introduced by axial load of the bolt

τ = shear stress introduced by axial load of the bolt

Each component along the plane of weakness is shown in Figure 6.16.

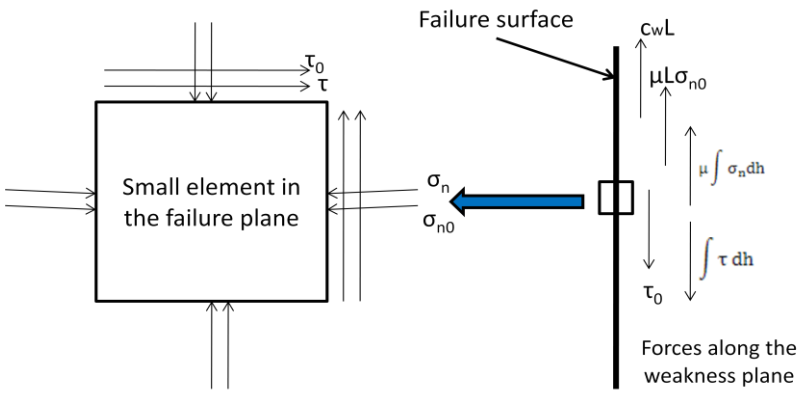

Figure 6.16 Forces on a small element along the plane of weakness

Substituting equations (6.53), (6.54) into failure function (6.55), yields:

$$f = T_0 - \frac{1}{\pi}(G_2 - tan\phi G_1)\, F \qquad (6.56)$$

In the equation, the expression $(G_2/\pi - tan\phi\, G_1/\pi)$ can be termed as the coefficient factor of the axial force (*F)*. It is in a range of [-1, 1], as an indicator of the rate of the axial load transferred to the shear load on the assumed weakness plane. In addition, the expression T_0 can be thought as the initial shear resistance on the plane.

6.5 PARAMETRIC STUDY OF BOLT PROFILE GEOMETRY

6.5.1 Bolt rib face angle

T2 bolt (Figure 4.1) used in laboratory push/pull tests and double shear test (Chapter four) was adopted for the study. According to Table 4.2, the rib geometric parameters of T2 bolt are estimated as (Figure 6.17):

- Rib spacing=12mm
- Stem length *c*=7mm
- Half of rib top width=1.6mm
- Rib height $b\sin\theta$ =1.5mm (Table 4.2)
- Length between the rib tips *L*=12-2x1.6=8.8mm
- Rib face angle $\theta = 60°$

The rib face angle is investigated according to the derived equation (6.56). The rib height ($b\sin\theta$) is fixed to be 1.5mm and the rib stem length *L* is to be constant at 8.8mm. In addition, the grout material is assumed to be resin and accordingly $tan\phi$ = 0.7 (Table 4.5).

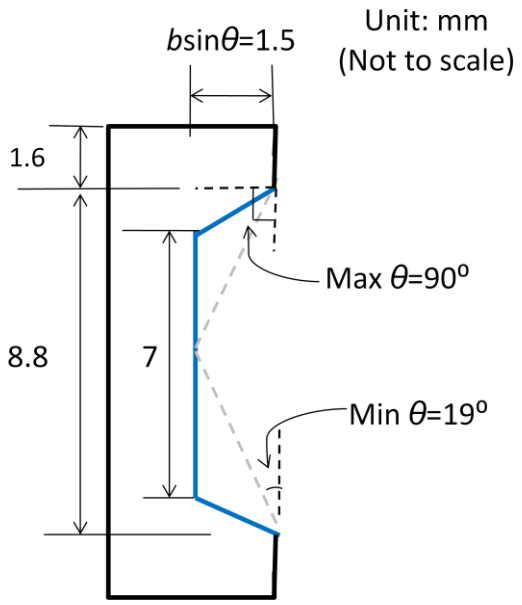

Figure 6.17 Geometric parameters of T2 bolt.

It should be noted that there is a minimum rib face angle due to geometric constrains (grey dashed lines in Figure 6.17), for the investigated bolt:

$$\theta \geq \tan^{-1}\left(\frac{\text{rib height}}{\text{L}/2}\right) = 19°$$

Thus, rib face angles less than 19° do not exist.

According to the calculated values using equation (6.56), the coefficient factor of axial force $(G_2/\pi - \mu G_1/\pi)$ with changing rib face angle θ from 19° to 90° is plotted and shown in Figure 6.18.

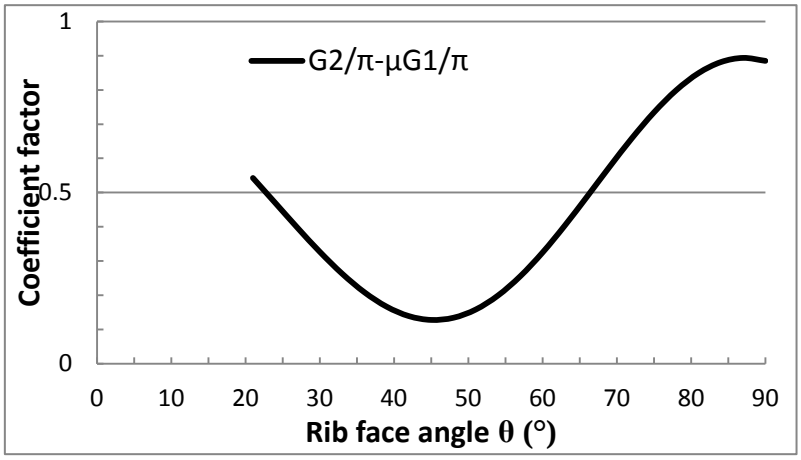

Figure 6.18 Coefficient factor of axial force at different rib face angle for T2 bolt.

From this diagram, it is found that

Case (1): rib face angle $\theta \in (0°,\ 19°)$ does not exist.

Case (2): rib face angle $\theta \in (20°,\ 45°)$

In this stage the influence of the axial load on the assumed weakness surface decreases with increasing rib face angle.

Case (3): rib face angle $\theta \approx 45°$

There is a stationary point around θ=45°, which is the most difficult case to cause parallel shear failure on the weakness plane. At this point:

$$\frac{1}{\pi}(G_2 - tan\phi G_1) \approx 0.13$$

Hence, to cause parallel shear failure on the supposed weakness plane (f=0):

$$F = 7.7T_0$$

In other words, if the rib face angle is around 45°, the axial load will be transferred to a direction perpendicular to the bolt axis and the rockbolting will have the greatest ability to resist parallel shear failure of the resin.

Case (4): face angle $\theta \in (45°,\ 90°)$

With increasing the rib face angle above 45°, increasing coefficient factor of the axial force indicates that parallel shear failure on the assumed weakness plane becomes easier. For example, if the face angle is designed to be 85°, then:

$$\frac{1}{\pi}(G_2 - tan\phi G_1) = 0.9$$

Consequently, axial load of $1.1T_0$ will be sufficient to commence parallel shear

failure of the rockbolting system

6.5.2 Bolt rib spacing

If the rib height is fixed at 1.5mm, for different profile stem length, *L*, the influence of rib face angle on load transfer is plotted in Figure 6.19.

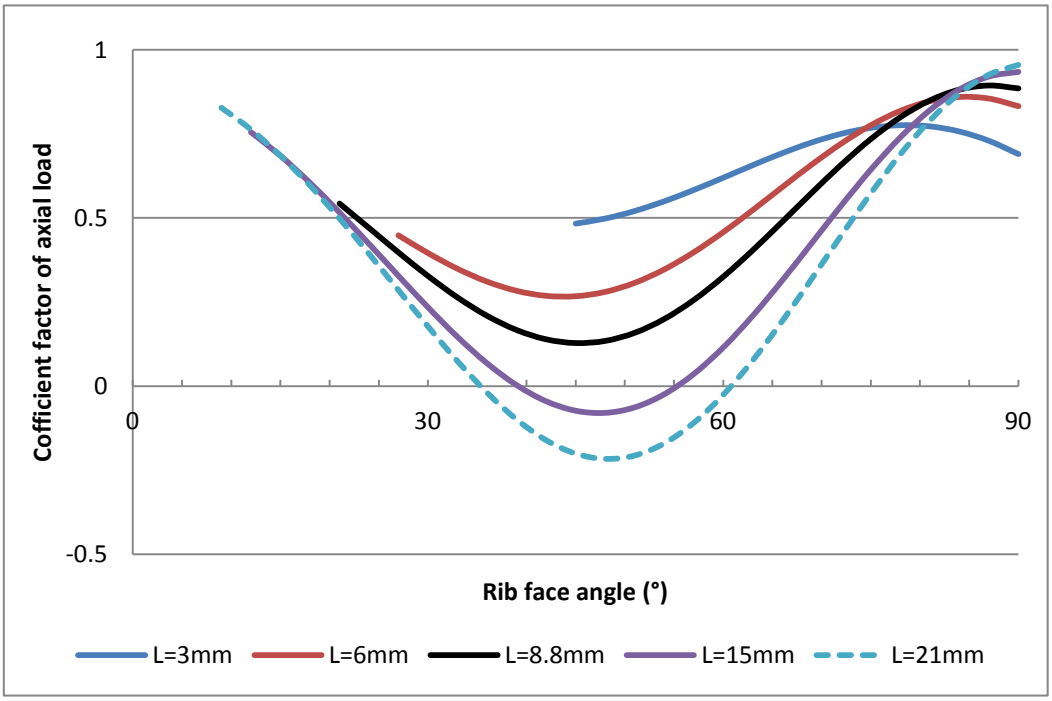

Figure 6.19 The influence of rib face angles for different stem lengths of the bolt.

It can be seen that for large profile spacing the coefficient factor becomes negative. For example, a T2 bolt was modified to 25mm rib spacing in double shear tests. The influence of the axial loading of this bolt on the parallel shear failure of the resin annulus was calculated and plotted as dashed line in Figure 6.19. In case of rib face angle $\theta \in (35°,\ 61°)$, the failure criterion, f (equation 6.56), is always positive. It indicates that parallel shear failure of the resin annulus will never occur at this bolt profile configuration. Consequently, dilational slip failure of the resin, as discussed in Chapter five, will be inevitable as the majority of the axial load is transferred radially.

6.5.3 Bolt rib height

If the rib face angle is to be constant at 60°, the efficiency of axial load to commence parallel shear failure of the resin is demonstrated in Figure 6.20.

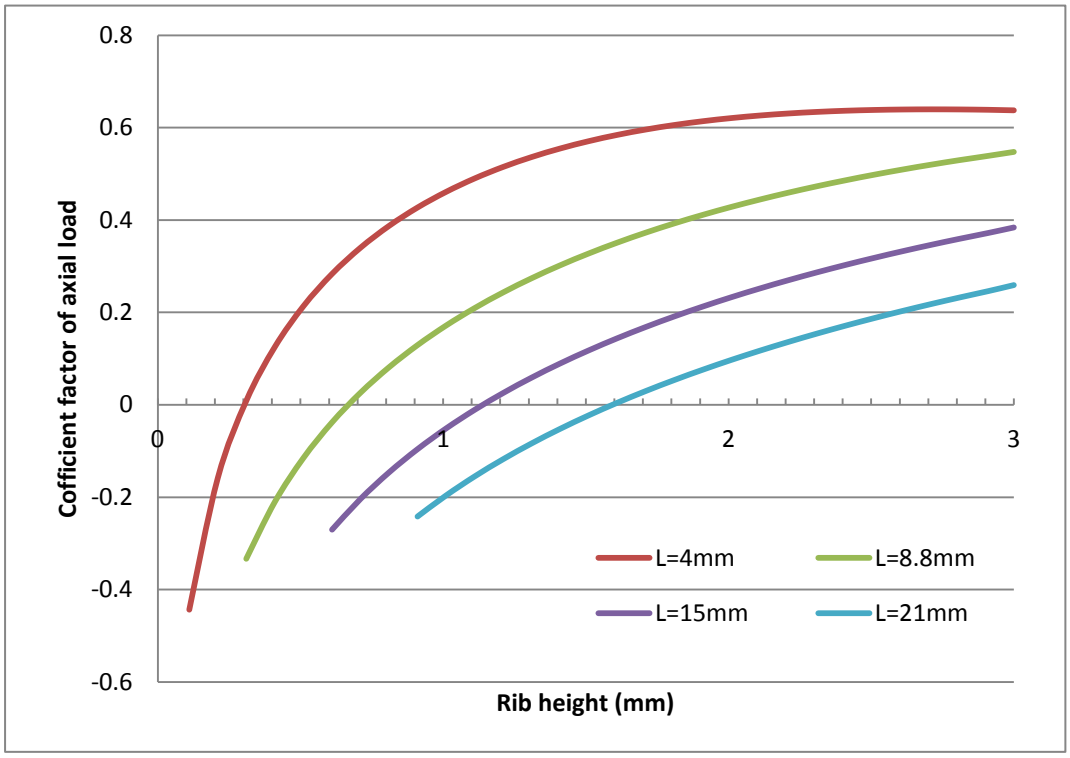

Figure 6.20 Coefficient of axial load with varying rib height at different stem length

The results indicate that the increase in the rib height, increases the rate of load transferred to a direction parallel to the axis of the bolt. In addition, if the rib height is very small, say less than 8% of the stem length, parallel shear failure of the grout material will not occur.

6.5.3 Bolt rib height to length ratio

Results shown in Figure 6.19 and 6.20 suggest that the rib height and length should be studied together. Therefore, the coefficient of axial load is plotted for varying rib length to height ratios, and shown in Figure 6.21. As expected, results show that if the rib length to height ratio is greater than 13, parallel shear failure of the resin cannot

occur due to insufficient load transfer.

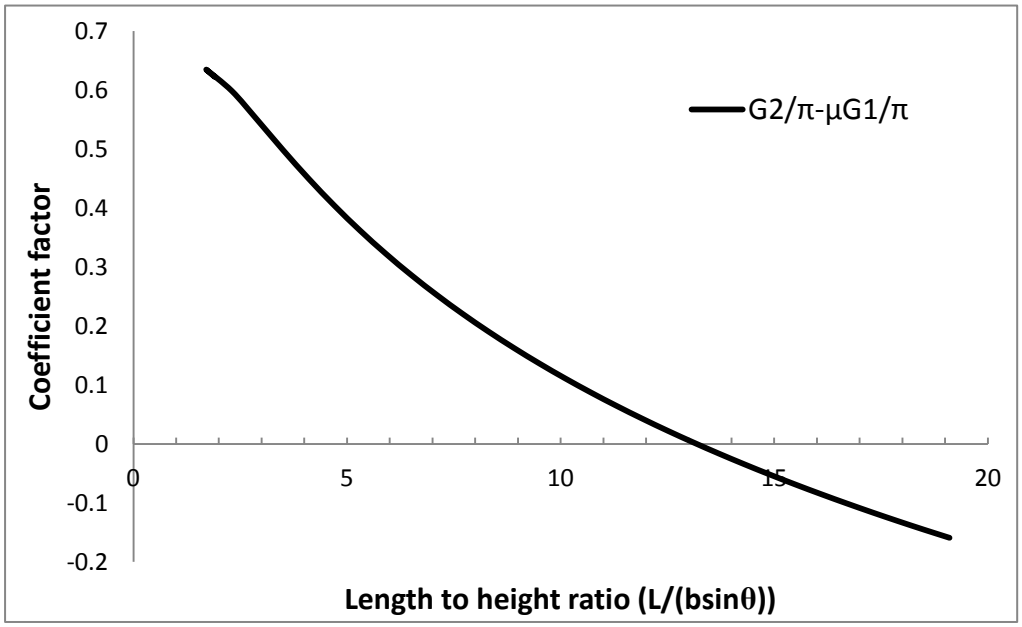

Figure 6.21 Rate of load transfer with varying of length to height ratio

6.6 DISCUSSION

The novel idea of coupling the bolt profile geometry with the introduced stress field detailed in this chapter provides a tool to investigate the bolt profile configuration and its effects on the load transfer mechanism for the benefit of the mining industry and science in general. A new development in calculating load transfer capacity between two rib profiles of varying geometries is discussed. The derived mathematical equations presented in this chapter calculate the stress distribution adjacent to the fully grouted bolt subjected to axial load.

The parametric study suggests that the axial load can be transferred to surrounding material laterally and longitudinally. The transfer rate is very sensitive to changes in bolt rib geometry. In general, lower rib face angle and/or small profile height to length ratios are favourable to transfer load radially. As a result, dilation is inevitable. On the

contrary, high rib face angle with larger rib height to length ratio will transfer the majority of axial load to a direction parallel to the bolt axis. In this case, parallel shear failure would most likely occur. Therefore, this study suggests that the rock bolt with smaller rib face angle and larger spacing is suitable in high confinement such as hard rock, while the rock bolt with high profile height and larger rib face angle should be used in soft rock.

There are limitations on the applications of derived mathematical expressions to rib profile design. The boundary effect becomes a problem for some rib geometry. For example, if the rib is closely spaced, then the grout material can no longer be represented by a half space. In addition, for the larger rib face angles, the calculation error increases.

Dilational slip failure of the bolt can also be investigated in a similar manner as demonstrated in this chapter. However, due to the boundary effect in a half-space, failure surfaces close to the bolt are inaccurate.

If the weakness plane is assumed at the resin rock interface, shown in Figure 6.22-a, the half-space analysis is applicable. In this case, another variable, resin thickness *d*, has to be introduced (Figure 6.22-b). The coordinate is shown in Figure 6.23.

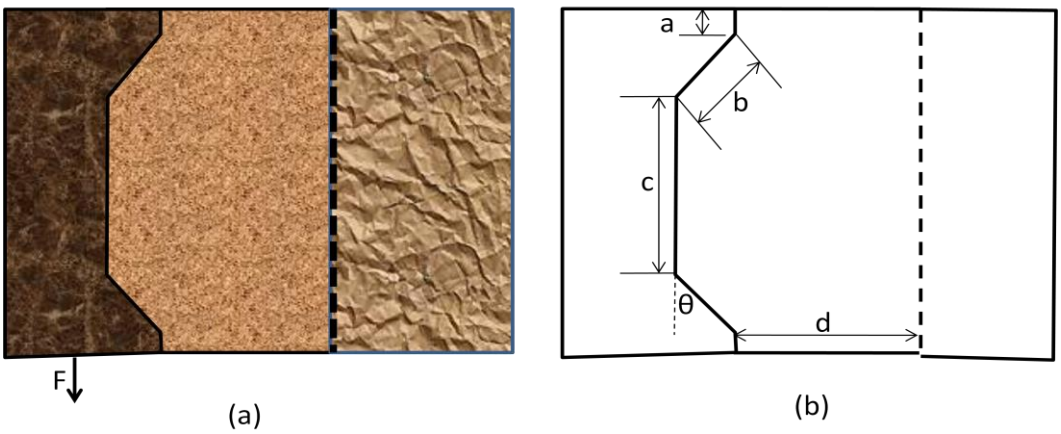

Figure 6.22 Resin rock interface weakness plane

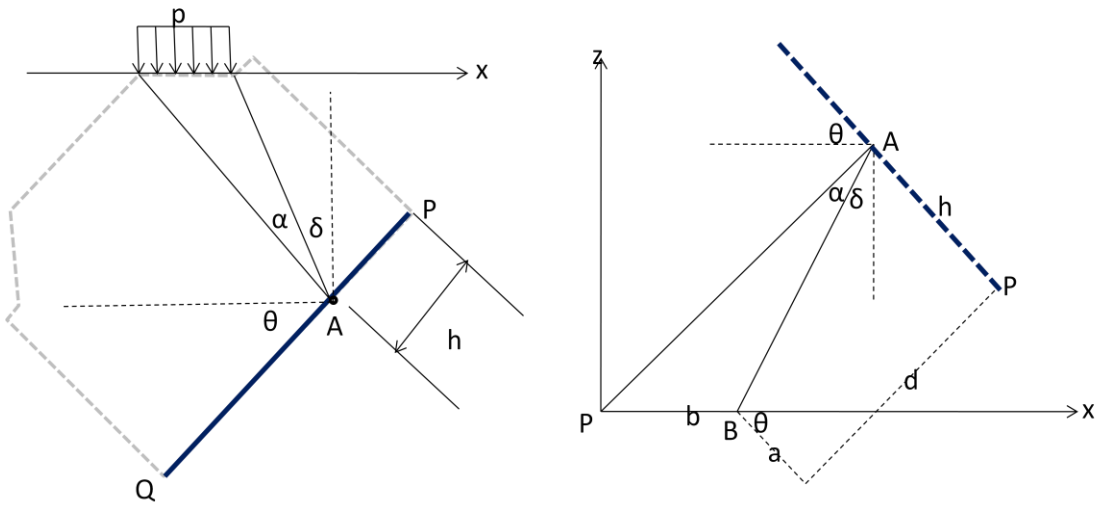

Figure 6.23 Coordinate for resin rock interface failure

The mathematical expressions are tedious, for example, in the problem

$$\sin\alpha = \frac{[(h-a)\sin\theta + d\cos\theta]b}{\sqrt{(h^2-2ah+a^2+d^2)(h^2-2ah+a^2+d^2+b^2+2b(a\cos\theta+d\sin\theta-h\cos\theta))}}$$

Compared with equation (6.34) $sin\alpha = \frac{bsin\theta}{\sqrt{b^2+h^2-2bhcos\theta}}$. In addition, the closed form solution is hard to achieve. Hence, step based calculation has to be employed.

Mohr-Coulomb's failure criterion is employed in this study as it is widely used for rock, soil and concrete studies. Energy criterion is recommended as an alternative or in conjunction. Shear failure criterion is suitable for the bolt but not suitable for the resin material.

Analytical results should be compared with computer simulations and experimental observations. However, to the best knowledge of author, current numerical simulation software often requires their users to pre-define the potential failure surface. Consequently, the problem of optimum design of rib profile cannot be simulated directly.

Identification of resin crack initiation in pull-out tests is difficult. To obtain

experimental verification of this study, the CNS tests were conducted. However, experimental observations suggested that dilation cannot be supressed properly under current experimental assemblage (Figure 4.43, 4.49 and 4.50). Therefore, more controllable experimental verification is recommended for further work of this study.

6.7 CONCLUSIONS

The important outcome of this study shows that there is another novel way to examine resin failure around the bolt for different profile configurations that can be potentially compared with the laboratory tests and numerical modelling. This method can provide very good understanding of the bolt-resin interaction with rock reinforcement.

The study of the bolt profile shape presented here shows how the mathematical equations were derived and used to calculate the axial force needed to fail the resin for different bolt profile configurations. The derived mathematical equations consist of in-built bolt geometry parameters and these can be changed to optimise the bolt shear strength capacity.

According to the parametric study, it can be concluded that lower bolt profile face angle and/or small rib height to length ratio bolts are favourable to transfer load radially. Hence, they are suitable for installation in hard rock. Larger rib face angle with higher height to length ratio bolts will transfer the greater part of the axial load to a direction parallel to the bolt axis. They should be used in soft rock condition.

Various types and bolt geometries and profile configurations can be trialled using the described approach. This method provides another step towards designing more efficient bolt profiles to optimise the support capacity in the mining industry.

CHAPTER SEVEN

CONCLUSIONS AND RECOMENDATIONS

CONCLUSIONS AND RECOMENDATIONS

7.1 CONCLUSIONS

7.1.1 Conclusions of the up-to-date understanding

The up-to-date understanding of the reinforcement system can be briefly summarised. The rock bolting is the main element of the support systems. In roof bolting, strata binding effects is by one or a combination of several basic mechanisms: suspension, beam building, arching and keying

For rock bolts subjected to axial loading, an exponential decay pattern of axial load and shear stress along the bolt length in the elastic stage is widely accepted. The ISS model is the biggest achievement of rockbolting mechanisms study. The mechanisms of cable bolting can be theoretically described by the BSM and untwisting model. In tunnelling design, the rock bolting effects are simulated as internal pressure on ground sewing, or structure making, or ground arch making, or improving rock properties.

. The anchorage is affected by parameters such as resin annulus thickness, grout strength, bolt profile characteristics, rock roughness, rock strength, and mechanical properties of the bolt. The shear resistance of the bolt-resin interface is the key element in transferring the load from the bolt to the rock. A fully grouted rock bolt can transfer greater loads than expanded shell or wedge type anchorages. Resinous grouts can meet the high strength required for short anchorages. Resin mechanical properties play an important role in load transfer of the rockbolting mechanism, especially when subjected to axial loading.

The ultimate failure of rockbolts may occur in the bolt, grout or rock, or at the interfaces, or a combination of these failures.

7.1.2 Conclusions of the new research presented in this study include:

There are two ways to describe the residual strength of the resin. If the confinement is low, the cohesional strength will diminish immediately after failure and dilational slip dominates the post failure performance. If the confinement is large, the cohesional strength will gradually decay.

Differentiation of each failure mode is the key to conduct rock bolting mechanism analysis. For example, the steel bolt may fail in tension or bending when subjected to shear loading.

In all laboratory tests, the failure modes of the resin around a bolt profile have been classified into two categories: "*parallel shear failure*" and "*dilational slip failure*". Parallel shear failure of the resin is characterised by a cylindrical failure surface, which just passes through the tips of the bolt profiles. It occurs if the bolt has closely spaced profiles, or is installed in hard rock environment, or is confined by high radial stiffness materials such as a steel tube in the laboratory experiments. Dilational slip failure is characterised by lodged resin in front of the bolt profile forming a conical shaped failure surface. It occurs in lower confinement stiffness or when rib spacing is large.

Results of double shear tests suggest that the bolt rib profile affects the behaviour of rockbolting in shear. In addition, changing of shear modulus of the reinforced joint in the shear test is associated with the commencement of axial load development measured at the end plate.

When bolt is subjected to axial load, direct parallel shear failure is the simplest failure mode along the bolt, which always occurs on smooth bars and closely spaced rebars. This failure mode is formulated by equations (5.11) to (5.15). The theoretical prediction when compared to the experimental data, shows very good agreement.

The governing equation of the dilational slip failure has been derived and presented as equation (5.27).

For dilational slip failure of rock bolting, the dilational slip face angle is normally different to the bolt rib face angle. A universal upper limit of dilational slipping face angle is the complementary angle of the internal friction angle of the grouting material. The domain of the dilational slip face angle of a bolt can be evaluated using equation (5.25), and the most vulnerable slip surface can be estimated.

As shown in Figure 5.20, whenever dilational slip failure occurs, the grouting material between two bolt profiles can be categorised into three parts:

- the resin above the slip angle will be coupled with the bolt profile and move with the bolt,
- middle section of the resin will undergo shear deformation,
- the resin below the slip angle will be unaffected.

The failure mode of T2 bolts in laboratory SEPT has been identified as parallel shear failure after dilational slip. Consequently, the load-displacement curves of pullout tests have been predicted according to derived failure model and shows good agreement with experimental results.

The governing equation of the parallel shear failure of the resin annulus has been derived as equation (6.21).

According to the parametric study, it can be concluded that smaller rib face angle or smaller profile height to length ratio bolts are favourable to transfer load radially. Hence, they should be used in hard rock environments. Large bolt rib face angles with higher rib height to length ratio will transfer the major part of axial load into the resin annulus at a direction parallel to the bolt axis. They are desirable for use in soft rock conditions.

7.2 RECOMMENDATIONS

The further studies are recommended to enhance research in the following field:

- The mechanical properties of the grouting material, such as residual strength and shear resistance under high compressive stress, are major concern of rockbolting performance. It is necessary to develop new model to describe them based on micro-structural deformation.
- Factors that affect the bond stiffness (tangent modulus of the load displacement curve) have to be researched to enable accurate prediction of bonding performance. To achieve that, pullout tests with loading-unloading cycles within the linear range are recommended.
- In the case of high confinement stress, the failure mode of bolts with large profile spacing does not follow direct parallel shear failure mode or simple dilational slip. Computer simulation is recommended to identify its failure mode more accurately.

REFERENCE

Aydan, O. (1989), The stabilisation of rock engineering structures by rock bolts, Geotechnical Engineering, Ph.D. Thesis, Nagoya, Nagoya University, 202p.

Aziz, Z., Campbel, D. and Levay, J. (1992), Experience with resin anchored bolts in large permanent underground excavation, Int. Symp. of Rock Support in Mining and Underground Construction, Canada, pp.467-472.

Aziz, N, (2002), A New Technique to Determine the Load Transfer Capacity of Resin Anchored Bolts, in Aziz, N (ed), Coal 2002: Coal Operators' Conference, University of Wollongong & the Australasian Institute of Mining and Metallurgy, 2002, 176-184. http://ro.uow.edu.au/coal/208/

Aziz, N.I, Pratt, D. and Williams, R.,(2003). Double shear testing of bolts, Proc.4th Underground Coal Operators Conference, Coal 2003, February 12-14,), Wollongong, pp 154-161. http://ro.uow.edu.au/coal/172/

Aziz, N.I. and Webb, B., (2003), Study of load transfer capacity of bolts using short encapsulation push test, Proc. 4th Underground Coal Operators Conference, Coal 2003, February 12-14, Wollongong, pp 72-80. http://ro.uow.edu.au/coal/162/

Aziz, N, (2004), An Update of Roof Bolt Research at the University of Wollongong, in Aziz, N (ed), Coal 2004: Coal Operators' Conference, University of Wollongong & the Australasian Institute of Mining and Metallurgy, 2004, 215-224. http://ro.uow.edu.au/coal/147/

Aziz, N, Hossein, J and Hadi, MSN, (2005), The Effect of Resin Thickness on Bolt-Grout-Concrete Interaction in Shear, Aziz, N (ed), Coal 2005: Coal Operators' Conference, University of Wollongong & the Australasian Institute of Mining and

Metallurgy, 2005, 3-9. http://ro.uow.edu.au/coal/64/

Aziz, N.I., and Jalalifar, H. (2005), Experimental and numerical methodology assessment of load transfer capacity of bolts, Proc. 24th International Conference on Ground Control in Mining, August, 2-4, Morgantown, WV, USA, pp 285-293.

Aziz, N. I**.,** Jalalifar H. and Concalves, J., (2006). Bolt surface configurations and load transfer mechanism, *Proc.7th Underground Coal Operators Conference, Coal 2006,* Wollongong, 5-7 July, pp. 236-244. http://ro.uow.edu.au/coal/51/

Aziz, N, Jalalifar, H, Remennikov, A, Sinclair, S, Green, A, (2008), Optimisation of the Bolt Profile Configuration for Load Transfer Enhancement, in *Proc.8th Underground Coal Operators Conference, Coal 2003, February 14-15, Wollongong,* pp 125-131. (*ed N Aziz and J Nemcik,* <http://ro.uow.edu.au/coal/11/>

Bawden, W. F., Hyett A. J., Lausch, P. (1992). Technical Note: An Experimental Procedure for the In Situ Testing of Cable Bolts, Int. J. Rock Mech. Min. Sci. & Geomech. Abstr. Vol. 29. No. 5, pp. 525--533.

Benmokrane, B., A. Chennouf, et al. (1995). "Laboratory evaluation of cement-based grouts and grouted rock anchors." International Journal of Rock Mechanics and Mining Science & Geomechanics Abstracts **32**(7): 633-642.

Bjurstrom,S. (1974), Shear strength of hard rock joints reinforced by grouted untensioned bolts, International congress of rock mechanics, pp.1194-1199.

Blumel, M, (1996), Performance of grouted rock bolts in squeezing rock, Proceedings EUROCK'96, Predictions and performance in rock mechanics an rock engineering, Rotterdam, Balkema, Pp 885-891

Blumel, M., Schweger, H.F. and Golser, H., (1997), Effect of rib geometry on the mechanical behaviour of grouted rock bolts, World Tunnelling Congress '97, 23rd

General Assembly of the International Tunnelling Ass. Wien. 6 p.

Brown E.T., Bray J.W., Ladanyi B. and Hock E. (1983). Ground response curves for rock tunnels. J. Georech. Engng. Am. Soc. civ. Engrs 109, 15-39.

Cai Y, Esaki T, Jiang Y J. (2004a) An analytical model to predict axial load in grouted rock bolt for soft rock tunneling. Tunnel Undergr Space Technol 2004; 19:607-18

Cai Y, Esaki T, Jiang Y J. (2004b) A rock bolt and rock mass interaction model. Int J Rock Mech Min Sci 2004; 41:1055-67

Compton, C. Oyler, D. (2004), Investigation of Fully Grouted Roof Bolts Installed Under In Situ Conditions, NIOSHTIC-2 No. 20028265

Craig, P and Aziz, N, Shear testing of 28mm hollow strand "TG" cable bolt, in Aziz, N (ed), 10th Underground Coal Operators' Conference, University of Wollongong & the Australasian Institute of Mining and Metallurgy, 2010, 171-179. http://ro.uow.edu.au/coal/303/

Dight.P.M. (1982), Improvements to the stability of rock walls to open pit mines, Ph.D.Thesis, Melborn, Monash University, 495p.

Dulacska.H. (1972), Dowel action of reinforcement crossing cracks in concrete, Journal of the American Concrete Institute, 69(12), pp.754-757.

Ewoldsen, H. M., McNiven, H. D. (1968 b). Rockbolting of tunnels for structural support part II: deign of rockbolt systems. lnt, J. Rock, Mech. Min. Sci. Vol. 6, pp. 483-497.

Fabjanczyk, M.W. and Tarrant, G.C. (1992), Load transfer mechanisms in reinforcing tendons, Proceedings of the 11th International Conference on Ground Control in Mining, The University of Wollongong, pp1-8.

Fabjanczyk, M., Hurt, K. & Hindmarsh, D. (1998). Optimisation of Rockbolt Performance, Proceedings of the International Conference on Geomechanics/Ground Control in Mining and Underground Construction, The University of Wollongong, pp413-424.

Farmer I. W., (1975), Stress distribution along a resin grouted rock anchor, int. J. Rock Mech. Min. Sci. Geomech. Abstr., 12, 347-351.

Gray P.A., Hunt N., Fabjanczyk M. (1998), New developments in ground support with particular reference to high capacity high load transfer rock bolts, Proceedings of the International Conference on Geomechanics/Ground Control in Mining and Underground Construction, The University of Wollongong, pp513-524.

Goto Y. (1971): Cracks Formed in Concrete Around Deformed Tension Bars. Journal of the American Concrete Institute Vol. 68, No. 4, April 1971, pp 244-251.

Haas.C.J. (1976), Shear resistance of rock bolt, Journal of Transactions, Society of Mining Engineers of AIME, pp.32-40.

Hearn E J, (1977), Mechanics of Materials, Pergamon Press Ltd, Ocford OX3 0BW, England, ISBN 0-08-020618-2

Hollingshead.G.W. (1971), Stress distribution in rock anchors, Canadian Geotechnical Journal, 8, pp.588-592.

Holmberge.M. (1991), The mechanical behaviour of untensioned grouted rock bolts, Ph.D. Thesis, Stockholm, Royal Institute of Technology, 127p.

Hyett, A. J., Bawden, W. F. and Reichert, R. D. (1992). The effect of rock mass confinement on the bond strength of fully grouted cable bolts, Int. J. Rock mechanics and Min. Sci. & Geomech. Abstr., 29(5), pp.503-524.

Hyett, A. J., Bawden, W. F., Macsporran, G. R. and Moosavi, M. (1995), A constitutive law for bond failure of fully-grouted cable bolts using a modified Hoek cell, Int. J. of Rock Mechanics and Min. Sci. & Geomech. Abstrs., 32(1), pp.11-36.

Hyett. A.J, Mossavi.M and Bawden. W.F. (1996), Load distribution along fully grouted bolts, with emphasis on cable bolt reinforcement, Int. J. for Numerical and Analytical Methods in Geomechanics, 20, pp.517-544.

Indraratna B and Kaiser P.K. (1990 a), Analytical model for the design of grouted rock bolts, Int.J. of Numerical and Analytical Methods in Geomechanics, 14, pp.227-251.

Indraratna B and Kaiser P. K. (1990 b), Design for grouted rock bolts based on the convergence control method, Int. J. of Rock Mechanics and Min. Sci. & Geomech. Abstrs, 27(4), pp.269-281.

Indraratna. B and Haque.A. (2000), Shear behaviour of rock joints, Rotterdam, Netherlands, Balkema. 165p.

Ito F, Nakahara F, Kawano R, Kang SS, Obara Y (2001). Visualization of failure in a pull-out test of cable bolts using X-ray CT. Construction and Building Materials. 2001; 15; 263-70

Ivanovic A., Neilson, R. D, Rodger, A. A. (2002). Influence of prestress on the dynamic response of ground anchorages. J Geotech Geoenviron Eng ASCE 2002;128(3): 237–249

Ivanovic, A. and Neilson, R.D. (2009). Modelling of debonding along the fixed anchor length, Int J Rock Mech Min Sci 46 (4) (2009), pp. 699–707.

Jalalifar, H, Aziz, N & Hadi, M, Modelling of Sheared Behaviour Bolts Across Joints, in Aziz, N (ed), Coal 2004: Coal Operators' Conference, University of Wollongong & the Australasian Institute of Mining and Metallurgy, 2004, 225-232.

Jalalifar H. (2006). A new approach in determining the load transfer mechanism in fully grouted bolts. PhD thesis, University of Wollongong, Australia. http://ro.uow.edu.au/coal/149/

Jalalifer, H, Aziz, NH and Hadi, M, An Assessment of Load Transfer Mechanism Using the Instrumented Bolts, in Aziz, N (ed), Coal 2006: Coal Operators' Conference, University of Wollongong & the Australasian Institute of Mining and Metallurgy, 2006, 255-265. http://ro.uow.edu.au/coal/53/

Khair, A.W. (1998). Roofbolting Concepts. 3rd international symposium on roofbolting in mining, RWTH, 3-4 Haziran, Band 15, 285-300

Kaiser, P. K., Yazici, S. and Nose, J. (1992), Effect of stress change on the bond strength of fully grouted cables, Int. J. of Rock Mechanics and Min. Sci. & Geomech. Abstrs, 29(3), pp.293-306.

Kilic A., Yasar E. and Atis C.D., (2002 a). Effect of bar shape on the pull out capacity of fully grouted rockbolts. Tunnelling and Underground Space Technology, 18 pp1-6.

Kilic, A., Yasar, E. and Gelik, A.G., (2002 b). Effect of grout properties on the pull out load capacity of fully grouted rockbolt. Tunnelling and Underground Space Technology, 17, pp355-362.

Li C, and Stillborg B. (1999). Analytical models for rock bolts. Int J Rock Mechanics and Min. Sci. & Geomech. Abstrs, 1999; 36(8);1013-29.

Littlejohn.G.S and Bruce.D.A. (1975), Rock anchors-state of the art, Part 1:design, Ground Engineering, pp.25-32 (Cited in Jalalifar 2006).

Littlejohn.S. (1993), Rock reinforcement-technology, testing, design and evaluation. Comprehensive Rock Engineering Principals, Practice and Projects (Ed.J.A.Hudson),V.4, pp. 413-451.

Luo J., Haycocks C., Karmis M., Westman E. (1998), A critical overview of US rock bolting practices, 5th Int. Symposium Roofbolting in Mining, pp13-34

Luo J. (1999). A new rock bolt design criterion and knowledge-based expert system for stratified roof. PhD thesis, Virginia Polytechnic Institute and State University.

Lutz L. A., (1970). Analysis of stresses in concrete near a reinforcing bar due to bond and transverse cracking. ACI J. pp778-787. Detroit.

Mark C., Compton C, Oyler D. and Dolinar D. (2002), Anchorage pull testing for fully grouted roof bolts. 21st International Conference on Ground Control in Mining, Morgantown,W.V. pp.105-113.

Martin, L. B., Tijani, M., Hadj-Hassen, F.. (2011). A new analytical solution to the mechanical behaviour of fully grouted rockbolts subject to pull-out tests. Construction and Building Materials 25 (2011) 749-755.

McNiven, H.D., Ewoldsen, H.M. (1968 a). Rockbolting of tunnels for structural support part I: theoretical analysis. Int. J. Rock Mech. Min. Sci. Vol. 6, pp. 465-481.

Moosavi, M., Jafari, A. and Khosravi, A. (2005), Bond of cement reinforcing bars under constant radial pressure, Cement and Concrete Composites, Elsevier, pp.103-109, (available on line @www.sciencedirect.com).

Nemcik J. and Aziz N, (2012), via communication

Nitzsche. R.N and Haas. C.J (1976), Installation induced stresses for grouted roof bolts. Int. J. of Rock Mechanics and Min. Sci. & Geomech. Abstrs 13(1), pp.17-24.

Noresi A.P., Schmidt R.J., Sidebottom O.M. (1993), Advanced Mechanics of Materials, 5ed, ISBN 0-471-55157-0, John Wiley and sons, New York, USA.

Oliveira, D. (2012), Application of a transversely isotropic brittle rock mass model in

roof support design, 12th Coal Operators' Conference, University of Wollongong & the Australasian Institute of Mining and Metallurgy, 2012, 15-22.

Oreste P.P. and Peila D. (1996), Radial passive rockbolting in tunneling design with a new convergence confinement model, Int. J. Rock Mech. Min. Sci. & Geomech. Abstr. Vol. 33, No. 5, pp. 443-454, 1996

Pellet.F and Egger P. (1996), Analytical model for the mechanical behaviour of bolted rock joints subjected to shearing. Journal of Rock mechanic and rock engineering 29 (2), pp.73-97.

Peng, S. (1984), Coal Mine Ground Control. 3rd, Morgantown, WV: Dept. of Mining Engineering/College of Engineering and Mineral Resources. ISBN 9780978938345, pp. 131-173

Peng, S. and S. Guo (1992), An improved numerical model of grouted bolt-roof rock interaction in underground openings. Int. Symp. on Rock support in mining and underground construction, Canada, pp.67-74.

Poulos H, Davis E. (1974), Elastic solutions for rock mechanics. John Willey & Sons Inc, New York; 1974; TA710 P67 624.1513 73-17171, Printed in New York.

Ren F F, Yang Z J, Chen J F, Chen W W, (2010), An analytical analysis of the full-range behaviour of grouted rockbolts based on a tri-linear bond-slip model. Construction and Building Materials Vol24 (2010) pp361-370

Richards, R., (2001), Principles of solid mechanics, ISBN 0-8493-0114-9, CRC Press, Boca Raton, USA.

Saleh, S.Y., Reddish, D.J., Stace, L.R. and Whittles, D.N., (2004). Investigating the interaction between pre-stressed cable bolts and the rock mass using numerical modelling techniques. In: Aachen International Mining Symposia: 5th International

Symposium on Roofbolting in Mining, Aachen, Germany. pp. 241-258

Seed G M (2000), Strength of Material, published by Saxe-Coburg Publications, Edinburgh, UK, ISBN 1-874672-12-1, pp 175-190.

Serbouski, M.O. and Signer S.P. (1987), Linear load transfer mechanics of fully grouted roof bolts, US Bureau of Mines, 15p.

Signer, S. P. (1990), Field verification of load transfer mechanics of fully grouted roof bolts, US Bureau of Mines, (9301).

Spang, K. and Egger. P. (1990), Mode of action and calculation of fully grouted rock bolts as reinforcement in stratified or jointed rock mass, Int. J. of Rock Mechanics and Min. Sci. & Geomech. Abstrs 7(4), pp.181-189.

Stillborg. B. (1994), Professional users handbook for rock bolting, Series on rock and soil mechanics, 2nd Ed. Atalas Copco. Sweden. pp.1-85.

Stille, H., Holmberge, M. and Nord, G. (1989), Support of weak rock with grouted bolts and shotcrete, Int. J. of Rock Mechanics and Min. Sci. & Geomech. Abstrs., 26(1), pp.99-113.

Stille.H. (1992), Rock support in theory and practice, Int. Symp. of Rock support in Mining and Underground Construction, Canada, pp.421-437.

Sun, X. (1983) Grouted rock bolt used in underground engineering in soft surrounding rock or in highly stressed regions, Proc. int. Symp. Rock Bolting, Abisko, 1983, pp. 345-352.

Tepfers R. (1973): A theory of bond applied to overlapped tensile reinforcement splices for deformed bar. Dissertation, Publication 73:2, Chalmers University of Technology, Division of Concrete Structures, Göteborg, Sweden, 1973, 328 pp.

Tepfers, R. (1979) Cracking of concrete cover along anchored deformed reinforcing bars. Magazine of Concrete Research Vol. 31, No 106, March 1979, pp. 3-12.

Wijk, G. (1978). A theoretical remark on the stress field around prestressed rock bolts. Int. J. of Rock Mechanics and Min. Sci. & Geomech. Abstrs. Vol. 15, pp.289-294.

Windsor, C.R and Thmpson, A.G. (1993), Rock reinforcement-technology, testing, design and evaluation. Comprehensive Rock Engineering Principals, Practice and Projects (Ed.J.A.Hudson), V.4, pp. 451-484.

Winsdor C.R. (1997), Rock reinforcement systems, Int. J. of Rock Mechanics and Min. Sci. & Geomech. Abstrs., 34(6), pp.919-951.

Xiao S J, Chen C F. (2008) Mechanical mechanism analysis of tension type anchor based on shear displacement method. J Central South Univ Technol 2008; Vol15 pp106 -110

Yap, L. P. and Rodger, A. A. (1984), A study of the behaviour of vertical rock anchors using the finite element method, Int. J. of Rock Mechanics and Min. Sci. & Geomech. Abstrs, 21(2), pp.47-61.

Yazici, S. and Kaiser, P. K. (1992), Bond strength of grouted cable bolts, Int. J. of Rock Mechanics and Min. Sci. & Geomech. Abstrs, 29(3), pp.279-292.

Yoshinaka, R., Sakaguch, S., Shimizu, T., Arai, H. and Kato, E. (1987), Experimental study on the rock bolt reinforcement in discontinuous rocks, Proc. of Int. Society for rock Mechanics, Australia, NWU, Balkema and Canadian rock Mechanics Association, pp.1329-1332.